Scanning tunneling microscopy studies of fivefold surfaces of icosahedral Al-Pd-Mn quasicrystals and of thin silver films on those surfaces

by

Baris Unal

A dissertation submitted to the graduate faculty

in partial fulfillment of the requirements for the degree of

DOCTOR OF PHILOSOPHY

Major: Materials Science and Engineering

Program of Study Committee:
Patricia A. Thiel, Major Professor
Rohit K. Trivedi
Krishna Rajan
Alan I. Goldman
Gordon J. Miller

Iowa State University

Ames, Iowa

2008

Dedicated to Gülden, my loving wife, to my family and
to everybody who have played a crucial role in my life.

TABLE OF CONTENTS

GENERAL INTRODUCTION

In conventional crystallography, crystals are constructed by unit-cells repeated in a periodic fashion.[1] This periodic long range order is only compatible with two-, three-, four- and six-fold point symmetries. Therefore, certain rotational symmetries are forbidden by the requirement of the translational symmetry or invariance. In other words, a crystal with a five-fold or more than six-fold rotational symmetry is impossible.

In 1982, everything changed with the discovery of the Al-Mn alloy produced by rapid solidification via melt-spinning process.[2] With a transmission electron microscope, Shechtman et al.[2, 3] observed relatively sharp Bragg peaks with ten-, six- and two-fold rotational symmetries. The solid was showing its icosahedral symmetry and the material possessed a long range rotational order without translational symmetry. This was a shocking discovery and, more importantly, it was an announcement for a new state of condensed matter so-called quasicrystal.[2] Ten years later, in 1992, the International Union of Crystallography redefined "crystal" as "a solid having an essentially discrete diffraction pattern".[4]

However, the icosahedral phase was truly metastable, because, although this phase nucleated and grew at different cooling rates, after heating at 673 K it was transformed to a stable Al_6Mn crystalline phase.[2] Only after 2 years, the first stable quasicrystal (i-Al-Li-Cu) was found. It was prepared by conventional casting and solidification techniques not by rapid solidification.[5] After this discovery, lots of new quasicrystals have been identified. Today, most of the known quasicrystals are Al rich binary or ternary intermetallics.[6]

There are two main groups of quasicrystals, namely, icosahedral and decagonal.[7, 8]

Icosahedral quasicrystals are aperiodic in three dimensions while decagonal ones are aperiodic in two dimensions and periodic in one dimension.[7, 8] The most success has been achieved in producing centimeter size, single grain icosahedral quasicrystals in Al-Cu-Fe and Al-Pd-Mn systems,[9, 10] and decagonal quasicrystals in Al-Ni-Co system.[11, 12] Hence, these are the most commonly studied quasicrystals among the others.

Quasicrystals have peculiar physical and electronic properties compared to their constituent elements and even compared to their crystalline cousins which have similar chemical compositions.[7] For example, all of the known quasicrystals are relatively brittle and hard. Moreover, they exhibit low electrical and thermal conductivities. Especially, as temperature decreases, their electrical resistivity increases. For crystalline metals or metallic alloys, the ratio of the resistances, $\rho(4K)/\rho(300K)$ is about 10^{-3} while for quasicrystals it is about 2 to 10.[13] The other special properties of quasicrystals are low coefficients of friction, low surface energy and high oxidation resistance.[14]

There has been a great success in resolving the atomic structure of a particular binary icosahedral quasicrystal, namely i-Cd-Yb.[15] However, several models have been proposed to describe the bulk structure of Al rich ternary icosahedral quasicrystals (i.e. i-Al-Pd-Mn and i-Al-Cu-Fe)[16-26] and the discussion about which bulk structural model describes the true atomic structure of these quasicrystals has not been settled down, yet. In these models, the bulk structure has been described as a network of both Mackay and Bergman type clusters. The Mackay cluster is a three-shell-cluster centered on a single atom. On average, it has 51 atoms. The Bergman is a cluster of 33 atoms, consisting of two concentric shells centered on a single atom as well. These two clusters sometimes overlap and sometimes

intersect each other. It has been shown that these two clusters cover the entire atomic positions except for a few percent of the atomic sites.

Today, whether the Bergman and the Mackay clusters are inherently stable units or they are just geometric entities for the convenience of describing the bulk structures for icosahedral quasicrystals is still a hot discussion topic in the quasicrystal field. This is partially due to the lack of information about how these clusters form and overlap during the growth. On the other hand, some physical phenomena in quasicrystals, such as electrical and thermal conductivity, as well as fracture and plastic deformation, can be explained easily in terms of localized properties of the clusters.[27-31] Alternatively, the structure of icosahedral quasicrystals can be described by quasiperiodic stacking of aperiodic dense flat planes along the fivefold axis.[20, 32, 33]

Quasicrystals have also drawn considerable interest in the field of surface science. Many state-of-the-art surface sensitive techniques including, but not limited to, scanning tunneling microscopy (STM),[34-37] low energy ion scattering (LEIS),[38, 39] low energy electron diffraction (LEED)[32, 33] and x-ray photoelectron diffraction (XRD)[40] have been used to investigate their surface structures as well as their surface chemistry. It should be noted that all of these techniques provide complementary information regarding to surface structure and surface chemistry. More importantly, these types of studies require a clean, well prepared surface and this is only possible if the surface is prepared in ultra-high vacuum (UHV) environments.

There are several ways to prepare a clean surface in UHV. For quasicrystals, fracture,[29, 41, 42] mechanical scraping [43] and sputter-annealing [34, 35, 44-46] techniques have been employed so far. For example, fracturing in-situ can produce a clean

surface that is free of bulk contamination but the surface may not be the true equilibrium surface. Mechanical scraping can remove the surface contaminants; however, it damages the surface structure and may induce a formation of a disordered surface phase. In sputter-annealing method, first, the surface is bombarded with a high energy beam of noble-gas atoms, generally Ar^+, to remove the contaminations from the surface. However, while cleaning, sputtering destroys the surface structure and also it changes the surface compositions in alloys due to the preferential removal of lighter elements. For example, preferential sputtering of Al from icosahedral Al-Pd-Mn and also from icosahedral Al-Cu-Fe quasicrystal surfaces is well known.[47, 48] Therefore, to restore the surface structure as well as surface composition, after the sputtering step, annealing at a proper temperature is necessary.[36, 49-61]

However, the surface equilibration process involves extensive structural and chemical changes. For instance, annealing between 300 and 700K yields a very rough crystalline surface phase.[62] This phase is relatively Al deficient.[62] Annealing around 700K may results in an intermediate phase that is both rough and quasicrystalline.[63, 64] Above 700K, generally, a *laterally* bulk terminated quasicrystalline phase with step-terrace morphology forms.[32, 33, 36, 59, 61, 65-67]. On the other hand, the factors which favor some planes over others as surface terminations are more complex and very subtle and still a hot debate topic since, in the bulk, there are many dense planes and in principle none of them are identical.[68] To address this, in this dissertation, we present the first systematic surface preparation study done on the icosahedral Al-Pd-Mn system between 900 and 950K.

For the fivefold clean surface, from the STM studies, it is known that terraces are separated both by 0.660 nm (L) and 0.408 nm (S) steps in a sequence that forms a part of

Fibonacci chain.[46, 69] The ratio of the step heights is the golden mean ($\tau = 2\ \mathrm{Cos}\ (\pi/5) = ((1+\sqrt{5})/2)=1.618\ldots$). It should be noted that sometimes, surfaces have defects which can lead to a non-Fibonacci sequence,[59, 60] nevertheless, the existence of two types of step heights is a robust property of the quasicrystalline fivefold surfaces.[36, 46, 50, 59-61, 66, 67, 70] Using dynamical LEED in conjunction with LEIS, it has been shown that the surfaces of i-Al-Pd-Mn qc are *laterally* bulk terminated and the preferred terminating layers are Al rich self similar planes.[32, 33] In addition, the terminating layer is composed of two closely spaced planes whose total density is around 13.6 atoms/nm^2.[32, 33]

High resolution STM studies have revealed the atomic structure of the clean surfaces of the quasicrystals. On fivefold surface, several distinctive recurring local motifs have been observed. Those are star-shaped hollow sites so-called dark stars.[36, 37, 61, 66, 71-73]. It has been shown that the dark stars have the same orientation within the terrace, and across all the terraces.[37] In addition, the density of the dark stars varies from terrace to terrace.[37] The origin of dark stars sites has been a discussion topic so far. Based on purely geometric considerations, several authors[24, 36, 37] proposed that dissected Bergman clusters form the dark stars. However, recently, this interpretation has been challenged by the *ab initio* DFT simulations for the high resolution STM images.[74] The calculations have suggested that dissected Mackay clusters should be the dark stars.[74] It should also be noted that the DFT calculations were not done on quasicrystals, because the aperiodic structure leads to open boundary conditions. Therefore, the calculations have been done for large unit-cell crystalline approximants. Moreover, only one type of chemical decoration for the dark star site has been considered in the calculations. Therefore, the conclusions regarding the quasicrystalline surface structure as well as the dark stars were drawn from these results. In

this dissertation we present the first and the most comprehensive analyses for the available bulk structural models of i-Al-Pd-Mn quasicrystal to shed light on this debate.

Besides the interesting clean surface structure, the interaction of adsorbate with the quasicrystalline surface is also a fascinating topic due to their intriguing symmetries and physical properties. There are several interesting questions one can ask, such as: Is there a specific adsorption site for the film nucleation? If there is, how does this film nucleate? Is it, in principle, possible to obtain a single element monolayer quasicrystalline film? How does the quasicrystalline substrate affect the growth of the film? Some of these questions have been partially answered. For example, based on LEED and HAS studies, Franke et al.[75] reported that Bi and also Sb grown on the fivefold surface of icosahedral Al-Pd-Mn and the tenfold surface of decagonal Al-Ni-Co formed quasicrystalline monolayer. Later, several research groups have performed STM investigations on the nucleation of several adsorbates including, but not limited to, Al on fivefold surfaces of i-Al-Cu-Fe,[76] and Cu,[37, 77] and C_{60}[55] on fivefold surfaces of i-Al-Pd-Mn at very low coverage (i.e. less than 10% of a monolayer).

Especially, at coverage of about 0.04 monolayer, Al adatoms formed small fivefold clusters (called starfish) at room temperature, and all the starfish oriented along the same direction in a single terrace and even across the terraces. This was the first real space observation for an adsorbate which adopted fivefold symmetry. In addition, the island density, as a function of deposition flux has also been studied while keeping the deposition temperature constant at 300K. And, it has been observed that island density didn't vary from 8×10^{-5} to 7×10^{-3} monolayer per second (ML/s).[76] The independence of island density on the deposition flux is a good indication of inhomogeneous nucleation in which certain sites

serve as nucleation sites.[78] Indeed, with the help of high resolution STM images, the nucleation sites for Al adatoms were unambiguously determined as dark stars.[76] Moreover, recent Kinetic Monte Carlo (KMC) simulations of an appropriate 'disordered bond network' lattice gas model have supported that the dark star sites are the strong adsorption sites for Al adatoms.[79, 80]

Using a STM, Fournee et al.[81] studied the nucleation of Ag films on fivefold surfaces of i-Al-Pd-Mn at room temperature. At a coverage of 0.2 monolayer, it was found that from 5×10^{-4} to 5×10^{-2} ML/s, Ag island density was independent of deposition flux. Again like for Al adatoms, in this system, some special sites were acting as traps for Ag adatoms. This observation provided an additional support for the characteristics of heterogeneous nucleation on these surfaces. However, no high resolution STM images which may show the structure of the film was achieved for Ag clusters or islands. And, no temperature dependent experiments were done. There were still some important questions that need to be answered. For example, what is the smallest stable cluster size for Ag? This dissertation fills those gaps in the literature.

Fournee et al.[81] also studied the growth of Ag thin films on fivefold surfaces of i-Al-Pd-Mn. At room temperature, the STM images indicated that as the total coverage increased from 0.2ML to 1ML, Ag grew vertically and formed needle-like islands.[81] At 1ML coverage, the film roughness was higher than that of predicted for kinetically-limited growth where almost no interlayer mass transport is allowed.[78] This was an indication that the up-hill diffusion process was facile. Furthermore, from 1ML up to 5ML total coverage, no significant change in roughness was observed; instead, three-dimensional Ag islands formed at 1ML and then they spread laterally and coalesced and formed relatively flat top

islands.[81] All this observations have indicated that the quasicrystal surface plays an important role in the growth process of the films. Unfortunately, no temperature depended experiments for the growth of the Ag films were explored. In this dissertation, we have investigated and presented the growth of Ag islands on these surfaces in great detail.

Dissertation Organization

Eight papers are included in this dissertation. The first paper, "Terrace selection during equilibration at an icosahedral quasicrystal surface", is published in Physical Review B 71, 165411, 2005. The second paper, "Voids and pits on sputter-annealed fivefold terraces of icosahedral Al-Pd-Mn quasicrystals, is published in Philosophical Magazine 86, 816, 2006. The third paper, "Comparison between experimental surface data and bulk structure models for quasicrystalline AlPdMn: Average atomic densities and chemical compositions", is published in Physical Review B 77, 195419, 2008. The fourth paper, "Adsorption sites on quasicrystal surfaces: Dark stars and white flowers", will be submitted to Journal of Physics: Condense Matter. The fifth paper, "Nucleation and growth of Ag islands on fivefold Al-Pd-Mn quasicrystal surfaces: Dependence of island density on temperature and flux" is published in Physical Review B 75, 064205, 2007. The sixth paper, "Terrace-dependent nucleation of small Ag clusters on a five-fold icosahedral quasicrystal surface", is published in Philosophical Magazine 87, 2995, 2007. The seventh paper, "Growth of height-selected Ag islands on fivefold icosahedral AlPdMn quasicrystalline surfaces: STM analysis and step dynamics modeling", will be submitted to Physical Review Letters. The last paper, "Scanning tunneling microscopy and density functional theory study of initial bilayer growth of Ag films on NiAl(110)", is published in Physical Review B 76, 195410, 2007. Following

this paper are general conclusions and the appendices. The first appendix reports supplementary materials for the third paper. The second appendix is an organized record of the collected STM data. The third appendix shows a brief summary of low energy electron microscopy studies.

References

[1] L. Azarroff, *Introduction to Solids* (McGraw-Hill New York, 1960).

[2] D. Shechtman, I. Blech, D. Gratias, and J. W. Cahn, Phys. Rev. Lett. 53, 1951 (1984).

[3] D. Shechtman, and C. I. Lang, MRS Bull. 22, 40 (1997).

[4] I. U. o. Crystallography, *Acta Crystallographia* 1992), Vol. A48, p. 922.

[5] B. Dubost, J. M. Lang, M. Tanaka, P. Sainfort, and M. Audier, Nature 324, 48 (1986).

[6] P. A. Thiel, Prog. Surf. Sci. 75, 69 (2004).

[7] J. M. Dubois, *Useful Quasicrystals* (World Scientific, Singapore, 2005), p. 482.

[8] C. Janot, *Quasicrystals: A Primer* (Clarendon Press, Oxford, 1992), Vol. 48.

[9] A. P. Tsai, A. Inoue, Y. Yokoyama, and T. Masumoto, Mat. Trans. JIM 31, 98 (1990).

[10] A. P. Tsai, A. Inoue, and T. Masumoto, J. Appl. Phys. 26, 1505 (1987).

[11] T. J. Sato, T. Hirano, and A. P. Tsai, J. Crystal Growth 191, 545 (1998).

[12] I. R. Fisher, M. J. Kramer, Z. Islam, A. R. Ross, A. Kracher, T. Wiener, M. J. Sailer, A. I. Goldman, and P. C. Canfield, Phil. Mag. B 79, 425 (1999).

[13] S. J. Poon, Adv. Physics 41, 303 (1992).

[14] C. J. Jenks, and P. A. Thiel, Langmuir 14, 1392 (1998).

[15] H. Takakura, C. P. Gomez, A. Yamamoto, M. De Boissieu, and A. P. Tsai, Nature Materials 6, 58 (2007).

[16] V. Elser, in *Proceedings of the 6th International Conference on Quasicrystals (ICQ6)*, edited by S. Takeuchi, and T. Fujiwara (World Scientific, Singapore, 1998), pp. 19.

[17] A. Yamamoto, H. Takakura, and A. P. Tsai, Phys. Rev. B 68, 094201 (2003).

[18] A. Katz, and D. Gratias, J. Non-Cryst. Solids 153-154, 187 (1993).

[19] A. Katz, and D. Gratias, in *Proceedings of the 5th International Conference on Quasicrystals (ICQ5)*, edited by C. Janot, and R. Mosseri (World Scientific, Singapore, 1995), pp. 164.

[20] M. Boudard, M. de Boissieu, C. Janot, G. Heger, C. Beeli, H.-U. Nissen, H. Vincent, R. Ibberson, M. Audier, and J. M. Dubois, J. Phys. Condens. Matter 4, 10149 (1992).

[21] Z. Papadopolos, P. Kramer, and W. Liebermeister, in *Aperiodic '97: Proceedings of the International Conference on Aperiodic Crystals*, edited by M. de Boissieu, J.-L. Verger-Gaugry, and R. Currat (World Scientific, Singapore, 1998), pp. 173.

[22] P. Kramer, Z. Papadopolos, and W. Liebermeister, in Proceedings of the 6th International Conference on Quasicrystals (ICQ6), edited by S. Takeuchi, and T. Fujiwara (World Scientific, Singapore, Singapore, 1998), pp. 71.

[23] G. Kasner, Z. Papadopolos, and P. Kramer, Mater. Sci. Eng., A A294-296, 355 (2000).

[24] G. Kasner, Z. Papadopolos, P. Kramer, and D. E. Bürgler, Phys. Rev. B 60, 3899 (1999).

[25] A. Fang, H. Zou, F. Yu, R. Wang, and X. Duan, J. Phys.: Condense. Matter 15, 4947 (2003).

[26] M. Quiquandon, and D. Gratias, Phys. Rev B 74, 214205 (2006).

[27] C. Janot, and M. de Boissieu, Phys. Rev. Lett. 72, 1674 (1994).

[28] C. Janot, Phys. Rev. B 53, 181 (1996).

[29] P. Ebert, M. Feuerbacher, N. Tamura, M. Wollgarten, and K. Urban, Phys. Rev. Lett. 77, 3827 (1996).

[30] M. Feuerbacher, C. Metzmacher, M. Wollgarten, K. Urban, B. Baufeld, M. Bartsch, and U. Messerschmidt, Mater. Sci. Eng. A 233, 103 (1997).

[31] R. Mikulla, P. Gumbsch, and H.-R. Trebin, Phil. Mag. Lett. 78, 369 (1998).

[32] M. Gierer, M. A. Van Hove, A. I. Goldman, Z. Shen, S.-L. Chang, C. J. Jenks, C.-M. Zhang, and P. A. Thiel, Phys. Rev. Lett. 78, 467 (1997).

[33] M. Gierer, M. A. Van Hove, A. I. Goldman, Z. Shen, S.-L. Chang, P. J. Pinhero, C. J. Jenks, J. W. Anderegg, C.-M. Zhang, and P. A. Thiel, Phys. Rev. B 57, 7628 (1998).

[34] T. M. Schaub, D. E. Bürgler, H.-J. Güntherodt, J. B. Suck, and M. Audier, Appl. Phys. A 61, 491 (1995).

[35] T. M. Schaub, D. E. Bürgler, H.-J. Güntherodt, and J.-B. Suck, Z. Phys. B 96, 93 (1994).

[36] Z. Papadopolos, G. Kasner, J. Ledieu, E. J. Cox, N. V. Richardson, Q. Chen, R. D. Diehl, T. A. Lograsso, A. R. Ross, and R. McGrath, Phys. Rev. B 66, 184207 (2002).

[37] J. Ledieu, and R. McGrath, J. Phys. Cond. Matter 15, S3113 (2003).

[38] C. J. Jenks, and R. Bastasz, Progress in Surface Science 75, 147 (2004).

[39] C. J. Jenks, A. R. Ross, T. A. Lograsso, J. A. Whaley, and R. Bastasz, Surf. Sci. 521, 34 (2002).

[40] J.-C. Zheng, C. H. A. Huan, A. T. S. Wee, M. A. Van Hove, C. S. Fadley, F. J. Shi, E. Rotenberg, S. R. Barman, J. J. Paggel, K. Horn, P. Ebert, and K. Urban, Phys. Rev. B 69, 134107 (2004).

[41] P. Ebert, F. Kluge, B. Grushko, and K. Urban, Phys. Rev. B 60, 874 (1999).

[42] P. Ebert, F. Kluge, M. Yurechko, B. Grushko, and K. Urban, Surf. Sci. 523, 298 (2003).

[43] Z. M. Stadnik, D. Purdie, M. Garnier, Y. Baer, A.-P. Tsai, A. Inoue, K. Edagawa, and S. Takeuchi, Phys. Rev. Lett. 77, 1777 (1996).

[44] A. R. Kortan, R. S. Becker, F. A. Thiel, and H. S. Chen, Phys. Rev. Lett. 64, 200 (1990).

[45] M. Erbudak, T. Fluckiger, A. R. Kortan, and R. Luscher, Progress in Surface Science 75, 161 (2004).

[46] T. M. Schaub, D. E. Bürgler, H.-J. Güntherodt, and J. B. Suck, Phys. Rev. Lett. 73, 1255 (1994).

[47] Z. Shen, P. J. Pinhero, T. A. Lograsso, D. W. Delaney, C. J. Jenks, and P. A. Thiel, Surf. Sci. 385, L923 (1997).

[48] C. J. Jenks, J. W. Burnett, D. W. Delaney, T. A. Lograsso, and P. A. Thiel, Appl. Surf. Sci. 157, 23 (2000).

[49] P. A. Thiel, C. J. Jenks, and A. I. Goldman, in *Physical Properties of Quasicrystals*, edited by Z. Stadnik (Springer-Verlag, Berlin, 1999), pp. 327.

[50] Z. Shen, C. R. Stoldt, C. J. Jenks, T. A. Lograsso, and P. A. Thiel, Phys. Rev. B 60, 14688 (1999).

[51] P. A. Thiel, Ann. Rev. Phys. Chem. 59, 129 (2008).

[52] V. Fournée, and P. A. Thiel, J. Phys. D: Appl. Phys. 38, R83 (2005).

[53] J. Alvarez, Y. Calvayrac, J. L. Joulaud, and M. J. Capitan, Surf. Sci. 423, L251 (1999).

[54] G. Cappello, F. Schmithüsen, J. Chevrier, F. Cominb, A. Stierle, V. Formoso, M. de Boissieu, M. Boudard, T. A. Lograsso, C. Jenks, and D. Delaney, Mat. Sci. Eng. A 294-296, 822 (2000).

[55] J. Ledieu, C. A. Muryn, G. Thornton, R. D. Diehl, T. A. Lograsso, D. W. Delaney, and R. McGrath, Surf. Sci. 472, 89 (2001).

[56] D. Naumović, P. Aebi, L. Schlapbach, and C. Beeli, Mat. Sci. Eng. 294-296, 882 (2000).

[57] F. Schmithüsen, M. de Boissieu, M. Boudard, J. Chevrier, and F. Comin, Mat. Sci. Eng. 294-296, 867 (2000).

[58] Z. Shen, W. Raberg, M. Heinzig, C. J. Jenks, V. Fournée, M. A. Van Hove, T. A. Lograsso, D. W. Delaney, T. Cai, P. C. Canfield, I. R. Fisher, A. I. Goldman, M. J. Kramer, and P. A. Thiel, Surf. Sci. 450, 1 (2000).

[59] T. Cai, F. Shi, Z. Shen, M. Gierer, A. I. Goldman, M. J. Kramer, C. J. Jenks, T. A. Lograsso, D. W. Delaney, P. A. Thiel, and M. A. Van Hove, Surf. Sci. 495, 19 (2001).

[60] T. Cai, V. Fournée, T. A. Lograsso, A. R. Ross, and P. A. Thiel, Phys. Rev. B 65, 140202 (2002).

[61] L. Barbier, D. Le Floc'h, Y. Calvayrac, and D. Gratias, Phys. Rev. Lett. 88, 085506 (2002).

[62] Z. Shen, M. J. Kramer, C. J. Jenks, A. I. Goldman, T. A. Lograsso, D. W. Delaney, M. Heinzig, W. Raberg, and P. A. Thiel, Phys. Rev. B 58, 9961 (1998).

[63] J. Ledieu, A. W. Munz, T. M. Parker, R. McGrath, R. D. Diehl, D. W. Delaney, and T. A. Lograsso, Mater. Res. Soc. Symp. Proc. 553, 237 (1999).

[64] J. Ledieu, A. W. Munz, T. M. Parker, R. McGrath, R. D. Diehl, D. W. Delaney, and T. A. Lograsso, Surf. Sci. 433-435, 666 (1999).

[65] J. Ledieu, R. McGrath, R. D. Diehl, T. A. Lograsso, D. W. Delaney, Z. Papadopolos, and G. Kasner, Surface Sci. 492, L729 (2001).

[66] L. Barbier, and D. Gratias, Progress in Surface Science 75, 177 (2004).

[67] H. R. Sharma, V. Fournée, M. Shimoda, A. R. Ross, T. A. Lograsso, A. P. Tsai, and A. Yamamoto, Phys. Rev. Lett. 93, 165502 (2004).

[68] A. Yamamoto, Phys. Rev. Lett. 93, 195505 (2004).

[69] R. McGrath, L. Leung, S. D. Barrett, and J. Ledieu, Proc. Royal Microscopical Society 40, 215 (2005).

[70] M. Shimoda, H. R. Sharma, and A. P. Tsai, Surface Science 598, 88 (2005).

[71] Z. Papadopolos, P. Pleasants, G. Kasner, V. Fournée, C. J. Jenks, J. Ledieu, and R. McGrath, Phys. Rev. B 69, 224201 (2004).

[72] R. McGrath, J. Ledieu, E. J. Cox, S. Haq, R. D. Diehl, C. J. Jenks, I. Fisher, A. R. Ross, and T. A. Lograsso, J. Alloys Compd. 342, 432 (2002).

[73] R. McGrath, J. Ledieu, E. J. Cox, and R. D. Diehl, J. Phys.: Condens. Matter 14, R119 (2002).

[74] M. Krajci, J. Hafner, J. Ledieu, and R. McGrath, Phys. Rev B 73, 024202/1 (2006).

[75] K. J. Franke, H. R. Sharma, W. Theis, P. Gille, P. Ebert, and K. H. Rieder, Phys. Rev. Lett. 89, 156104 (2002).

[76] T. Cai, J. Ledieu, R. McGrath, V. Fournée, T. A. Lograsso, A. R. Ross, and P. A. Thiel, Surf. Sci. 526, 115 (2003).

[77] J. Ledieu, J. T. Hoeft, D. E. Reid, J. A. Smerdon, R. D. Diehl, T. A. Lograsso, A. R. Ross, and R. McGrath, Phys. Rev. Lett. 92, 135507 (2004).

[78] J. W. Evans, P. A. Thiel, and M. C. Bartelt, Surf. Sci. Rep. 61, 1 (2006).

[79] C. Ghosh, D.-J. Liu, C. J. Jenks, P. A. Thiel, and J. W. Evans, Phil. Mag. 86, 831 (2006).

[80] C. Ghosh, D.-J. Liu, K. J. Schnitzenbaumer, C. J. Jenks, P. A. Thiel, and J. W. Evans, Surf. Sci. 600, 2220 (2006).

[81] V. Fournée, T. C. Cai, A. R. Ross, T. A. Lograsso, J. W. Evans, and P. A. Thiel, Phys. Rev. B 67, 033406 (2003).

TERRACE SELECTION DURING EQUILIBRATION AT AN ICOSAHEDRAL QUASICRYSTAL SURFACE

A paper published in *Physical Review B*

B. Unal, T. A. Lograsso, A. Ross, C. J. Jenks, and P. A. Thiel

Abstract

We investigate the equilibration of a fivefold surface of the icosahedral Al-Pd-Mn quasicrystal at 900–915 and 925–950 K, using scanning tunneling microscopy. After annealing at the lower temperatures, there is a high density of shallow voids on some terraces but not on others; at 925–950 K, the void-rich terraces are much rarer. The terminations that are consumed by voids exhibit a distinctive local atomic configuration, called a "ring" by previous authors. Apparently, through growth and coalescence of the voids, a different termination becomes exposed on the host terraces, which also leads to a change in step heights at the edges of the terraces. We suggest that the shallow steps associated with the voids, and the ring configuration, signal a surface that is in an intermediate stage of structural equilibration.

I. Introduction

Quasicrystals are *nonperiodic*, yet well-ordered, intermetallics. Most known quasicrystals are icosahedral, and most contain 60–70 at. % of aluminum. Studies of their surfaces are motivated by the fact that the icosahedral, aluminum-rich alloys exhibit unusual

surface properties, including low adhesion to polar liquids and low friction.[1–3] Clean surfaces of quasicrystals have been studied intensely, and some general principles have emerged. First, a rich diversity of structures can form, depending upon the history of sample treatment and the length scale of the structural examination. This array of surface morphologies includes rough surfaces,[4–9] faceted voids,[10] and smooth (to within a few tenths of an angstrom) terraces.[6,8,9,11–16] The latter type of structure—flat terraces—is the topic of this paper.

Second, the terraces typically exhibit a fine structure, probed by scanning tunneling microscopy (STM), which is consistent with bulk models of quasicrystalline structure.[13,15–17] This indicates that the lateral sin-planed atomic structure is bulk terminated, resolving a previous controversy over whether bulk termination of a quasicrystal was compatible with a flat surface.

Third, in the bulk-terminated quasicrystal surface, only a subset of all possible bulk planes corresponds to surface terminations. The surface terminations are believed to actually be pairs of planes, separated by 0.48 Å in the bulk, but contracted at the surface to 0.38–0.42 Å. These two planes have a combined density comparable to that of the close-packed surface of pure Al and a combined composition higher in Al than the bulk average.[14,18–23]

Fourth, the quasicrystalline terraces are separated by steps whose heights are not integral multiples, but rather successive multiples of τ, the golden mean **(**$\tau = 2\cos(\pi/5) = (1+\sqrt{5})/2 = 1.618\ldots$**)**. Reports of the step height values have ranged from 6.2 to 6.8 Å for the longest (*L*), 4.0 to 4.2 Å for the medium step (*M*), and 2.4 to 2.6 Å for the shortest (*S*), with uncertainties of about ±0.2 Å. (In some other papers, these three steps have been named *L*, *S*, and S/τ, respectively.) Here, we are not so concerned with the actual step height values

as with their frequencies of occurrence. Previous reports have been inconsistent. One study reported *only* L and M, arranged in a Fibonacci sequence, which implies a relative abundance of $L/M=\tau$.[11] In contrast, another paper noted that the L and S steps were common, and the M steps were rare.[12] A quantitative analysis in yet another paper indicated that the relative abundance decreased from L to M to S, with frequency ratios $L/M\approx M/S\approx\tau$.[14]

Fifth, the method used to produce the bulk-terminated terraces involves massive changes in both surface composition and surface structure. Ion bombardment at room temperature produces an Al-deficient phase. Annealing between 300 and 700 K yields a very rough crystalline surface phase (lacking discernible terraces) that is relatively Al deficient. There is evidence that migration of bulk vacancies to the surface contributes to this roughness.[10] At higher temperatures, the surface usually changes to a flat quasicrystalline phase.[24] An intermediate phase that is both quasicrystalline and rough may form around 700 K.[8] Flat *crystalline* phases can also form above 700 K.[25–29] The factors that select between crystalline and quasicrystalline surface phases above 700 K are poorly understood.

In this paper, we show that equilibration during annealing is a more complex and subtle process than previously thought. Even after the quasicrystalline terrace-step structure appears, it evolves with time and temperature. There is a selection among possible terminations, during which some terraces disappear, while other (slightly different) types of terraces survive. This evolution also affects the step heights and may explain previous discrepancies in the literature.

II. Experimental Description

A single grain of icosahedral Al-Pd-Mn was grown by the Bridgman method. Its bulk composition was $Al_{70.2}Pd_{20.7}Mn_{9.1}$, based on scanning electron microscopy and energy dispersive spectroscopy. The grain was sliced perpendicular to its fivefold axis and polished to a mirror finish, using 6-, 1-, and 0.25-mm diamond paste on Texmet cloth. The resultant sample was a flat wafer with an area of 6 X 5 mm^2 and thickness of 1.5 mm, identification No. ARR-4-12-2.1.

The wafer was then mounted on a Ta plate and put into an ultrahigh-vacuum (UHV) chamber equipped for low-energy electron diffraction (LEED), Auger electron spectroscopy (AES), STM, ion bombardment, mass spectrometry, and sample heating. A clean surface was gained after cycles of Ar+ sputtering at room temperature (RT) for 30 min and annealing at 900 K for 3 h. The Ar+ ion energy was reduced from 2 to 1 keV by 0.5-keV increments in the first two cycles and kept constant at 1 keV during the rest of the etching process. The total times for sputtering and annealing were 3 and 18 h, respectively. A sharp LEED pattern was achieved after this cleaning process.

After its initial cleaning, the sample was used for other types of experiments. Consequently, it underwent 26 sputter-anneal cycles and about 60 cumulative hours of annealing at 950 K in UHV. At that point, the experiments described in this paper began. Several observations were made after 950 K anneals. The annealing temperature was then successively lowered to the 900–915 K range, while several more observations were recorded. After this, the sample was removed, repolished, and recleaned in UHV, and more experiments were done in the 900–915 K range. The data reported herein were reproducible and consistent throughout.

Before each individual STM experiment, we sputtered the sample with Ar+ at 1 keV (2.4 μA sample to ground with +20 V bias) for 30 min and then annealed it for 3 h at a specified temperature in the range 900–950 K, by changing the power of the heating element. After annealing, the sample was cooled slowly to RT. The cooling rate from the annealing temperature to 700 K was controlled at about 12.5 K/min. Before annealing, the surface cleanliness was verified by AES. All the STM images were taken at RT with tunneling conditions of +0.97 V and 0.47 nA. The typical base pressure during an STM measurement was below 4 X 10^{-11} Torr.

Temperature was monitored using an infrared pyrometer with emissivity set at 0.35.[25] Sources of error in the measurement include film deposition on the window used for pyrometry (due to evaporation from the sample and other sources), stray radiation from the filament heater, and thermal gradients across the (poorly conductive) sample. Based upon comparisons with two sets of K-type thermocouples located at different spots on the sample holder and upon pyrometer readings taken from different points on the sample itself, we estimate that the accuracy in sample temperatures reported here is about ±25 K, and this should be kept in mind when comparing temperatures reported by other laboratories. Reproducibility is better, although it still is affected by thermal gradients within the sample and hence by the region chosen for imaging.

III. Experimental Results and Interpretation

Figure 1(a) shows a large-scale STM image—5000 Å X 5000 Å—of a 5*f* Al-Pd-Mn surface, after annealing at 900 K for 3 h. It is clear that there are two types of terraces. One type has many pockets, or voids, and hence has a mottled appearance. The other type is

smooth and nearly void free. Figures 1(b) and 1(c) also illustrate the existence of these two types of terraces, after annealing at 915 K for 3 h. The steps in Fig. 1 fall into the three known groups identified in Sec. I as *L*, *M*, and *S*. Almost all of the voids on the mottled terraces are bordered by *S* steps.

Figure 2(a) is a 1000 Å X 1000 Å image from a surface prepared in a different experiment, but under nominally identical conditions. Four layers are visible and are labeled [1–4], with layer 1 being topmost. Figure 2sad is essentially an im-age of a very large, mottled terrace, in which about half of layer 1 has been removed and half of layer 2 has been exposed. In a localized region of Fig. 2(a), deeper layers—3 and 4—are also visible. Figure 2(b) is a line profile across the arrow in Fig. 2(a). This shows that layers 1 and 2 are separated by *S* steps, whereas layers 2 and 3 are separated by an *M* step.

As an aside, note that the height values that we report for the *L*, *M*, and *S* steps, such as the values given in Fig. 2(b), are not extracted from line profiles, since we find that such values are unreliable. Presumably, this is due to short-scale roughness on the terraces, and longer-range curvature sometimes occurring near the step edges. Both effects are visible in Fig. 2(b). Instead, step height values are much more precise if they are extracted from a histogram of pixel heights in a *rectangular area* that encompasses the step and adjoining terraces, a procedure developed originally by Cai *et al.*[14]

Figure 3 reveals regions of this same surface at higher resolution. Panels (a), (b), and (c) are taken from layers 1, 2, and 3, respectively. A number of local motifs, previously identified in other work,[16] can be seen in each of the three layers. Following previous nomenclature,[16] these are labeled as white stars, dark stars, and white flowers. In Figs. 3(a) and 3(c) (layers 1 and 3), certain additional local configurations look like rings. Rings cannot be found on layer

2 [panel (b)]. Therefore, we postulate that the mottled terraces belong to the class of surfaces that include the "ring" planes in previous previous work by Papadopolos *et al.*[16] and that the nearly-void free terraces belong to the class of surfaces that include the "clear" planes and "Schaub" planes.[16] Figure 4(a) shows the terrace structure that results after annealing at 925 K. Three points are noteworthy. First, at this higher temperature, the mottled terraces are much less frequent, and the surviving terraces are generally larger. Second, a number of small islands are visible on the middle terrace, particularly within the oval. These small islands are 2.5 Å high and are probably remnants of a void-rich termination that was present at an earlier stage. In other words, this entire terrace was probably 2.5 Å higher, earlier in its evolution. Third, pits are visible on the middle terrace, but they are different than the voids on the mottled terraces represented in Fig. 1, because these depressions are circumscribed by *M*-type steps. Deeper levels—about 2.5 Å lower—are also becoming exposed at the bottoms of the pits. These aspects of the pits are illustrated by the line profile in Fig. 4(b). The sharp dip at $x<1400$ Å corresponds to a void at the bottom of the larger pit; its depth and shape, however, are not resolved completely because it is small relative to the size of the image. Apparently, void-rich terminations comprise the floors of these *M*-type pits.

The fine structure on relatively smooth terraces, such as those in Fig. 4(a), is illustrated in Figs. 5(a) and 5(b). No rings can be found. Hence, annealing to higher temperature significantly reduces the occurrence of the terminations that contain ring configurations.Upon heating to 950 K, the data are very similar to those at 925 K. Some void-rich terraces can still be found, but they are significantly less abundant than at the lower range of annealing temperature, 900–915 K.

IV. Discussion

Our main postulate is that, by annealing to 900–915 K and 925–950 K, we are capturing the surface in two different stages of evolution.

First, consider the 900–915 K surface. The data (e.g., Fig.1) show that the voids are bordered by *S* steps. This means that the surface must evolve as illustrated in Fig. 6, which is a schematic cross section of the surface. Loss of material from the crosshatched regions first creates the voids and gives the terrace a mottled appearance. The growth of the voids increasingly exposes a lower termination. When the voids have completely overtaken the terrace, its level is lowered by the step height of the voids, *S*. Hence, the lowering of the terrace changes the down-going step (the one in the left side of Fig. 6) from *L* to $L-S=M$, and the up-going step sin the right sided from *M* to $M+S=L$. The step heights *L* and *M* are chosen arbitrarily for illustration.

The atomic nature of the void-rich versus (nearly) void-free terminations can be identified on the basis of local configurations in the STM images. The critical difference is that the void-rich terminations display the ring configuration, while the others do not.

Papadopolos *et al.*[16] related STM images to specific types of terminations in their three-dimensional tiling model of bulk structure. Within the context of that model and in agreement with experimental work from many groups (as reviewed in Sec. I), all terminations consist of pairs of planes separated (in the bulk) by 0.48 Å. Furthermore, the combined density of these two planes is constant.

In the work of Papadopolos *et al.*[16] two different types of terminations could be identified in the STM data, based on different local configurations. They interpreted these as terminations with different relative densities in the top and underlying plane (the *q* and *b*

plane, respectively, in their nomenclature). In the termination where the density of the top plane is less than the density of the second, the rings shown in Figs. 3(a) and 3(c) were predicted and observed. In the termination where the densities were reversed, no rings were observed and the planes were called "clear." The combined densities of the two planes was effectively constant.

The relative densities could provide a rationale for a slightly lower stability of terminations containing the ring configuration, since higher density is known to be associated with lower surface energy—in elemental metals.[30–32] It has been proposed that this rule also applies to quasicrystals.[22] Since the termination containing rings has a higher atomic density in the very outermost plane, it would have a lower stability. Differences in chemical composition could also contribute to different stabilities of different terminations.

Two detailed structural analyses of this system have been carried out, using two different techniques (low-energy electron diffraction and x-ray photoelectron diffraction) but both based upon electron scattering.[18,19,23] Both analyses found that a certain group of terminations gave the best agreement with experiment, but another group of terminations gave moderately good agreement with experiment. This second group included terminations in which the outermost plane had a lower density than the underlying plane, analogous to the ring-plane terminations of Papadopolos *et al.*[16] The electron scattering analyses left open the possibility that this second group made a minor contribution to the experimental electron scattering data and hence made a minor contribution to the total surface area, in accordance with our model.

Consider the sequence of morphological changes that the surface undergoes. This sequence is illustrated schematically in Fig. 7. Starting from a rough surface without

discernible terraces, extensive mass transport allows terraces to emerge between 700 and 900 K. Apparently, there are kinetic limitations in this stage that lead to different types of terraces with different stabilities. At 900 K, new processes begin which lead to selection among the terrace terminations.There are two possibilities for these new processes.

The first is evaporation into the gas phase. Schmithüsen *etal.*[26] reported that evaporation of Mn begins at 900 K and of Al at 1000 K, this order corresponding to the order of the elemental vapor pressures. Hence, evaporation at these temperatures is sonstoichiometric. The irreversible loss of Mn at 900 K could trigger rearrangements on the terraces that lead to the voids. At 900 K, the remaining Al and Pd could diffuse away to segregate at step edges or defect sites, or to form crystalline surface phases.

The second possibility is that new diffusion processes become activated at 900 K. However, mass transport is already extensive below 900 K—so extensive that the terraces form. For example, the root-mean-square displacement of a bulk Mn atom sthe slowest diffuser in this alloyd is 25 and 50 mm, at temperatures of 900 and 950 K, over 3 h.[33] The fact that this displacement is very large and differs only by a factor of 2 over the temperature range 900–950 K supports the hypothesis that mass transport is extensive already at or below 900 K and does not change dramatically between 900 and 950 K. It has been suggested that surface modification due to migration of bulk defect vacancies also begins in a significantly lower temperature range.[10] Hence, it seems unlikely that new diffusion processes begin around 900 K.

An entirely different interpretation might be that the void-rich terraces do not reflect the relative stability of different terminations, but rather are the result of vacancies migrating from the bulk to the surface and condensing there.[10,34,35] Indeed, there is evidence that this

type of diffusion eventually produces a vacancy-depleted near-surface region that is a few microns deep.[34] In that case, one would expect the void-rich terraces to occur early in the life of the sample and to disappear over time. However, this is the opposite of the sequence of our experiments, wherein most of the higher temperature observations of void-free terraces preceded the lower-temperature observations of void-rich terraces. See Sec. II. Furthermore, in order to account for our observations, the bulk vacancies would have to accumulate preferentially on specific terraces. Taken together, these facts make the vacancy condensation hypothesis seem unlikely. It is commonly accepted that the "best" surfaces on *i*- Al-Pd-Mn, for purposes of STM work, are produced by annealing at 950–975 K or even higher. This falls above the temperature range where the voids are most abundant, 900–915 K. (There may be some small overlap when the probable uncertainty of ±25 K, described in Sec. II, is taken into account and applied both to our own temperatures and to those from other laboratories.) Hence, one would expect that the void-rich terraces are rather rare on the "best" surfaces. Perhaps this is why the evolution of terrace structure has gone unnoticed until now. It is interesting to note that some narrow, void-rich terraces are discernible in STM data published by Ledieu *et al.*, notably Fig. 1 of Ref. 22.

V. Conclusion

The terraced, bulk-terminated quasicrystal undergoes equilibration at 900–950 K, in which certain terraces are modified by the growth and coalescence of voids. This process leads to a change in step heights, particularly a reduction in the density of the *S* steps. The process also leads to a reduction of the terminations that exhibit local ring configurations. We postulate that both the *S* steps and the local ring configurations occur on terminations that

are higher in energy than the others (metastable). A new process—one that was not operative during initial terrace formation—takes effect at and above 900 K. This process, which may be evaporation into the gas phase, facilitates selection among different terminations.
The ring terminations may be less stable because of subtle differences in the densities of the top two planes. Specifically, in the ring terminations the outermost plane is less dense than the (very-close) second plane. In the other terminations, the densities of these two planes are reversed. The combined density of the two planes is nearly constant. A minor contribution from terminations with relative densities corresponding to the ring termination would be consistent with previous structural analyses that were based upon dynamical electron scattering.

Acknowledgments

We thank Zorka Papadopolos for many helpful discussions. This work was supported by the Director, Office of Science, Office of Basic Energy Science, Materials Science Division of the U.S. Department of Energy under Contract No. W-405-Eng-82.

References

1. J. M. Dubois, P. Brunet, W. Costin, and A. Merstallinger, J. Non-Cryst. Solids **334-335**, 475 (2004).

2. J. M. Dubois, J. Non-Cryst. Solids **334-335**, 481 (2004).

3. J. M. Dubois, V. Fournée, and E. Belin-Ferré, in *Quasicrystals 2003—Preparation, Properties and Applications*, edited by E. Belin-Ferré, M. Feuerbacher, Y. Ishii, and D. J. Sordelet, MRS Symposia Proceedings, No. 805 (Materials Research Society,

Warrendale, PA, 2004), p. 287.

4. P. Ebert, M. Feuerbacher, N. Tamura, M. Wollgarten, and K. Urban, Phys. Rev. Lett. **77**, 3827 (1996).

5. P. Ebert, F. Yue, and K. Urban, Phys. Rev. B **57**, 2821 (1998).

6. G. Cappello, F. Schmithüsen, J. Chevrier, F. Cominb, A. Stierle, V. Formoso, M. de Boissieu, M. Boudard, T. A. Lograsso, C. J. Jenks, and D. Delaney, Mater. Sci. Eng., A **294-296**, 822 (2000).

7. P. Ebert, F. Kluge, B. Grushko, and K. Urban, Phys. Rev. B **60**, 874 (1999).

8. J. Ledieu, A. Munz, T. Parker, R. McGrath, R. D. Diehl, D. W. Delaney, and T. A. Lograsso, Surf. Sci. **433-435**, 666 (1999).

9. G. Cappello, J. Chevrier, F. Schmithüsen, A. Stierle, V. Formoso, F. Comin, M. de Boissieu, M. Boudard, T. Lograsso, C. Jenks, and D. Delaney, Phys. Rev. B **65**, 245405 (2002).

10. P. Ebert, M. Yurechko, F. Kluge, T. Cai, B. Grushko, P. A. Thiel, and K. Urban, Phys. Rev. B **67**, 024208 (2003).

11. T. M. Schaub, D. E. Bürgler, H.-J. Güntherodt, and J. B. Suck, Phys. Rev. Lett. **73**, 1255 (1994).

12. Z. Shen, C. Stoldt, C. Jenks, T. Lograsso, and P. A. Thiel, Phys. Rev. B **60**, 14 688 (1999).

13. J. Ledieu, R. McGrath, R. D. Diehl, T. A. Lograsso, D. W. Delaney, Z. Papadopolos, and G. Kasner, Surf. Sci. **492**, L729 (2001).

14. T. Cai, F. Shi, Z. Shen, M. Gierer, A. I. Goldman, M. J. Kramer, C. J. Jenks, T. A. Lograsso, D. W. Delaney, P. A. Thiel, and M. A. Van Hove, Surf. Sci. **495**, 19 (2001).

15. T. Cai, V. Fournée, T. Lograsso, A. R. Ross, and P. A. Thiel, Phys. Rev. B **65**, 140202(R) (2002).

16. Z. Papadopolos, G. Kasner, J. Ledieu, E. J. Cox, N. V. Richardson, Q. Chen, R. D. Diehl, T. A. Lograsso, A. R. Ross, and R. McGrath, Phys. Rev. B **66**, 184207 (2002).

17. L. Barbier, D. Le Floc'h, Y. Calvayrac, and D. Gratias, Phys. Rev. Lett. **88**, 085506 (2002).

18. M. Gierer, M. A. Van Hove, A. I. Goldman, Z. Shen, S.-L. Chang, C. J. Jenks, C.-M. Zhang, and P. A. Thiel, Phys. Rev. Lett. **78**, 467 (1997).

19. M. Gierer, M. A. Van Hove, A. I. Goldman, Z. Shen, S.-L. Chang, P. J. Pinhero, C. J. Jenks, J. W. Anderegg, C.-M. Zhang, and P. A. Thiel, Phys. Rev. B **57**, 7628 (1998).

20. M. J. Capitan, J. Alvarez, J. L. Joulaud, and Y. Calvayrac, Surf. Sci. **423**, L251 (1999).

21. C. Jenks, A. Ross, T. A. Lograsso, J. A. Whaley, and R. Bastasz, Surf. Sci. **521**, 34 (2002).

22. Z. Papadopolos, P. Pleasants, G. Kasner, V. Fournée, C. J. Jenks, J. Ledieu, and R. McGrath, Phys. Rev. B **69**, 224201 (2004).

23. J.-C. Zheng, C. H. A. Huan, A. T. S. Wee, M. A. Van Hove, C. S. Fadley, F. J. Shi, E. Rotenberg, S. R. Barman, J. J. Paggel, K. Horn, P. Ebert, and K. Urban, Phys. Rev. B **69**, 134107 (2004).

24. Z. Shen, M. J. Kramer, C. J. Jenks, A. I. Goldman, T. A. Lograsso, D. W. Delaney, M. Heinzig, W. Raberg, and P. A. Thiel, Phys. Rev. B **58**, 9961 (1998).

25 J. Ledieu, C. A. Muryn, G. Thornton, G. Cappello, J. Chevrier, R. D. Diehl, T. A. Lograsso, D. Delaney, and R. McGrath, Mater. Sci. Eng., A **294-296**, 871 (2000).

26. F. Schmithüsen, G. Cappello, M. D. Boissieu, M. Boudard, F. Comin, and J. Chevrier,

Surf. Sci. **444**, 113 (2000).

27. D. Naumovic, P. Aebi, L. Schlapbach, C. Beeli, K. Kunze, T. A. Lograsso, and D. W. Delaney, Phys. Rev. Lett. **87**, 195506 (2001).

28. C. J. Jenks, T. E. Bloomer, M. J. Kramer, T. A. Lograsso, D. W. Delaney, A. R. Ross, D. J. Sordelet, M. F. Besser, and P. A. Thiel, Appl. Surf. Sci. **180**, 57 (2001).

29. V. Fournée, A. R. Ross, T. A. Lograsso, J. W. Anderegg, C. Dong, M. Kramer, I. R. Fisher, P. C. Canfield, and P. A. Thiel, Phys. Rev. B **66**, 165423 (2002).

30. H. L. Skriver, and N. M. Rosengaard, Phys. Rev. B **46**, 7157 (1992).

31. M. J. Mehl, and D. A. Papaconstantopoulos, Phys. Rev. B **54**, 4519 (1996).

32. L. Vitos, A. V. Ruban, H. L. Skriver, and J. Kollár, Surf. Sci. **411**, 186 (1998).

33. W. Sprengel, T. A. Lograsso, and H. Nakajima, Phys. Rev. Lett. **77**, 5233 (1996).

34. F. Schmithüsen, Ph.D. thesis, Université J. Fourier, 2001.

35. S. Agliozzo, J. Gastaldi, H. Klein, J. Härtwig, J. Baruchel, and E. Brunello, Phys. Rev. B **69**, 144204 (2004).

Figure Captions

Figure 1. STM images of 5f-Al-Pd-Mn, illustrating the existence of void-rich and nearly-void-free terraces. (a) 5000 Å X 5000 Å, after annealing at 900 K. (b) 5000 Å X 5000 Å, after annealing at 915 K. (c) 5000 Å X 3650 Å, after annealing at 915 K.

Figure 2. (a) 1000 Å X 1000 Å STM images of the 5f-Al-Pd-Mn surface after annealing at 900 K. (b) Line profile across (a). For step-height evaluation, see text.

Figure 3. Magnified regions of the three layers labeled in Fig. 2. All images have been filtered. White circles and labels point out local features identified in Ref. 16. (a) 77 Å X 77 Å STM image of layer No. 1 in Fig. 2(a). (b) 77 Å X 77 Å STM image of layer No. 2 in Fig. 2(a). (c) 77 Å X 77 Å STM image of layer No. 3 in Fig. 2(a).

Figure 4. (a) 5000 Å X 5000 Å STM image after annealing at 925 K. (b) Line profile as indicated by the arrow in (a).

Figure 5. High-resolution views of two void-poor terraces, like those shown in Fig. 4(a). The images are both 150 Å X 150 Å in size and have been filtered.

Figure 6. Schematic depiction of the proposed model for terrace selection at 900–915 K.

Figure 7. Schematic depiction of the proposed model for evolution of long-range surface morphology at 700–950 K.

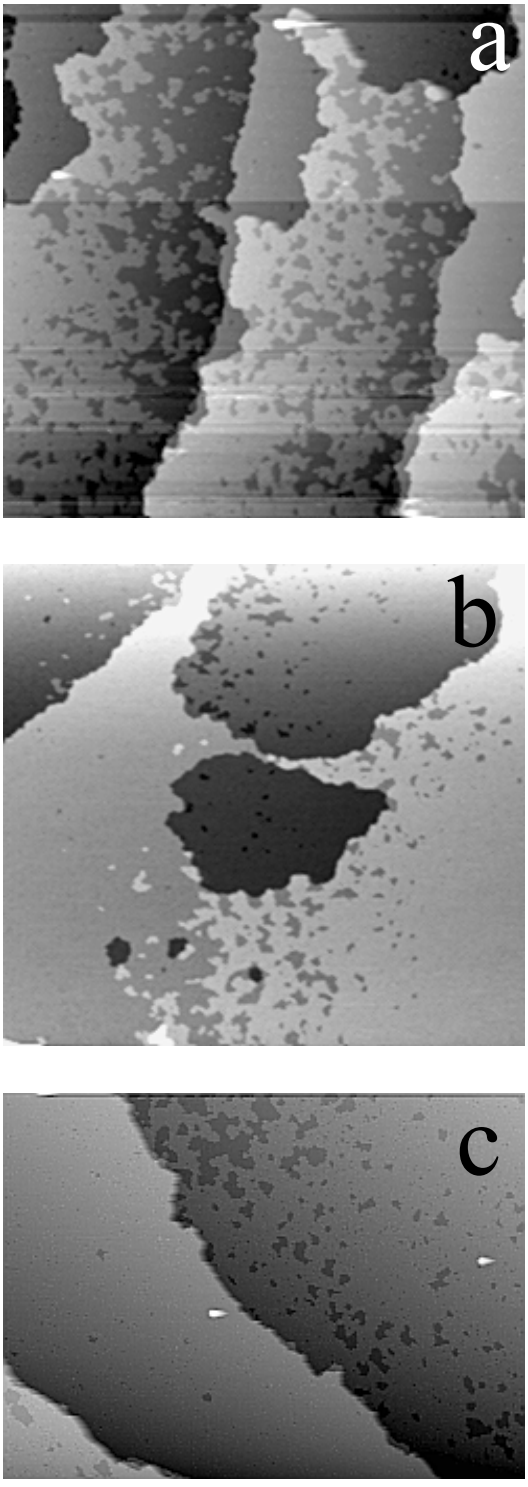

Figure 1

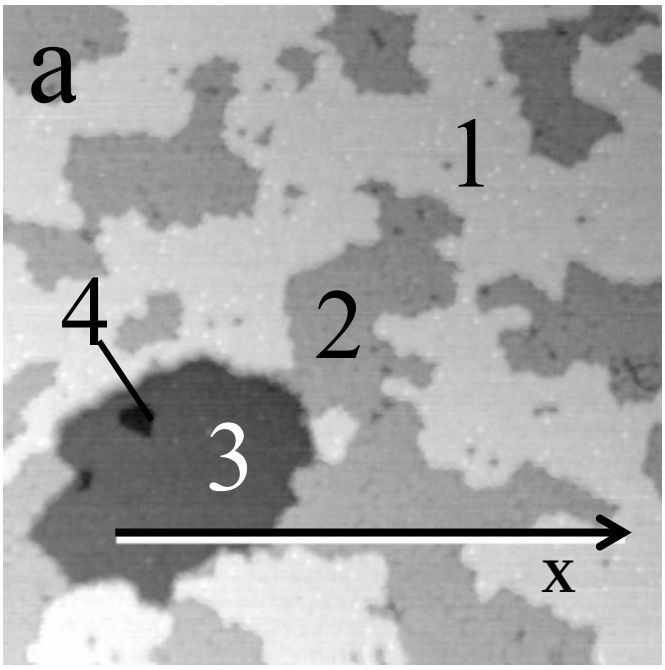

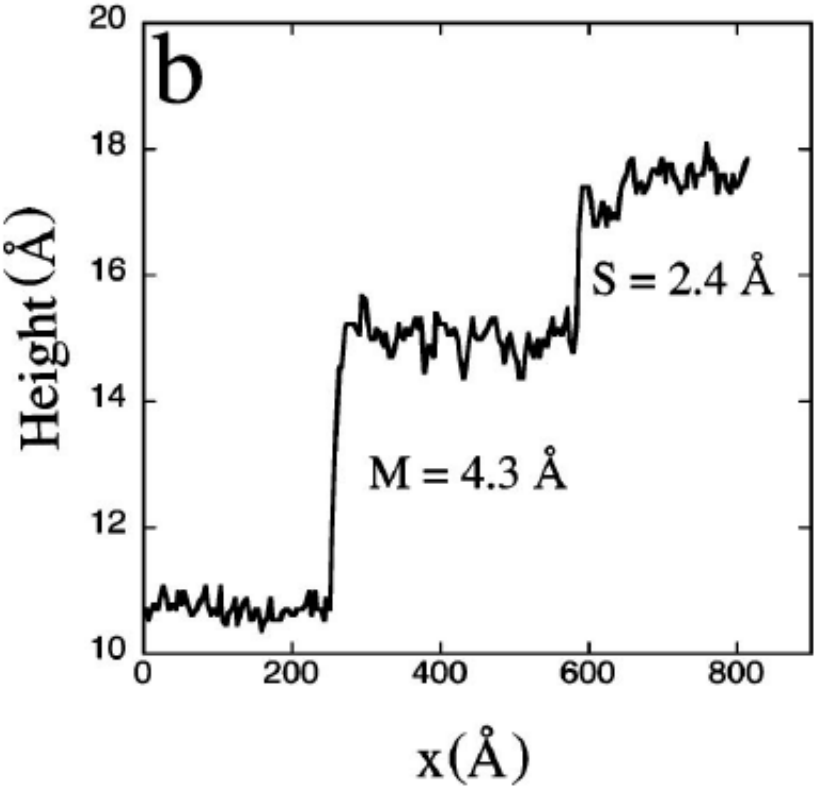

Figure 2

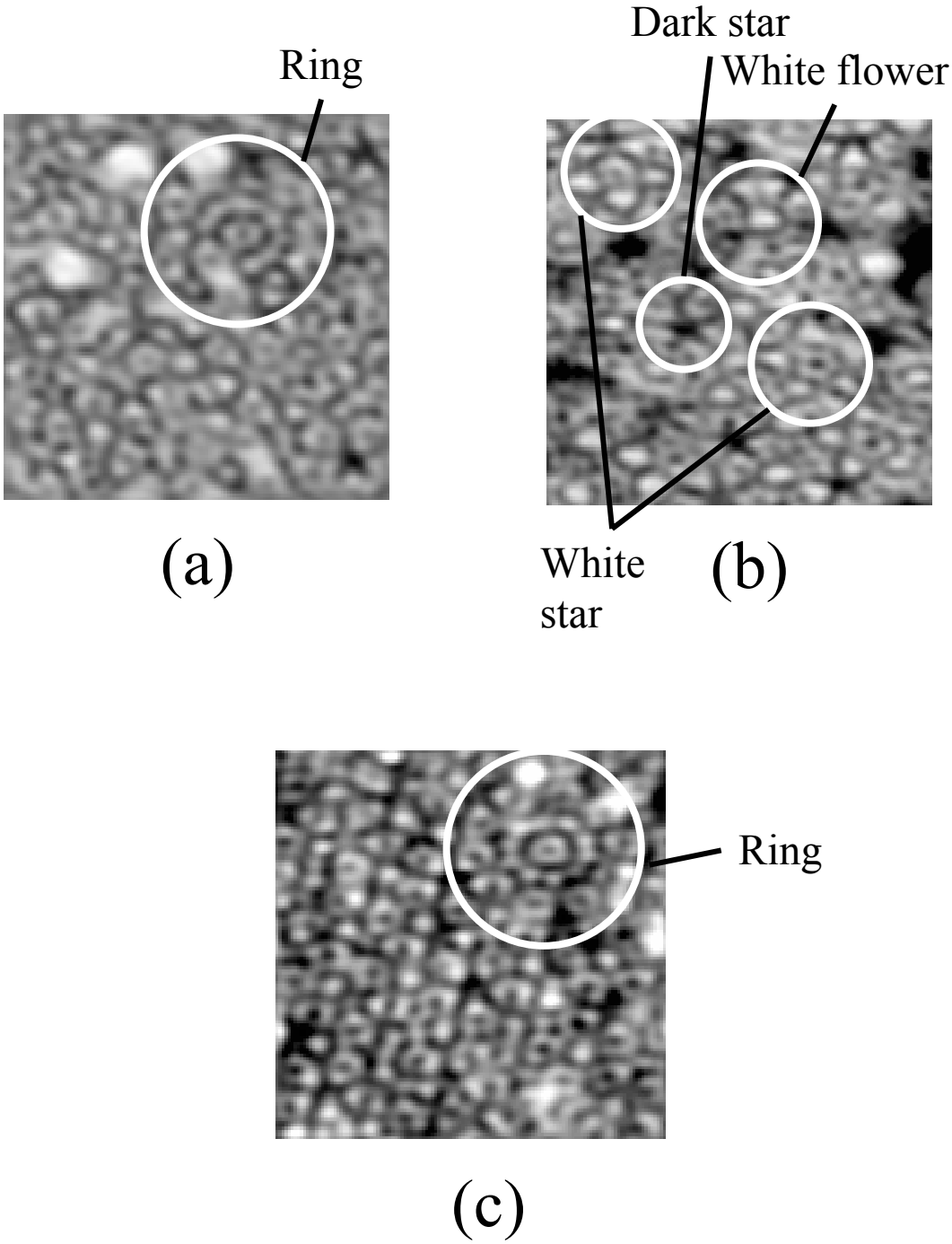

Figure 3

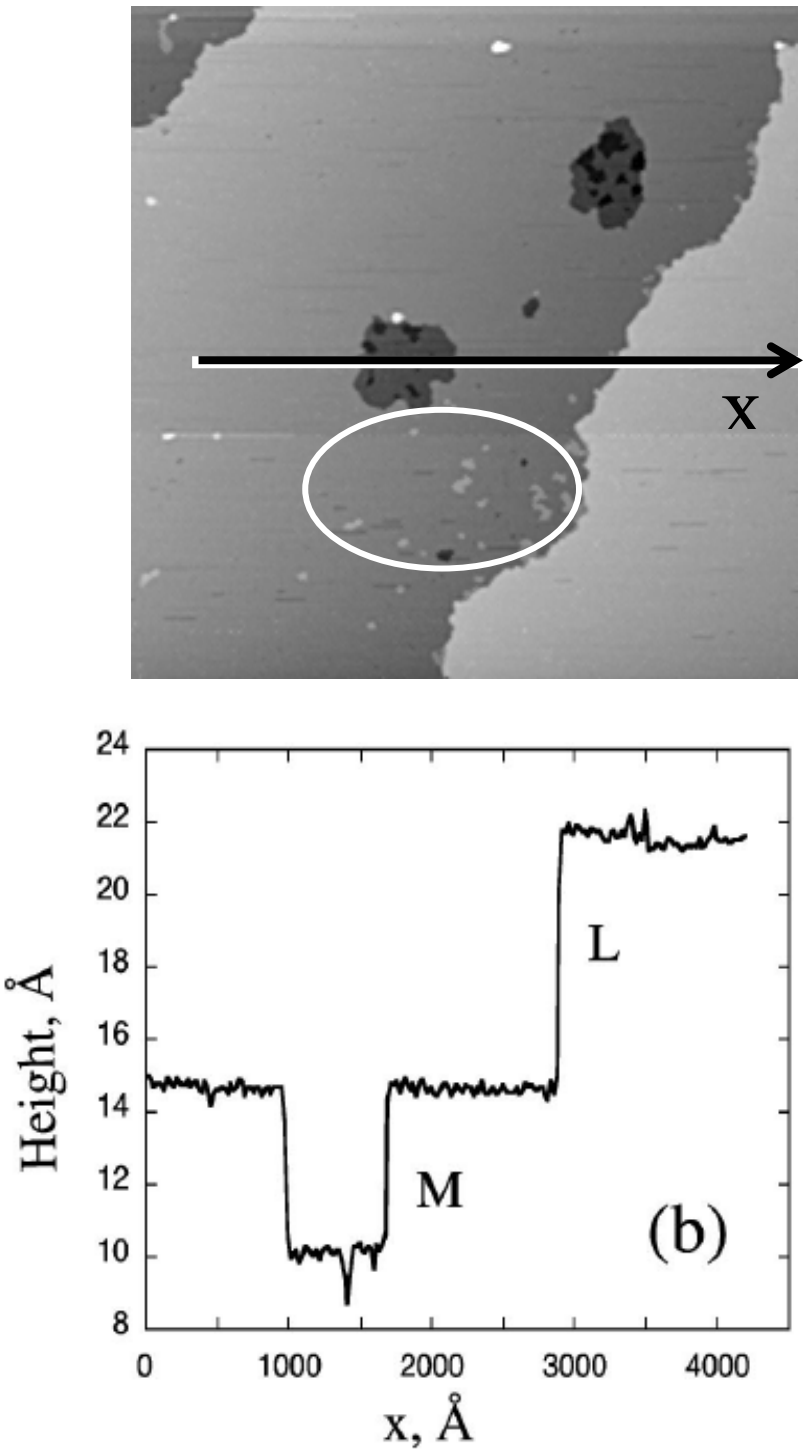

Figure 4

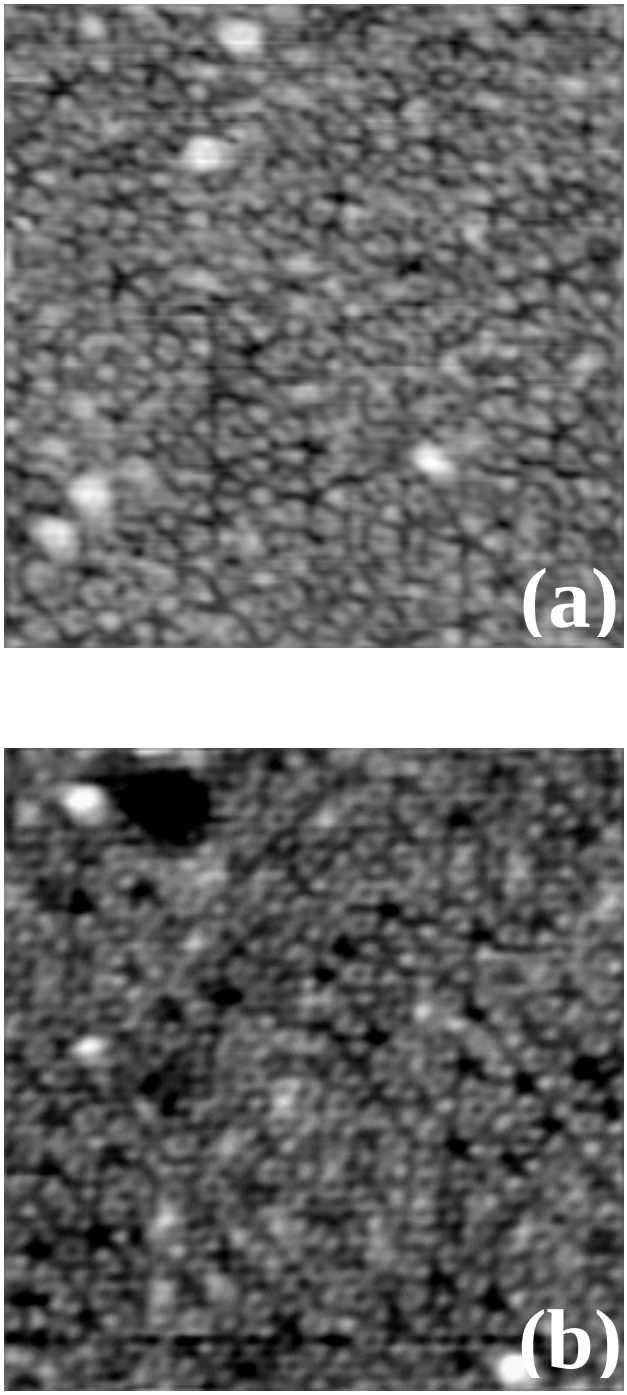

Figure 5

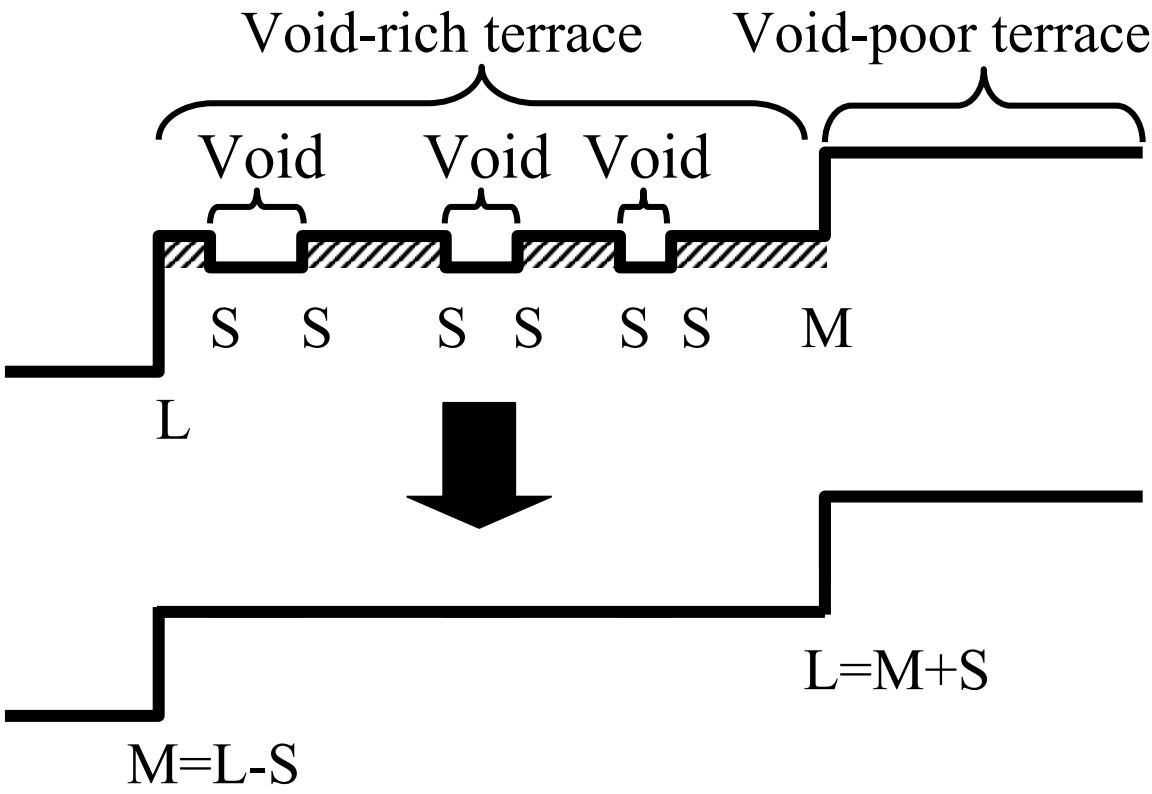
Void-rich terrace
Void-poor terrace
Void
Void
Void
S S S S S S M
L
L=M+S
M=L-S

Figure 6


ΔT
ΔT
Rough Surface
Terraced Surface with Many Ring-Terminations
Terraced Surface With Few Ring-Terminations

Figure 7

VOIDS AND PITS ON SPUTTER-ANNEALED FIVEFOLD TERRACES OF ICOSAHEDRAL AL-PD-MN QUASICRYSTALS

A paper published in *Philosophical Magazine*

B. Unal, T. A. Lograsso, A. R. Ross, C. J. Jenks, and P. A. Thiel

Abstract

Our scanning tunneling microscope studies on clean surfaces of fivefold icosahedral $Al_{70.2}Pd_{20.7}Mn_{9.1}$ reveal that, after annealing at 900 K, two types of flat depressions are visible on terraces: voids (small, shallow, flat-bottomed depressions bordered by 2.5Å steps) and pits (deeper, and often larger, depressions). They are different not only in their dimensions but in their behavior: voids preferentially nucleate on some of the terraces and, after annealing at 925 K, their coalescence and growth leads a new type of termination to be exposed. Pits, however, do not destroy the terraces on which they exist, under the experimental conditions. At the bottom of 4.1Å-deep pits, 2.5Å -deep voids nucleate, so that the total depth of the pit is 6.6Å. We propose that 2.5 Å void-rich terraces are metastable terminations, and that these metastable terminations are also exposed at the bottom of the 4.1 Å -deep pits.

Introduction

Clean surfaces of single-grain samples of crystalline and quasicrystalline metals typically exhibit terrace-step structures, with terrace widths on the order of10^2–10^3Å. Hence,

any macroscopic or even mesoscopic area encompasses many terraces and steps. In a crystalline material, terraces are usually identical (except perhaps for rotational domains), and are energetically degenerate, because a single kind of termination is strongly favored over a small and finite number of other possibilities. Within this context, surfaces of quasicrystals (specifically, of icosahedral quasicrystals) are fundamentally different than crystalline surfaces. This difference arises from the fact that many terminations are very similar, but not identical, either in structure or composition. Hence, a macroscopic surface area of an icosahedral quasicrystal presents an ensemble of different terminations spanning a distribution of surface energies. One could expect that this distribution would narrow during equilibration. In this paper, we focus on experimental evidence that the quasicrystal surface does evolve continuously with time above 900K, peeling away different terminations to expose others, and that different terminations have different stabilities. Hence, the data support the existence of an ensemble of terminations with different surface energies.

The ability to prepare a clean icosahedral quasicrystalline surface in terrace-step morphology, with bulk-termination, is now well established.[1–4] The present paper deals with the fivefold (5f) surface of icosahedral (i) Al–Pd–Mn. On this surface, and also on the 5f surface of i-Al–Cu–Fe, the terraces are generally separated by three kinds of steps, with heights of about 6.6Å , 4.1 Å and 2.5 Å . For simplicity, we refer to them here as 6-, 4- and 2-steps, where the number is the first significant digit in the value of the height. The 6-step can be considered a combination of 4+2, and higher combinations are also observed.[4] Their abundance depends upon sample preparation conditions.

In this paper, the evolution of terraces is characterized by the appearance and growth of flat-bottomed depressions, which are bounded at their edges with one of the three common

values of step height. Depressions with different step-edge values appear to have different behaviors. To distinguish between the two main types of behavior, depressions bounded by 2-steps are called voids, while depressions bounded by higher steps are called pits. Pits bounded by 4- and 6-steps are referred to as 4-type and 6-type pits, respectively. The formation of these features at elevated temperatures may be triggered by evaporation [5], or by diffusion of bulk vacancies to the surface.[6]

Experimental Description

Our sample is a single grain of i-$Al_{70.2}Pd_{20.7}Mn_{9.1}$. The details of sample preparation and characterization are given elsewhere.[7] In brief, we sputtered the sample with Ar^+ at 1 keV for 30 min and then annealed it for 3 h in the range of 900–950 K. Each set of data is obtained in a single sputter-anneal cycle, that is, the sample is never annealed at sequentially higher temperatures in a single run. After heating, the sample is cooled down to 700K at a controlled rate of 12.5Kmin^{-1}. All of the STM images are taken at room temperature under tunneling conditions of 0.47 nA and +0.97 V. They are interpreted as reflecting a morphology that was formed at elevated temperature, and frozen in place during cooling. The base pressure of the UHV chamber throughout the STM experiments is below 4 X 10^{-11} Torr.

Experimental Results and Discussions

We have reported that some terraces contain high densities of voids, after annealing in the temperature range 900–915K.[7] An example is shown in figure 1, which is a 10000Å X 10000 Å STM image of the 5f i-Al–Pd–Mn surface, after annealing at 900K for 3 h. As seen from figure 1 there are two kinds of terraces. One type has many depressions, which give it a

rough appearance. The other type is nearly free of depressions, and hence is relatively smooth. Three types of steps (6, 4 and 2) can be found in figure 1. Nearly all of the depressions on the rough terraces are bordered by 2-steps.

While this provides a description of the two main types of terrace appearance, it should be noted that some terraces bridge these two extremes. For instance, in the terrace below the void-free example in figure 1, two small depressions are visible, and in the next terrace down, a few tens of depressions are visible. These depressions are the 2-type voids.

We have also reported that annealing at higher temperatures (around 925–950 K) significantly reduces the void density.[7] We interpreted this to mean that at higher temperatures, voids coalesce and hence eliminate the termination that was previously exposed on the void-rich terrace. Evidence for this is shown in figure 2a, which is a 5000Å X 5000 Å STM image obtained after annealing at 925K for 3 h. The 2.5 Å high islands within the oval suggest the remnants of a void-rich termination.

These data suggest that the void-rich terminations are relatively unstable; they form at low temperature (<900 K), then are attacked by voids (900–915 K), and eventually disappear at higher temperature (925–950 K). Furthermore, the fact that the void density is variable suggests that there is a continuum of stabilities in the exposed terminations.

The void-rich terraces are almost always bordered by 6-steps in the downward direction. This means that coalescence of the voids lowers the terrace and converts the downward step from 6-type to 4-type. In fact, if the void-rich terraces were bordered by 4-steps in the downward direction, then void coalescence would result in a new step with 1.5Å height. In our experiments, we have never observed terrace steps with 1.5Å height. (Void coalescence would not result in a 1.5Å step if two void-rich terraces were immediately

adjacent and evolved simultaneously, in which case the step separating them would simply remain constant in height. We have observed this phenomenon once, but it does not seem to be common.)

High-resolution STM images have revealed that a local atomic configuration, ring, distinguishes the terminations consumed by the voids.[7] In the Papadopolos–Kasner geometrical model of 5f icosahedral Al–Pd–Mn ,[3, 8, 9] two different kinds of terminations are identified based on the different local atomic configurations.
In the terminations containing ring local configurations, the density of the topmost planes can vary considerably [9] although the sum of the densities of the top two planes (which are separated by ≤0.5Å) is constant.[3] This difference in densities may provide a rationale for the relative instability of a subset of terminations.

The second type of depression is the pits. These are the predominant type of depression at the higher annealing temperature, 925–950 K, although they are never as common as are the voids after the lower annealing temperature, 900–915 K. An example is shown in figure 2a, where a pit is traversed by the white line. There, a 4-type pit is in the middle of the terrace, but it contains some small, deeper (darker) features. The nature of these deeper features is revealed by figure 2b, which is a line profile corresponding to the white line in figure 2a. This shows that some of the regions at the bottom of the pit are 2.5Å deeper and the total depth at the lowest point in the pit, relative to the majority of the terrace, is 6.6Å. In our work, this is a common observation: 4-type pits have 2-type voids in their floors.

We interpret this to mean that terrace evolution also continues at the bottoms

of the 4-type pits. This could mean that the planes exposed by the formation of 4-type pits are relatively unstable. Based upon data such as shown in figure 1, one would expect the 2-type voids at the bottom of the pit to grow faster than the 4-type pit itself, leading to formation of a 6-type pit. We do observe occasional 6-type pits, although they are even more rare than the 4-type pits, under the conditions of our experiments, after annealing in the range 925–950 K. We postulate that they evolve from 4-type pits.

The pits never accumulate preferentially on certain terraces, as do the voids. That is, we never observe terraces that are rich in pits, while others are not. Thus, there is no evidence that the pits aggressively consume the terraces, as do the voids.

The experimental data reveal one other trend concerning the pits. The terraces containing 4-type pits (with 2-type voids in the floor) are usually bordered by 6-steps in the downward direction. This means that if the entire depression in the terrace was to grow indefinitely, the terrace would disappear entirely; it would not simply convert to a different termination, as in the case of the voids.

Our model for the evolution of these surfaces is summarized in figure 3. The evolution of a void-rich terrace to a void-free terrace is shown on the left. Some islands, remnants of the previous termination, are illustrated on the void-free terrace, corresponding to the data of figure 2a. The step heights that border the terrace change. The evolution of a pit is shown on the right. For both the terrace and the pit, the key step in its evolution is the growth and coalescence of voids, which appears to be triggered by annealing to temperatures in the range 900–950 K.

Conclusions

The evolution of this 5f icosahedral surface at elevated temperature is rich and complex. It appears to proceed via the formation of voids and, to a lesser extent, of pits. Voids (depressions with 2.5Å walls) signal metastable terminations. The void density across different terraces suggests a distribution of terminations with different stabilities. Pits with 4.1Å walls expose a metastable termination at the floor, which later will be destroyed by the formation of voids, leading to pits with 6.6Å walls.

Acknowledgment

This work was supported by the Director, Office of Science of Basic Energy Science, Materials Science Division of the U.S. Department of Energy under Contract No. W-405-Eng-82.

References

1. P.A. Thiel, C.J. Jenks and A.I. Goldman, in Physical Properties of Quasicrystals, edited by Z. Stadnik (Springer-Verlag, Berlin, 1998).

2. L. Barbier, D. Le Floc'h, Y. Calvayrac, et al., Phys. Rev. Lett. 88 085506 (2002).

3. Z. Papadopolos, G. Kasner, J. Ledieu, et al., Phys. Rev. B 66 184207 (2002).

4. H.R. Sharma, V. Fourne´ e, M. Shimoda, et al., Phys. Rev. Lett. 93 165502 (2004).

5. F. Schmithu¨ sen, G. Cappello, M.D. Boissieu, et al., Surf. Sci. 444 113 (2000).

6. P. Ebert, M. Yurichko, F. Kluge, et al., Phys. Rev. B 67 024208 (2003).

7. B. Unal, T.A. Lograsso, A. Ross, et al., Phys. Rev. B 71 165411 (2005).

8. G. Kasner, Z. Papadopolos, P. Kramer, et al., Phys. Rev. B 60 3899 (1999).

9. G. Kasner and Z. Papadopolos, Phil. Mag. 86 813 (2006).

Figure Captions

Figure 1. 10000Å X 10000 Å STM image of 5f i-Al–Pd–Mn after annealing at 900 K.

Figure 2. (a) 5000 Å X 5000 Å STM image of 5f i-Al–Pd–Mn after annealing at 925 K, (b) line profile as indicated by a white line in (a).

Figure 3. Schematic of the proposed evolution of (a) terraces and (b) pits, primarily as a function of temperature. The terraces and pits are shown in cross-section, that is, the 5f axis is vertical. The numbers give the first significant digit of the step height.

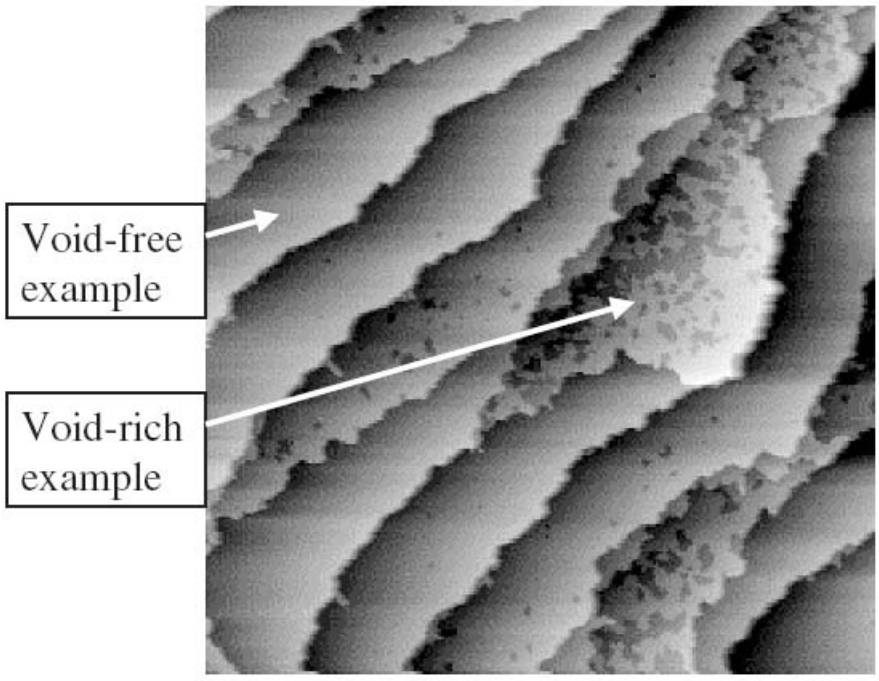

Figure 1

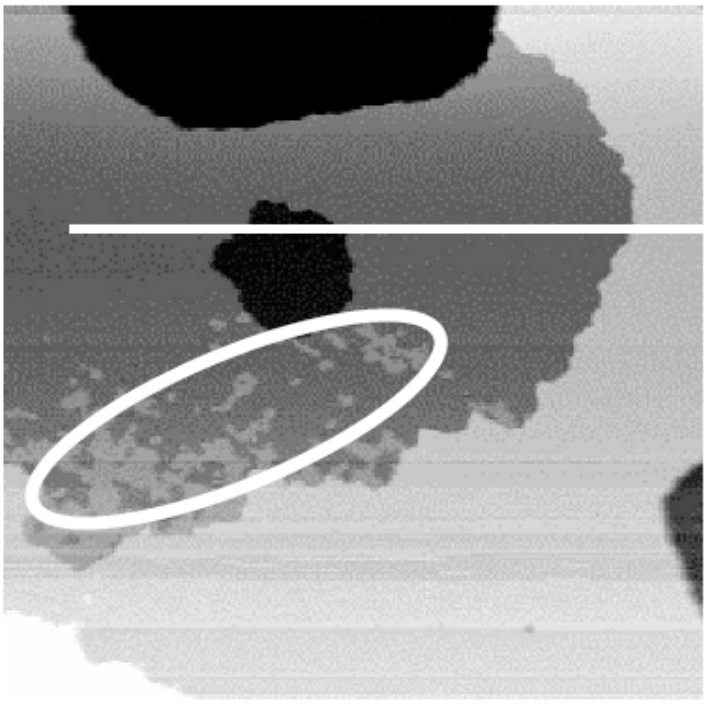

(a)

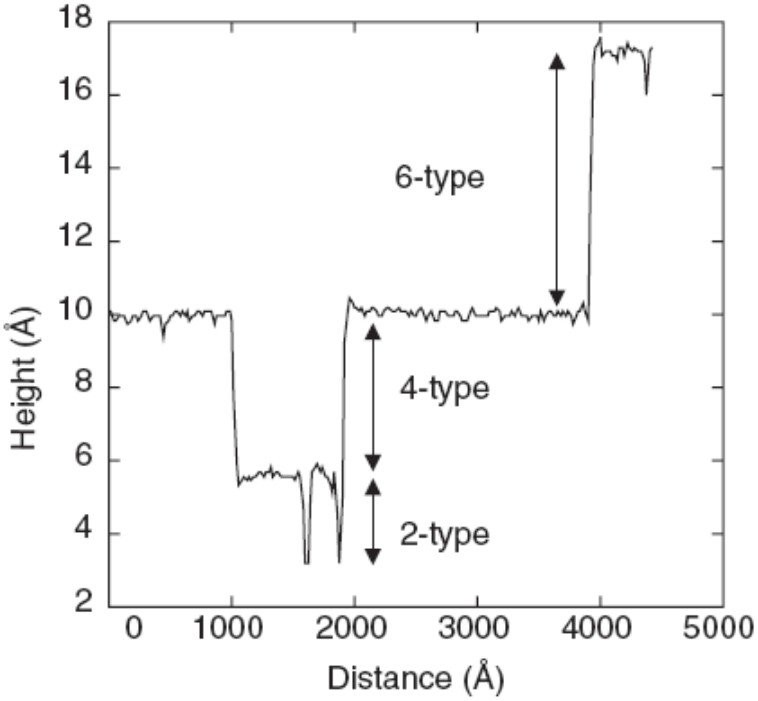
18
16
14
12
10
8
6
4
2
Height (Å)
6-type
4-type
2-type
0
1000
2000
3000
4000
5000
Distance (Å)

(b)

Figure 2

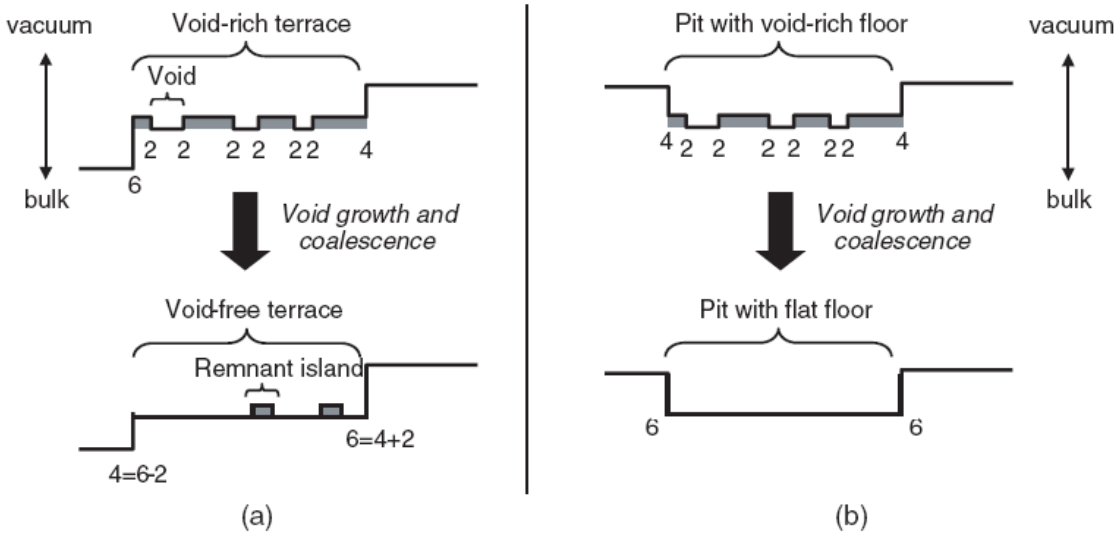
vacuum
Void-rich terrace
Void
2 2 2 2 2 2 4
6
bulk
Void growth and coalescence
Void-free terrace
Remnant island
6=4+2
4=6-2
(a)
Pit with void-rich floor
vacuum
4 2 2 2 2 2 2 4
bulk
Void growth and coalescence
Pit with flat floor
6
6
(b)

Figure 3

COMPARISON BETWEEN EXPERIMENTAL SURFACE DATA AND BULK STRUCTURE MODELS FOR QUASICRYSTALLINE AL–PD–MN: AVERAGE ATOMIC DENSITIES AND CHEMICAL COMPOSITIONS.

A paper published in *Physical Review B*

Baris Unal, C.J. Jenks, and P.A. Thiel

Abstract

We have examined bulk structure models for icosahedral Al–Pd–Mn in terms of the densities, compositions, and interplanar spacings for the 5-fold planes that might represent physical surface terminations. We focus on four models that contain no partial or mixed occupancies, but some comparison is made to a fifth model containing such sites. Each of the four models contains paired planes (layers) that can be separated into two main families on the basis of three features: the relative densities of the two planes, the gap separating the layer from the nearest atomic plane, and the Pd content in the topmost plane. The experimental data and other arguments lead to the conclusion that the family with no Pd in the top plane is favored. Finally, all models show that correlations should be expected between the heights of steps that delineate terraces, and average compositional/structural features of the terraces.

I. Introduction

Quasicrystals are solid materials that are well-ordered, but not periodic.[1-3] They typically exhibit evidence of a forbidden rotational symmetry. Their intriguing atomic structure engenders unusual physical properties, including surface properties such as good oxidation resistance and low friction. This is well-established, at least for the Al-rich, icosahedral (i-) intermetallics, which comprise a large fraction of the hundred or so known quasicrystals.

This type of quasicrystal has proven to be a rich and versatile platform for investigating basic surface phenomena, such as film growth and friction.[4-8] This is largely because the bulk atomic structure propagates up to the surface plane, provided that surface preparation conditions are chosen appropriately.[4-8] Furthermore, clean surfaces with flat terraced morphologies such as that shown in **Fig. 1** can be prepared using fairly standard techniques.[4-8]

Nonetheless, uncertainty remains about significant aspects of the surface structure. This is true in part because different models exist for the bulk structures of these quasicrystals: about 7 different bulk models exist for i-Al–Pd–Mn,[9-20] although not all have been derived independently. Until now, each surface experiment has been compared with a single bulk structural model.[5, 7, 17, 21-32] This limited approach leaves open the question of whether different models might yield different degrees of agreement with experimental surface data. The present paper is the first to provide an analysis or comparison of measurable surface properties that are predicted from *different* models.

Another source of uncertainty about the surface structure lies in the fact that within even a single model, there are a large number of bulk planes that can serve as the surface termination—in principle, no two planes are identical.[13, 33] The solution to this conundrum was originally recognized by Boudard et al.[13] and later exploited by Gierer et al.,[22, 23] who realized that the bulk structure can be classified into groups of self-similar planes, and that one or more groups are probably favored over others as surface terminations. At present, there is a debate as to which group of planes is favored.[29, 34, 35]

A third subtlety arises from the different emphasis that can be placed on the two main components of 'structure:' the atomic positions and their chemical decorations. When comparing experimental data with bulk models, atomic positions have often been emphasized,[24, 26, 27, 29, 31] but chemical identities are important as well, particularly for understanding chemical reactivity of surfaces.

This paper deals with the long-range, average surface structure and surface composition of quasicrystals. Our main goal is to find and differentiate among viable terminations for the 5-fold surface of i-Al–Pd–Mn, and to see how such terminations vary among different structural models. (Because i-Al–Cu–Fe and i-Al–Cu–Ru are considered isomorphic with i-Al–Pd–Mn, some data for their 5-fold surfaces are included as well.) We choose the surface with 5-fold symmetry because it has been documented more extensively than the other high-symmetry, icosahedral surfaces. The strongest, most consistent experimental data lead to the conclusion that three families of planes are possible surface terminations. We discuss the similarities and differences between these families, and conclude that one particular family is more likely than the others. We also analyze whether there is a correlation between the characteristics of a termination (terrace), and the height of the step which bounds it.

In the following section, we introduce the bulk structure models. In Section III we define the two main families of possible terminations, and subsequently compare them with respect to atomic densities, gaps between planes, and chemical compositions. These three factors are known to affect or reflect surface stabilities. We then compare the two families with regards to cut clusters. In Section IV we introduce a third (minority) family. Section V gives some ideas on surface equilibration and how that may affect the surface terminations. Section VI presents a non-deterministic model, and Section VII points out correlations between characteristics of terminations, and heights of adjoining steps.

II. The Bulk Structure Models

The first structure model reported for an icosahedral quasicrystal was based on neutron diffraction data for i-Al–Cu–Fe.[36] With time, it was modified and became known as the Katz-Gratias (KG) model.[11, 12] Second, using X-ray and neutron diffraction, Boudard et al.[13] constructed a bulk structural model for i-Al–Pd–Mn, and this is commonly referred to as the Boudard model. Although its structure was mainly based on the KG model, the Boudard model originally contained unreasonably short bond lengths between some pairs of atoms. Therefore, it was slightly modified to alleviate this problem. In this work, we use the modified version.[23] Recently, using the skeleton of the KG model, Quiquandon and Gratias (QG) proposed another global structural model for both i-Al–Pd–Mn and i-Al–Cu–Fe quasicrystals[20] based on the previous neutron[36] and X-ray[13] diffraction data, combined with magnetic properties. The fourth model used in this paper was proposed by Papadopolos and Kasner (PK).[16, 18]

The above four models contain no sites with mixed or partial occupancy. Models without such sites are sometimes called ‘deterministic’ within the quasicrystal community.

These four models are analyzed in this paper. Non-deterministic models have also been reported by Elser[9] and by Yamamoto.[10] In Sec. VI, we include some analysis of the Yamamoto model as well.

Each of the four deterministic models was originally derived in six-dimensional (6D) space. The structures analyzed here are three-dimensional (3D) slabs. The atomic coordinates within the slabs were provided by authors of the respective models, either directly (by private communication) or indirectly (by posted information on a public web site). Table I gives information about the compositions and sizes of the volumes that were analyzed in this work. It should be noted that each analyzed volume was selected in a way that areas of each 5-fold plane in that slab were the same within a factor of 2. For this reason, the analyzed volumes did not always encompass the entire volume available from the source. In calculating average quantities, the characteristics of each plane were weighted according to its area, although we tested different weighting schemes and found that average quantities varied by less than 2%.

Figure 2 shows an example of the density and composition of planes of atoms, versus their location (x coordinate) in one of the deterministic models (KG). It is assumed that vacuum is on the right and bulk solid is on the left, i.e. a viewer looks “down” at a 5-fold surface plane from right to left. Independent of model, most of the distances (gaps) between any two adjacent planes take values of 0.048, 0.078 and 0.156 nm. Gaps of 0.030 nm can also be found, but rarely and only between planes with very low density. The four deterministic models are very similar with regard to atomic positions and planar densities, and they are virtually identical when represented in the style of **Fig. 2**. Figures showing the other three models in the same fashion are given in the supplemental materials.[37]

The reason for the similarity between the deterministic models can be found in their 6D representations. The 6D space is conventionally divided into two three-dimensional (3D) subsets, called physical or parallel space, and inverse or perpendicular space. [1, 3]

In perpendicular space, each bulk structural model has at least *three atomic surfaces* (also called acceptance domains, or occupation domains) which contain information about the positions of the atoms and their chemical identities. The sizes and the shapes of the atomic surfaces differ from each other within a given model. Indeed, most of the atoms are confined in two large atomic surfaces while a small fraction of atoms are in the third atomic surface.[12, 13, 20, 30] In perpendicular space, the atomic surfaces are 3D objects composed of several concentric shells. The shape and the size of the shells vary from model to model, as well as their chemical decoration. However, in all of the bulk structural models, the two main atomic surfaces are located at the same two kinds of nodes in the 6D lattice. For example, in the Boudard model,[13] one of the large atomic surfaces is located at the (000000) or n_0 node while the other large one is centered at the (100000) or n_1 node. This is a robust property for all the deterministic models discussed in this paper. (See Table I in Papadopolos et al.[38] for comparison of the nodes in several 6D models). The location of the third atomic surface is model dependent but since its contribution is much smaller than the others we will not discuss it here.

By projecting the atomic surfaces from 6D space to 2D space following known procedures, the planes perpendicular to any direction can be generated.[39] Our interest here is in the planes orthogonal to any 5-fold axis. It has been reported that each 5-fold plane is generated by *only one* atomic surface.[27, 30] Therefore, since all the bulk models have the main two atomic surfaces at the same nodes, each 5-fold plane can be classified according to their

atomic surfaces in all those models. In addition, the densities and compositions of the planes depend very much on the part of the atomic surfaces from which the planes are generated.[27] For example, in the KG model, there are dense 5-fold planes that contain only Al atoms. This means that these planes are formed by the central part of the atomic surface at (000000) nodes since the atomic surface at these nodes has only Al atoms.[27] The other dense planes contain Al, Pd and Mn atoms so those planes are generated from the central part of the atomic surface at (100000) nodes. Projections from the periphery of any atomic surface will result in less dense planes.

III. The Two Main Families

Several experiments have shown that the preferred terminations of 5-fold surfaces of i-Al–Pd–Mn and i-Al–Cu–Fe exhibit a structural fingerprint. That is, they consist of two dense planes (a "layer" herein) that are closely spaced. This has been deduced from analysis of intensity-voltage (I-V) data in low energy electron diffraction (LEED),[22, 23, 25] from X-ray photoelectron diffraction (XPD),[40] from low-energy ion scattering (LEIS),[41] and from X-ray scattering.[42, 43] The spacing between the planes at the surface is about 0.04 nm, a contraction of 20% from the bulk value of 0.05 nm.

Another useful input is the heights of steps on surfaces exhibiting terrace-step morphology, such as shown in **Fig. 1**. A number of groups have reported heights of 0.660 nm (L) and 0.408 nm (M), based on STM results for the 5-fold surface of i-Al–Pd–Mn. SPA-LEED analysis of step heights have shown similar values.[44] Analogous values have been reported for 5-fold i-Al–Cu–Ru and i-Al–Cu–Fe. Step heights that are combinations of L and

M have also been observed.[31, 45] The L and M heights sometimes, but not always, constitute a Fibonacci sequence in reported STM images.[31, 46, 47]

In selecting viable surface terminations from the bulk structure models, we only consider layers as defined above. Furthermore, the layers must be separated from adjacent planes by L and M distances, or by linear combinations of L and M. Layers that are viable terminations are labeled at the bottom of **Fig. 2** with brackets. They fall into two distinct families or sets. For reasons presented later, we call them Pd- (without Pd) and Pd+ (with Pd). Note that if the volume is inspected from the opposite direction (with vacuum on the left), then the Pd- terminations become Pd+ terminations, and vice versa. Analyzing from both directions increases the number of terminations in each set, which we employ to maximize the statistical significance of our conclusions. An example of an atomic plane is shown in **Fig. 3.**

Below, we analyze four aspects of these two families. The first three of these are known to influence or reflect surface stability in crystalline materials: Atomic densities, interplanar spacings, and chemical compositions. The atomic density is covered by Bravais' rule, which is an empirical generalization. It states that surface planes with high two-dimensional densities, and correspondingly small interplanar spacings, are most common (although exceptions exist). This is usually taken to mean that these surfaces are most stable.[30] Indeed, calculated surface energies of a single element in the solid phase are usually lowest for the hexagonally close-packed surface.[48] In alloys, one expects chemical composition to also play a major role, which can be predicted to first order from the surface energy of the constituent elements. In the quasicrystals under consideration here, Al has a surface energy that is lower than that of the transition metals. For example, the surface

energy of Al is 1.2-1.3 J/m^2, whereas that of Pd is 1.9-2.1 J/m^2.[48] Thus, if atomic densities are equal, one would expect the Al-richest planes to be preferred terminations. Both density and composition may be reflected in interplanar gaps, then, with larger gaps corresponding to more stable terminations.

A. Atomic densities

Densities, both of planes and layers, are shown in Table 2. Consider first the total density of the terminating layer. This is very similar for the two families. For all models, this ranges from 13.1 to 14.3 nm^{-2}, with an average of about 13.6 nm^{-2}. Turning to individual planes, the *average* density of the topmost plane is clearly different for the two families; it is about 7.6 for the Pd- set, and 6.2 for the Pd+ set, with a range of 4.3 to 9.1 nm^{-2}. The numbers reflect different *relative* densities of the two top planes in the two families. About 70% of layers in the Pd- set have top planes that are more dense than the plane that is 0.05 nm beneath, while about 70% in the Pd+ set have top planes that are less dense. This complementarity stems from the fact that any given layer can belong to either family, depending only upon viewing direction as noted above.

Experimental data are currently insufficient to distinguish between the two families on the basis of relative or absolute densities. A value of 13.5 nm^{-2} is frequently quoted from the LEED I-V analysis,[22, 23] for the composite density averaged over many terraces.[22] However, this value actually rests upon the assumption of a particular bulk structure model (the modified Boudard model). The number was calculated from the densities of planes that provided the optimal fit to the experimental data *within that model*, and hence cannot be regarded as a model-independent value. Another potential source of atomic densities is STM,

but several assumptions and ambiguities are involved in this approach too.[49] One problem is that an image of a single terrace may not represent the ensemble average. In our experience, different terraces are more or less amenable to high-resolution imaging. It is natural to select terraces that provide the best images, but this may result in selection of non-representative terminations (e.g. those with lowest density in the top plane might provide poorer images). Keeping these reservations in mind, numbers can be derived from STM. An atomic density of 8 nm^{-2} has been reported for the top plane,[31] and values of about 4 nm^{-2} can be derived from other images.[27, 50] These values fall within the range of densities (4.3 to 9.1 nm^{-2}) of the topmost plane for either the Pd- or the Pd+ set in the models. See Table II. (Comparison with average values is not useful since the available STM data do not provide averages.)

B. Gaps Between Planes

A second point of comparison between the two families is the width of the gaps that are cleaved to form the surface. From **Fig. 2**, it can be seen that all of the Pd- terminations cleave the bulk at 0.156 nm wide gaps, the widest possible spacing between two adjacent planes. (This value of 0.156 nm is not the step height, since that would be the spacing *between adjacent* 0.156 nm gaps.) All of the Pd+ terminations cleave the bulk at smaller gaps of 0.078 nm. In quasicrystals, it has been proposed that the spacing between adjacent planes influences the selection of terminations.[13, 31] This reflects the fact that a large interplanar gap implies weaker bonding between planes, and hence a lower total surface energy for the two adjacent planes. This correlation between interplanar spacing and surface energy suggests that the Pd- set should be the preferred type of termination.

C. Chemical Composition

Table III shows that in the Pd- set, the top plane is mainly or completely Al. It may contain some Mn, but *never* Pd. In the Pd+ set, the top plane *always* contains Pd (on average in excess of 40 atomic %), typically being a mixture of Al, Pd, and Mn. This general description applies to all 4 models. Papadopolos et al.[29] have proposed that the Pd+ set are terminations on 5-fold surfaces of i-Al–Pd–Mn (although we wish to note that Papadopolos et al. have expressed reservations about the chemical decoration used.[51, 52]) On the other hand, a termination similar to those in the Pd- family has been used in density functional simulations of surface properties of Al–Pd–Mn rational approximants. [35, 53-55]. In addition, a termination belonging to the Pd- family was used for generating potential energy surfaces and subsequent Kinetic Monte Carlo simulations of Al adatoms.[56, 57]

The models can be compared with experimental data for both Pd and Mn content. Regarding Pd content, LEED I-V data for 5-fold i-Al–Pd–Mn were fit best by terminations that contained an average of 93 at% Al, 7 at% Mn, and no Pd in the top plane, within the context of the modified Boudard model. In other words, there was a clear preference for the Pd- set over the Pd+ set. An analogous result was obtained for the 5-fold surface of i-Al–Cu–Fe, i.e. no Fe was found in the topmost plane.[25] LEIS also indicated that the top plane is Al-rich, whereas the second plane is relatively rich in Pd.[41] Other types of surface sensitive analyses—X-ray photoelectron spectroscopy or Auger electron spectroscopy—have provided information that is not useful in the present context since these techniques average over many layers and therefore give bulk compositions. Overall, the LEED I-V data and the LEIS data indicate that the majority of surface planes belong to the Pd- set.

Regarding Mn content in the top plane, there are two reports based on low-energy ion scattering data. The first indicated a range of 0.4 to 6.3 at% Mn, while the second, more sophisticated study indicated an upper limit of 1 at%. The LEED I-V analysis set an upper limit of 10 at%. An STM study reported a mean surface Mn concentration of about 0.2 nm^{-2}, assuming that every adsorbed Si atom occupied a Mn site.[58] This translates into a top-layer Mn concentration of 2.5-3.3 at%, using the average densities of the top planes in either the Pd- or Pd+ sets (cf. Table II). Taken together, the data indicate that the average Mn concentration in the topmost plane is between 0 at% and 10 at%, and most probably $\leq$ 4 at%.

Table III contains the information needed to predict Mn content from the 4 models, for both the Pd- and Pd+ terminations. It can be seen that the range of average Mn content in the top plane, across the different models, is about the same for the two families: from 0 to 15% in the Pd- set, and 0 to 19% in the Pd+ set. These ranges certainly encompass all of the experimental values. Hence, Mn content cannot be used to discriminate between the two main families.

D. Cut Clusters

Much past discussion of surface structure has revolved around the local structure, which in turn relates to clusters that can be identified in the bulk.[1-3] These clusters are nested polyhedra consisting of a few tens of atoms. In the deterministic models, two types of clusters are commonly identified, called Bergman and Mackay. In icosahedral materials, any plane through the bulk intersects some of these clusters. Cut clusters have been associated with certain local features in STM images of the 5-fold surfaces, the so-called dark stars, which are important adsorption sites.[5, 56, 57, 59-61]

The two main families differ in the way that the top planes cut bulk clusters in the models. The Pd- family cuts Mackay clusters 0.252 nm above or 0.204 nm below the equator, thereby producing features that are strong candidates for the dark star sites. The Pd+ family cuts Bergman clusters 0.078 nm below the equator, producing a competing candidate for the dark star sites. From our assertion that the Pd- family is more likely to be the preferred termination, it follows that the dark star sites are more likely to be cut Mackay clusters than cut Bergmans.

IV. A Third Family

A third type of termination can be described as a group of three planes, separated by two gaps of 0.05 nm. The middle plane is denser than the two outer ones. We call these groups "triplets." One such group is enclosed by a light rectangle in **Fig. 2**. Most triplets contain a pair of planes that is comparable in density to the pairs in the two main families.

The triplets cannot account for all of the surface terminations, because the experimental M step height is 0.408 nm, while the separation between triplets is at least 0.864 nm, using the dense middle plane of each triplet to define its location. However, it is possible that the triplets coexist with other terminations. Indeed, two LEED I-V studies[22, 23, 25] and one XPD study[40] showed previously that the ensemble of surface terminations contains 10-30% triplets. For examples, see the terminations labeled B and E in Fig. 4 of Ref. [40], or the fifth arrow from left in Fig. 9 of Ref. [25].

Each of the less dense planes at the edge of a triplet, 0.05 nm from the middle plane, is formed by a projection from the periphery of one of the two main atomic surfaces in 6D. (See Sec. II.) We note that there is no fundamental difference between the dense paired

planes in the Pd+ and Pd- families, and the planes in the triplets, with respect to the 6D representation. The distinction between triplets and the other two families appears in 3D when we impose the simplifying constraint that planes with very low atomic density (< 1 nm^{-2}) are unimportant.

V. Surface Equilibration

The degree to which triplets, or even mixtures of Pd+ and Pd- terminations, are present on a real surface probably depends upon conditions of preparation. In all of the data reviewed in this paper, surfaces were prepared by ion bombardment at room temperature, followed by annealing. After the initial structural and chemical disruption caused by ion bombardment, the surface must regenerate, with the bulk sample serving as both template and reservoir. During re-growth, metastable phases and features can appear and disappear. For instance, a cubic phase forms at moderate annealing temperatures, and is replaced by the quasicrystalline phase around 700 K.[62]

In one study it was found that if the quasicrystalline surface phase is annealed no higher than 915 K, it includes metastable terminations.[63] The signature of these transitory terminations is a dense network of voids, through which the more stable termination at the bottom of the voids becomes progressively exposed with increasing annealing temperature.[45, 63, 64] On i-Al–Pd–Mn, the voids have a depth of 0.25 nm.[63] This value can be reconciled with transitions between terminations in different families. These arguments will be presented elsewhere. The main point here is that the voids provide evidence that terminations from different families coexist, at least under some circumstances. Further evidence for coexisting families can be inferred from an XPD study[40] in which the surface was heated to a relatively

low temperature, 800 K. Under these conditions, equal contributions from Pd+ and Pd- families were found, together with triplets. It is possible that the Pd+ set is metastable at such low preparation temperatures.

VI. A Non-Deterministic Model

Some characteristics of the Yamamoto model, a non-deterministic model, are included in Tables I-III. In calculating average densities and compositions for this model, we weighted each atomic position according to its statistical occupancy and composition. The bulk atomic density is 61.6 nm^{-3}. This is low compared with the densities of the other models, which fall in the range 65.4-66.6 nm^{-3}. The lowness of the value may be related to the partial occupation of sites.

The densities and compositions of atomic planes are shown in **Fig. 4** for the Yamamoto model. There are many atomic planes, but gaps exist between groups of planes. The clustering of planes suggests a natural grouping as shown by the brackets at the bottom of the x-axis in **Fig. 4**. Each bracket is 0.11 nm wide. We call each such group of planes a "layer," by analogy with the deterministic models, even though they do not consist of simple paired planes. The layers can be divided into two families of plausible terminations that are very similar to the Pd+ and Pd- families discussed in Sec. III.

One difference between this model and the deterministic models, is that a layer in the Yamamoto model cannot be divided into two planes separated by 0.050 nm, so the composition of a layer is more spatially continuous. Nonetheless, the compositional trends are the same: There is a Pd- family, in which the Pd concentration increases from top to bottom, and vice-versa in the Pd+ family. Another difference between this model and the

deterministic models, is that the atomic density of the terminating layers is only 12.5 nm^{-2} on average, to be compared with 13.6 nm^{-2} in the deterministic models. This mimics the difference in bulk density noted above, and undoubtedly has the same origin.

Triplets can also be identified in the Yamamoto model, and one example is shown by the gray rectangle in **Fig. 4**.

VII. Correlations between Characteristics of Terminations, and Heights of Adjoining Steps

It has been reported that different terraces can behave much differently as templates for nucleation and growth of metal films.[65, 66] It has also been reported that terrace width is smaller if the terrace is bounded by an M-type step than an L-type step.[67] Furthermore, step bunching on these 5-fold surfaces has been attributed to differences between different terminations.[31] Because of such observations, there has been speculation that step heights on quasicrystals, such as L and M, may correspond to certain densities, compositions, or other features on the adjoining terraces.[67] Our analysis of the models shows that such correlations indeed exist.

To assess correlations in atomic structure, we chose to evaluate the density of the top *plane* in the terminating layer. This metric can be applied to the four deterministic models, but not to the Yamamoto model because in the latter, terminating layers do not consist of only two planes. Table IV shows the result: The density of the topmost plane, for terraces bordered by L-steps, is about 80% lower than the other type of terrace. This is true for the Pd- family. Because of the complementary relationship between the two families, the inverse relationship would hold in the Pd+ family: Top planes of terraces bordered by M-steps would

be about 80% less dense than the other. Table IV shows that the results are nearly identical for the four models, which should be expected since they are so similar in terms of the 6D structure (Sec. II). We do not expect that the Yamamoto model would be significantly different if an analogous metric were devised.

To assess correlations in composition, we evaluate the average Al, Pd, and Mn concentrations in the terminating *layer*. The result is shown in Table IV. Again, there is always a difference between L- and M-type terraces, but now the difference depends strongly on the model. Taking Mn concentration in the Pd- set as an example, terminating layers on L-type terraces contain *more* Mn than M-type terraces in the KG and Boudard models. The L-type terraces contain *less* Mn in the other three models. The average Mn concentration on the two types of terraces differs by as much as a factor of 10 (e.g. KG model).

These results show that there is both a structural and chemical correlation between step height and characteristics of the terminations. The correlation is model-independent for atomic densities of the topmost plane, where the relationship L < M always holds true. However, it is strongly model-dependent for the composition in the terminating pair of planes (layer). Either or both of these correlations could be related to the experimental observations mentioned above. Finally, it should be noted that the correlations apply only to *average* quantities. The distributions sometimes overlap, as can be seen by inspecting the ranges given in Table IV.

VIII. Discussion

In the two main families, we hypothesize that the Pd- set is the more stable type of termination. This is partly because of the larger interplanar gap where the surface is formed,

which signals a lower surface energy. It is also because experimental data indicates that the top plane contains no Pd in i-Al–Pd–Mn, and (analogously) no Fe in i-Al–Cu–Fe. Furthermore, LEIS indicates that the top plane is Al-rich, while the second plane is relatively Pd-rich. The Pd+ family always contains significant Pd in the topmost plane. Our hypothesis has implications for atomic-scale structure on surfaces, because it implies that the dark-star features in STM are cut Mackays rather than cut Bergmans as had been previously proposed by Papadopolos et al.[29]

If one accepts the hypothesis that the Pd- set is the more stable type of termination, can surface science distinguish between the bulk structural models? On the basis of long-range, average information (i.e. information averaged over many terraces) of the type that has been emphasized in this paper, we conclude that it cannot. However, future research may provide such a result by taking advantage of the fact that the structural models differ, not so much in their atomic locations as in their chemical decorations. Specifically, an experiment could be designed to determine the correlation between the chemical composition of individual terraces, and the adjoining step heights. Our analysis (Section VII) reveals that this correlation is quite model-dependent. This approach would differ from experiments designed to date, in that it would provide chemical compositions on individual terraces, as opposed to compositions that are averaged over many terraces.

IX. Conclusions

We have examined 4 deterministic models and 1 non-deterministic model for i-Al–Pd–Mn in terms of the densities, interplanar spacings, and compositions of the 5-fold planes which are viable surface terminations, and we have compared them with available data for 5-

fold surfaces. Each of the 4 deterministic models contains sets of paired planes (layers), and the non-deterministic model contains similar groups of planes. Two main families of layers, which we call Pd- and Pd+, are viable terminations based upon their planar structure and the step heights associated with them. Each layer can belong to either family, depending only upon viewing direction. Besides Pd content, these two sets differ in the average relative densities of the two planes (Pd- having the denser plane on top, usually) and the width of the interplanar gap where the surface forms (Pd- having the larger gap by a factor of 2). The experimental data and other arguments lead to the conclusion that the Pd- family is favored over the Pd+. This implies that a distinctive type of adsorption site, known from STM studies as a dark star, is a cut Mackay cluster. There is evidence that a third family, consisting of triplets, is also present as a minority. Finally, analysis of the models shows correlations between average structure and composition of terminations, and the height of the step adjoining the terrace.

Acknowledgments

This work was supported by the Office of Science, Basic Energy Sciences, Materials Science Division of the U.S. Department of Energy (USDOE). This manuscript has been authored by Iowa State University of Science and Technology under Contract No. DE–AC02–07CH11358 with the U.S. Department of Energy. We are grateful to Denis Gratias, Marianne Quiquandon, Gerald Kasner, Zorka Papadopolos, Akiji Yamamoto, and Marc de Boissieu for supplying us with 3D atomic coordinates of the quasicrystal models. We thank Gerald Kasner for his careful reading and valuable suggestions on this manuscript. We thank Denis

Gratias for his careful reading and also pointing out the common positions of the atomic surfaces in the 6D representations of different models.

References

[1] C. Janot, *Quasicrystals: A Primer* (Clarendon Press, Oxford, 1992).

[2] H.-R. Trebin ed., *Quasicrystals. Structure and Physical Properties* (Wiley-VCH, Weinheim, 2003).

[3] J. M. Dubois, *Useful Quasicrystals* (World Scientific, Singapore, 2005).

[4] R. McGrath, J. Ledieu, E. J. Cox, and R. D. Diehl, J. Phys.: Condens. Matter **14**, R119 (2002).

[5] V. Fournée and P. A. Thiel, J. Phys. D: Appl. Phys. **38**, R83 (2005).

[6] J. Y. Park, D. F. Ogletree, M. Salmeron, R. A. Ribeiro, P. C. Canfield, C. J. Jenks, and P. A. Thiel, Science **309**, 1354 (2005).

[7] H. R. Sharma, M. Shimoda, and A. P. Tsai, Advances in Physics **56**, 403 (2007).

[8] P. A. Thiel, Ann. Rev. Phys. Chem. **59**, 129 (2007).

[9] V. Elser in Proceedings of the 6th International Conference on Quasicrystals (ICQ6), edited by S. Takeuchi and T. Fujiwara (World Scientific, Singapore, 1998) p. 19.

[10] A. Yamamoto, H. Takakura, and A. P. Tsai, Phys. Rev. B **68**, 094201 (2003).

[11] A. Katz and D. Gratias, J. Non-Cryst. Solids **153-154**, 187 (1993).

[12] A. Katz and D. Gratias in Proceedings of the 5th International Conference on Quasicrystals (ICQ5), edited by C. Janot and R. Mosseri (World Scientific, Singapore, 1995) p. 164.

[13] M. Boudard, M. de Boissieu, C. Janot, G. Heger, C. Beeli, H.-U. Nissen, H. Vincent, R. Ibberson, M. Audier, and J. M. Dubois, J. Phys. Condens. Matter **4**, 10149 (1992).

[14] Z. Papadopolos, P. Kramer, and W. Liebermeister in Aperiodic '97: Proceedings of the International Conference on Aperiodic Crystals, edited by M. de Boissieu, J.-L. Verger-Gaugry and R. Currat (World Scientific, Singapore, 1998) p. 173.

[15] P. Kramer, Z. Papadopolos, and W. Liebermeister in Proceedings of the 6th International Conference on Quasicrystals (ICQ6), edited by S. Takeuchi and T. Fujiwara (World Scientific, Singapore, Singapore, 1998), p. 71.

[16] G. Kasner, Z. Papadopolos, and P. Kramer, Mater. Sci. Eng., A **A294-296**, 355 (2000).

[17] G. Kasner and Z. Papadopolos, Phil. Mag. **86**, 813 (2006).

[18] G. Kasner, Z. Papadopolos, P. Kramer, and D. E. Bürgler, Phys. Rev. B **60**, 3899 (1999).

[19] A. Fang, H. Zou, F. Yu, R. Wang, and X. Duan, J. Phys.: Condense. Matter **15**, 4947 (2003).

[20] M. Quiquandon and D. Gratias, Phys. Rev B **74**, 214205 (2006).

[21] P. Ebert, M. Feuerbacher, N. Tamura, M. Wollgarten, and K. Urban, Phys. Rev. Lett. **77**, 3827 (1996).

[22] M. Gierer, M. A. Van Hove, A. I. Goldman, Z. Shen, S.-L. Chang, C. J. Jenks, C.-M. Zhang, and P. A. Thiel, Phys. Rev. Lett. **78**, 467 (1997).

[23] M. Gierer, M. A. Van Hove, A. I. Goldman, Z. Shen, S.-L. Chang, P. J. Pinhero, C. J. Jenks, J. W. Anderegg, C.-M. Zhang, and P. A. Thiel, Phys. Rev. B **57**, 7628 (1998).

[24] Z. Shen, C. R. Stoldt, C. J. Jenks, T. A. Lograsso, and P. A. Thiel, Phys. Rev. B **60**, 14688 (1999).

[25] T. Cai, F. Shi, Z. Shen, M. Gierer, A. I. Goldman, M. J. Kramer, C. J. Jenks, T. A. Lograsso, D. W. Delaney, P. A. Thiel, and M. A. Van Hove, Surf. Sci. **495**, 19 (2001).

[26] J. Ledieu, R. McGrath, R. D. Diehl, T. A. Lograsso, D. W. Delaney, Z. Papadopolos, and G. Kasner, Surface Sci. **492**, L729 (2001).

[27] L. Barbier, D. Le Floc'h, Y. Calvayrac, and D. Gratias, Phys. Rev. Lett. **88**, 085506 (2002).

[28] T. Cai, V. Fournée, T. A. Lograsso, A. R. Ross, and P. A. Thiel, Phys. Rev. B **65**, 140202 (2002).

[29] Z. Papadopolos, G. Kasner, J. Ledieu, E. J. Cox, N. V. Richardson, Q. Chen, R. D. Diehl, T. A. Lograsso, A. R. Ross, and R. McGrath, Phys. Rev. B **66**, 184207 (2002).

[30] Z. Papadopolos, P. Pleasants, G. Kasner, V. Fournée, C. J. Jenks, J. Ledieu, and R. McGrath, Phys. Rev. B **69**, 224201 (2004).

[31] H. R. Sharma, V. Fournée, M. Shimoda, A. R. Ross, T. A. Lograsso, A. P. Tsai, and A. Yamamoto, Phys. Rev. Lett. **93**, 165502 (2004).

[32] F. Yu, H. Zou, J. Wang, and R. Wang, J. Phys.: Condens. Matter **16**, 6821 (2004).

[33] A. Yamamoto, Phys. Rev. Lett. **93**, 195505 (2004).

[34] J. Ledieu and R. McGrath, J. Phys. Cond. Matter **15**, S3113 (2003).

[35] M. Krajci, J. Hafner, J. Ledieu, and R. McGrath, Phys. Rev B **73**, 024202/1 (2006).

[36] M. Cornier-Quiquandon, A. Quivy, S. Lefebvre, E. Elkaim, G. Heger, A. Katz, and D. Gratias, Phys. Rev. B **44**, 2071 (1991).

[37] See EPAPS Document No. E-PRBMDO-77-004819 for the schematic depiction of atomic planes in the PK, QG and Boudard models and also for the compositions and densities of individual planes and layers in the Pd- and Pd+ types of terminations in the KG, PK, QG, Boudard and Yamamoto models. For more information on EPAPS, see http://www.aip.org/pubservs/epaps.html. .

[38] Z. Papadopolos, R. Klitzing, and P. Kramer, J. Phys. A: Math. Gen. **30**, L143 (1997).

[39] L. Barbier and D. Gratias, Progress in Surface Science **75**, 177 (2004).

[40] J.-C. Zheng, C. H. A. Huan, A. T. S. Wee, M. A. Van Hove, C. S. Fadley, F. J. Shi, E. Rotenberg, S. R. Barman, J. J. Paggel, K. Horn, P. Ebert, and K. Urban, Phys. Rev. B **69**, 134107 (2004).

[41] C. J. Jenks, A. R. Ross, T. A. Lograsso, J. A. Whaley, and R. Bastasz, Surf. Sci. **521**, 34 (2002).

[42] M. J. Capitan, Y. Calvayrac, D. Gratias, and J. Alvarez, Physica B (Amsterdam) **283**, 79 (2000).

[43] J. Alvarez, Y. Calvayrac, J. L. Joulaud, and M. J. Capitan, Surf. Sci. **423**, L251 (1999).

[44] R. D. Diehl, J. Ledieu, N. Ferralis, A. W. Szmodis, and R. McGrath, J. Phys.: Condens. Matter **15**, R63 (2003).

[45] M. Shimoda, H. R. Sharma, and A. P. Tsai, Surface Science **598**, 88 (2005).

[46] T. M. Schaub, D. E. Bürgler, H.-J. Güntherodt, and J. B. Suck, Phys. Rev. Lett. **73**, 1255 (1994).

[47] R. McGrath, L. Leung, S. D. Barrett, and J. Ledieu, Proc. Royal Microscopical Society **40**, 215 (2005).

[48] H. L. Skriver and N. M. Rosengaard, Phys. Rev. B **46**, 7157 (1992).

[49] *Other sources of uncertainty are the assumptions that (a) there is a 1:1 correspondence between the bumps in the STM image and the atoms in the topmost plane; and (b) there is no contribution to the STM image from the second plane of atoms*.

[50] B. Unal, J. C. Jenks, and P. A. Thiel, unpublished results (2007).

[51] Z. Papadopolos, O. Gröning, and R. Widmer in Models, Mysteries and Magic of Molecules, edited by J. C. A. Boeyens and J. F. Ogilvie (Springer, 2008).

[52] http://www.quasi.iastate.edu/Papadopolos.html.

[53] M. Krajci and J. Hafner, Phys. Rev. B **75**, 224205 (2007).

[54] M. Krajci and J. Hafner, Surf. Sci. **602**, 182 (2008).

[55] M. Krajci and J. Hafner, Phys. Rev. B **71**, 184207 (2005).

[56] C. Ghosh, D.-J. Liu, C. J. Jenks, P. A. Thiel, and J. W. Evans, Phil. Mag. **86**, 831 (2006).

[57] C. Ghosh, D.-J. Liu, K. J. Schnitzenbaumer, C. J. Jenks, P. A. Thiel, and J. W. Evans, Surf. Sci. **600**, 2220 (2006).

[58] J. Ledieu, P. Unsworth, T. A. Lograsso, A. R. Ross, and R. McGrath, Phys. Rev. B **73**, 012204/1 (2006).

[59] J. Ledieu, C. A. Muryn, G. Thornton, R. D. Diehl, T. A. Lograsso, D. W. Delaney, and R. McGrath, Surf. Sci. **472**, 89 (2001).

[60] T. Cai, J. Ledieu, R. McGrath, V. Fournée, T. A. Lograsso, A. R. Ross, and P. A. Thiel, Surf. Sci. **526**, 115 (2003).

[61] B. Unal, V. Fournée, K. J. Schnitzenbaumer, C. Ghosh, C. J. Jenks, A. R. Ross, T. A. Lograsso, J. W. Evans, and P. A. Thiel, Phys. Rev B **75**, 064205 (2007).

[62] Z. Shen, M. J. Kramer, C. J. Jenks, A. I. Goldman, T. A. Lograsso, D. W. Delaney, M. Heinzig, W. Raberg, and P. A. Thiel, Phys. Rev. B **58**, 9961 (1998).

[63] B. Unal, T. A. Lograsso, A. R. Ross, C. J. Jenks, and P. A. Thiel, Phys. Rev. B **71**, 165411/1 (2005).

[64] B. Unal, T. A. Lograsso, A. R. Ross, C. J. Jenks, and P. A. Thiel, Phil. Mag. **86**, 819 (2006).

[65] H. R. Sharma, M. Shimoda, A. R. Ross, T. A. Lograsso, and A. P. Tsai, Phil. Mag. **86**, 807 (2006).

[66] B. Unal, J. W. Evans, T. A. Lograsso, A. R. Ross, C. J. Jenks, and P. A. Thiel, Phil. Mag **87**, 2995 (2007).

[67] J. Ledieu, E. J. Cox, R. McGrath, N. V. Richardson, Q. Chen, V. Fournée, T. A. Lograsso, A. R. Ross, K. J. Caspersen, B. Unal, J. W. Evans, and P. A. Thiel, Surf. Sci. **583**, 4 (2005).

Table and Figure Captions

Figure 1. (Color online) Semi-three-dimensional STM image of the 5-fold surface of icosahedral Al-Pd-Mn. Size of the image is 250nmx250nm; the tunneling conditions are +0.97V, 0.47nA.

Figure 2. Schematic depiction of atomic planes in the KG model. The x-axis is the 5-fold axis. The spatial coordinate is labeled "(x)" because this is the notation used by the authors of the model. The height of each line is proportional to the planar atomic density. Within each vertical bar, black is Al, gray is Pd, and white is Mn. The light rectangle encloses a triplet.

Figure 3. Atomic arrangements in two adjacent, dense, 5-fold planes in the KG model. The two planes combined would be one layer. The sizes of the figures are 6nmx6nm (a) Pure Al, x=8.58 nm. This would be a top plane in the Pd- family. (b) A mixture of Al, Pd and Mn, x=8.53 nm. This would be a top plane in the Pd+ family. Circle is Al, square is Pd and triangle is Mn.

Figure 4. (color online) Schematic depiction of atomic planes in the Yamamoto model. The z-axis is the 5-fold axis. The spatial coordinate is labeled "(z)" because this is the notation used by the authors of the model. The height of each line is proportional to the planar atomic density. Planes are color–coded for chemical composition, where black is Al, green is Pd, and red is Mn. There are very many planes, but gaps between groups of planes suggest the natural grouping scheme indicated by the

series of 0.11 nm-wide brackets at the bottom. The light rectangle encloses the equivalent of a triplet.

Table I. Information about the bulk structure models of the quasicrystal, i-Al–Pd–Mn, used in this paper. In calculating total number of atoms in the Yamamoto model, sites are weighted according to occupancy. In the four deterministic models, a layer is a pair of planes. In the Yamamoto model, a layer is a group of planes as defined in Sec. VI and Fig. 4.

Table II. Densities of planes and layers in the Pd- and Pd+ types of terminations. Densities are in units of atoms nm^{-2}. For information about individual planes, see supplemental materials.[37] In the four deterministic models, a layer is a pair of planes. In the Yamamoto model, a layer is a group of planes as defined in Sec. VI and Fig. 4.

Table III. Compositions of planes and layers in the Pd- and Pd+ types of terminations, in units of atomic percent. Ranges and averages are given here. For information about individual planes, see supplemental materials.[37] In the four deterministic models, a layer is a pair of planes. In the Yamamoto model, a layer is a group of planes as defined in Sec. VI and Fig. 4.

Table IV. Correlations between densities and compositions of terminations, and step heights, in the Pd- family. Heights of L- and M-type steps are 0.660 nm and 0.408 nm, respectively, for the 5-fold surface of i-Al–Pd–Mn. In the four deterministic models, a layer is a pair of planes. In the Yamamoto model, a layer is a group of planes as defined in Sec. VI and Fig. 4.

Table I

Model	Composition			Size of the region analyzed		Total number of layer identified as viable terminations in the analyzed space
	Al	Pd	Mn	Total number of atoms	Volume (nm^3)	
KG	70.2	21.3	8.5	29,938	4.5×10^2	26
Boudard	68.7	21.9	9.5	293,061	4.4×10^3	36
PK	72.6	20.8	6.6	65,439	1.0×10^3	35
QG	70.4	21.3	8.3	375,825	5.6×10^3	66
Yamamoto	73.0	18.8	8.2	123,204	2.0×10^3	18

Table II

Model	Range of densities of first (top) plane in Pd- or second plane in Pd+	Average density of first plane in Pd- or second plane in Pd+	Range of densities of second plane in Pd- or first plane in Pd+	Average density of second plane in Pd- or first plane in Pd+	Range of lateral densities of terminating layer	Average density of terminating layer
KG	4.60 to 9.12	7.52	4.25 to 8.91	6.48	13.51 to 14.30	13.92
Boudard	4.63 to 8.85	7.57	4.27 to 8.58	5.95	13.07 to 13.71	13.53
PK	4.67 to 8.96	7.61	4.48 to 8.80	6.21	13.31 to 14.15	13.82
QG	4.59 to 8.95	7.56	4.34 to 8.72	6.02	13.16 to 13.89	13.59
Yamamoto	n/a	n/a	n/a	n/a	11.44 to 13.54	12.45

Table III

Model	Range of compositions of first (top) plane in Pd- or second plane in Pd+	Average composition of first plane in Pd- or second plane in Pd+	Range of compositions of second plane in Pd- or first plane in Pd+	Average composition of second plane in Pd- or first plane in Pd+	Range of compositions of terminating layer	Average composition of terminating layer
KG	Al(100.00)	Al(100.00)	Al(23.84-50.60) Pd(18.86-69.58) Mn(0.59-36.93)	Al(36.20) Pd(44.56) Mn(19.24)	Al(56.49-83.40) Pd(9.91-26.12) Mn(0.20-19.74)	Al(70.58) Pd(19.38) Mn(10.04)
Boudard	Al(87.10-100.00) Mn(0.00-12.90)	Al(95.41) Mn(3.59)	Al(26.40-78.20) Pd(21.80-66.83) Mn(0.00-26.25)	Al(38.52) Pd(49.20) Mn(12.18)	Al(57.58-84.22) Pd(7.05-25.55) Mn(2.50-17.04)	Al(69.86) Pd(21.39) Mn(8.76)
PK	Al(82.88-100.00) Mn(0.00-17.12)	Al(95.04) Mn(4.96)	Al(26.11-87.79) Pd(12.21-72.62) Mn(0.00-14.62)	Al(51.77) Pd(43.99) Mn(4.24)	Al(64.56-87.09) Pd(4.16-31.37) Mn(0.00-11.29)	Al(74.67) Pd(19.97) Mn(5.36)
QG	Al(69.35-100.00) Mn(0.00-30.88)	Al(84.83) Mn(15.17)	Al(34.95-82.67) Pd(17.33-65.05) Mn(0.00)	Al(58.38) Pd(41.62) Mn(0.00)	Al(62.12-78.17) Pd(5.69-36.00) Mn(0.00-19.71)	Al(71.06) Pd(19.48) Mn(9.46)
Yamamoto	n/a	n/a	n/a	n/a	Al(72.56–89.75) Pd(2.69–23.37) Mn(2.46–8.86)	Al(79.14) Pd(14.52) Mn(6.34)

Table IV

Model	Type of step bordering termination in down-going direction	Average atomic density in top plane of termination, nm^{-2}	Average atomic density in top plane, L:M ratio.	Average concentration of elements in terminating layer, at% (Range of values for individual terminating layers is given in parentheses.)		
				Al	Pd	Mn
KG	L	6.6	0.74	66.39 (56.49–75.38)	18.13 (9.91–25.74)	15.57 (3.15–19.74)
	M	8.9		76.71 (71.32–83.40)	21.56 (16.40–26.12)	1.73 (0.20–2.92)
Boudard	L	6.8	0.78	65.08 (57.58–72.27)	24.32 (23.18–25.25)	10.59 (3.04–17.04)
	M	8.8		76.85 (72.69–83.34)	17.52 (8.05–24.08)	5.62 (2.50–8.60)
PK	L	6.9	0.78	70.61 (64.56–81.24)	24.54 (12.92–31.13)	4.94 (1.11–9.33)
	M	8.8		81.57 (79.62–84.55)	11.67 (4.16–15.25)	6.76 (5.13–11.29)
QG	L	6.8	0.78	69.83 (62.12–75.90)	25.87 (8.98–36.00)	4.29 (0.00–15.18)
	M	8.8		72.68 (67.29–78.17)	8.98 (6.04–13.67)	18.06 (15.45–19.71)
Yamamoto	L	n/a	n/a	76.70 (72.56–86.34)	17.74 (5.85–23.37)	5.56 (2.46–8.86)
	M	n/a		84.03 (77.77–89.75)	8.08 (2.69–13.81)	7.89 (7.15–8.65)

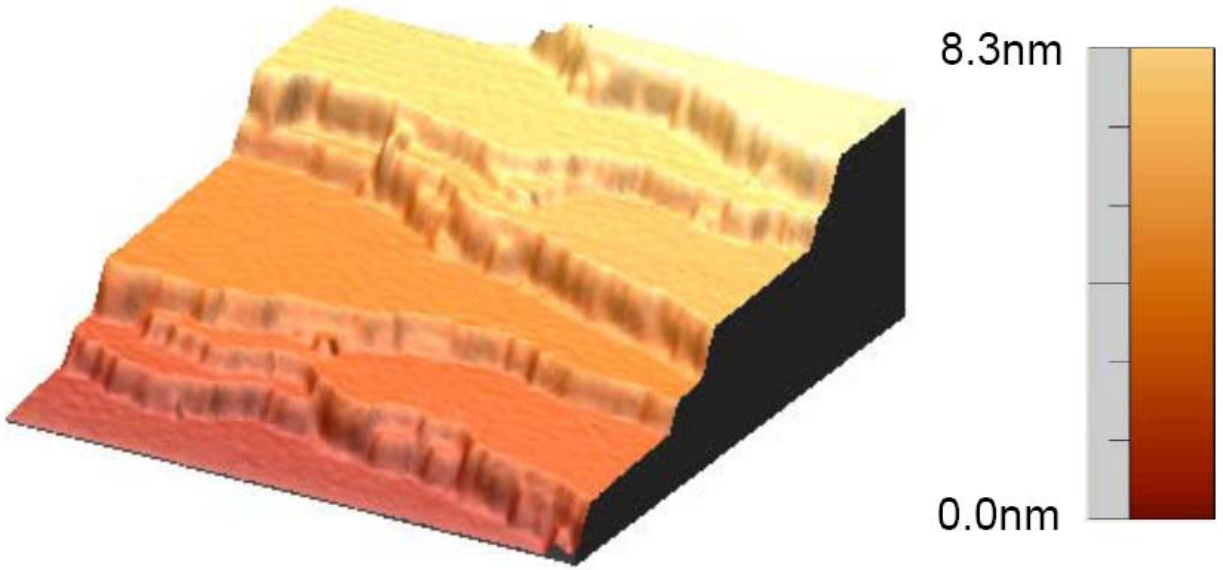

Figure 1

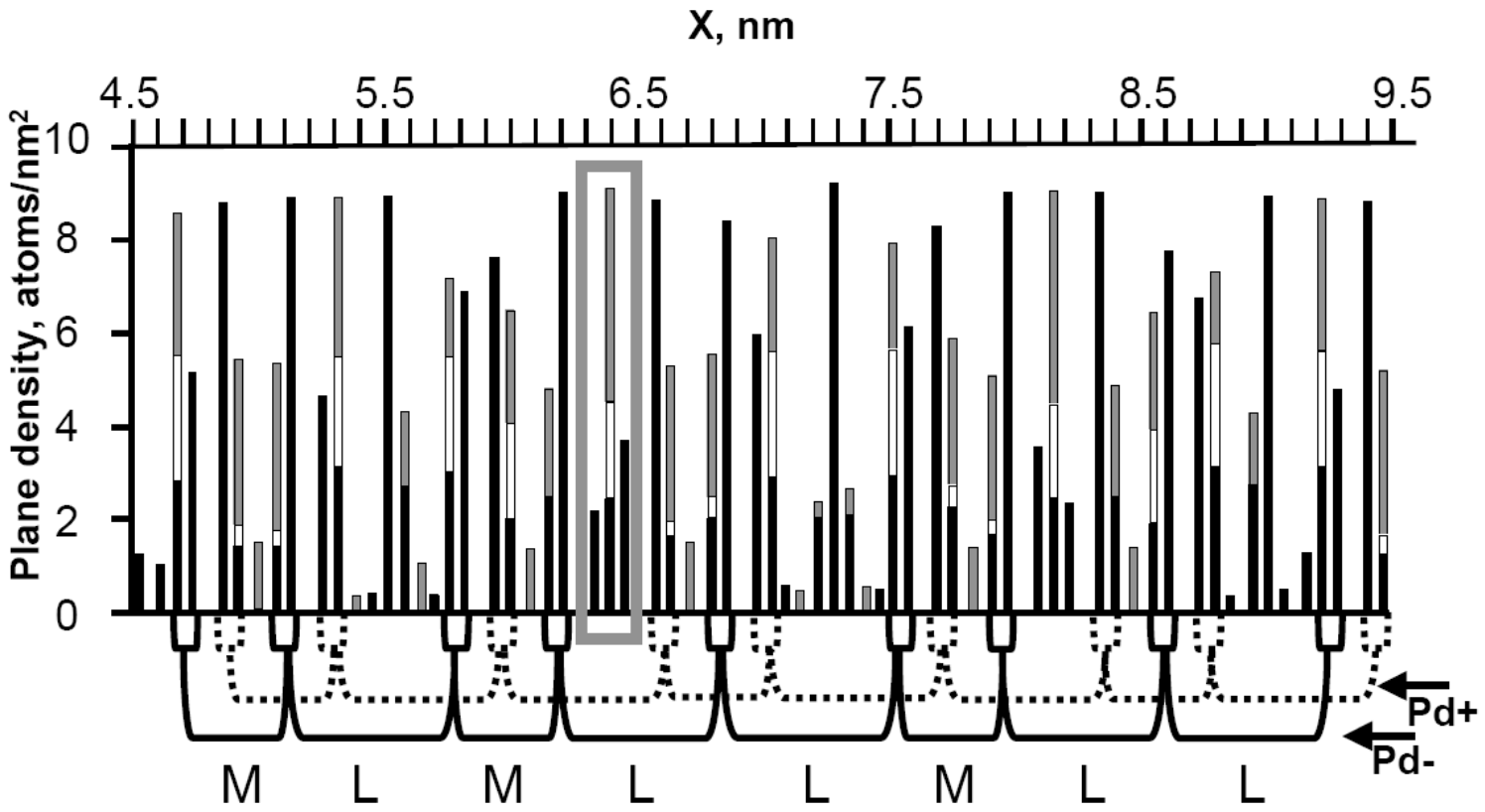
X, nm
4.5
5.5
6.5
7.5
8.5
9.5
Plane density, atoms/nm²
10
8
6
4
2
0
Pd+
Pd-
M
L
M
L
L
M
L
L

Figure 2

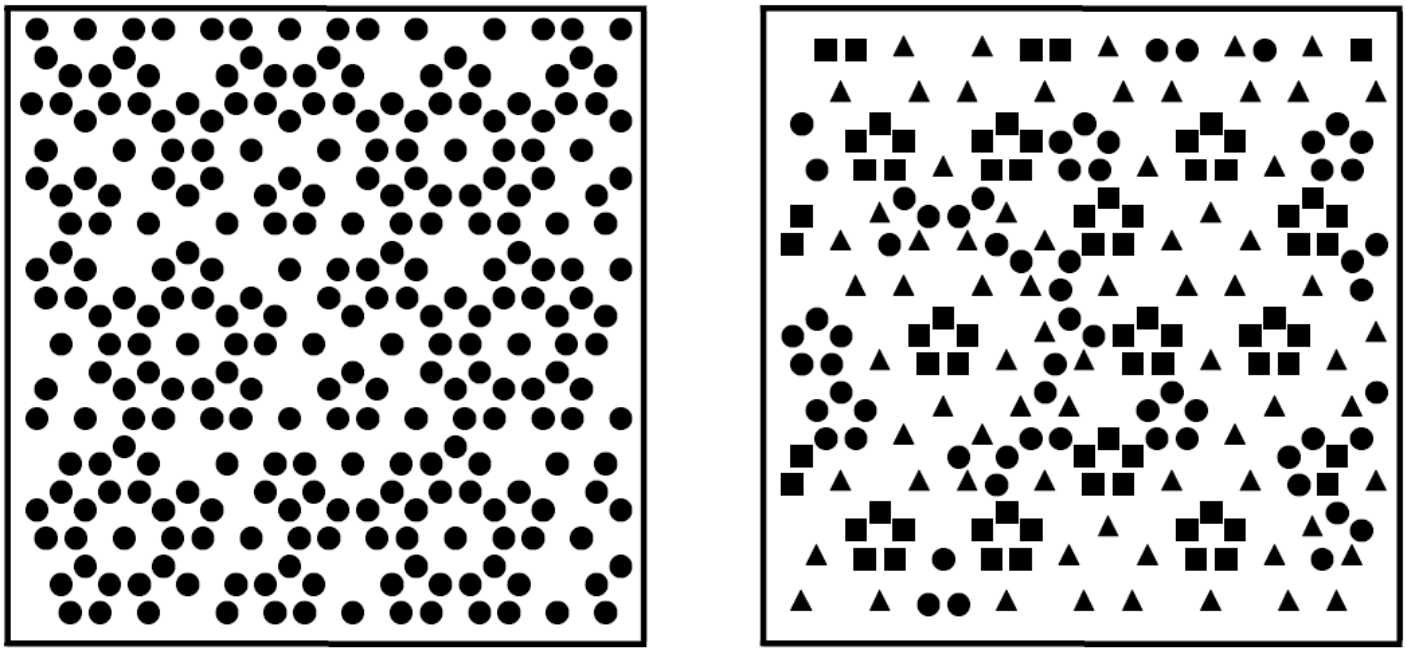

Figure 3

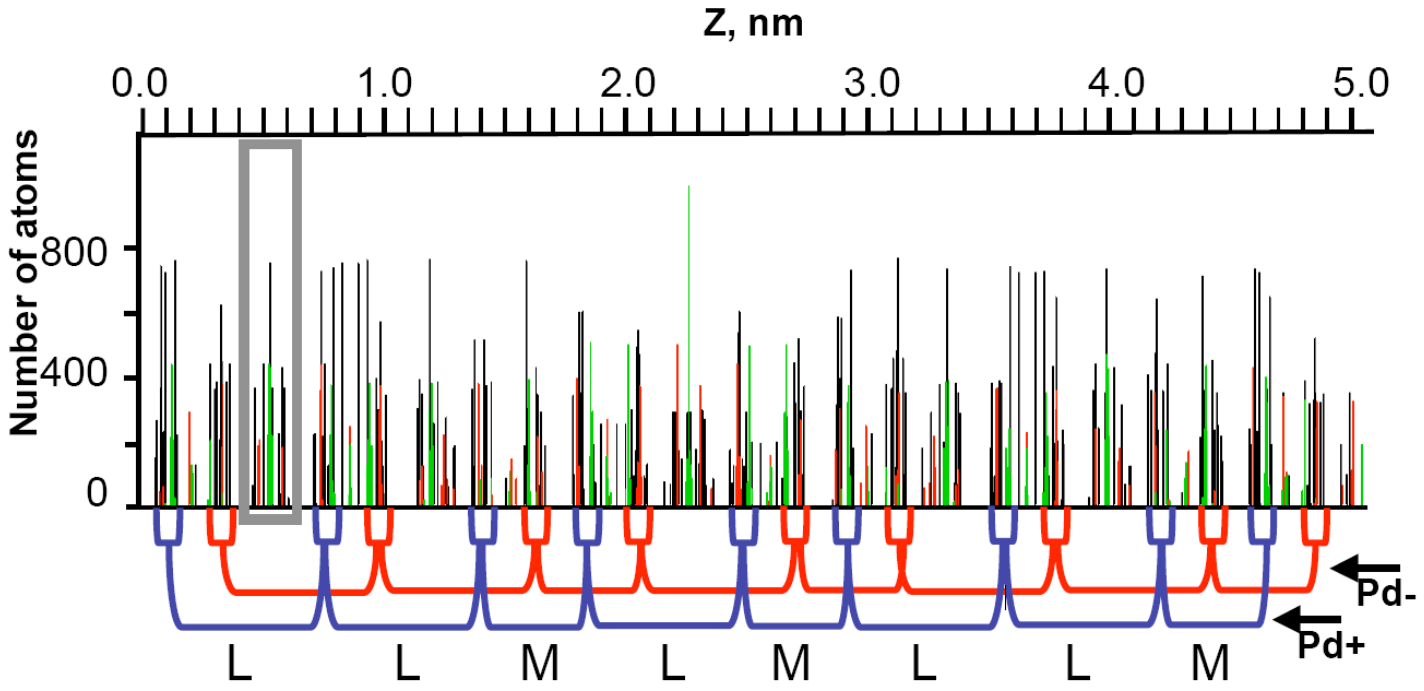

Figure 4

ADSORPTION SITES ON QUASICRYSTAL SURFACES: DARK STARS AND WHITE FLOWERS

A paper will be submitted to *Journal of Physics: Condensed Matter*

Baris Unal, C.J. Jenks, and P.A. Thiel

Abstract.

From other work, two preferred sites have been suggested for metals and semimetals adsorbed on the five-fold surfaces of icosahedral, Al-based quasicrystals. Because of their appearance in scanning tunneling microscopy (STM) images, these sites are known as dark stars and white flowers. In this paper, we analyze (mainly) four bulk structural models in physical space to determine the types, densities and chemical decorations of these two adsorption sites for the fivefold planes. We determine not only how these characteristics vary from model to model, but also from terrace to terrace within a single model, and even from site to site within a single terrace of a single model. We draw four main conclusions: (1) The chemical decorations of dark stars and white flowers vary from from model to model and also from site to site; (2) In all models, there exist correlations between the heights of steps and densities/types of adsorption sites on adjoining terraces; (3) The pentagonal hollow sites known as dark stars are formed by dissected Mackay clusters, not cut Bergman clusters as previously suggested; and (4) In all models, on a subset of terraces, cut Mackays and cut Bergmans co-exist.

1. Introduction

The surface adsorption site of a molecule or an atom is one of the most basic pieces of information that is needed to understand chemisorption. However, extracting this simple piece of information poses special challenges when studying chemisorption on a certain type of intermetallic alloy known as a quasicrystal. These challenges ultimately derive from the fact that quasicrystals are well-ordered, but are not periodic. A direct consequence for surface science is that quasicrystals naturally present a variety of different types of adsorption sites, where a site is defined as a local minimum in the potential energy surface. A good illustration of the variety expected for a quasicrystal is shown in Fig. 2 of Ref.[1], which is a potential energy surface calculated for an Al adatom on 5-fold i-Al-Cu-Fe. The range of adsorption sites is due to the range of local atomic configurations that can be identified.

A particular type of quasicrystal—the icosahedral (i-), Al-based alloys—has received much attention from surface scientists, because materials in this class are available as large single-grain samples, because they are tractable in ultrahigh vacuum (UHV), and because they represent a large fraction of known quasicrystals. This paper focuses primarily upon i-Al-Pd-Mn, although some mention is made of two alloys believed to be isostructural, i-Al-Cu-Ru and i-Al-Cu-Fe. The 5-fold surfaces of these alloys are believed to be bulk-terminated, except for interplanar relaxation [2-8].

Experimental work has shown that, depending upon the adsorbate, two particular adsorption sites are preferred[9]. For Al, Ag, Sn and C_{60} adsorbates[9-14], the preferred site is imaged as a dark star in scanning tunneling microscopy (STM) of the clean 5-fold surfaces of i-Al-Pd-Mn and i-Al-Cu-Fe[10, 11]. In nucleation and growth of Ag films, this site acts as a ‘trap’ site, skewing the nucleation kinetics so that they resemble heterogeneous

nucleation[13, 15]. For Bi adsorbate[9], the preferred site is imaged as a white flower in STM of the same surfaces. While the nucleation kinetics have not been studied in the latter systems, one expects a trapping effect to be exhibited by the white flowers as well.

In this paper, we explore the possible chemical nature of the dark star site and, to a lesser extent, of the white flower site. The spectrum of possibilities for these sites is much more complex than in a normal crystal, because of factors that will be discussed in Section 2. In short, the complicating factors include the existence of different models for the bulk structure; the existence of different possible families of terminations within any given model; and the possibility of sites that are structurally identical but chemically different, even within a single family of a single model. This work builds upon a previous report, in which we analyzed the variation in the long-range, average structure and composition of surface terminations for different models of the bulk structure and for different families of terminations[16]. The present work is different because it focuses on the chemical composition of a very local feature—the adsorption site—instead of the long-range average composition.

Some other publications have analyzed aspects of dark star and white flower sites (and other motifs), but there has been no comprehensive comparison among different models, nor among different types of terminations, such as that presented here. Thus, while this paper overlaps somewhat with published work by other authors, it presents many new pieces of information—both from experiment and from analysis of the models—that serve to build a more comprehensive and useful picture. For instance, by pointing out the variability in chemical decoration of dark star sites among different models, one can comment on the robustness of published DFT analyses of adsorption on approximants.

This paper also analyzes the spectrum of densities of the dark star sites. We find that the density should correlate with the height of the step that adjoins the terrace, which fits well with certain experimental observations. These have shown that different quasicrystal terraces can behave differently in adsorption. Finally, we present new experimental data that support the existence of different types of dark star sites on real terraces.

2. Background

2.1. Families of terminations.

Bulk structure models of quasicrystals are often called "deterministic" if they contain no sites of partial or mixed occupancy. In this paper, we focus on four deterministic bulk structure models, and make some brief comments about one non-deterministic model. These five models are chosen because their authors have made available large three-dimensional volumes containing atomic coordinates. We refer to them as the Boudard model, the Katz-Gratias (K-G) model, the Quiquandon-Gratias (Q-G) model, and the Papadopolos-Kasner (P-K) model. Details of our approach have been given previously[16].

It is known that surfaces of quasicrystals can be prepared in a terrace-step structure, in which the terraces are essentially flat[7, 17-21]. Therefore, it useful to break down the bulk models into atomic planes, for purposes of comparison with surfaces. Fig. 1 shows an example of the density and composition of planes of atoms, versus their location along the 5-fold axis in one of the deterministic models (P-K). If we ignore the low-density planes (lower than about 1 atom/nm^2), the four deterministic models are virtually identical when represented in the style of Fig. 1[16]. This is not surprising; it has been said that about 85%

of the atomic sites overlap in these models, a fact which derives from certain common features in their six-dimensional structure[16, 22].

Several experiments have shown that the preferred terminations of 5-fold surfaces of i-Al–Pd–Mn and i-Al–Cu–Fe consist of two dense planes that are closely spaced. The spacing between the planes at the surface is about 0.04 nm, a contraction of 20% from the bulk value of 0.05 nm[2-5]. We shall call such a pair of planes a ***layer***. Furthermore, experiments show that terraces are separated by steps of various heights, where the heights are related by the golden mean, $\tau = (1+\sqrt{5})/2 \sim 1.618\ldots$[7, 17-21, 23]

Matching these two features to the models, we identified two main families of layers as viable terminations. Some are labeled at the bottom of Fig. 1 with brackets. In one family, the top plane contains Pd, and in the other it does not. Hence, we call them Pd- (without Pd) and Pd+ (with Pd). Besides Pd content, these two families differ in the average relative densities of the two planes (Pd- having the denser plane on top, usually) and the width of the interplanar gap where the surface forms (Pd- having the larger gap by a factor of 2). A third family is also present but as a minority. Based upon comparison with experimental data, and upon the widths of the gaps in the models, we concluded that the Pd- family is most likely to be the real type of termination.

2.2. Clusters in the bulk models

The analysis of the dark star and white flower sites is typically couched in terms of clusters that can be identified in the bulk solid. When a surface plane intersects a cluster, the cluster is truncated (cut). In the bulk, the clusters contain a few tens of atoms arranged in

concentric shells. In the deterministic models, the two main types of clusters are called Mackay and Bergman.

The Bergman cluster is a 2-shell cluster. The central site can be filled with a single atom, or empty. The inner shell is an icosahedron (12 vertices), and the outer is a dodecahedron (20 vertices) with diameter 0.83 nm. If all sites are filled and the structure is geometrically ideal, the number of atoms in a Bergman cluster is 33.

The Mackay cluster has 3 shells and 50 atoms on average, including a central atom. In this cluster, the inner polyhedron is an incomplete dodecahedron, sometimes termed a disordered dodecahedron because the number and positions of atoms vary from cluster to cluster. This incomplete dodecahedron is enclosed by 2 interpenetrating polyhedra containing (ideally) 42 atoms: a complete icosahedron (12 vertices), plus a complete icosidodecahedron (30 vertices). The diameters of the last two shells are both 0.96 nm. [Note that here we are defining the terms “Bergman cluster” and “Mackay cluster” in a way that is consistent with current discussions of quasicrystals. In the *original* definitions given by Bergman et al.[24] and by Mackay[25], both clusters had more, larger shells. The clusters discussed in this paper are thus geometrical subsets of the original clusters.]

In Al-Pd-Mn quasicrystals, Mackay and Bergman clusters are not independent. Rather, they are complementary because they often overlap. The overlap is illustrated, for instance, by Fig. 10 of Ref [26]. Because of overlap, the clusters are almost space-filling. In the Q-G model, for example, they fill 98% of the volume of the solid[27]. The interpenetration of these clusters leads to variations in structural and chemical order within a given type of cluster.

Many clusters are imperfect. They can deviate from ideality due to missing atoms, extra atoms, and/or distortion. In this vein, an extensive analysis of Mackay clusters in the Boudard model has shown that at least 22% of the Mackay clusters lack one or more atom in the outer two shells[28]. Further insight into structural variation has been provided by analyses of the K-G and Q-G models[26, 27], showing that the number of atoms in Bergman clusters ranges from 32 to 35, with numbers in excess of 33 indicating distortion. In this paper, surface features are described as cut Bergman (cB) or cut Mackay (cM) clusters if the number and arrangement of atoms *in the first surface layer* (i.e. in the first pair of planes) matches expectation for a truncated cluster of that type, regardless of whether the remainder of the cluster is perfect. We believe that this definition of a cut cluster is good for comparison with experimental STM data. However, it may be different than that which has been adopted by other authors, for instance Papadopolos et al.[29], in their analyses of densities of cBs in surface terminations.

Chemical variations are also common in the bulk, both from cluster to cluster and from model to model. For instance, consider the Mackay clusters. The central atom can be either Al or Mn in the Boudard and K-G models. It can be either Al or Pd in the Q-G model. The icosahedron (one of the two outer shells) can contain Al, Mn, and/or Pd in the Boudard model, but it is either pure Pd or pure Mn in the Q-G model. The distorted dodecahedron (the innermost shell of the Mackay) is always pure Al in perfect clusters, but it can contain other kinds of atoms in imperfect clusters.

The clusters in the Yamamoto model are larger than those of the other models. For example, there are two main clusters with 2.0 nm diameter. These clusters have 12 and 11 concentric shells, respectively (see Figs. 10 and 11 in ref [30]). In the 12-shell clusters, there

are no central atoms, but 11-shell clusters have a central atom, which can be Al or Mn. Although these clusters are larger than those in the deterministic models, in both of these clusters, the first two inner shells form so-called Bergman clusters. Therefore, here, we only mention their first few shells. In 12-shell clusters, the vertices of the first inner icosahedron are decorated by Pd and/or Mn and the vertices of the dodecahedron are decorated by Al and/or Mn. However, in 11 shell clusters, the chemical decorations of the first inner two shells are reversed.

In the Yamamoto model, there are also two types of 3-shell Mackay clusters (see Fig. 12 in ref[30]). The first has a fully occupied icosahedron as the inner shell while the second one has a partially occupied dodecahedron. The chemical decorations of both clusters can vary.

In summary, the clusters in the Yamamoto model are similar to those in the deterministic models, if one considers only the inner shells.

3. Results and discussion

3.1. Experimental Surface Data

A high resolution STM image of the 5-fold surface of i-Al-Pd-Mn is shown in Fig. 3. There, examples of dark stars and white flowers are marked, as well as two other motifs known as white stars and rings. Previously, other groups also observed these local atomic configurations with STM[17, 18, 20, 29, 31, 32]. Among all of the local structures, dark stars and white flowers are the most abundant motifs. The following observations can be made about these two features:

(a) All dark stars in Fig. 3a have the same size and shape, but a close inspection reveals that there are three types of local environments in the STM image. Each dark star is surrounded by 3, 4, or 5 complete pentagons. Based on this, we classify the dark stars as A, B and C-type, respectively. These types are marked in the STM image of Fig. 3a, and are also drawn schematically in Fig. 3b. Whenever a pentagon is missing between two arms of a dark star, a single protrusion stands in its place.

(b) The depth of the dark stars varies within the same terrace. This is illustrated by the line profiles in Fig. 4, which cut across three dark star sites. One is significantly deeper than the other two.

(c) The orientation of the dark stars is the same within a single terrace as shown in Fig. 3a and also the same across different terraces. (This is not shown here, but see Fig. 3 in Ref.[33] and Fig. 4 in Ref.[32])

(d) The density of dark stars changes from terrace to terrace. (This is not shown here, but see Fig. 3 in Ref.[33], Fig. 4 in Ref.[32], or Fig. 2 in Ref.[34] for examples.)

(e) As shown by comparing Fig. 4a with 4b, there is some dependence upon whether the image is raw or filtered. The apparent density of dark stars increases with fast Fourier transformation (FFT) filtering, because filtering converts some poorly-imaged features into dark stars. Examples are encircled in Fig. 4. On the other hand, the conclusion that dark stars have different depths is not affected by filtering. Also, once a dark star has been identified, its classification as A, B, or C-type does not depend upon filtering.

(f) An ideal white flower is formed by five small pentagons centered on a single small protrusion, but most of the white flowers are not perfect. This is because, in a typical white flower, one or more of the pentagons appear incomplete as shown in Fig. 3a.

3.2. Surface Structure from the Bulk Models.

3.2.1. Positions of atoms.

Previously, Papadopolos et al. carried out an extensive analysis, showing that the basic motifs seen with STM—dark star, white flower, white star, ring—can be identified in the Pd+ family of terminations within the P-K model. Most notably, the dark star site was identified as a cB (see below). For the same family of terminations, we have examined all four deterministic models and have found that the same local features can be found in all models, which is not surprising because of the overlap in atomic positions between models (cf. Section 2.1). However, as noted in Sec. 2.1, this family of terminations is less likely than the Pd- family.

The same basic motifs can also be identified in the Pd- family of terminations. Fig. 5 shows atomic positions within the top two planes of a Pd- termination from the P-K model. Each circle represents an atom, irrespective of the type of element. As marked in Fig. 5, a hollow site surrounded by small pentagons is a reasonable candidate for a dark star, and five small pentagons centered on a single atom in the top plane is a good match to a white flower. A small pentagon surrounded by five atoms occupying the vertices of a larger pentagon can be a white star. Ten small pentagons centered on a small pentagon can be a ring motif.

Previously, Krajci et al.[35], also showed that 2 of these 4 local features—dark star and white flower—could be identified in the Pd- family in a 3/2-type approximant.

Focusing now on the pentagonal hollow motifs, Fig. 6a demonstrates that not all have the same local structural environment. They are surrounded by either 5, 4, or 3 complete pentagons, making them analogous to the A, B, and C-type dark stars observed experimentally (cf. Fig. 2). When a pentagon is absent, it is replaced by a single atom in the topmost plane, which corresponds well to the single protrusion present at these locations in STM. Thus, three types of pentagonal hollow sites exist in the models, and these may well be the three types of dark stars identified in experiment, based upon local environment.

If a Mackay is cut 0.252 nm from the center atom, a pentagon of atoms with an edge length of 0.48 nm is produced, which gives the main geometry of the dark star[35, 36]. This top pentagon arises from atoms in the icosidodecahedral shell. In the plane immediately beneath is another pentagon of atoms, rotated by 36^{o}, arising from the icosahedral shell. In STM, one would expect the vertices of the second pentagon to be aligned with the arms of the dark stars. A similar result can be obtained if a Mackay cluster is cut 0.204 nm below the center, except now the origins of atoms in the two pentagons are reversed. These, and other aspects of the dark star structure, are shown by the cross-sections in Fig. 6b. Note that these two cuts yield identical atomic configurations in the top layer, and would be indistinguishable with STM.

Even though all the pentagonal hollows have the same orientation, both within a given termination and for different terminations, their density changes from termination to termination. This is consistent with STM observations[32-34]. The range and average of densities of each pentagonal hollow type, for each model, are summarized in Table 1. One sees that there is almost no variation among different models, because the atomic positions in the dense planes are so similar among the models. For completeness, Table 1 also gives the

range and average densities of pentagonal hollows arising from cB configurations, although we do not believe that these are the dark star sites.

From experimental data, the density of dark star sites has been indirectly estimated at 0.03 to 0.1 nm^{-2}[13, 15]. This was based upon the density of adsorbed Ag islands that are plausibly 'trapped' at the dark star sites. These numbers represent averages over many terraces. The lower value, 0.03 , is in reasonable agreement with the average density of A-type dark stars in Table 1 (0.038 nm^{-2}), but the range of 0.03-0.1 nm^{-2} is incompatible with the total density of (A+B+C)-type dark stars, 0.26 nm^{-2}. This suggests that not all dark stars are equally effective as nucleation sites for Ag islands.

The densities of pentagonal hollows, for a set of individual Pd- terminations in the P-K model, are given in Table 2. One sees here that the density of pentagonal hollows decreases as the density of atoms in the topmost plane increases; some terminations contain no hollows. This trend is also shown in Fig. 8. The rationale for this correlation involves the disordered dodecahedron.

Atoms from the disordered dodecahedron (the inner shell) can occupy positions close to the center of a pentagonal hollow in either the top plane, or in the second plane. These two cases are shown in Fig. 6b and 6c, respectively. If atoms are in the top plane, they probably prevent cMs from being imaged as dark stars with STM. Therefore, we do not count such configurations as dark stars in our analyses. (In potential energy surface calculations, atoms in these positions cause the pentagonal hollows to have a banana-like appearance[1, 35-37]). The population of these atoms increases as the atomic density of the top plane increases, hence causing a decrease in dark star density.

Atoms from the disordered dodecahedron can also be in the second plane. For the A, B, and C-type dark stars there are 0, 1, and 2 such atoms, respectively. We speculate that the contribution of this inner shell may be the reason for the different depths of dark stars observed in the STM images.

The type of dark star on a terrace also changes systematically with the step height. For example, in all models, *only* A-type dark stars exist on the terraces bordered by descending M type steps, as summarized in Table 3.

Turning now to the white flower sites in the Pd- family of terminations, they can be formed in two ways. First, a surface plane can cut the Mackay cluster at its waist. The five leaves of the white flower belong to the five Bergman clusters surrounding it. Here, the atom at the center of the white flower is actually the center atom of the Mackay cluster. In the second way, Mackays are not cut at their equator positions, but white flowers could still be seen in the STM images, based on the configuration of atoms in the top layer only. The latter type of white flower is formed by a Mackay hanging down from the surface plane, with five surrounding *truncated* Bergman clusters. Here, the center atom belongs to the icosahedron of the Mackay, *not its center*. Analogous to the dark stars, these two cuts yield identical atomic configurations in the top layer, and would probably be indistinguishable with STM. Previously, the white flower has only been identified with one of these two configurations, the Mackays cut at the waist[35].

3.2.2. Identities of atoms.

In this analysis, we consider the dark star sites to be cMs. The chemical decorations of the dark stars, within the top two planes, are shown in Table 4. For two of the geometric

features, the chemical decorations are relatively invariant. The first is the pentagon of atoms in the top plane, with edge length of 0.48 nm. This is almost always entirely Al. The sole exception is the Q-G model, where one of the pentagonal vertices is occasionally occupied by Mn. Second, the second-plane atoms that arise from the inner dodecahedron are usually Al, but some C type dark stars have one or two Pd atoms in the second planes in both Q-G and K-G models.

More chemical variation exists in the pentagon of atoms in the second plane, which is rotated by 36^{o} with respect to the top one. This is qualitatively summarized in Table 4. For instance, in the Boudard model, the atoms at the vertices of the second-plane pentagon can be Mn, Pd, or a mixture of Mn and Pd. In the Q-G model, they can be Al, Pd, or a mixture of Al and Pd. In the K-G and P-K models, the pentagons can consist of any of the three elements alone, and in addition some terminations have a mixture of Al, Pd and Mn at these sites. The chemical decoration of the second-plane pentagon varies considerably among models, among terminations within a given model, and among clusters within a given termination of a single model.

The chemical identities of the white flowers are given in Table 5. Since there are not many white flowers whose leaves are complete, we focus on the chemical decoration of the main features of the white flowers such as the centers, the ten atom-ring and the vertices of the pentagons in the second planes. In all models, the center atom is either Al or Mn, except for the K-G model where the center is always Al. We see another exception in the ten-atom rings in the white flowers of the Q-G model. When the center is occupied by Mn, the ring is decorated by either Al or Al+Mn, while in other models the positions are occupied by Al atoms only. We see significant chemical variations in the decoration of the second plane

pentagon. Especially, in the Boudard model, those sites are occupied by only Pd or both Al and Pd or in some terminations a mixture of Al, Pd and Mn. In all models, the vertices of the pentagons in the second plane are sometimes *partially* occupied, and on some terraces none of these positions are occupied.

We note that some sites have incomplete ten atom rings which may be seen in STM images as half-white flowers. In addition, their density compared to the full white flowers is low. Therefore, in this analysis, we exclude them.

3.2.3. Coexistent cut Bergman and cut Mackay clusters.

As described previously, if a termination cuts Mackay clusters at specific heights (i.e. 0.252 nm above or 0.204 nm below the center), pentagonal hollows can be formed. The edge lengths of the pentagons are 0.48 nm. Pentagons with the same size but different orientations can be formed if a plane cuts a Bergman cluster 0.078 nm below its center. In most of the Pd- terminations, pentagons originate exclusively from dissected Mackay clusters, according to our analysis of the models. However, about 30% of the terminations cut across both Bergman and Mackay clusters in such a way that both types of dissected clusters form pentagons as described above. Both types of pentagons are the same size in the top plane, but they are rotated by 36^{o}, as illustrated in Fig. 7a. In the Pd- terminations, these cut Bergmans are always imperfect in the bulk. The main point is that the bulk structure models predict that for some terminations, both cut Bergmans and cut Mackays should be observable.

Compare this prediction with the STM image shown in Fig. 7b for one particular terrace. Besides the deep dark stars, there are also shallow features that resemble dark stars. They are rotated by 36^{o} with respect to the deep dark stars, exactly as predicted. We therefore

suggest that these shallow dark stars may be incomplete, dissected Bergman clusters, whereas the deeper dark stars may be dissected Mackay clusters.

Recently, Papadopolos et al.[38] have simulated STM images for both Pd- and Pd+ terminations in the P-K model. In their simulations, cut Bergman clusters are shallow pentagonal holes whereas cut Mackay clusters are deeper, darker pentagonal holes. These observations are consistent with the above interpretation of the STM data, such as the image in Fig. 7.

There are also some correlations between density of cut Bergmans and step heights. For instance, as given in Table 3, there are no cut Bergman type pentagonal holes on the terraces bordered by descending M steps apart from the P-K model. We also note that those cut Bergmans have Mn atoms on the vertices of the pentagon in the first plane shown in Table 4.

4. Discussion

No other work has compared different bulk models in the context of surfaces. Instead, the standard approach has been to adopt a single model as a benchmark for comparison with experimental surface data, or as a platform for theoretical simulations and calculations. An analysis of the variability among different models may shed light on the robustness of previous analyses, and even allow surface science experiments to be designed that could discriminate between different models.

There has been some controversy over whether dark star sites are Mackay or Bergman clusters, truncated at specific levels. The debate has centered on the nature of the atomic *positions* in the dark star site, with little or no attention to different possibilities for the

chemical decoration. Any conclusions about this site directly translate into conclusions about the white flower site; the two are directly linked by the nature of the terminating plane.

Previously, Papadopolos et al. have proposed that the surface terminations belong to the Pd+ family, and that the dark star sites are Bergman clusters cut 0.076 nm below the center. They extensively analyzed STM images and demonstrated their compatibility with certain planes in the P-K model. On the other hand, Krajci et al. have used DFT to analyze the surface terminations of an Al-Pd-Mn approximant[35].

4.1. Consequences of chemical diversity on chemisorption.

It would not be unreasonable to expect chemical bonding of adsorbates at the dark star sites to be influenced by the chemical nature of the second pentagon. Hence, in chemisorption experiments, some dark star sites may act as trap sites whereas others may be more inert. This could explain the fact that the experimental estimates of dark star site densities, based upon adsorption and nucleation of Ag adatoms, is somewhat lower than the averages expected from the models.

Simulations of chemisorption have been carried out using two different models. In one, 5-fold surfaces of i-Al-Cu-Fe and i-Al-Pd-Mn were modeled using Leonard-Jones potentials to construct potential energy surfaces for Al and Ag adatoms, respectively[1, 13, 37]. In the results of these simulations, several adsorption sites were identified such as starfish (dark star) and incomplete starfish (banana). Each of these sites had different depths with respect to each other. Especially, the dark stars sites were much deeper at their centers than that of the other sites. The banana sites were formed due to the presence of the one Al

atom in the first plane close to the center of the dark stars. This Al atom belonged to the inner dodecahedron of the Mackay cluster[1, 13, 37].

In the second type of modeling study, the 5-fold-like surface of an approximant of i-Al-Pd-Mn was modeled using DFT to construct potential energy surfaces for a wide variety of adsorbates[39, 40]. However, even though the 2/1 rational approximant surface had some of the important local configurations, it did not have any true dark star sites. The lack of those sites was mainly due to the presence of one or two Al atoms in the first plane close to the center of the dark stars. Therefore, this surface had only banana sites for various adsorbates and may not represent the real dark star adsorption sites of the quasicrystal surfaces. If we ignore the presence of the Al atoms belong to the inner dodecahedron, we can say that the closest bulk model in terms of chemical decorations of those sites is the P-K model where all the A and B type dark stars have Al in the first plane and Pd in the second plane as given in Table 4.

4.2. Consequences of chemical diversity on STM imaging.

Using ab initio DFT method, Krajci et al have carried out several STM simulations for the fivefold surface of the 3/2 rational approximant[35]. In this approximant surface, there are pentagonal holes which are formed when the Mackay clusters are cut 0.252nm above the equator. The vertices of the first pentagon are decorated by Al while the vertices of the second pentagon in the second plane are decorated by Pd. Their calculations showed that in STM imaging the tunneling current was mainly formed by the Al atoms in the first plane while the Pd atoms had almost no contribution. As a result of this, Pd atoms which are in the second plane should be imaged as dark spots with STM[35]. Moreover, based on their STM

simulations and the comparison with the real STM images, they concluded that cut Mackay are the dark star sites. It should be noted that their simulations consider only one type of chemical decoration for darks star sites. However, from the quasicrystal models one should expect to see chemical variations for the darks star sites as given Table 4.

Ni-Al is another example for Al-transition metal system. These alloys are much simpler in terms of their structure and chemical order compared to the quasicrystals and their periodic approximants. Recently, Jurczyszyn et al. have carried out a theoretical study on formation of STM images of $Ni_3Al(001)$ and $Ni_3Al(111)$ intermetallics and compared the simulation results with the experimental STM images of $Ni_3Al(111)$[41]. Their study pointed that in STM images, Al atoms were imaged dominantly than Ni atoms although both Al and Ni were in the same surface plane. The authors concluded that the intra-atomic interference of the s and p_z orbitals of Al atom was main contributor to the tunneling current. In other words, in the transition metal alloy, the tunneling probability of Al with respect to that of Ni is much higher so that Al atoms are imaged as bright protrusions and Ni atoms are imaged as depressions in the STM images[41].

These two examples suggest that Al atoms should be imaged differently than transition metal atoms. More specifically, in STM images one should expect to see Al atoms as protrusions while transition atoms (e.g. Pd, Ni etc.) as depressions. Therefore, Al atoms in the second planes close to the center of the dark stars may affect the contrast in the STM images so that some of the dark stars should be imaged less deep than the others. Indeed, these arguments support the different depth of the dark stars in our STM observations.

4.3. White flowers and their chemical diversity on STM imaging.

Recently, it has been experimentally shown that Bi atoms have preferred to nucleate as pentagonal clusters with an edge-length of 0.49 nm at white flower sites, *not dark star sites*[42]. By comparing the STM images with the 3/2 rational approximant structure, the authors concluded that the flowers were formed by central cut Mackay clusters and hence, the central atom was Mn. Moreover, the authors claimed that Mn atoms in the center played a role in the nucleation process via substrate-mediated interaction. Our detailed analyses of the structural models suggest that the proposed definition of the white flowers was true but incomplete. Therefore it is important to understand the chemical and also structural nature of those sites for the nucleation and growth process of these types of adsorbates (e.i. Bi etc.).

Krajci et at claimed that the Mn atoms in the center of the flower should be imaged brighter than the others atoms and depending on their magnetic states their brightness may change. Indeed in the high resolution STM images some of the protrusions seem brighter compared to the others, for example see Fig. 3a. However, in the models, as discussed in section 3.2.2, not all the centers of the white flowers are occupied by Mn. Therefore, the cause of the brightness may not be solely explained by the magnetic state of the Mn atoms. A slight vertical relaxation in the positions of the central atoms (as well as the some others) with respect to the rest of the atoms may affect the contrast in the STM images. In other words, the details of the contrast may be partially topographic, which was not considered in the simulations. This might be due to the limitations of the DFT calculations.

5. Conclusions

We have examined four deterministic models for i-AlPdMn quasicrystal in terms of

types, densities and chemical decorations of adsorption sites for the fivefold planes. By comparing high resolution STM images with the models, we have concluded that the pentagonal hollow sites (dark stars) are formed by dissected Mackay clusters, not Bergman clusters as previously suggested. In addition, we have found that on some terraces both cut Mackays and cut Bergmans exist. Our analysis shows that in all models there are some correlations between the heights of steps and densities and/or types of dark stars. Finally, we have found that white flower sites are not always formed by dissected Mackays at their equator positions.

Acknowledgments

This work was supported by the Office of Science, Basic Energy Sciences, Materials Science Division of the U.S. Department of Energy (USDOE). This manuscript has been authored by Iowa State University of Science and Technology under Contract No. DE–AC02–07CH11358 with the U.S. Department of Energy. We are grateful to Denis Gratias, Marianne Quiquandon, Gerald Kasner, Zorka Papadopolos, Akiji Yamamoto, and Marc de Boissieu for supplying us with 3D atomic coordinates of the quasicrystal models. We are grateful James W. Evans for his careful reading and useful suggestions. We are thankful to Qisheng Lin for his helps for the Diamond software which was used for plotting Fig. 2.

References

[1] C. Ghosh, D.-J. Liu, K. J. Schnitzenbaumer, C. J. Jenks, P. A. Thiel, and J. W. Evans, Surf. Sci. 600, 2220 (2006).

[2] T. Cai, F. Shi, Z. Shen, M. Gierer, A. I. Goldman, M. J. Kramer, C. J. Jenks, T. A. Lograsso, D. W. Delaney, P. A. Thiel, and M. A. Van Hove, Surf. Sci. 495, 19 (2001).

[3] M. Gierer, M. A. Van Hove, A. I. Goldman, Z. Shen, S.-L. Chang, C. J. Jenks, C.-M. Zhang, and P. A. Thiel, Phys. Rev. Lett. 78, 467 (1997).

[4] M. Gierer, M. A. Van Hove, A. I. Goldman, Z. Shen, S.-L. Chang, P. J. Pinhero, C. J. Jenks, J. W. Anderegg, C.-M. Zhang, and P. A. Thiel, Phys. Rev. B 57, 7628 (1998).

[5] J.-C. Zheng, C. H. A. Huan, A. T. S. Wee, M. A. Van Hove, C. S. Fadley, F. J. Shi, E. Rotenberg, S. R. Barman, J. J. Paggel, K. Horn, P. Ebert, and K. Urban, Phys. Rev. B 69, 134107 (2004).

[6] H. R. Sharma, M. Shimoda, and A. P. Tsai, Advances in Physics 56, 403 (2007).

[7] M. Shimoda, H. R. Sharma, and A. P. Tsai, Surface Science 598, 88 (2005).

[8] P. A. Thiel, Ann. Rev. Phys. Chem. 59, 129 (2008).

[9] J. A. Smerdon, H. R. Sharma, J. Ledieu, and R. McGrath, J. Phys.: Condens. Matter 20, 314005 (2008).

[10] J. Ledieu, C. A. Muryn, G. Thornton, R. D. Diehl, T. A. Lograsso, D. W. Delaney, and R. McGrath, Surf. Sci. 472, 89 (2001).

[11] T. Cai, J. Ledieu, R. McGrath, V. Fournée, T. A. Lograsso, A. R. Ross, and P. A. Thiel, Surf. Sci. 526, 115 (2003).

[12] V. Fournée, and P. A. Thiel, J. Phys. D: Appl. Phys. 38, R83 (2005).

[13] B. Unal, V. Fournée, K. J. Schnitzenbaumer, C. Ghosh, C. J. Jenks, A. R. Ross, T. A. Lograsso, J. W. Evans, and P. A. Thiel, Phys. Rev B 75, 064205 (2007).

[14] H. R. Sharma, M. Shimoda, A. R. Ross, T. A. Lograsso, and A. P. Tsai, Phys. Rev B 72, 045428/1 (2005).

[15] V. Fournée, T. C. Cai, A. R. Ross, T. A. Lograsso, J. W. Evans, and P. A. Thiel, Phys. Rev. B 67, 033406 (2003).

[16] B. Unal, C. J. Jenks, and P. A. Thiel, Phys. Rev.B 77, 195419 (2008).

[17] L. Barbier, D. Le Floc'h, Y. Calvayrac, and D. Gratias, Phys. Rev. Lett. 88, 085506 (2002).

[18] L. Barbier, and D. Gratias, Progress in Surface Science 75, 177 (2004).

[19] T. Cai, V. Fournée, T. A. Lograsso, A. R. Ross, and P. A. Thiel, Phys. Rev. B 65, 140202 (2002).

[20] H. R. Sharma, V. Fournée, M. Shimoda, A. R. Ross, T. A. Lograsso, A. P. Tsai, and A. Yamamoto, Phys. Rev. Lett. 93, 165502 (2004).

[21] T. M. Schaub, D. E. Bürgler, H.-J. Güntherodt, and J. B. Suck, Phys. Rev. Lett. 73, 1255 (1994).

[22] D. Gratias, and M. Quiquandon, Phil. Mag. in Press (2008).

[23] R. McGrath, L. Leung, S. D. Barrett, and J. Ledieu, Proc. Royal Microscopical Society 40, 215 (2005).

[24] G. Bergman, Acta Cryst. 10, 254 (1957).

[25] A. L. Mackay, Acta Cryst. 15, 916 (1952).

[26] D. Gratias, F. Puyraimond, M. Quiquandon, and A. Katz, Phys. Rev. B 63, 024202 (2000).

[27] M. Quiquandon, and D. Gratias, Phys. Rev B 74, 214205 (2006).

[28] L. Loreto, R. Farinato, S. Catallo, C. Janot, G. Gerbasi, and G. De Angelis, Physica B: Condensed Matter (Amsterdam, Netherlands) 328, 193 (2003).

[29] Z. Papadopolos, G. Kasner, J. Ledieu, E. J. Cox, N. V. Richardson, Q. Chen, R. D. Diehl, T. A. Lograsso, A. R. Ross, and R. McGrath, Phys. Rev. B 66, 184207 (2002).

[30] A. Yamamoto, H. Takakura, and A. P. Tsai, Phys. Rev. B 68, 094201 (2003).

[31] G. Kasner, and Z. Papadopolos, Phil. Mag. 86, 813 (2006).

[32] J. Ledieu, and R. McGrath, J. Phys. Cond. Matter 15, S3113 (2003).

[33] B. Unal, T. A. Lograsso, A. R. Ross, C. J. Jenks, and P. A. Thiel, Phys. Rev. B 71, 165411 (2005).

[34] R. McGrath, J. Ledieu, and R. D. Diehl, Progress in Surface Science 75, 131 (2004).

[35] M. Krajci, J. Hafner, J. Ledieu, and R. McGrath, Phys. Rev B 73, 024202/1 (2006).

[36] M. Krajci, and J. Hafner, Phys. Rev. B 71, 054202 (2005).

[37] C. Ghosh, D.-J. Liu, C. J. Jenks, P. A. Thiel, and J. W. Evans, Phil. Mag. 86, 831 (2006).

[38] Z. Papadopolos, O. Groning, and R. Widmer, in *Models, Mysteries and Magic of Molecules*, edited by J. C. A. Boeyens, and J. F. Ogilvie (Springer, New York, 2008).

[39] M. Krajci, and J. Hafner, Phys. Rev. B 71, 184207 (2005).

[40] M. Krajci, and J. Hafner, Phys. Rev. B 75, 224205 (2007).

[41] L. Jurczyszyn, A. Rosenhahn, J. Schneider, C. Becker, and K. Wandelt, Phys. Rev.B 68, 115425 (2003).

[42] J. A. Smerdon, J. K. Parle, L. H. Wearing, T. A. Lograsso, A. R. Ross, and R. McGrath, Phys. Rev. B 78, 075407 (2008).

Table and Figure Captions.

Table 1. Range of densities of cut Mackay (cM) and cut Bergman (cB) pentagonal hollow sites in Pd- terminations, from four bulk structure models. In calculating the averages, each plane is weighted according to its area.

Table 2. Densities of pentagonal hollow sites, and of top planes, in specific Pd- terminations in the P-K model.

Table 3. Correlations between step heights (L or M), and densities of terminations and densities of pentagonal holes, in the Pd- family, for the four deterministic models. Heights of L- and M-type steps are 0.660 nm and 0.408 nm, respectively, for the 5-fold surface of i-Al–Pd–Mn. In the four deterministic models, a layer is a pair of planes.

Table 4. Chemical decorations of A, B, and C-type pentagonal hollows from cut Mackays, and of pentagonal hollows from cut Bergmans (cB), in the bulk structural models of i-Al-Pd-Mn quasicrystals. The letters in parentheses denote the type of pentagonal hole, as defined in the text.

Table 5. Chemical decorations of white flowers in the bulk structural models of i-Al-Pd-Mn quasicrystals.

Figure 1. Schematic depiction of atomic planes in the P-K model. The z-axis is the fivefold axis. The spatial coordinate is labeled '(z)' because this is the notation used by the authors of the model. The height of each line is proportional to the planar atomic density. Within each vertical bar, black is Al, gray is Pd, and white is Mn.

Figure 2. A Mackay cluster. Black marks the vertices of the icosahedron and grey is for the vertices of the icosidodecahedron. p

Figure 3. (a) An *unfiltered* STM image of a clean fivefold surface of i-Al-Pd-Mn quasicrystal. The tunneling conditions: 0.47 nA and +0.97 V. Size of the image is 25.1 x 12.1 nm^2 . Letters A, B, and C denote the three types of dark stars. Two types of white flowers are marked as WF (complete) and WF/ (incomplete). A special local motif called "Ring" is also marked. (b) A schematic description of different dark stars and a complete white flower, and note that only the first plane atoms are shown.

Figure 4. STM images of the clean fivefold surface of i-Al-Pd-Mn quasicrystal. The image size is 8.6 x 4.5 nm^2. (a) Raw data. (b) FFT filtered. Circles show dark stars that appear to have extra atom(s) near the central site. This central material is suppressed, and the dark star character is enhanced, by filtering. Dashed arrow indicates the cut of the line profiles shown at right.

Figure 5. A top view of a layer from the P-K model at 2 nm. The size of the layer is 10 x 10 nm^2. Each ball represents an atom and black is Al, blue is Mn and grey is Pd. The circle marks the "Ring" motif. Several white flower motifs are also marked by circles.

Figure 6. (a) A top view of a layer from the P-K model at 3.78 nm. Three types of dark stars are marked by circles as A, B and C. Several white flower motifs are also marked by circles. In the middle region, a white rectangle shows the region of the cross-section in Fig. 6 (b). This is a cut across a B type darks star. It intersects an atom from the disordered inner dodecahedron. (b) and (c) a cut 0.252 nm *above* Mackay cluster. Each ball represents an atom and black is Al, blue is Mn and grey is Pd. Al atom in second (first) plane, from the inner dodecahedron. The atoms in top-plane pentagon are from the icosidodecahedron. The atoms in second-plane pentagon are from the icosahedron. A central atom in the cluster is also shown.

Figure 7. (a) An FFT filtered STM image of the clean fivefold surface of i-Al-Pd-Mn quasicrystal. The size of the image is 7.6 x 6.3 nm^2. (b) A layer from the Boudard model is formed by a pair planes at 2.39 nm and 2.34 nm, respectively. The size of the layer is 9.7 x 7.9 nm^2. A dark star in (a) and a cut-Mackay in (b) are encircled. Arrows are pointing two Al atoms in the second plane.

Figure 8. A plot shows the density of dark stars (cut-Mackays) versus densities of top planes in the P-K model. The plot also shows the density of cut-Bergman type pentagonal holes versus top plane density of the layers.

Table 1

	Densities of A-type cM pentagonal hollows, nm^{-2}		Densities of B-type cM pentagonal hollows, nm^{-2}		Densities of C-type cM pentagonal hollows, nm^{-2}		All types of cM pentagonal hollows combined (A+B+C), nm^{-2}		Density of cB pentagonal hollows, nm^{-2}	
Model	Range	Average	Range	Average	Range	Average	Range	Average	Range	Average
Boudard	0-0.170	0.038	0-0.150	0.022	0-0.840	0.190	0-0.840	0.250	0-0.810	0.097
K-G	0-0.131	0.036	0-0.150	0.024	0-0.833	0.208	0-0.833	0.268	0-0.770	0.135
Q-G	0-0.180	0.038	0-0.130	0.024	0-0.890	0.194	0-0.890	0.257	0-0.860	0.106
P-K	0-0.160	0.039	0-0.150	0.024	0-0.940	0.183	0-0.940	0.246	0-0.930	0.125

Table 2

Position of top plane in the termination, along the fivefold axis (nm)	Density of A-type cM pentagonal hollows (nm^{-2})	Density of B-type cM pentagonal hollows (nm^{-2})	Density of C-type cM pentagonal hollows (nm^{-2})	Total density of cM pentagonal hollows (nm^{-2})	Density of cB pentagonal hollows (nm^{-2})	Atomic density of top plane (nm^{-2})
4.800	0.160	0.000	0.000	0.160	0.000	8.170
4.140	0.000	0.000	0.000	0.000	0.030	8.900
3.730	0.030	0.050	0.270	0.350	0.000	6.980
3.070	0.060	0.000	0.000	0.060	0.000	8.600
2.660	0.000	0.000	0.810	0.810	0.930	4.780
2.000	0.080	0.150	0.040	0.270	0.000	7.710
1.340	0.000	0.000	0.000	0.000	0.000	8.820
0.930	0.000	0.000	0.610	0.610	0.280	5.790
0.270	0.160	0.000	0.000	0.160	0.000	8.180
-0.390	0.000	0.000	0.000	0.000	0.040	8.860
-0.800	0.040	0.040	0.330	0.410	0.000	6.870
-1.460	0.050	0.000	0.000	0.050	0.000	8.640
-1.870	0.000	0.000	0.940	0.940	0.640	4.980
-2.520	0.090	0.090	0.000	0.180	0.000	7.760
-3.190	0.000	0.000	0.000	0.000	0.010	8.850
-3.600	0.010	0.000	0.530	0.540	0.100	6.500
-4.250	0.070	0.000	0.000	0.070	0.000	8.460

Table 3

Model	Type of step bordering termination in down-going direction	Average atomic density in top plane of termination, nm^{-2}	Average density of pentagonal holes in the terminating layer, nm^{-2}. (Range of values is given in parentheses.)	
			Mackay-like pentagonal holes [type is given in brackets]	Bergman-like pentagonal holes
K-G	*L*	6.6	0.405 (0.060-0.940) [A, B, C]	0.238 (0.000-0.723)
	M	8.9	0.025 (0.000-0.063) [A]	0.000
Boudard	*L*	6.8	0.431 (0.090-0.840) [A, B, C]	0.189 (0.000-0.810)
	M	8.8	0.010 (0.000-0.030) [A]	0.000
P-K	*L*	6.9	0.405 (0.060-0.940) [A, B, C]	0.207 (0.000-0.930)
	M	8.8	0.016 (0.000-0.060) [A]	0.009 (0.000-0.773)
QG	*L*	6.8	0.428 (0.090-0.860) [A, B, C]	0.186 (0.000-0.860)
	M	8.8	0.015 (0.000-0.060) [A]	0.000

Table 4

Model Types				
Type of Features	Boudard	KG	QG	P-K
Pentagon in top plane	Al (A, B, C, cB)	Al (A, B, C, cB)	Al (A, B, C, cB), Mn (A)	Al (A, B, C, cB), Mn (cB)
Pentagon in second plane	Pd(A, cB), Mn[A, B, C], Al+Pd(cB), Pd+Mn(A, B, C, cB), Al+Pd+Mn(C, cB)	Al(A, B, C), Pd(A), Mn(A, B, C), Al+Mn(B, C, cB), Pd+Mn(C, cB), Al+Pd+Mn(C, cB)	Al (A), Pd(A, B, C, cB), Al+Pd(B, C, cB)	Al(cB), Pd (A, B, C), Al+Pd (cB), Al+Mn(C, cB), Pd+Mn(C, cB), Al+Pd+Mn(C, cB)

Table 5

Model Types							
Type of Features	Boudard		KG	QG		P-K	
Center atom	Al	Mn	Al	Al	Mn	Al	Mn
Ten atom ring in first plane	Al	Al	Al	Al	Al, Al+Mn	Al	Al
Pentagon in second plane	Pd, Al+Pd, Al+Pd+Mn	Al, Al+Pd	Al, Pd, Al+Pd	Al, Pd	Al, Al+Pd	Pd, Al+Pd	Al

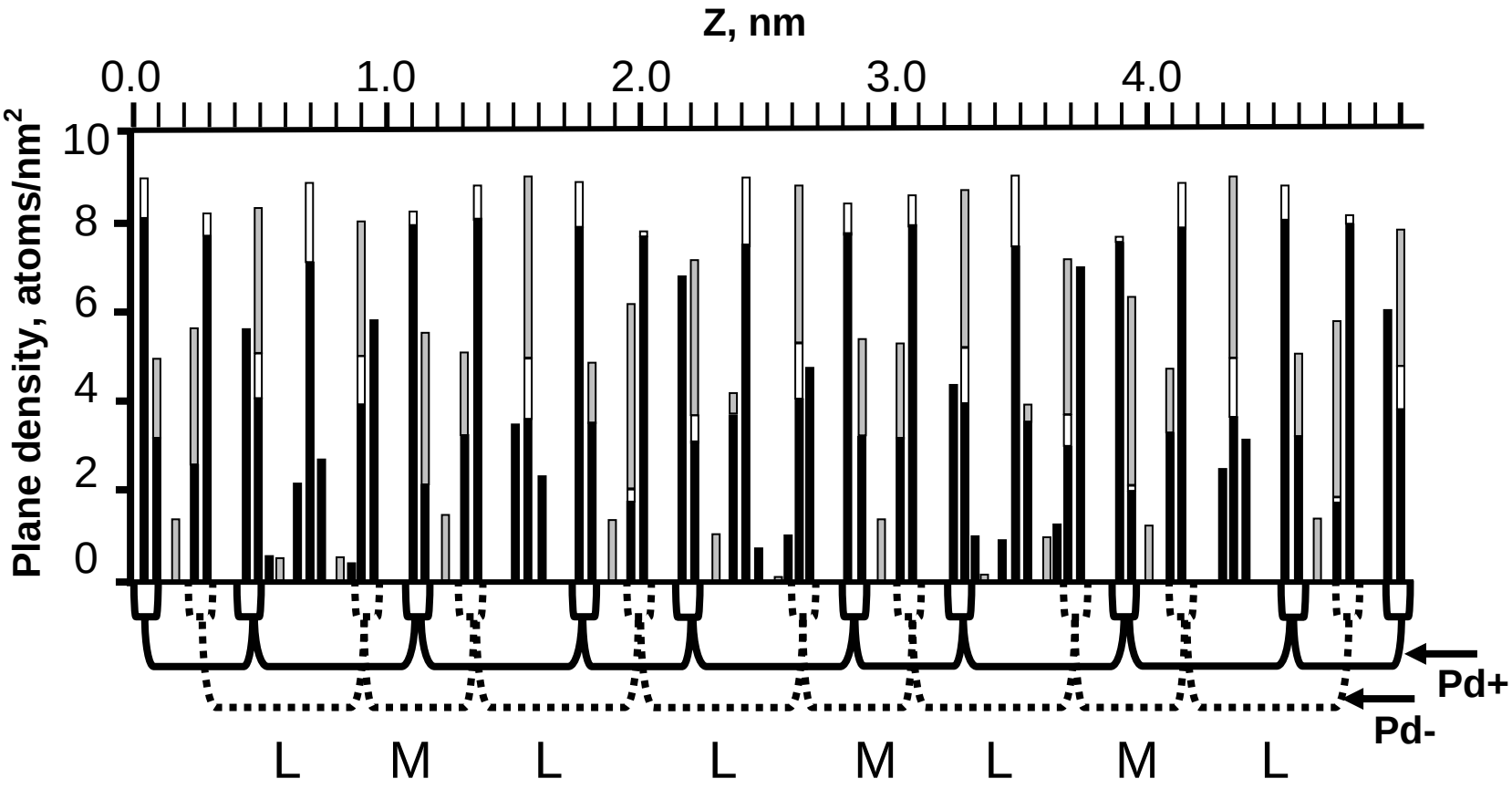
Z, nm
0.0
1.0
2.0
3.0
4.0
Plane density, atoms/nm²
10
8
6
4
2
0
Pd+
Pd-
L
M
L
L
M
L
M
L

Figure 1

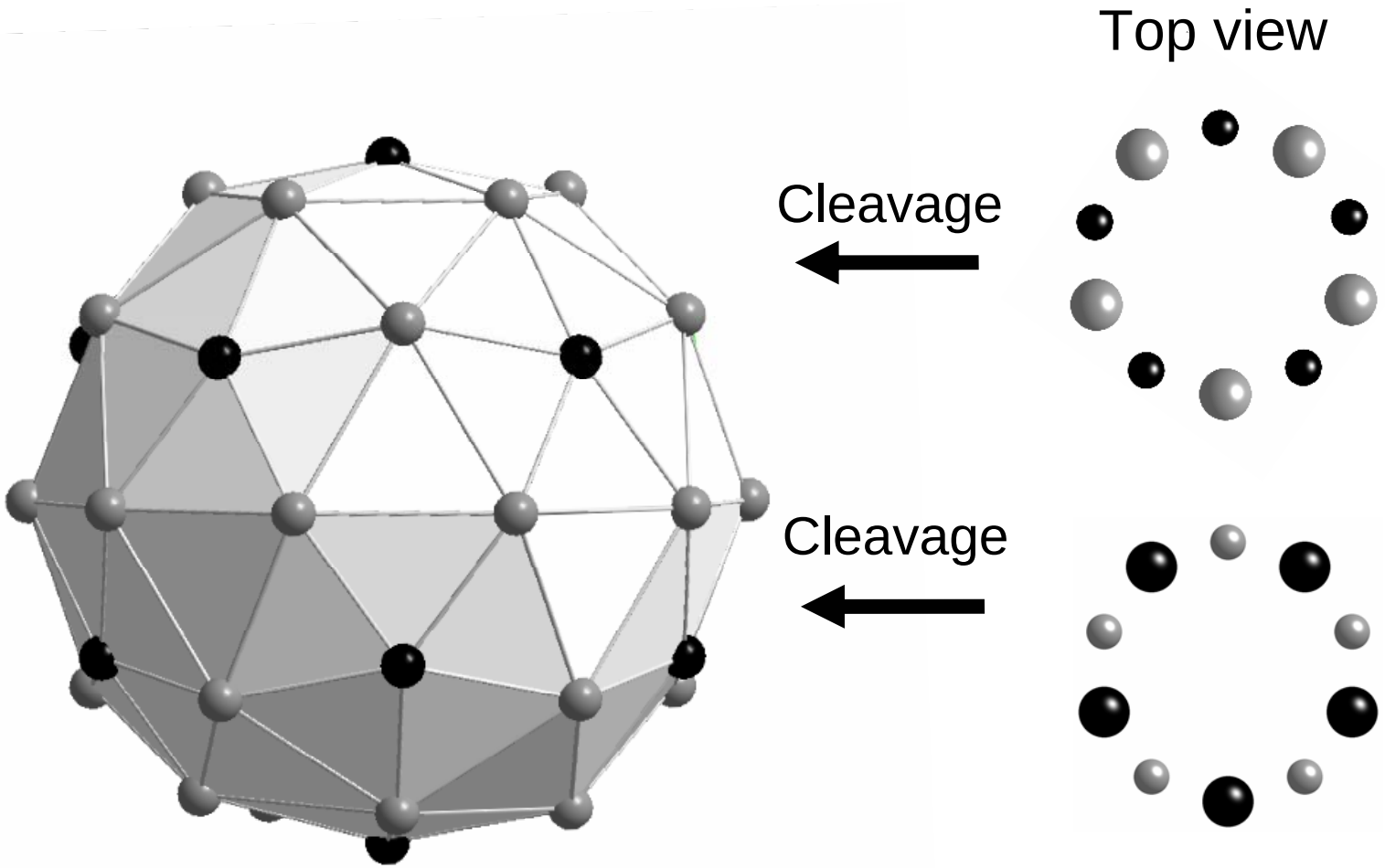

Figure 2

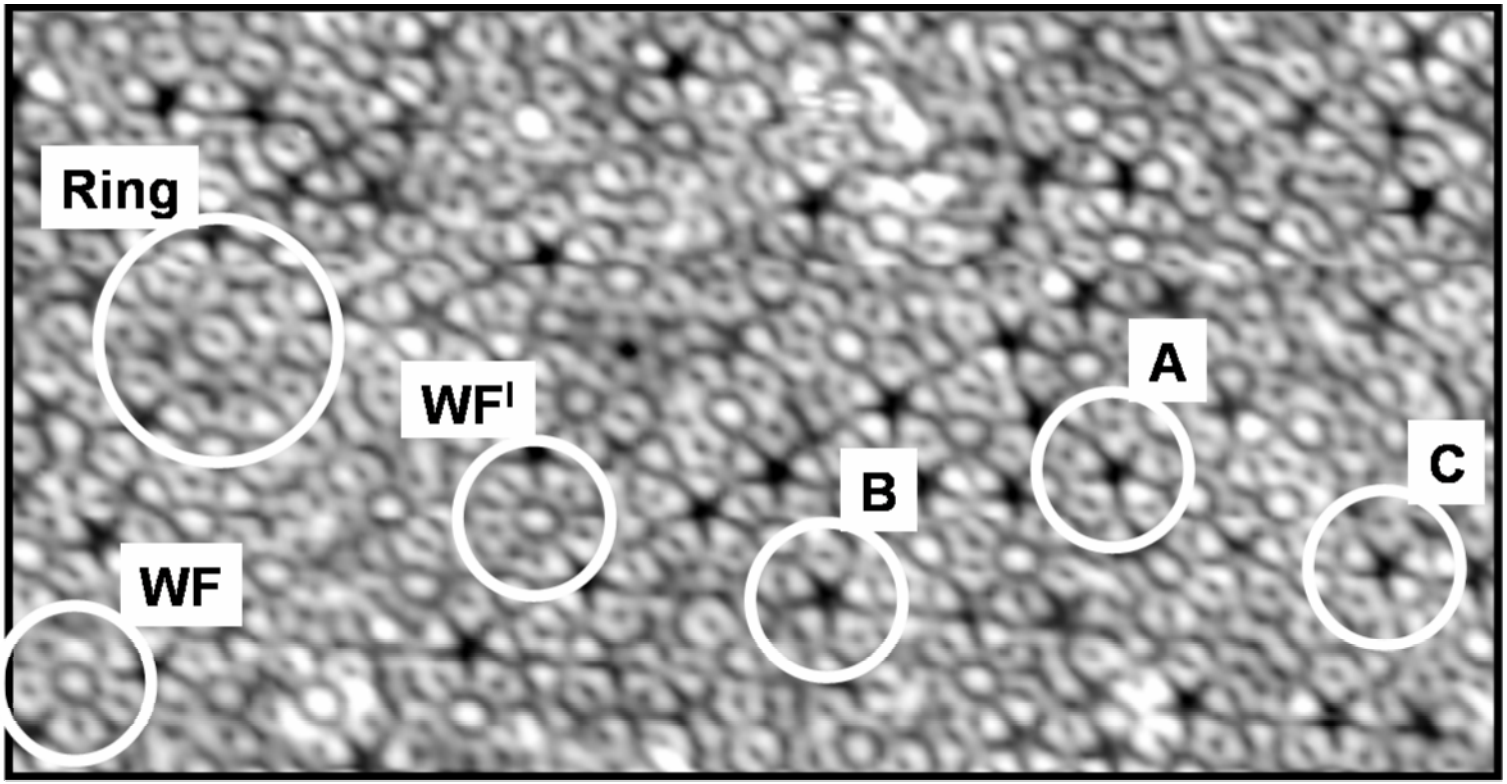

Figure 3 (a)

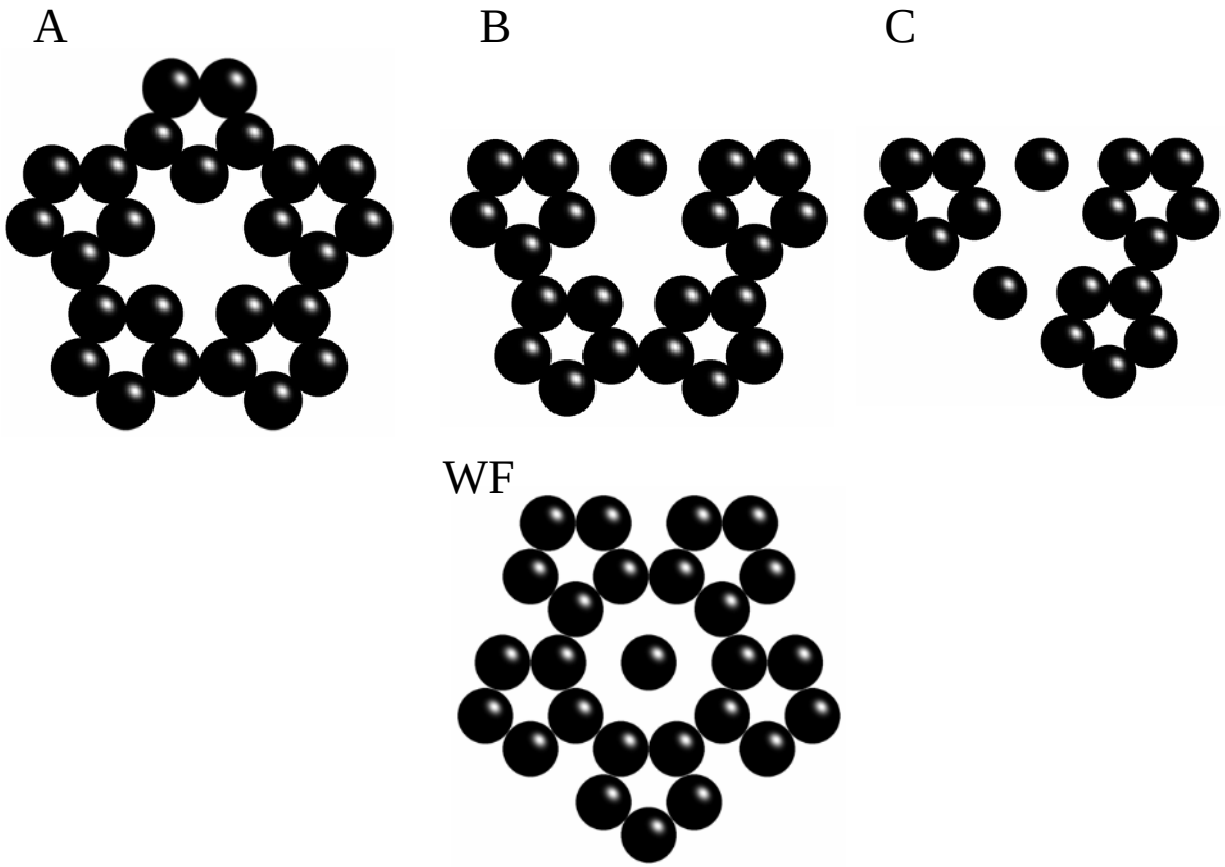

Figure 3 (b)

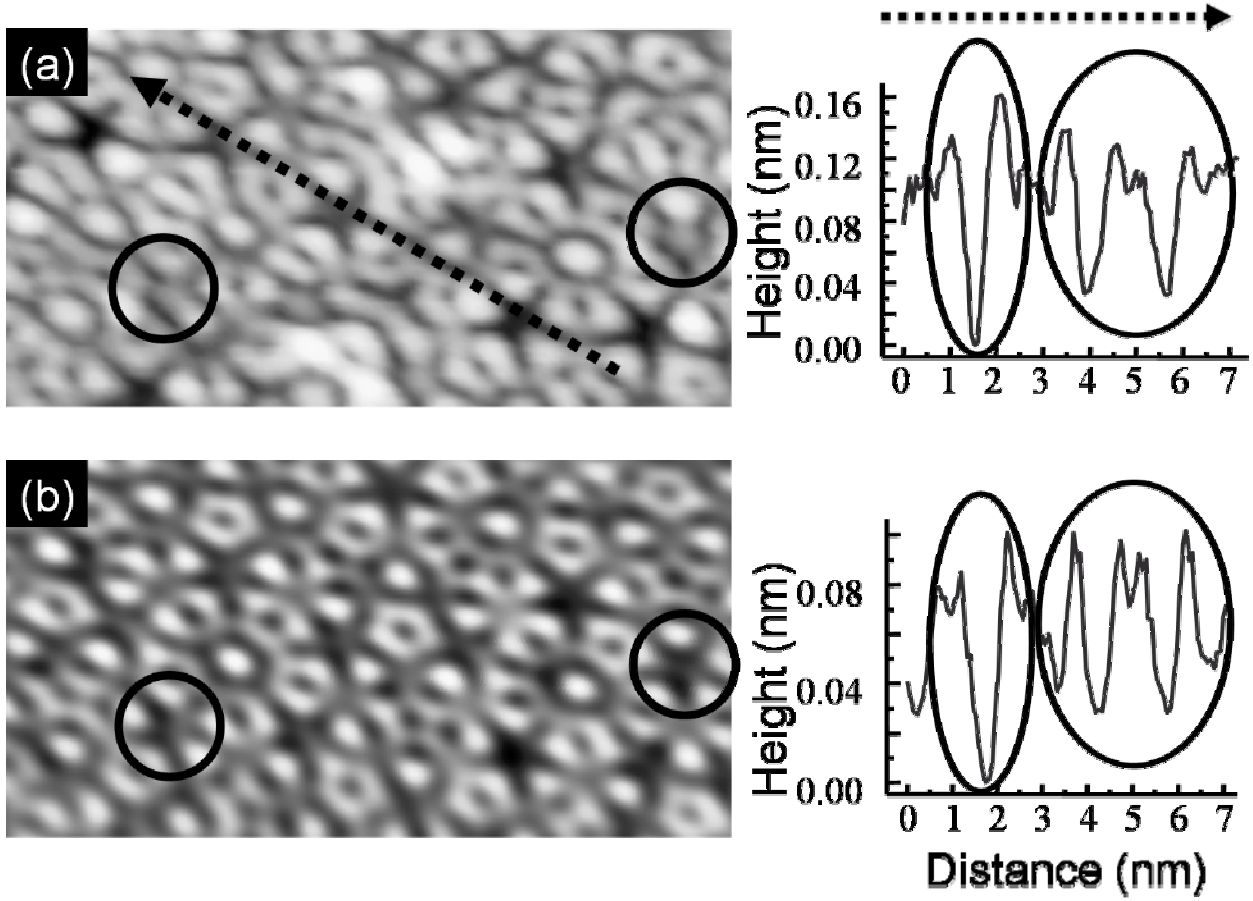

Figure 4

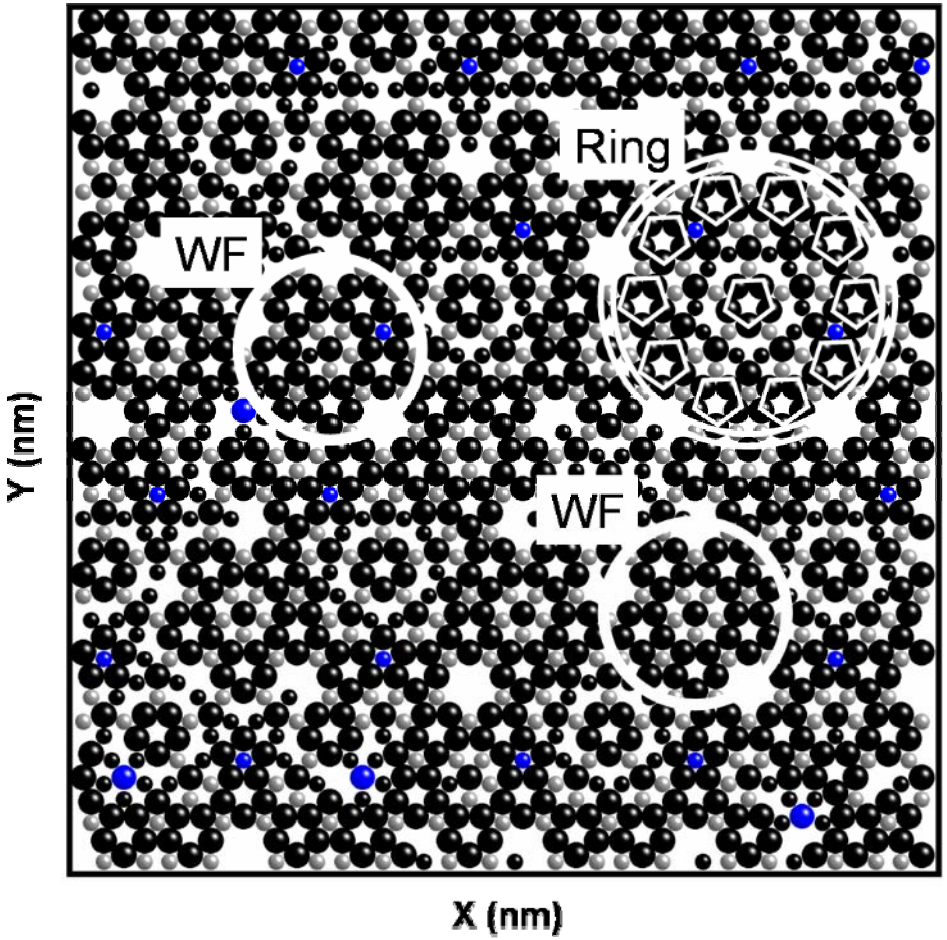

Figure 5

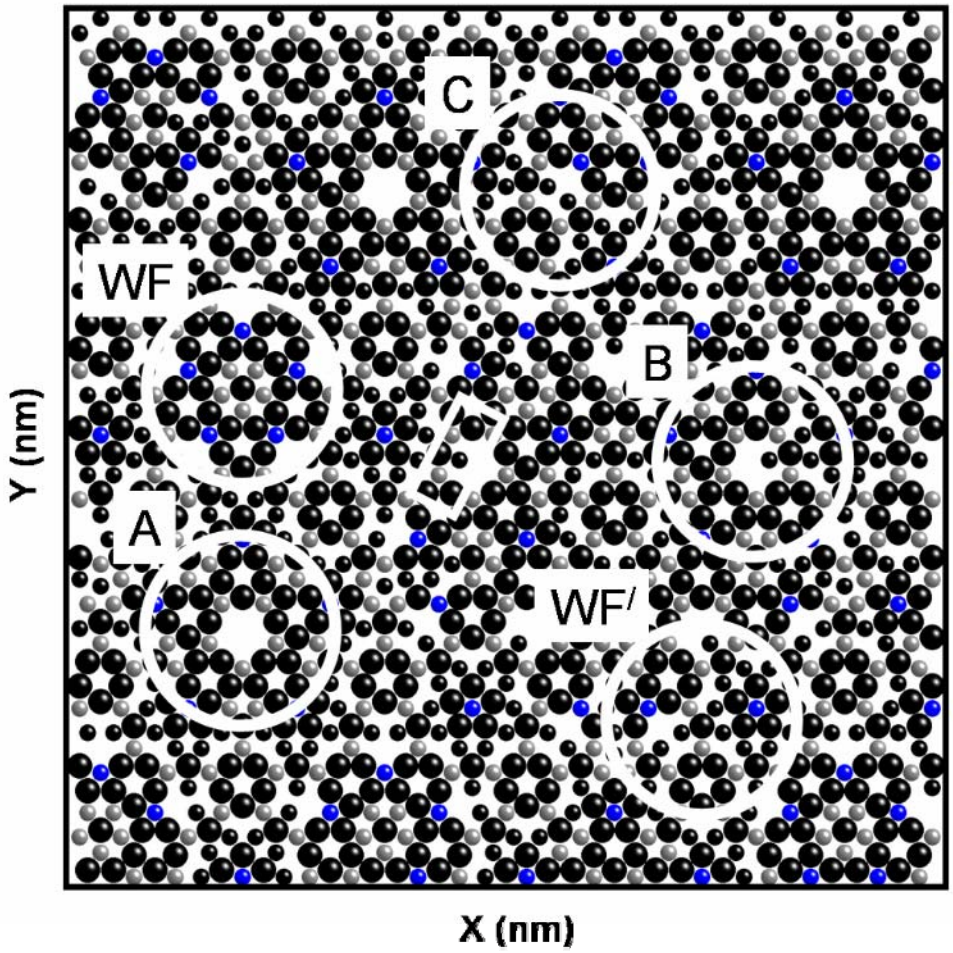

Figure 6 (a)

(b)

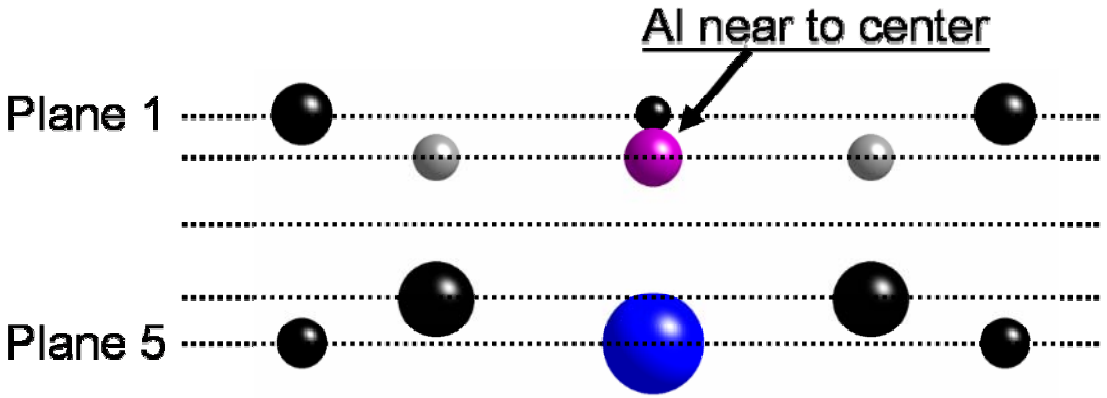

(c)

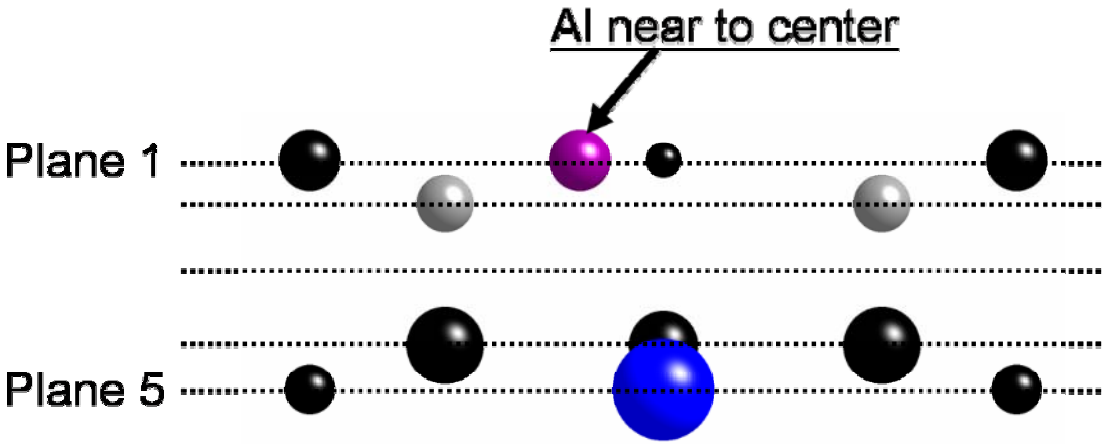

Figure 6 (b) and (c)

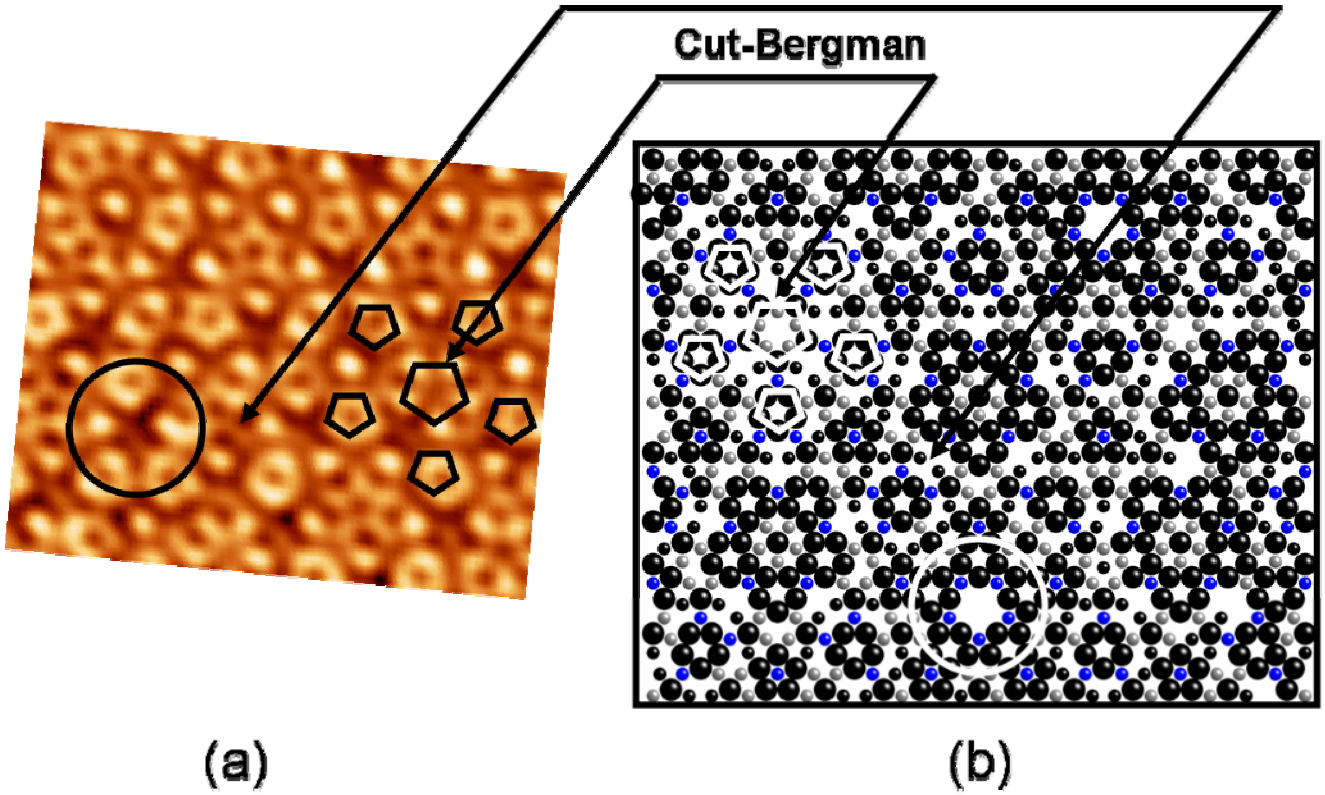

Figure 7

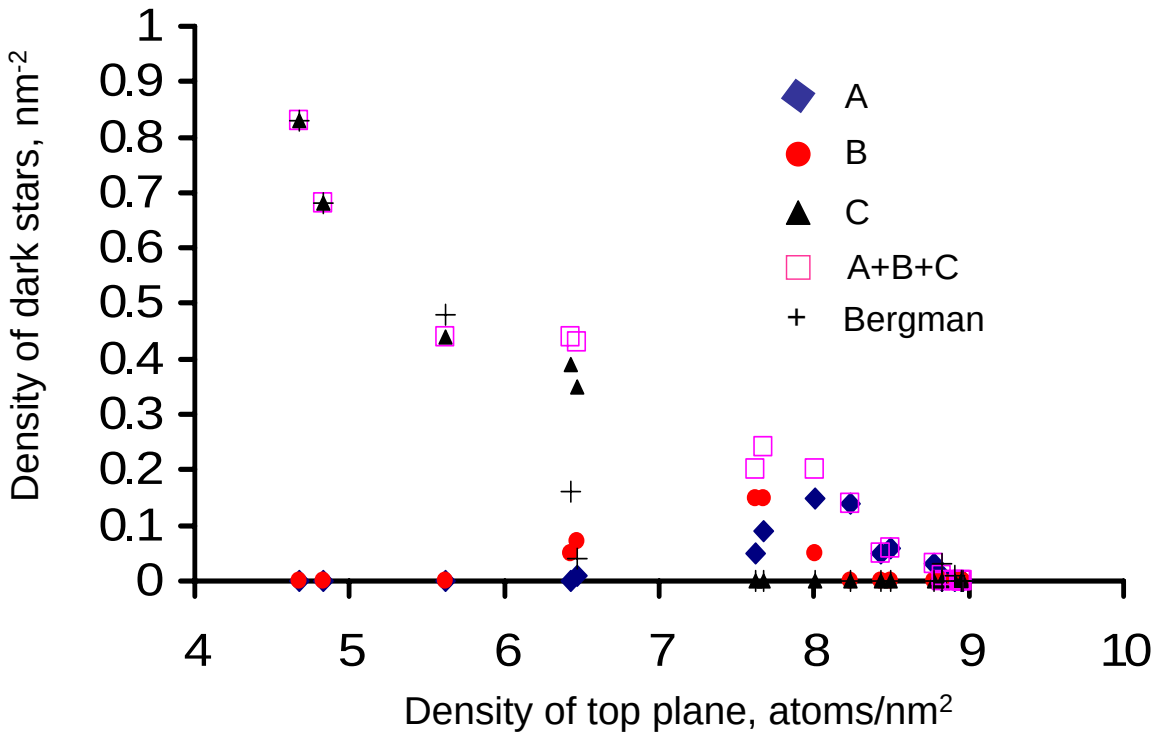
Density of dark stars, nm-2
1
0.9
0.8
0.7
0.6
0.5
0.4
0.3
0.2
0.1
0
4
5
6
7
8
9
10
Density of top plane, atoms/nm2
A
B
C
A+B+C
Bergman

Figure 8

NUCLEATION AND GROWTH OF AG ISLANDS ON FIVE-FOLD AL-PD-MN QUASICRYSTAL SURFACES: TEMPERATURE AND FLUX-DEPENDENCE OF ISLAND DENSITY

A paper published in *Physical Review B*

B. Unal, V. Fournée, K.J. Schnitzenbaumer, C. Ghosh, C.J. Jenks, A.R. Ross, T.A. Lograsso, J.W. Evans, and P.A. Thiel

Abstract

Scanning tunneling microscopy (STM) has been used to investigate the nucleation and growth of Ag islands on the five-fold surface of an icosahedral Al-Pd-Mn quasicrystal. Analysis of the data as a function of deposition temperature, from 127 K to 300 K, reveals that island density is constant, while at higher temperature it decreases. To model this behavior, we first show that the potential energy surface describing bonding of Ag at various locations on the surface is complex, with a few sites acting as traps for clusters of adatoms. We then develop a rate equation model which incorporates enhanced nucleation at trap sites relative to nucleation at regular sites on terraces. It recovers the temperature-dependence of the island density, plus previous flux-scaling data. Our model suggests that the critical size for both types of nucleation sites is large–corresponding to stable clusters of at least 6 Ag atoms– and that binding between atoms at trap sites is significantly stronger than at free terrace sites. The data and the model, combined, provide guidance about the conditions of temperature and flux under which saturation of trap sites can be expected. This, in turn,

provides a general indicator of the conditions that may favor localized pseudomorphic growth at low coverage, here and in other systems.

Introduction

Quasicrystals are well-ordered but non-periodic materials.[1] Their atomic structure is associated with interesting surface properties[2, 3] such as enhanced oxidation resistance [4] and low friction.[5] In recent years, much attention has been paid to the possibility that films might be grown pseudomorphically on quasicrystal surfaces, thereby yielding surfaces that derive the benefits of the quasiperiodic structure, but with a wider range of chemical composition than is accessible in bulk samples.[6-8] Pseudomorphic growth was indeed demonstrated experimentally, originally by Franke et al.,[9] and later by other groups, for certain types of elemental adlayers.[10-12] Pseudomorphic growth has also been explored theoretically.[13, 14] The properties of such films remain largely unexplored, but preliminary measurements of their electronic structure suggest that they adopt the pseudogap at the Fermi edge which is associated with the underlying substrate.[15]

Many studies of film growth have focused on coverages of a complete monolayer (ML) or above, since contiguous coatings would be desirable for some applications. However, lower coverages may also be interesting. For example, individual pseudomorphic islands might exhibit novel magnetic properties. Pseudomorphism could be more prevalent at submonolayer coverages, where adsorbate-adsorbate interactions are more localized, and distortions from the bulk structure of the film are thus more easily accommodated. This appears to be illustrated by our previous study of Al adsorbed on the five-fold surface of the icosahedral (i-) quasicrystal Al-Cu-Fe, where small five-fold clusters were observed at a

coverage of about 0.04 ML.[10] In comparison, pseudomorphism was not observed in studies of Al at or above coverages of 1 ML on a similar substrate, i-Al-Pd-Mn.[16] Formation of the pseudomorphic clusters in the former case was corroborated theoretically using a kinetic Monte Carlo (KMC) simulation of an appropriate "disordered bond network" lattice gas model.[17]

An equally-important advantage of studying low coverages is that a wealth of information can be extracted about the *kinetics* of island nucleation and growth in the initial stages of film formation. This has been shown by the large body of work on crystalline substrates and films.[18] For this purpose, STM provides invaluable detailed insight. This is because the spatial characteristics of films at low coverages, such as the island density, reflect the kinetics of non-equilibrium adlayer evolution during deposition. Based upon just such data, we previously found evidence for heterogeneous nucleation of Ag on the five-fold surface of i-Al-Pd-Mn at 300 K.[19] We interpreted the observed flux-*in*dependence of island density to mean that nucleation occurred preferentially at specific sites--not defect sites, but rather trap sites intrinsic to the quasicrystalline structure. We speculated that these trap sites were analogous to those that stabilized the pseudomorphic Al starfish on i-Al-Cu-Fe.

In this paper, we extend the previous Ag work by measuring the temperature dependence of Ag island density at ~0.2 ML, and by showing the data to be compatible with a refined mean field-rate equation model that incorporates nucleation at trap sites. We delineate the conditions of temperature and flux under which one can expect saturation of trap sites, which provides a general indicator of the conditions that may favor localized pseudomorphic growth at low coverage, in this and other systems.

Experimental Description

We conduct our experiments using an Omicron variable-temperature STM in a standard UHV chamber with a base pressure of 4 x 10^{-11} mbar. Our sample is a single grain of icosahedral $Al_{70.2}Pd_{20.7}Mn_{9.1}$ quasicrystal with the surface oriented perpendicular to a five-fold axis. The clean surface is prepared following procedures described elsewhere.[20, 21] Ag is deposited from an electron-beam-heated evaporator, an Omicron EFM modified to resemble a Knudsen cell, onto the clean quasicrystal surface at fixed sample temperatures varying from 127 K to 420 K and at chamber pressures below 8 x 10^{-11} mbar. STM images are taken at the deposition temperature. STM data are processed using image processing freeware.[22]

Experimental Results

Figure 1 shows a series of STM images taken after deposition between 0.1 and 0.26 monolayers (ML) of Ag at a constant flux of 1 x 10^{-3} ML/s and various substrate temperatures. The brighter features in the images are Ag islands. For the temperature range of 127 K to 300 K, island sizes are very small as compared to those at higher temperatures, and the island density is high. A dramatic decrease in the island density and corresponding increase in size is apparent for temperatures above 300 K. At 420 K (Fig. 1f), most of the deposited Ag accumulates at step edges (not shown in the image). This indicates that the diffusion length has become comparable to the terrace width. However, particularly broad terraces still support island formation, an example of which is shown in Fig.1(f). This allows a rough assessment of island density at this temperature.

It should also be noted that, at these low coverages, islands are typically two-dimensional (2D) at $T \leq 300$ K, but three-dimensional (3D) at $T > 300$ K. The 3D growth has

been ascribed to a quantum size effect.[23] While this crossover from 2D to 3D shapes does not affect our determination and modeling of island densities, it will affect the interpretation of island sizes, as discussed later in this section.

At and below 300 K, the determination of coverage or of island number density is complicated by the fact that the clean surface has a rather high intrinsic corrugation, together with occasional protrusions. In high-resolution images of well-ordered regions of clean terraces, the peak-to-peak corrugation is about 0.12 to 0.16 nm, to be compared with the expected step height for a Ag island of about 0.2 nm. (Note that these values depend somewhat on tunneling bias.) The corrugation and step height are sufficiently close that scanning across Ag islands on the quasicrystal produces a continuum of heights without a clear separation of island and substrate contributions, as shown in Fig. 2 for a coverage of 0.2 ML at 300 K. The large maximum at about 0.1 nm represents the clean substrate, whereas the smaller maximum at about 0.3 nm represents the Ag islands. To determine the island density, we introduce a threshold for height located between these peaks, chosen such that regions with heights above the threshold are mainly associated with Ag islands (see Fig. 2). To further eliminate artifacts in island density estimation due to the existence of occasional protrusions on the quasicrystal surfaces,[24] we employ a threshold for the minimum areal size in addition to the height cutoff. This areal cutoff affects the data only at low temperature, where the Ag islands are small. The effect is shown by the error bars at and below 300 K in Fig. 3. The error bars demarcate minimum areal island sizes of 0.5 and 1.5 nm^2 (the first corresponding roughly to single atoms[25] and the last to larger clusters of ~6 atoms).[10] The data points are obtained with a middle value of 1.0 nm^2. At and below 300 K, in Figs. 3 and 4, the statistics are very good since the data are obtained from STM images after counting

thousands of islands spanning an area equal to 1 x 10^6 nm^2. Thus the statistical uncertainty is much smaller than the error bars shown, at these low temperatures. In contrast, at higher temperatures islands are identified unambiguously, and uncertainties are due to the limited number of islands. These uncertainties are fairly insignificant, at least on the log-scale of Fig.3.

Figure 3 shows quantitatively the temperature-dependence of average island density for a deposition flux of F = 1 x 10^{-3} ML/s. The island density is roughly constant up to 300 K, but abruptly decreases for higher temperatures. This is an indication that heterogeneous nucleation at trap sites dominates behavior at lower temperatures.

We also determine the influence of flux on the island density at constant temperature, 300 K. (The flux-scaling data were published previously; here, we present a re-analysis that employs the height- and size-thresholds described above.) From Figure 4, it can be seen that the island density is insensitive to flux over the range 5 x 10^{-2} to 1 x 10^{-3} ML/s (although there may be a slight drop-off at lowest flux). An independence of island density on deposition flux is also consistent with heterogeneous nucleation at specific trap sites on the surface.

Further analysis of the STM data yields the island size distribution (ISD). Results for 300 K were presented previously, although there was considerable ambiguity in determining the true ISD as it was combined with the distribution of higher substrate protrusions.[19] Figure 5 shows new results from analysis of 365 K data. The total number of islands is about 100, so the statistics are somewhat limited (and histogram bins are necessarily chosen to be quite broad). One could measure island size either in terms of lateral area, or in terms of the total number of atoms (i.e. in terms of volume). The latter is somewhat more generic. The two

approaches are equivalent for the single layer islands at lower T, but not when there is a mixture of multilayer islands of different heights as at higher T. The 365 K data reveal a monotonically decreasing ISD when size is measured as number of atoms. Such a monotonic decrease contrasts the monomodal shape of the distribution typical for homoepitaxial or heteroepitaxial growth.[26] This type of ISD could reflect unusually persistent island nucleation, and/or a diminution of growth rate with coverage.[27] Plausibly, for this system, island growth is inhibited with increasing size (a feature not incorporated into our simple rate equation analysis—see following sections) due to the five-fold symmetry of the substrate.

As an aside, we note that if the ISD at 365 K is determined by taking size as lateral area, it is instead monomodal, reflecting the feature that the largest islands are not single layer, but tend to have heights of two to four layers in this experiment.[23]

Development of the model for nucleation and growth of islands

A. Potential energy surface

In developing a model for formation of Ag islands on five-fold Al-Pd-Mn surfaces, it is valuable first to have a qualitative picture of the potential energy surface (PES) describing the binding energy of Ag as a function of lateral position on this substrate. In previous work,[28] we did this for Al adatoms, and here we extend the analysis to Ag adatoms. [Other authors have recently used LJ parameters to generate the PES of various adsorbates on quasicrystals, successfully explaining experimental structures of equilibrated Al monolayers and noble gas monolayers.[16, 29, 30] Our work differs in that it focuses on the kinetics of formation of localized structure.] In our previous work, we identified a subset of physically-reasonable five-fold terminations of the Boudard model for bulk Al-Pd-Mn structure. We

adopt one such termination here. We use pairwise-additive Lennard-Jones (LJ) potentials to describe the interaction of Ag with the substrate atoms. Parameters for the LJ potentials are chosen to recover diffusion barriers and adsorption site heights for several benchmark systems consisting of Ag on single crystal Al and Pd substrates.[31] With these interactions, we determine the binding energy of Ag as a function of lateral position while keeping substrate atoms frozen (apart from a contraction of the top layer spacings, as guided by experiment).[3, 32-38]

A portion of this PES is shown in Fig. 6a. One can identify three regions of strong bonding, each with local five-fold symmetry, in the upper left, lower left and lower right areas of the figure. One of these is labeled "trap site." Five other regions of strong bonding, where the local five-fold symmetry is broken, are apparent in the upper middle and right portion of the figure. In our previous study of Al binding on the related i-Al-Cu-Fe surface, these same regions provided the strongest bonding, the former being referred to as starfish (SF) sites and the latter as incomplete starfish (ISF) sites. In addition, there is a significant number of a third type of localized strong binding site.

Corresponding features in an STM image of the five-fold Al-Pd-Mn surface are shown in Fig. 6b. Here, we identify the SF sites with the "dark stars" often resolved in STM images of these surfaces. Experiments have proven that the dark stars are the adsorption sites of Al starfish on i-Al-Cu-Fe.[6, 10] The SF and ISF sites are strong candidates for the trap sites that are manifest so clearly in the experimental data of

Figs. 3 and 4.

In a complete analysis of the PES, we have identified all local minima or binding sites, which include a large number of shallower binding sites in addition to the above-

mentioned deep sites. Analysis of ~ 600 sites in a 10 x10 nm^2 region of the model[39] finds 0.5% of sites are SF, 1% are ISF, 4.5% are other localized deep sites, and 94% are shallow sites. The average separation between adjacent minima, regardless of depth, is ~ 0.4 nm. We will use this value as the typical nearest-neighbor separation between adatoms in the modeling that follows.

Utilizing the above information, we can provide the following overview of the deposition process (cf. Ref. 17 & 28): Ag atoms are deposited primarily at shallow adsorption sites, and hop between such adjacent sites; occasionally they reach strong bonding "trap" sites where they remain longer and are more likely to become incorporated into stable Ag islands. (We emphasize that these trap sites are intrinsic to the surface quasicrystalline structure, and are not defects.) In principle, aggregation into islands on regions of the terrace associated with shallow sites is also possible. In our previous modeling of Al deposition on Al-Cu-Fe and Al-Pd-Mn, six atom clusters forming at SF sites (and also smaller clusters forming at ISF sites) were stabilized more effectively than clusters at non-(I)SF sites, since neighboring Al adatoms could readily reduce their separation below the typical value of ~0.4 nm noted above to maximize Al–Al adatom bonding. This stabilization was not so readily achieved at other terrace sites since the large adatom separation of ~0.4 nm is not compatible with strong Al–Al bonding. We adopt this feature—namely, different adatom interaction strengths at different types of nucleation sites —in the Ag modeling below.

B. Rate equation analysis

Rate equations are developed for a model of competitive island formation at trap sites and on terraces, similar to the ones in the literature for nucleation of metal clusters on oxide surfaces with defects.[40] Figure 6c shows a schematic of the model. The model parameters describing the system are as follows: the trap density (n_t); the trap energy ($E_t > 0$) reflecting the additional binding at trap sites; the critical nucleus size (i) above which islands are stable (and for which we allow different values i_t for islands at traps, and i_f on trap-free terrace regions); the effective diffusion barrier ($E_d > 0$), which describes diffusion between heterogeneous weaker-binding adsorption sites; and the pairwise-additive nearest-neighbor adatom binding energy ($E_b > 0$). We allow E_b to take different values at traps (E_{bt}) than on the "free" parts of the terraces (E_{bf}), and set $E_{bf} = R\,E_{bt}$ with $R \leq 1$ for reasons discussed above. The effective hop rate between neighboring sites on terraces is given by $h = \nu e^{-E_d/(kT)}$ where $\nu = 10^{13}$ s^{-1}. The trap density, n_t, is determined experimentally from the plateau value in Figure 3.

Key variables to be determined by integration of the rate equations are the density of isolated adatoms, n_1 (which is the sum of contributions from traps, n_{1t}, and from "free" terrace regions, n_{1f}) and the density of stable islands, n_x (which also is a sum of contributions from traps, n_{xt}, and terraces, n_{xf}). In this model, stable clusters are regarded as immobile. We adjust values of the model parameters described above until the predicted total island density, n_x, matches experimental behavior.

We assume that a quasi-equilibrium is established between the adatom densities at the traps (n_{1t}) and on the free terrace regions (n_{1f}). Accounting for the feature that adatoms are

bound more strongly at traps by an amount E_t and that stable islands at traps (with density n_{xt}) block the occupation of those traps by adatoms, this quasi-equilibrium assumption yields the relation (cf. Ref. 40)

$$\frac{n_{1t}}{n_t - n_{xt}} \approx \frac{n_{1f} e^{E_t/(kT)}}{1 + n_{1f} e^{E_t/(kT)}} \qquad (1)$$

where we assume that $n_{1f} << 1$.The rate equations for densities of stable islands are determined by the nucleation rates

$$\frac{dn_{xt}}{dt} = K_{nuct} \propto h n_{1f} n_{it} \qquad (2)$$

and

$$\frac{dn_{xf}}{dt} = K_{nucf} \propto h n_{1f} n_{if} \qquad (3)$$

where $n_{if}(n_{it})$is the density of critical clusters of i atoms at free terrace (trap) sites which are stabilized by addition of one further adatom. In determining these densities, we also adopt a quasi-equilibrium Walton relation $n_{if} \approx e^{E_{if}/(kT)} (n_{1f})^{i_f}$ and $n_{it} \approx e^{E_{it}/(kT)} n_{1t} (n_{1f})^{i_t - 1}$. Here, $E_i = m_i E_b$ denotes the binding energy for critical clusters, which is determined by adding the appropriate number, m_i, of bond energies, with relevant values of i and E_b for islands at traps or on terraces. The aggregation rates $K_{aggf} \propto h(n_{1f}) n_{xf}$ and $K_{aggt} \propto h(n_{1f}) n_{xt}$ also appear in the rate equation for the adatom density

$$\frac{dn_{1f}}{dt} \approx F - K_{aggf} - K_{aggt} - (i_f + 1)K_{nucf} - (i_t)K_{nuct} \qquad (4)$$

The constants of proportionality (not shown) in the expressions for nucleation rates and aggregation rates are the capture numbers for critical and stable clusters, respectively. These are always of order unity, and are set equal to unity in the following analysis. We also note that these rate equations are numerically stiff, so a natural rescaling[41] is applied before numerical integration in order to facilitate integration.

In general, the value of m_i depends upon the assumed cluster geometry. The two cluster sizes that will be most useful in the modeling will contain 5 and 11 atoms, for which we count $m_i = 7$ and 16, respectively.

C. Model limitations and simplifications

A significant potential limitation of the rate equation analysis is the assumption of a quasi-equilibrium between the population of isolated adatoms at trap sites and free terrace sites, and between the population of atoms and critical clusters (i.e., the Walton relation). This assumption is expected to be valid at high temperatures, but less so at low temperatures, where slow diffusion is expected to inhibit equilibration. A second simplification is the fact that the model uses averages or effective values for certain quantities instead of distributions. An example is the assumption of a single value of E_{bf} for atoms in clusters on the free terrace sites. On the real surface, there is a distribution of separations between adsorption sites, and also of the binding energy at those sites. (Again, see Fig. 6a.) This means that interactions between adatoms probably vary as well. A third assumption is that bond energies, E_b, are

pairwise-additive within the Ag clusters. Because of these limitations, we do not regard the model as quantitatively reliable. We do regard it as useful, however, for showing major trends and providing physical insight into the relative importance of the various processes in fitting the experimental data.

Modeling Results

First, let us consider the simplest case, where $i_t = i_f = 1$ (Ag adatom pairs form stable nuclei) and thus E_b is not relevant. Such a model has only 2 adjustable parameters: E_t and E_d. In this case, Fig. 3 shows that the model can reproduce average island density in the low temperature regime when E_d and E_t are 0.18 and 0.60 eV, respectively. (We denote this set of parameters as Set A, and summarize it in Table I.) While the model reproduces the low-temperature plateau, it fails to produce a sufficiently rapid decrease in island density above 300 K with these parameters.

Next, we allow $i_t = i_f > 1$, with E_b fixed at a single nonzero value, i.e. $E_{bf} = E_{bt}$ so $R = E_{bf}/E_{bt} = 1$. In this case, the model fails to fit the plateau in island density below 300 K. The reason is that, for a single binding energy and single critical size, there is no difference between the formation of stable clusters at free terrace sites and at trap sites. The vastly higher density of the free terrace sites favors nucleation there. Indeed, depending on the adjustable parameters below 300 K the number of islands on free terrace sites is 5 to 20 times larger than at trap sites, since the latter are limited by n_t. (Changing n_t within the limits of experimental uncertainty does not help.) In our model, this problem cannot be avoided by allowing the two critical sizes to take different values. This is true at least for $2 < i_f < 20$ and $2 < i_t < 5$. (We regard these two ranges as having physically-reasonable limits.) This

shows that introducing a larger critical size at free sites does not provide sufficient bias against nucleation at those sites.

In order to fit the entire range of data, we find it necessary to allow E_{bt} and E_{bf} to take independent values, i.e. to use R, their ratio, as an adjustable parameter. As mentioned in Section IV, values of $R < 1$ have some physical justification from the potential energy surface. In the rate equation model, introducing $R < 1$ gives a way to strongly destabilize clusters on free terraces. In this case, the trends in the experimental data can be reasonably well captured (see Fig. 3) by choosing a single value of critical size, $i_t = i_f = 5$, together with $E_{bt} = 0.090$ eV , $E_d = 0.66$ eV and $R = 0.10$. We denote this set of parameters as Set B. It does much better than Set A in matching the
high-temperature data.

However, $R = 0.10$ is perhaps unrealistically low. Indeed, using the LJ potentials for bulk Ag, we estimate that the ratio of the binding energies for Ag-Ag bonds at their equilibrium separation, relative to Ag-Ag bonds elongated to 0.40 nm, is 0.33. Consequently, we explore the possibility of using higher values of R, coupled with two distinct critical sizes for trap and free sites with $i_f > i_t$. Choosing a larger critical size for free terrace sites provides some bias against nucleation on free terraces, which compensates for the higher values of R. While keeping $i_t = 5$, we find that experimental data can be fit well for a range of $i_f \geq 8$ and $R = 0.15$-0.20. The best fit is obtained when $i_t = 5$ and $i_f = 11$, together with $E_{bt} = 0.090$ eV, $E_d = 0.66$ eV, and $R = 0.20$. See Figure 3. We call this Set C. The parameters for the three best-fit models are summarized in
Table I.

The inset in Figure 3 shows the island density on free terrace sites as a function of temperature, using Sets B and C. This indicates that some Ag island nucleation does occur on regular terrace sites between 200 K and 300. However, it should also be emphasized that the contribution of free sites to average island density is low compared to that of trap sites, with these parameters.

What features of the deposition process produce the particular form of $n_x(T)$ shown in Fig. 3? Insight is provided by Fig. 8. Here, the rate of nucleation at trap sites, K_{nuct}, is shown as a function of coverage, for four different values of T. The value of K_{nuct} peaks at low coverage and decays. The peak is higher and the decay is faster at low T. At 300 K or below, K_{nuct}, has effectively decayed to zero by 0.2 ML, i.e. all traps are saturated by 0.2 ML. For higher T, the slower decay of K_{nuct} means that traps are not saturated by 0.2 ML, so $n_x(T)$ in Fig. 3 drops to lower values. It follows that the temperature at which n_x begins to fall in Fig. 3 would shift to higher values for higher coverages.

Finally, the flux-independence of the island density at 300 K can also be fit well. The solid lines in Fig. 4 represent the results for Sets B and C. It can be seen that with both sets of parameters, the model shows no significant variation with flux for $F \geq 1 \times 10^{-3}$ ML/s. However, below this value, the model indicates that traps sites are not saturated (at this temperature and coverage), so n_x falls with decreasing flux.

Flux scaling for homogenous nucleation of stable islands that require aggregation of i ≥ 1 diffusing adatoms in the steady-state regime suggests $n_X \propto F^{i/(i+2)}$.[26, 42] The dash-dotted line in Figure 4 reflects this scaling relationship for i = 5. Clearly this behavior does not fit experimental observations.

Using our model, we can predict n_x versus F at different deposition temperatures (Fig. 7). The model suggests that at high temperatures such as 345 K and above, the density depends on flux for the typical experimental range of fluxes shown (in contrast to behavior at 300 K and below). It would be interesting to test this prediction experimentally. The lines are slightly curved at low flux, but straighten as temperature increases. At 420 K, where the relationship is very linear, analysis of the scaling with flux indicates that $n_x \propto F^{0.66}$, rather than the relationship given above for homogeneous nucleation with i = 5, which would be $n_x \propto F^{5/7} = F^{0.71}$. To understand this discrepancy, we note that in this regime, n_{xf} is negligible and most traps are saturated with single adatoms, so $n_{1t} \approx n_t$. (Clusters are rare at the traps, since $n_x < n_t$ in the curves of Fig. 7.) Thus, in our rate equation analysis, one can neglect n_{xf} and simplify the equation for n_{xt} to $dn_{xt}/dt \propto (n_{1f})^{i_t}$. Then using a steady-state approximation that $F - K_{aggt} \approx 0$, it follows immediately that $n_x \propto F^{(i_t-1)/(i_t+1)}$. This yields an exponent of 2/3, consistent with the numerical results for $i_t = 5$.

Discussion

The main result is the experimental observation that, for a typical flux, the island density is independent of temperature up to 300 K but decreases abruptly above 300 K, for a coverage of about 0.2 ML. This signifies that the island density equals the density of intrinsic surface traps up to 300 K, but falls at higher T because inhibited nucleation prevents trap saturation. The experimental flux dependence of n_x at 300 K shows no significant variation, except perhaps at lowest flux. Our interpretation is that the island density is again equal to

the trap density. Limited data are also presented for the experimental island size distribution, showing a monotonic decrease at a single coverage, temperature, and flux.

A rate equation model shows that two main features must be incorporated to fit the temperature-dependent data: (1) the critical size must be significantly greater than 1, both at trap and free terrace sites; and (2) the binding energy of adatoms in the critical cluster must be significantly higher at traps than at free terrace sites. The model parameters that provide good fits for the temperature-dependence of n_x also provide good fits for the flux-dependence of n_x. The model predicts significant flux dependence at
$T > 300$ K, where n_x is well below the trap density so that the effect of traps is reduced.

The growth dynamics that are incorporated into the model can be envisioned as follows. Adatoms are deposited on the surface and then diffuse, sometimes visiting trap sites. Additional atoms can join to form clusters, potentially either at trap sites or on terraces. However, these clusters constantly dissolve and re-form if they are below the size of a stable nucleus, i+1. In order for nucleation to be favored at traps, the population of critical clusters of size i must be enhanced at the traps. In the case i = 1 (when critical clusters are *single atoms*), the only important factor is the population of *single atoms* at trap sites relative to free terrace sites, which is determined in our model by the trap site energy, E_t. As i increases above 1, the binding energy of additional atoms at traps relative to that on terraces, defined in our model by R, becomes increasingly important, since this determines the stability of *other atoms* in a trap cluster relative to its free-terrace counterpart. For large critical sizes, such as those in our best solutions (Sets B and C), varying E_t actually has far less effect than varying R, if E_t is above a minimum value. In fact, if $E_t \geq 0.40$ eV, it has no effect at all, which effectively reduces the number of variable parameters. In summary, our model shows that

traps are most effective for nucleation when i=1 because traps have a higher population of single atoms, and also when i>1 because traps have a higher affinity for additional atoms.

Although the values of the best-fit parameters are not absolute because of the model limitations noted in Section IV, the value of 0.66 eV for E_d is somewhat high when compared with simpler crystalline surfaces. For instance, E_d is about 0.5 eV both for Ag/Al(100) and Ag/Pd(100), and E_d is much lower—about 0.1 eV—for the (111) faces.[31] In general, for single crystals, one finds that E_d increases as the surface becomes more corrugated and less close-packed.[43] Thus, a relatively high value of E_d on the quasicrystal surface may be physically reasonable in light of its intrinsic roughness. It should be noted that in the REA, E_d is an effective diffusion barrier on the free terrace. Clearly, the surface heterogeneity results in a distribution of barriers that separate adjacent minima (Fig. 6a). The effective diffusion barrier reflects not only the distribution of real barrier heights but also the sampled diffusion paths. This concept of an effective barrier is standard in extensive treatments of transport in disordered systems based on homogenization or effective medium theories.[44] For our specific application, the effective barrier will be primarily controlled by the higher barriers for diffusion on the terrace.

It is interesting that the best value of i_t is 5, exactly the value expected given the stability of the 6-atom starfish clusters observed and modeled for Al on i-Al-Cu-Fe.[28] These clusters contained 1 atom at the center and 5 atoms at the arms, thus reflecting the local five-fold symmetry of the surface sites. Hence, the value of the critical cluster size at trap sites may be fundamentally related to the five-fold symmetry of the quasicrystalline surface.

This system bears certain similarities to transition metal clusters that form at defects on oxide[45, 46] and fluoride[40] surfaces. In some of those systems, the dependence of island density on temperature has been measured,[40, 45] showing a plateau and then a decline.[40, 45]

For one system, Pd/MgO, these data were initially interpreted in terms of a model like the one we have used, incorporating strong trapping of adatoms at defects and subsequent island nucleation (with i = 1) below the threshold temperature.[45] However, this model was challenged on the basis of DFT calculations, which indicated that cluster diffusion, as well as monomer diffusion, should be operative, and that the surface dimer binding energy necessary to fit the data, 1.2 eV, was unreasonably high.[47, 48]

We regard cluster diffusion in our system, however, as unlikely. This is because there are two primary scenarios wherein diffusion of small clusters on surfaces is expected to significantly affect growth: (1) weak bonding to the surface compared to intracluster bonding—as is the case for Pd/MgO;[48] or (2) a PES for the cluster amenable to concerted cluster motion, as for dimers in metal homoepitaxial systems where twisting or shearing motion is facile.[49] Neither scenario is operative for Ag on Al-Pd-Mn where Ag binds strongly to the surface. Inspection of the spatial distribution of absorption sites on the surface (e.g., from the LJ PES) suggests no easy twisting pathway. In fact, intracluster binding is likely weak due to a large typical separation between neighboring adsorption sites so clusters are more likely to dissociate than diffuse. Weak intracluster binding is supported by the low value of E_b, 0.090 eV. It is also impossible for clusters to migrate along with the underlying traps, as has been suggested for Au clusters on TiO_2.[46]

Our model is also qualitatively different regarding the metal-metal binding energy, which was disputed in the Pd/MgO system.[47, 48] Our values of E_b are low: 0.090 eV within

the traps, and less on the free terraces by a factor of R. For comparison, the Ag–Ag dimer binding energy on a Ag(100) surface is 0.22-0.26 eV.[50] The distortion from the equilibrium bond length that is imposed by the quasicrystal substrate makes the lower value of 0.090 eV plausible. There are also other differences. For instance, critical size was quite small in the rate equation analysis of the Pd/MgO system and so E_t was an important parameter. Our fits imply large critical sizes and hence virtually no dependence on E_t, for reasons discussed above. In spite of these differences, the approach that was pioneered by Haas and co-workers[45] appears to be very useful in interpreting results from the present system.

Finally, consider the possibility of place exchange between Ag and the quasicrystal substrate. We see no evidence of such a process, but if it occurred, its effect on island density would be different than our experimental observations. Typically, place exchange is an activated process, with a barrier higher than that for hopping-diffusion. Growth of islands at exchange sites competes with homogeneous nucleation and growth. These two factors mean that island density vs. T or T^{-1} is a V-shaped curve (or even more complex curve), as has been reported for Ni/Ag(100)[51] and Co/Cu(100).[52] In the case of island nucleation mediated *entirely* by place exchange, there is also a (predicted) strong dependence of island density on T, contrasting our experimental observations.[53] Hence, place exchange cannot explain our experimental observation of a plateau, followed by a decline at high T.

Conclusions

A main result in this paper is that the Ag island density on the five-fold surface of icosahedral Al-Pd-Mn is independent of temperature up to 300 K, but decreases abruptly above 300 K, for a typical flux. This indicates that nucleation is dominated by trap sites at

and below 300 K. This conclusion is reinforced by the experimental flux dependence of the average island density at 300 K. A rate equation model is developed, guided in part by a potential energy surface generated from Lennard–Jones potentials. For certain parameters, the model is consistent with all of the data. The optimal parameters indicate strong Ag–Ag binding at trap sites relative to free terrace sites, and large critical sizes at both types of sites. The island size distribution at 365 K is also presented, showing a broad monotonic decrease.

The data and the modeling, taken together, indicate that saturation of trap sites at low coverage is favored by low temperature and high flux. These qualitative guidelines may prove useful in searches for pseudomorphic clusters on quasicrystals at submonolayer coverages.

Note added in proof. Recently, it has come to our attention that a considerable body of work deals with heterogeneous nucleation of Co on Au, which exhibits some strong similarities to this system. See, for instance, Ref. 54.

Acknowledgments

BU, CJJ, ARR, TAL, and PAT were supported for this work by the Office of Science, Basic Energy Sciences, Materials Science Division of the U.S. Department of Energy (USDOE). VF, KJS, CG and JWE were supported by NSF Grant CHE-0414378. The work was performed at Ames Laboratory, which is operated for the USDOE by Iowa State University under Contract No. W-7405-Eng-82. BU is thankful to Da-Jiang Liu for his help during the writing of Mathematica codes.

References

[1] D. Shechtman, I. Blech, D. Gratias, and J. W. Cahn, Phys. Rev. Lett. **53**, 1951 (1984).

[2] J. M. Dubois, *Useful Quasicrystals* (World Scientific, Singapore, 2005).

[3] P. A. Thiel, A. I. Goldman, and C. J. Jenks, in *Physical Properties of Quasicrystals*, edited by Z. M. Stadnik (Springer, Berlin, 1999), Vol. 126, p. 327.

[4] D. Rouxel, M. Gil-Gavatz, P. Pigeat, and B. Weber, J. Non-Cryst. Solids **351**, 802 (2005).

[5] J. M. Dubois, P. Brunet, W. Costin, and A. Merstallinger, J. Non-Cryst. Solids **334&335**, 475 (2004).

[6] V. Fournée and P. Thiel, J. Phys. D: App. Phys. **38**, R83 (2005).

[7] R. McGrath, J. Ledieu, E. J. Cox, and R. D. Diehl, J. Phy.: Condens. Matter **14**, R119 (2002).

[8] R. McGrath, J. Ledieu, E. J. Cox, N. Ferralis, and R. D. Diehl, J. Non-Cryst. Solids **334&335**, 500 (2004).

[9] K. J. Franke, H. R. Sharma, W. Theis, P. Gille, P. Ebert, and K. H. Reider, Phys. Rev. Lett. **92**, 135507 (2002).

[10] T. Cai, J. Ledieu, R. McGrath, V. Fournee, T. Lograsso, A. Ross, and P. Thiel, Surf. Sci. **526**, 115 (2003).

[11] J. Ledieu, J. T. Hoeft, R. E. Reid, R. D. Diehl, T. A. Lograsso, A. R. Ross, R. McGrath, and J. A. Smerdon, Phys. Rev. Lett. **92**, 135507 (2004).

[12] J. Ledieu, J. T. Hoeft, D. E. Reid, J. A. Smerdon, R. D. Diehl, N. Ferralis, T. A. Lograsso, A. R. Ross, and R. McGrath, Phys. Rev. B **72**, 035420 (2005).

[13] M. Krajci and J. Hafner, Phys. Rev. B **71**, 184207 (2005).

[14] M. Krajci and J. Hafner, Phil. Mag. **86**, 825 (2006).

[15] V. Fournée, (Unpublished results).

[16] B. Bollinger, V. E. Dmitrienko, M. Erbudak, R. Luscher, H.-U. Nissen, and A. R. Kortan, Phys. Rev. B **63**, 052203 (2001).

[17] C. Ghosh, D.-J. Liu, K. J. Schnitzenbaumer, C. J. Jenks, P. A. Thiel, and J. W. Evans, Surf. Sci. **600**, 2200 (2006).

[18] P. A. Thiel and J. W. Evans, J. Phys. Chem. B **104**, 1663 (2000).

[19] V. Fournée, T. C. Cai, A. R. Ross, T. A. Lograsso, J. W. Evans, and P. A. Thiel, Phys. Rev. B **67**, 033406 (2003).

[20] B. Unal, T. A. Lograsso, A. Ross, C. J. Jenks, and P. A. Thiel, Phys. Rev. B **71**, 165411 (2005).

[21] B. Unal, T. A. Lograsso, A. R. Ross, C. J. Jenks, and P. A. Thiel, Phil. Mag. **86**, 819 (2006).

[22] WSxM 4.0 Develop 7.71 Copyright May 2005 Nanotec Electronica S.L. Available from <http://www.nanotec.es>

[23] V. Fournée, H. R. Sharma, M. Shimoda, A. P. Tsai, B. Unal, A. R. Ross, T. A. Lograsso, and P. A. Thiel, Phys. Rev. Lett **95**, 155504 (2005).

[24] J. Ledieu, A. W. Munz, T. M. Parker, R. McGrath, R. D. Diehl, D. W. Delaney, and T. A. Lograsso, Surf. Sci. **433-435**, 666 (1999).

[25] M. Bott, M. Hohage, M. Morgenstern, T. Michely, and G. Comsa, Phys. Rev. Lett. **76**, 1304 (1996).

[26] J. W. Evans, P. A. Thiel, and M. C. Bartelt, Surf. Sci. Rep. **61**, 1 (2006).

[27] We present a simple deterministic theory (cf. D. Robertson and G. M. Pound, J. Crystal Growth 19, 269 (1973)) for the distribution, f(s), of island sizes, s, at the final coverage, θ. Assume that islands are nucleated at rate $K_{nuc}(\varphi)$, and all grow at the same rate, $R_{agg}(\varphi)$, dependent on the instantaneous coverage, φ. The final size of an island nucleated at coverage $\theta' < \theta$ satisfies $s(\theta') \alpha \int_{\theta' < \varphi < \theta} d\varphi\, R_{agg}(\varphi)$, with maximum $s_{max} = s(0)$. One then has $f(s) \alpha K_{nuc}(\theta'(s))/R_{agg}(\theta'(s))$, for $s < s_{max}$. Here, $\theta'(s)$ is the unique nucleation coverage producing an island of size s, so $\theta'(s)$ decreases with increasing s. Thus, $K_{agg}(\varphi)/R_{agg}(\varphi)$ increasing with φ produces f(s) decreasing with s.

[28] C. Ghosh, D.-J. Liu, C. J. Jenks, P. A. Thiel, and J. W. Evans, Phil. Mag. **86**, 831 (2006).

[29] S. Curtarolo, W. Setyawan, N. Ferralis, R. D. Diehl, and M. W. Cole, Phys. Rev. Lett. **95**, 136104 (2005).

[30] R. A. Trasca, N. Ferralis, R. D. Diehl, and M. W. Cole, J. Phys.: Condens. Matter **16**, S2911 (2004).

[31] DFT calculations by Da-Jiang Liu (unpublished) indicate that the diffusion barrier for Ag/Al(100) is 0.53 eV and for Ag/Pd(100) is 0.48 eV. Furthermore, diffusion barriers of Ag on the "smooth" (111) faces are much lower, around 0.1 eV, as is expected. Fitting the values for the(100) surfaces suggests similar strengths for the LJ Ag-Al and Al-Pd interaction parameter.

[32] C. J. Jenks and R. Bastasz, Prog. Surf. Sci. **75**, 147 (2004).

[33] C. J. Jenks, A. R. Ross, T. A. Lograsso, J. A. Whaley, and R. Bastasz, Surf. Sci. **521**, 34 (2002).

[34] M. J. Capitan, Y. Calvayrac, D. Gratias, and J. Alvarez, Physica B **283**, 79 (2000).

[35] M. Gierer, M. A. V. Hove, A. I. Goldman, Z. Shen, S.-L. Chang, P. J. Pinhero, C. J. Jenks, J. W. Anderegg, C.-M. Zhang, and P. A. Thiel, Phys. Rev. B **57**, 7628 (1998).

[36] M. Gierer, M. A. V. Hove, A. I. Goldman, Z. Shen, S.-L. Chang, C. J. Jenks, C.-M. Zhang, and P. A. Thiel, Phys. Rev. Lett. **78**, 467 (1997).

[37] A. I. Goldman and P. A. Thiel, in *Quasicrystals the State of the Art*, edited by D. P. DiVincenzo and P. J. Steinhardt (World Scientific, Singapore, 1999), Vol. 16, p. 561.

[38] J.-C. Zheng, C. H. A. Huan, A. T. S. Wee, M. A. V. Hove, C. S. Fadley, F. J. Shi, E. Rotenberg, S. R. Barman, J. J. Paggel, K. Horn, P. Ebert, and K. Urban, Phys. Rev. B **69**, 134107 (2004).

[39] Coverage is defined as the ratio of the density of adsorbed particles to the density of adsorption sites. From the PES, the density of sites corresponds to area per adsorption site of 0.167 nm^2/site.

[40] K. R. Heim, S. T. Coyle, G. G. Hembree, J. A. Venables, and M. R. Scheinfein, J. Appl. Phys. **80**, 1161 (1996).

[41] J. W. Evans and M. C. Bartelt, Langmuir **12**, 217 (1996).

[42] D. Robertson and G. M. Pound, J. Crystal Growth **19**, 269 (1973).

[43] G. L. Kellogg, Surf. Sci. Rep. **21**, 1 (1994).

[44] L. Sanchez-Palencia and E. Zaoui, *Homogenization techniques for composite media* (Springer-Verlag, Berlin, 1985).

[45] G. Haas, A. Menck, H. Brune, J. V. Barth, J. A. Venables, and K. Kern, Phys. Rev. B **61**, 11105 (2000).

[46] E. Wahlstrom, N. Lopez, R. Schaub, P. Thostrup, A. Ronnau, C. Affrich, E. Laegsgaard, J. K. Norskov, and F. Besenbacher, Phys. Rev. Lett **90**, 026101 (4) (2003).

[47] L. Xu, G. Henkelman, C. T. Campbell, and H. Jónsson, Phys. Rev. Lett. **95**, 146103 (2005).

[48] L. Xu, G. Henkelman, C. T. Campbell, and H. Jónsson, Surf. Sci **600**, 1351 (2006).

[49] Z.-P. Shi, Z. Zhang, A. K. Swan, and J. F. Wendelken, Phys. Rev. Lett **76**, 4927 (1996).

[50] P. A. Thiel and J. W. Evans, J. Phys. Chem. B **108**, 14428 (2004).

[51] J. A. Meyer and R. J. Behm, Surf. Sci **322**, L275 (1995).

[52] R. Pentcheva, K. A. Fichthorn, M. Scheffler, T. Bernhard, R. Pfandzelter, and H. Winter, Phys. Rev. Lett. **90**, 076101 (2003).

[53] D. D. Chambliss and K. E. Johnson, Phys. Rev. B **50**, 5012 (1994).

[54] V. Repain, S. Rohat, Y. Girard, A. Tejeda, and S. Rousset, J. Phys.: Condens. Matter **18**, S17 _2006_

Table and Figure Captions.

Table 1. Parameters for best fits of the rate equation model to the experimental data.

Figure 1. STM images [(a)-(f)] showing the evolution of island density as a function of temperature for deposition of Ag onto 5f-i-Al-Pd-Mn quasicrystal. The size for images is 100 x 100 nm^2. The tunneling conditions are 0.97-0.99 V and 0.31-0.47 nA.

Figure 2. An area based height histogram taken from an STM image at Θ = 0.2 ML and T = 300 K. Dotted line shows the threshold which partially separates silver islands from the QC substrate.

Figure 3. Temperature dependence of the average island density, n_x, at F = 0.001 ML/s. Solid lines show the predictions obtained from the rate equation model. The inset shows the model's prediction for the number of islands on regular terrace sites (n_{xf}) as a function of temperature.

Figure 4. Average island density, n_x, versus flux for Θ = 0.2 ML and T = 300 K. The solid lines depict predictions from the rate equation model for two cases, Set B and Set C. The expected scaling behavior for homogenous nucleation for i = 5 is shown by the dash─dotted line.

Figure 5. Island size distribution from STM images for Ag/Al-Pd-Mn at 365 K, 0.26 ML and F = $1x10^{-3}$ ML/s.

Figure 6. (a) (Color online) Potential energy surface (8.6 x 8.6 nm^2) for Ag on i-Al-Pd-Mn QC. (b) 8.6 x 8.6 nm^2 STM image of clean five-fold surface of i-Al-Pd-Mn QC (+0.97 V, 0.47 nA). One of the traps is marked both on STM image and PES. (c) Model for nucleation at "trap" sites. n_{1t} is density of trapped single adatoms; n_t is density of traps, n_{1f} is density of free single adatoms, n_{xf} is density of critical clusters formed on terraces and n_{xt} is density of trapped stable clusters.

Figure 7. Predictions for average island density, n_x, as a function of flux from the rate equation model. Parameter values correspond to Set C: $n_t = 0.035\ nm^{-2}$, $E_d = 0.66$ eV, $E_{bt} = 0.090$ eV, $m_{11} = 16$, $R = 0.20$, $i_f = 11$ and $i_t = 5$.

Figure 8. The rate of nucleation at trap sites, K_{nuct}, versus coverage from the rate equation model for set C: $n_t = 0.035\ nm^{-2}$, $E_d = 0.66$ eV, $E_{bt} = 0.090$ eV, $m_{11} = 16$, $R = 0.20$, $i_f = 11$ and $i_t = 5$. The inset is an expanded view of the variation in K_{nuct} with coverage for the three lowest temperatures.

Table 1

Parameter Set	A	B	C
i_t	1	5	5
i_f	1	5	11
E_d (eV)	0.18	0.66	0.66
E_t (eV)	0.60	0.50	0.50
E_{bt} (eV)	--	0.090	0.090
$R = E_{bf} / E_{bt}$	--	0.10	0.20

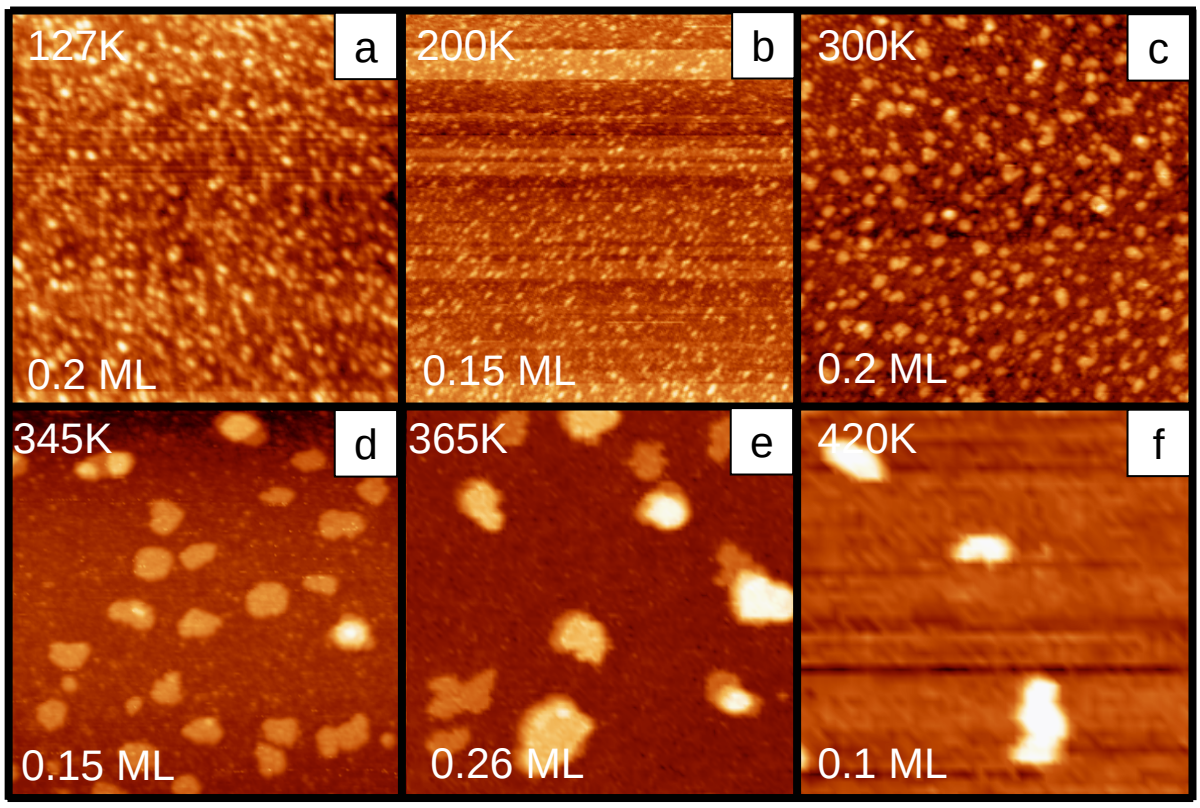
127K
a
0.2 ML
200K
b
0.15 ML
300K
c
0.2 ML
345K
d
0.15 ML
365K
e
0.26 ML
420K
f
0.1 ML

Figure 1

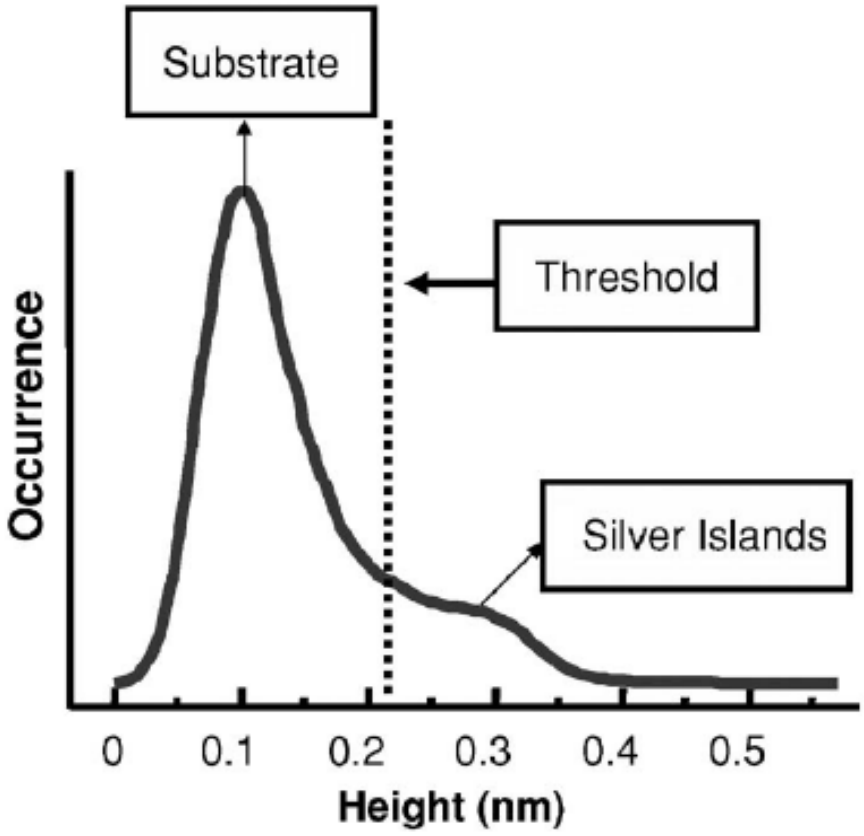
Substrate
Threshold
Silver Islands
Occurrence
0
0.1
0.2
0.3
0.4
0.5
Height (nm)

Figure 2

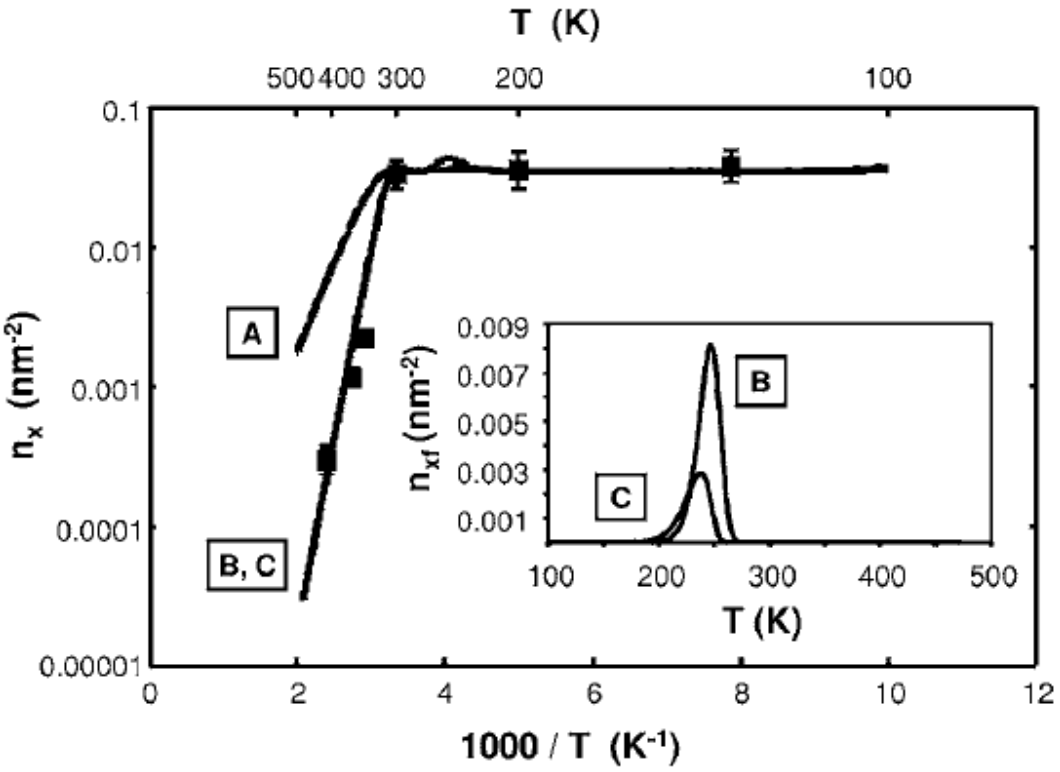
T (K)
500 400 300 200 100
0.1
0.01
0.001
0.0001
0.00001
n_x (nm^{-2})
A
B, C
0.009
0.007
0.005
0.003
0.001
n_{x1} (nm^{-2})
B
C
100 200 300 400 500
T (K)
0 2 4 6 8 10 12
1000 / T (K^{-1})

Figure 3

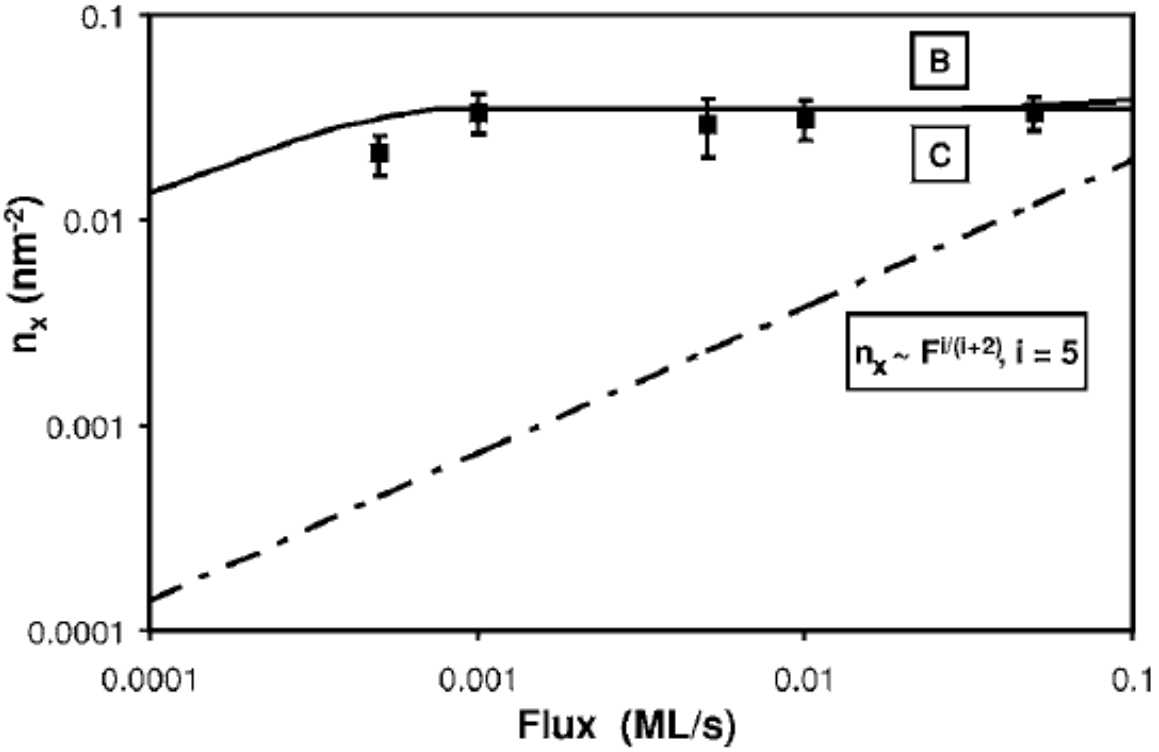
0.1
0.01
0.001
0.0001
n_x (nm^{-2})
B
C
$n_x \sim F^{i/(i+2)}$, i = 5
0.0001
0.001
0.01
0.1
Flux (ML/s)

Figure 4

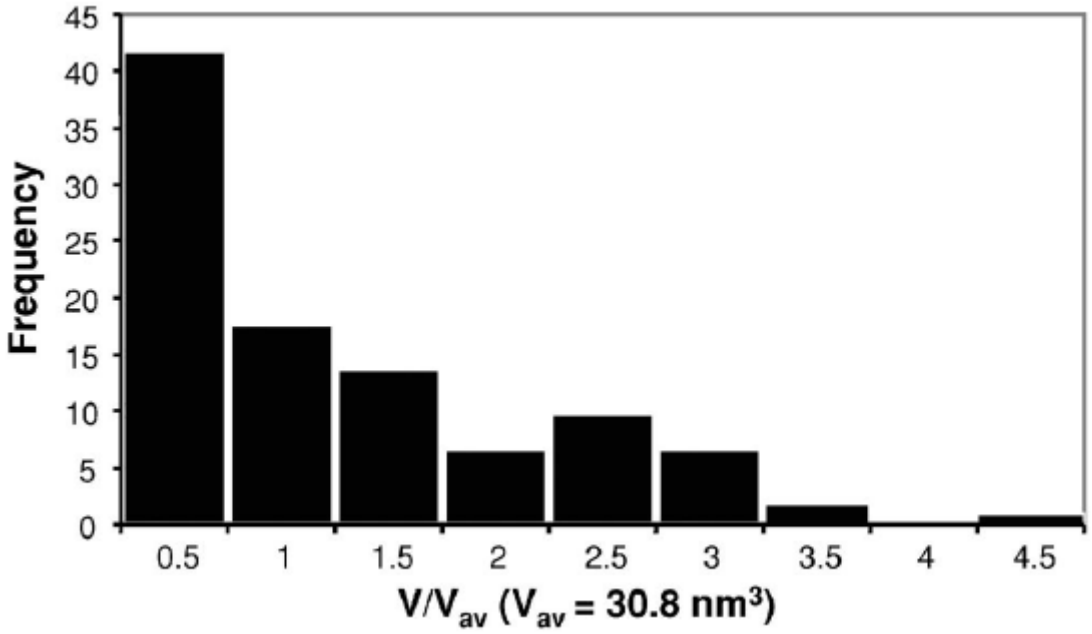
Frequency
45
40
35
30
25
20
15
10
5
0
0.5
1
1.5
2
2.5
3
3.5
4
4.5
V/V$_{av}$ (V$_{av}$ = 30.8 nm^3)

Figure 5

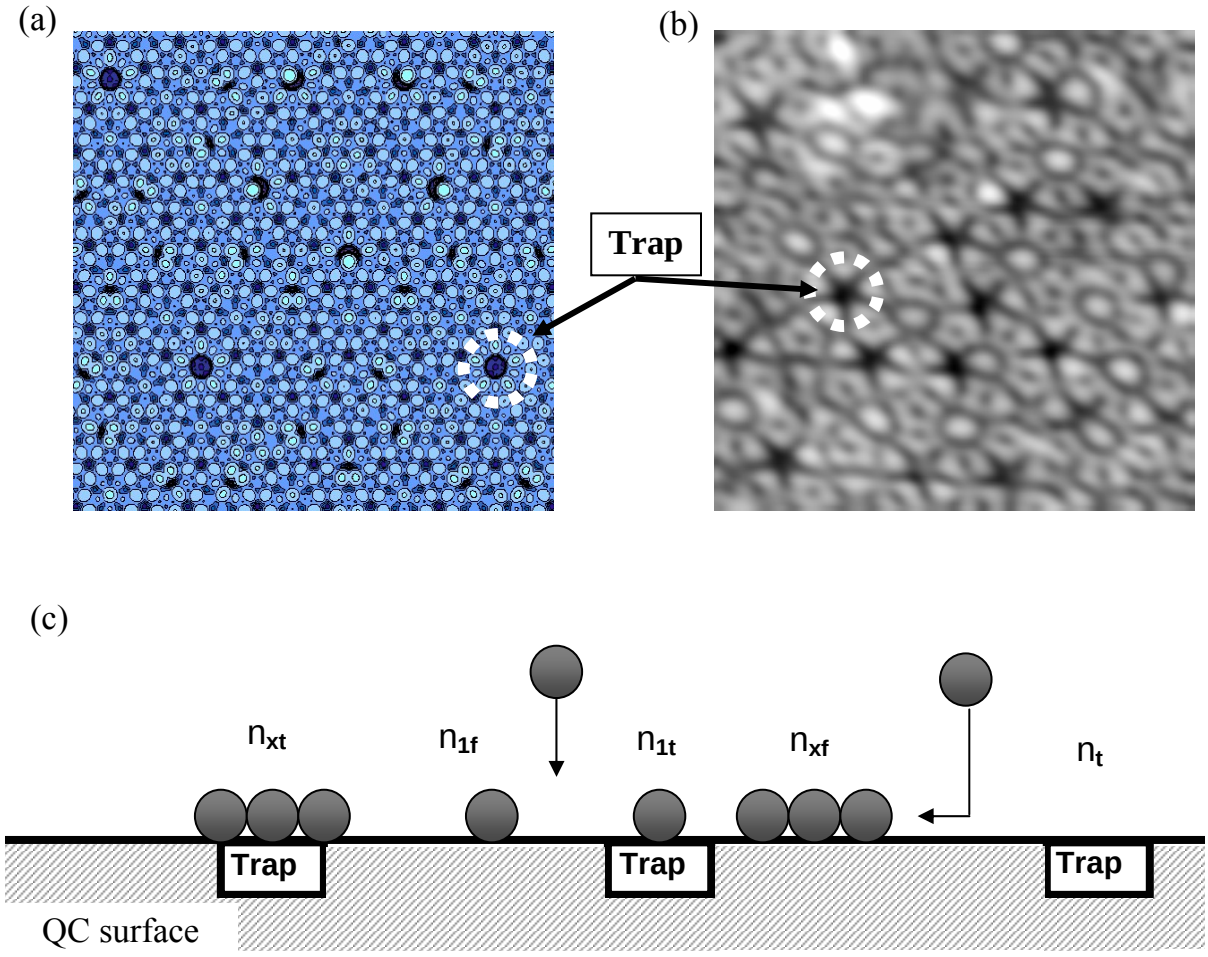

Figure 6

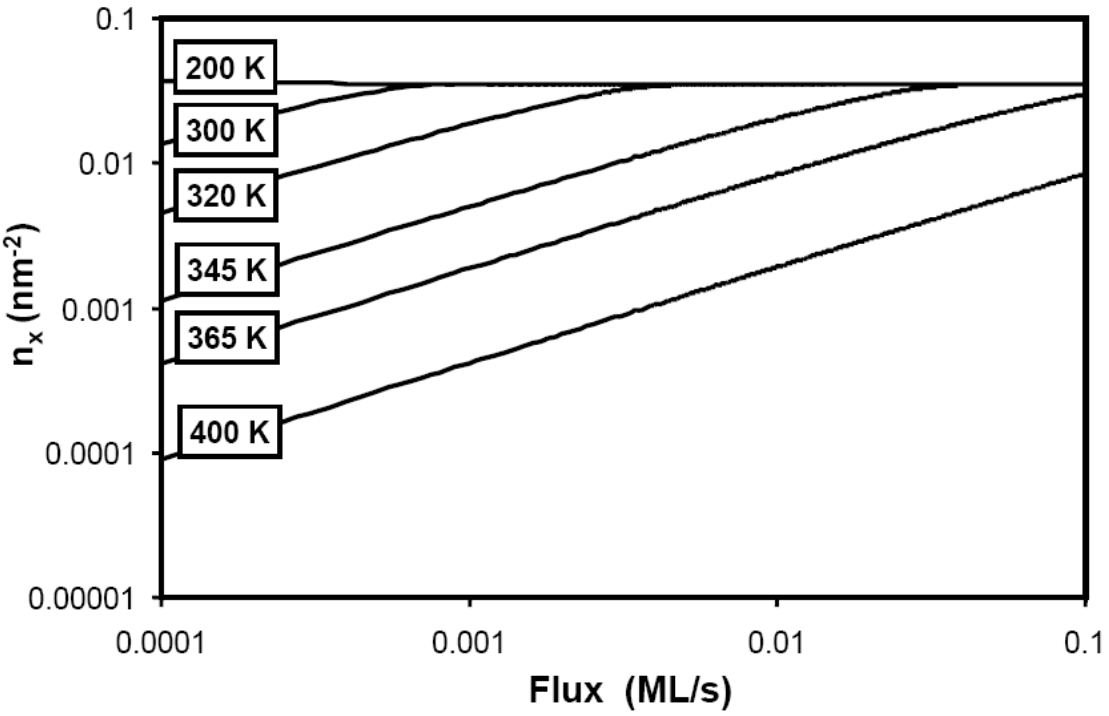
0.1
0.01
0.001
0.0001
0.00001
n_x (nm^{-2})
200 K
300 K
320 K
345 K
365 K
400 K
0.0001
0.001
0.01
0.1
Flux (ML/s)

Figure 7

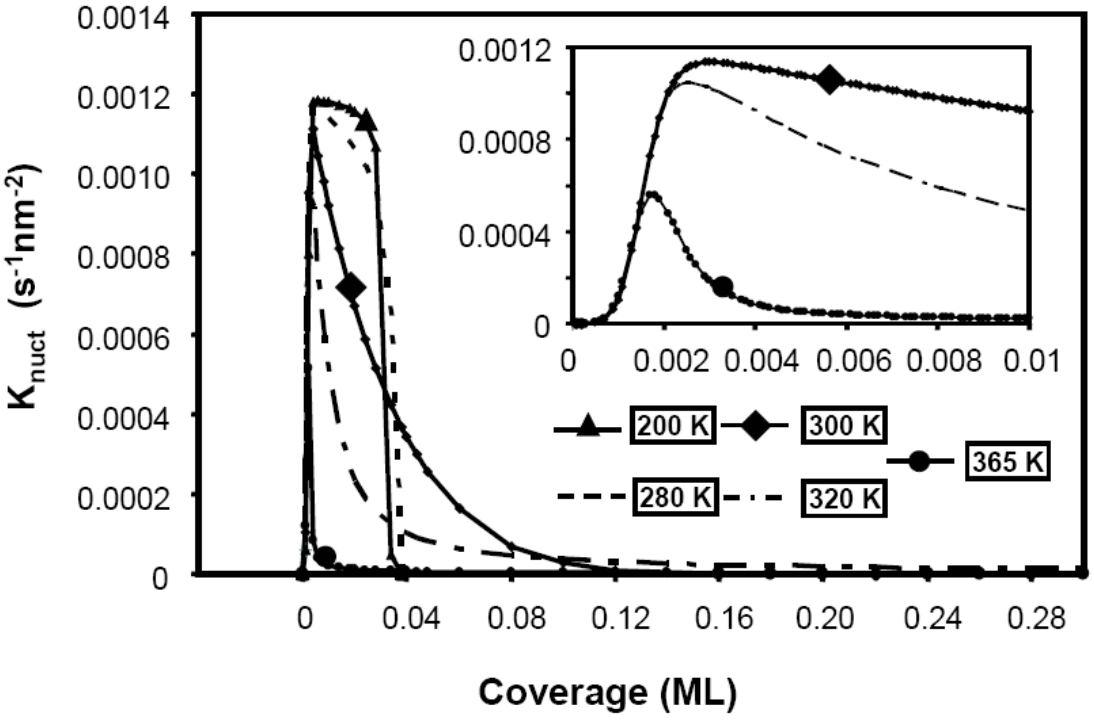
0.0014
0.0012
0.0010
0.0008
0.0006
0.0004
0.0002
0
K_{nuct} ($s^{-1}nm^{-2}$)
0
0.04
0.08
0.12
0.16
0.20
0.24
0.28
Coverage (ML)
0.0012
0.0008
0.0004
0
0
0.002
0.004
0.006
0.008
0.01
200 K
300 K
365 K
280 K
320 K

Figure 8

TERRACE-DEPENDENT NUCLEATION OF SMALL AG CLUSTERS ON A FIVE-FOLD ICOSAHEDRAL QUASICRYSTAL SURFACE

A paper published in *Philosophical Magazine*

B. Unal, J. W. Evans, T. A. Lograsso, A. R. Ross, C. J. Jenks And P. A. Thiel

Abstract

Nucleation of Ag islands on the five-fold surface of icosahedral Al–Pd–Mn is influenced strongly by trap sites. Submonolayers of Ag prepared by deposition at 365K and with a flux of 1 X 10^{-3} monolayers/s exhibit a variation in Ag island densities across different terraces. Comparisons with previous work and with rate equation analysis indicate that trap sites are not saturated under these experimental conditions and that the difference in island densities is not necessarily due to variation in trap densities. While it could have a number of different origins, our results point to a terrace-dependent value of the effective diffusion barrier for Ag adatoms.

Introduction

Studies of nucleation and growth of solid films on low-index surfaces of crystalline metals and semiconductors have yielded a wealth of information about surface kinetics and surface processes, often quite unexpected. Surfaces of quasicrystals are much more complex, both chemically and structurally, than the surfaces mentioned above. Therefore, one might expect a new range of phenomena to be discovered on quasicrystals and on other complex

surfaces. Studies of nucleation and growth on quasicrystals are still in their infancy. Previously, we have studied the characteristics, at low coverage, of Ag and Al islands on quasicrystalline Al–Pd–Mn and Al–Cu–Fe, respectively.[1–4] The data indicated that the islands nucleate at trap sites that are intrinsic to the surface structure, yet are so far separated that the system exhibits characteristics of heterogeneous nucleation. For Ag deposition, for instance, we have observed that island density is independent of both flux and temperature over large ranges of experimental parameters. These traits signify heterogeneous nucleation at trap sites. The trap sites were identified experimentally as the so-called 'dark stars' observed often in scanning tunneling microscopy of the clean surfaces.[5, 6] Kinetic Monte Carlo (KMC) simulation of an appropriate 'disordered bond network' lattice gas model supported the role of trap sites on the surface.[7] Rate equation analysis (REA) of the data indicated furthermore that the critical nucleus size is large ($i \geq 5$) and that Ag–Ag binding at trap sites is stronger than Ag–Ag binding at other types of terrace sites[8].

In this paper, we present new data for Ag islands deposited at 365K on the five-fold (5f) surface of icosahedral (i-) Al–Pd–Mn. The data show that island density is not uniform on all terraces. The previously-developed REA helps to interpret this observation.

Experimental Description

Our sample is a single grain of i-$Al_{70.2}Pd_{20.7}Mn_{9.1}$. The details of sample preparation and characterization are given elsewhere[9]. In brief, we sputter the sample with Ar^+ at 1 keV for 30 min and then anneal for 3 h in the range of 900–950 K. The sample is cooled to 700K at a controlled rate of 12.5 K/min. All of the Scanning Tunnelling Microscopy (STM) images are taken at room temperature under tunneling conditions of 0.47 nA and +0.97 V, using an

Omicron variable-temperature microscope. The base pressure of the ultrahigh vacuum chamber throughout the STM experiments is below 4 X 10^{-11} Torr. The Ag is deposited from an Omicron vapour deposition source at a flux of 1 X 10^{-3} monolayers/s, with the sample held at 365 K.

Experimental Results

Figures 1a and b show STM images taken in two experiments where Ag was deposited to a total coverage, θ, of about 0.1 monolayer (ML). Each frame gives a semi-three-dimensional view of the STM image. On each terrace, the small features – the bumps – are the Ag islands. One is encircled and labeled in figure 1a. There is also evidence that some Ag is captured at the edges of terraces, because it creates a step edge of different height than the clean terrace, although that is not obvious in the view shown in figure 1.

These data illustrate that the island density is not the same on all terraces. In particular, near the middle of each image one finds a terrace where the island density is much lower than on the adjoining terraces. The island density is roughly an order of magnitude lower on the island-deficient terraces than on the neighboring ones (although the low number of islands on the near-barren terraces leads to poor statistics). In our four observations of this phenomenon after deposition at 365 K, we found that a lower island density was always associated with a terrace bordered by a particular set of step heights. (On the 5f surfaces of i-Al–Pd–Mn and i-Al–Cu–Fe, two common step heights are 0.66 and 0.41 nm. In figure 1, these steps are labeled L and M, respectively). Terraces with few or no islands were bordered by a 0.66-nm (L) step in the uphill direction, and by a combined (0.41þ0.66 nm) (ML) step in the downhill direction. In the latter case, the 0.41-nm step – not the 0.66-nm step – was

always adjacent to the terrace in question, while the 0.66-nm step was below the 0.41-nm step. We could determine this sequence in two ways. First, in some cases (e.g. figure 1b), the ML steps diverge in some regions and combine in others. In other words, a pair of steps that is combined in one region breaks apart to make two single steps of different heights in another region. In the case of figure 1b, the region where the steps diverge is not shown. In other cases, we can distinguish the sequence because there is a small inflection between the steps. This is actually visible upon close inspection of the ML step of figure 1a.

In any given experiment, island density is constant on the other terraces – those that are bordered by step heights different than the values mentioned above – to within ±30% or better. It is not clear whether this variation represents statistical uncertainty alone, or if it also reflects a true variation among terraces. In either case, the island density on the island-deficient terraces in figure 1 is significantly different than the densities on the neighbouring terraces.

Rate equation analysis (REA)

The REA has been described in detail elsewhere.[8] Briefly, it assumes that deposited atoms diffuse at a rate governed by an average activation barrier for diffusion, E_d. The adsorption energy is stronger at trap sites than at other terrace sites by an amount E_t. Atoms can form islands, either at trap sites or at trap-free sites (i.e. 'free' sites) on terraces, with binding energy E_b per neighbouring pair. Different values of E_b are allowed at free sites and trap sites, with the ratio defined as R. Clusters at or below the critical size, i, are unstable; they are in quasi-equilibrium with single atoms on the terrace.

These parameters were adjusted until the temperature-dependence of the island density, $n_x(T)$, matched the experimental data (the experimental island density was obtained by averaging over many terraces). We found an optimal fit when i=5, R=0.10, and E_d=0.66 eV. An equally-good fit to the data could be obtained by allowing different values of i at free sites and at trap sites (i_f=11 and i_t=5, respectively), together with a more physically reasonable value of R=0.20. The same parameters that reproduced the temperature-dependence of the island density (at fixed flux and θ) also reproduced the flux-scaling of the island density (at fixed T and θ).

The form of $n_x(T)$ predicted by the model with optimal parameters, under the conditions of the present experiments, i.e. with F=1 X 10^{-3} ML/s and θ=0.1, is illustrated by curve A of figure 2. The curve is flat up to 300 K, where stable islands cover all trap sites, followed by a decline where stable islands cannot completely saturate the traps, at this flux and coverage. In the model, the value of n_x=0.035/nm^2 at the plateau in curve A is taken from experimental data and is set equal to the trap density, n_t.[8]

The REA produced a model for nucleation and growth of Ag islands that successfully described experimental data averaged over many terraces. However, on quasicrystalline surfaces, individual terraces are structurally and compositionally different[10]. To understand nucleation and growth on individual terraces, we assess the impact of changing the best-fit parameters at the coverage, flux and temperature of the experiments (figure 1). Relative to curve A, the effect of changing trap density (alone) is shown by curve B in figure 2. Here, the trap density is higher by a factor of 3, so the height of the plateau is three times higher. The curves do not overlap in the nonlinear region at high temperature (see figure 2 inset),

indicating that trap density would affect island density at 365 K. Relative to curve A, the effect of increasing the diffusion barrier slightly (by a factor of 1.06) is shown by curve C. This change displaces the curve to higher T, which would also affect island density at 365 K.

The sensitivity of n_x to these and other parameters at 365K is shown in figure 3. Here, the ordinate is the ratio of n_x to the value predicted by the model with all of the best-fit parameters, $n_{x0}=1.7 \times 10^{-3} nm^{-2}$. The abscissa is the variable parameter (S) normalized to its optimal value (S_0), over a range of ±10%. To generate each curve, all parameters were held at the 'best-fit' values listed in the inset to figure 3, except for the parameter that serves to label the curve in the figure. Clearly, the island density at this temperature, flux and coverage is most dependent upon E_d. There is also some variation with Ebt, but essentially no dependence on R, n_t or E_t over this range.

Discussion

We consider three possible explanations for the different island densities shown in figure 1.

The first is terrace widths. In principle, terrace widths can affect island densities due to competition between island nucleation and capture of deposited atoms at step edges (step flow). For sufficiently narrow terraces or high temperatures, capture at step edges can lead to lower island density. The temperature of 365K used in these experiments is sufficiently high to allow observable capture at step edges, along with island formation.[8] However, in each of the STM images of figure 1, the island deficient terrace is comparable in

width to at least one other terrace where the island density is visibly larger. Thus, terrace widths cannot account for the observed island depletion.

The second is the Ehrlich–Schwoebel (ES) barrier, which is an additional energy barrier (additional to the terrace diffusion barrier) encountered by a particle as it diffuses down a step. If steps of different heights were to have different ES barriers, then deposited atoms could more easily diffuse downward over some steps than others, leading to a depletion in islands near the low-barrier steps. This explanation is attractive, given that our depleted terraces are bound by steps with specific heights. However, it cannot account for the near-total absence of islands on certain terraces. The terraces with low ES barriers would be distinguished by a denuded zone near the downward step, but not by complete depletion, since the separation between islands on other terraces is far less than the terrace width.

The third possible explanation is that variations in atomic-scale structure of the terraces affect nucleation. Terraces of icosahedral quasicrystals are not expected to be structurally identical [10]. However, terraces are similar in the sense that they contain similar local configurations, albeit at different densities. Since a trap (a dark star) is a local feature, a first reaction to the data of figure 1 might be to say that a terrace with few islands must have few traps. However, the REA shows that this interpretation is too simplistic. At 365 K, the traps are far from saturation and changing the trap density has a rather small impact. The two parameters that significantly affect island density are E_d and E_{bt}. Of these, E_{bt} describes a local phenomenon that would be expected to be invariant between terraces. Specifically, the binding energy between Ag atoms at a trap island, E_{bt}, should depend mainly upon the configuration of surface atoms at the trap site. The diffusion barrier, E_d, on the other hand, is an effective diffusion barrier on the free terrace. The heterogeneity of the

quasicrystal surface results in a distribution of real, local barriers that separate adjacent minima. The value of E_d reflects not only the distribution of real barrier heights but also the sampled diffusion paths. Hence, it is reasonable to expect that Ed is sensitive to the long-range atomic arrangement. At the same time, the REA indicates that a very small change in this parameter affects island density strongly, under conditions where traps are not saturated. Hence, the diffusion barrier is an appealing candidate to explain the variation in island density among terraces, although, of course, other factors – including trap density – may contribute as well. If this interpretation is correct, then the Ag on the depleted terraces is preferentially captured at step edges and one should see more Ag decorating those step edges than others. From our STM images, however, it was not practical to compare the amount of Ag at the step edges.

Sharma et al.[11] have studied the growth of Sn on the 5f surface of i-Al–Cu–Fe. They observed Stranski–Krastanov growth, i.e. smooth growth followed by three-dimensional clusters. At high coverage (about 15 monolayers), they reported that the density and size of the Sn clusters varied from terrace to terrace. Despite the differences between their work and ours, both studies point to differences in film growth on different terraces. Sharma et al.[11] speculated that the inhomogeneity could be due to different densities of nucleation centres, diffusion barriers, and step edge barriers.

From a broad perspective, our work shows that there are two main regimes where differences in terraces can affect island densities at submonolayer coverage. Above room temperature (as in the present experiments), traps are not saturated and a variety of factors can contribute to non-uniform island densities. At lower temperatures (and at appropriate values of flux and coverage[8]), all traps are saturated and the island density simply equals the

trap density. This corresponds to the plateau region in the curves of figure 2. In this regime, terrace-dependent island densities could unambiguously be attributed to terrace-dependent trap densities. Future investigations in the latter regime may further clarify the terrace-dependence of trap densities, versus other factors, in nucleation at these intriguing surfaces.

Conclusions

At submonolayer coverage, we observe a variation in Ag island densities on terraces of i-Al–Pd–Mn at 365 K. Comparisons with previous work, and with rate equation analysis, indicate that trap sites are not saturated under these experimental conditions. Therefore, the different island densities could have a number of origins. Terrace-dependence in the effective diffusion barrier for Ag adatoms is a strong candidate.

Acknowledgments

BU, CJJ, ARR, TAL and PAT were supported in this work by the Office of Science, Basic Energy Sciences, Materials Science Division of the US Department of Energy (USDOE). JWE was supported by NSF Grant CHE-0414378. The work was performed at Ames Laboratory, which is operated for the USDOE by Iowa State University under Contract No. W-7405-Eng-82. BU is thankful to Da-Jiang Liu for his help in writing Mathematica codes for the REA.

References

1. T. Cai, J. Ledieu, R. McGrath, et al., Surf. Sci. 526 115 (2003).

2. V. Fournee, T.C. Cai, A.R. Ross, et al., Phys. Rev. B 67 033406 (2003).

3. V. Fournee, A.R. Ross, T.A. Lograsso, et al., Surf. Sci. 537 5 (2003).

4. V. Fournee and P.A. Thiel, J. Phys. D: Appl. Phys. 38 R83 (2005).

5. A. Barbier, D. Le Floc'h, Y. Calvayrac, et al., Phys. Rev. Lett. 88 085506 (2002).

6. Z. Papadopolos, G. Kasner, J. Ledieu, et al., Phys. Rev. B 66 184207 (2002).

7. C. Ghosh, D.-J. Liu, C.J. Jenks, et al., Phil. Mag. 86 831 (2006).

8. B. Unal, V. Fournee, K.J. Schnitzenbaumer, et al., Phys. Rev. B 75 064205 (2006)

9. B. Unal, T.A. Lograsso, A.R. Ross, et al., Phys. Rev. B 71 165411/1 (2005).

10. A. Yamamoto, Phys. Rev. Lett. 93 195505 (2004).

11. H.R. Sharma, M. Shimoda, A.R. Ross, et al., Phil. Mag. 86 807 (2006).

Figure Captions

Figure 1. STM images of Ag islands on terraces following deposition at 365 K. Steps are labeled with their height, where L=0.66nm and M=0.41 nm. (a) 326 X 326nm^2, 0.13 ML.(b) 500 X 500nm^2, 0.10 ML.

Figure 2. $n_x(T)$ for (A) the best-fit parameters, (B) the same as (A) except n_t=0.10 and (C) the same as (A) except E_d=0.70 eV. All curves are generated for F=1X10^{-3} ML/s and θ=0.10 to correspond to experimental conditions. The inset is a magnified view of the same three curves at temperatures where traps are not saturated.

Figure 3. Sensitivity of normalized island density to change in a single model parameter, S, at T=365 K, F=1 X 10^{-3}M/s, θ=0.10, corresponding to the experimental conditions of figure 1. The single parameter is varied, while all other parameters are held at the best-fit values indicated in the inset. Each curve in the figure is labeled with the parameter that was changed. Using all of the best-fit parameters, the model predicts a value of the island density, n_{x0}, of 1.7 X $10^{-3}$$nm^{-2}$ at 365 K.

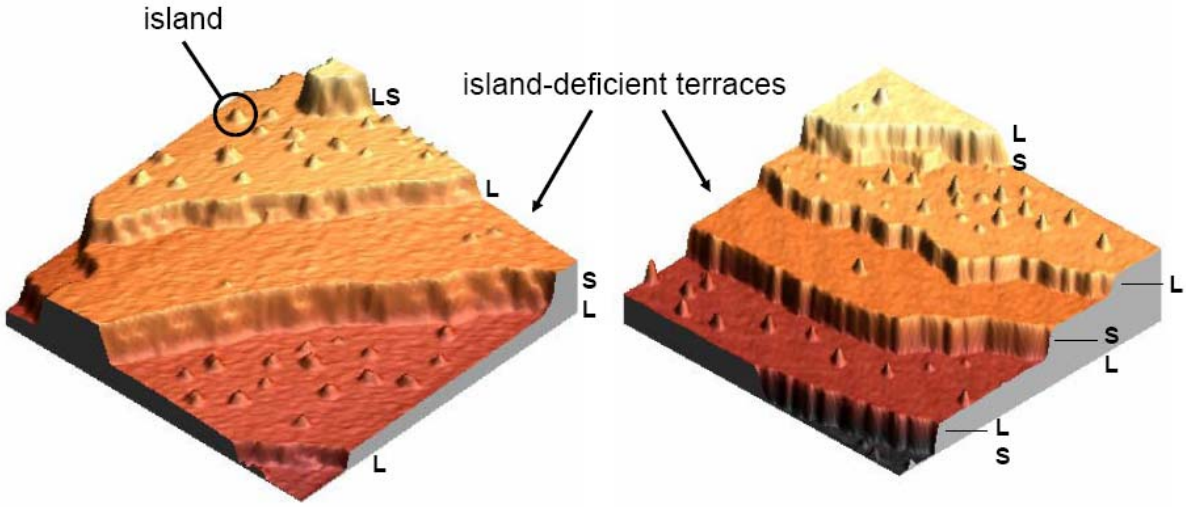

Figure 1

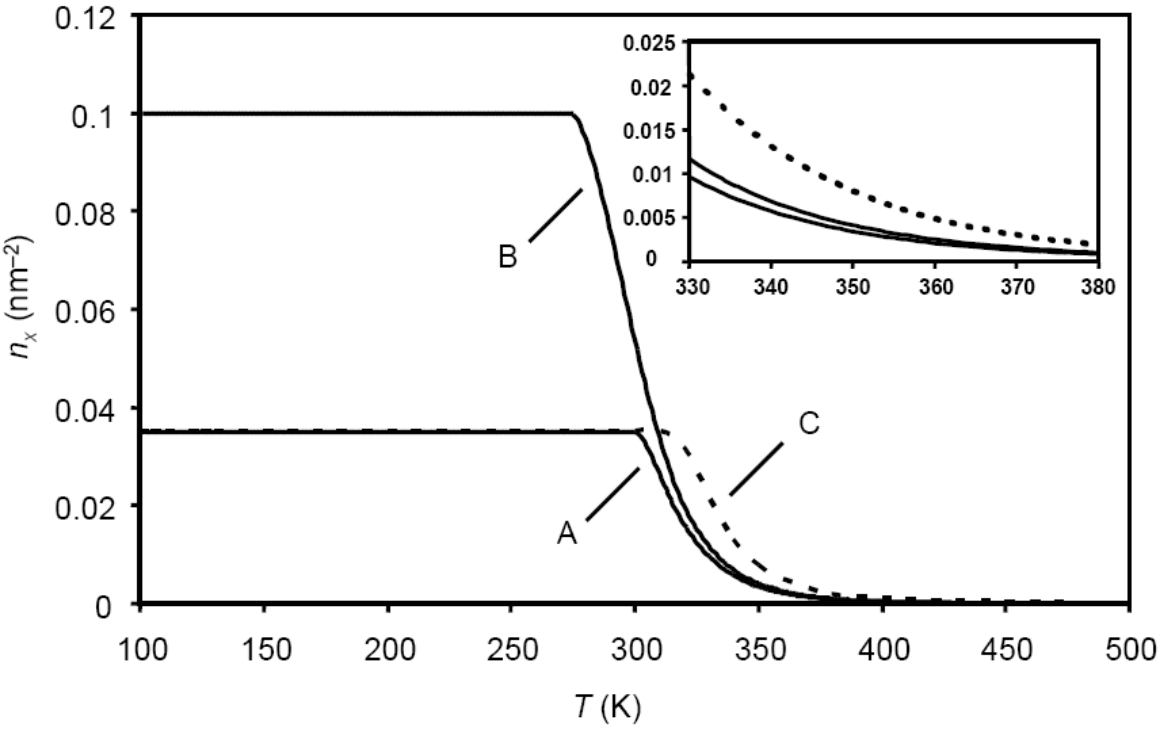
0.12
0.1
0.08
0.06
0.04
0.02
0
n_x (nm^{-2})
100
150
200
250
300
350
400
450
500
T (K)
B
C
A
0.025
0.02
0.015
0.01
0.005
0
330
340
350
360
370
380

Figure 2

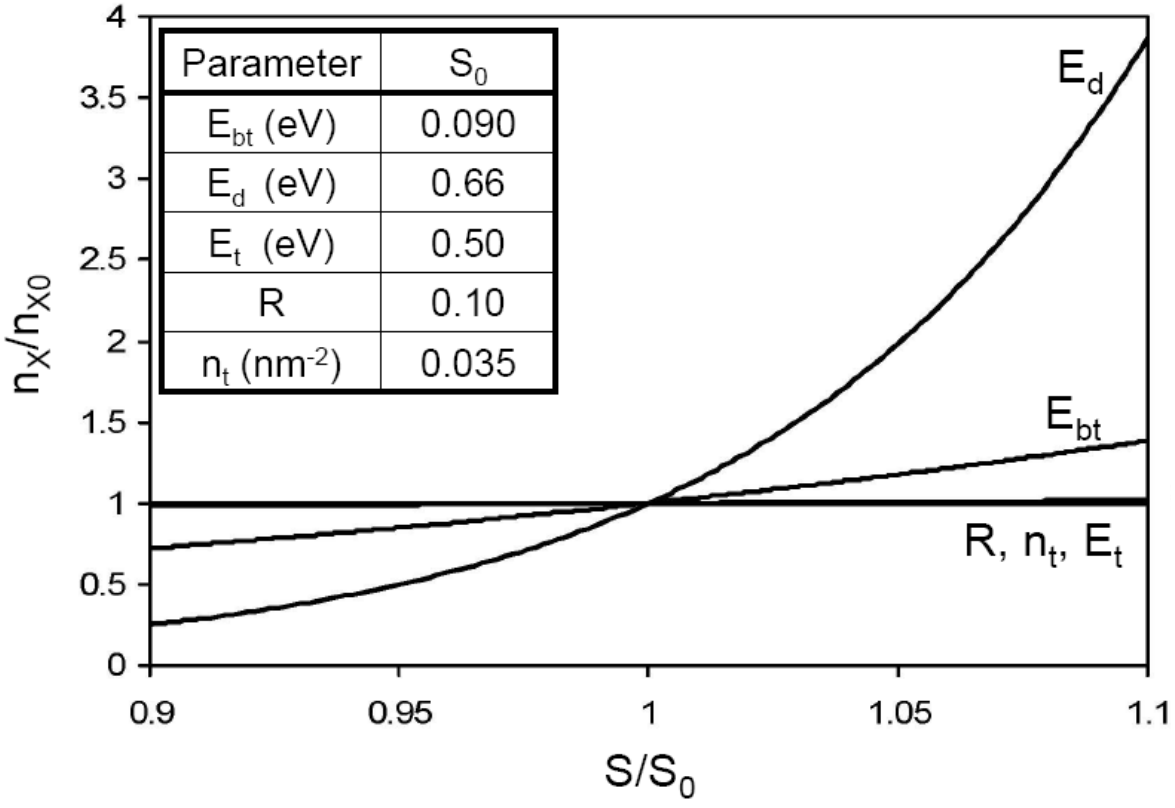
Parameter | S0
Ebt (eV) | 0.090
Ed (eV) | 0.66
Et (eV) | 0.50
R | 0.10
nt (nm-2) | 0.035
Ed
Ebt
R, nt, Et
nX/nX0
S/S0
0
0.5
1
1.5
2
2.5
3
3.5
4
0.9
0.95
1
1.05
1.1

Figure 3

GROWTH OF HEIGHT-SELECTED AG ISLANDS ON FIVE-FOLD I-ALPDMN QUASICRYSTALLINE SURFACES: STM ANALYSIS AND STEP DYNAMICS MODELING

A paper will be submitted to *Physical Review Letters*

Baris Unal, V. Fournee, P.A. Thiel, and J.W. Evans

ABSTRACT

We have investigated the growth of Ag films on fivefold surfaces of icosahedral Al-Pd-Mn quasicrystal using a variable temperature scanning tunneling microscope. We observe that at 365 K Ag nucleates heterogeneously and forms 2D quasiperiodic islands. Then as total coverage increases, those 2D islands quickly convert into 3D islands with a subsequent growth to a selected height of 3 layers followed by lateral spreading. We propose that increased strain for islands with larger radii, as well as enhanced lateral binding in higher layers, triggers the transition from 2D to 3D growth. A quantum size effect, reflected in stronger absorption by a few 10's of meV for atoms on top of the second layer, then suffices to produce the development of mesa-like, 3-layer-high islands and the associated inhibition of 4^{th} layer nucleation. This growth sequence for individual islands is modeled within a step dynamics formulation incorporating the above-mentioned features.

1. INTRODUCTION

Recent studies of the growth of thin metal films on certain substrates have revealed the presence of unexpected "quantum size effects" (QSE) [1]. The basic physical feature underlying QSE is that electrons are confined vertically in the metal film. This in turn leads to a significant dependence of the surface energy (and of the adsorption energy of individual metal atoms) on film thickness. As a result, novel film morphologies can develop exhibiting islands or mesas with selected heights corresponding to lower surface energies. The most commonly studied systems exhibiting QSE are Pb or Ag films on semiconductor and metal surfaces [1-4]. Examples of substrates for these Ag films include GaAs(110) [2], Si(111) [3], Fe(100) [5], NiAl(110) [6], and 5-fold symmetric surfaces of icosohedral (i-) AlPdMn quasicrystal [7]. In the latter system, considered exclusively in this study, thin films of roughly 0.3-1.5 monolayers (ML) of Ag deposited at 365 K were shown to exhibit a predominance of mesa-like 3-layer high islands. The origin of QSE in this system is believed to be a deep minimum in the electronic density of states at the Fermi level, called a pseudogap, which is a common feature for Al-rich quasicrystals due to both structural and sp-d hybridization effects [7].

The goal of this study is two-fold. First, in Sec.2, we shall provide a comprehensive characterization from scanning tunneling microscopy (STM) studies of the morphology of Ag films deposited on 5-fold i-AlPdMn at 365 K. We focus on the initial stages of growth as manifested by the development of separated 3D islands with selected heights of 3 layers. In addition to presenting images of the film morphology, we shall characterize the height and shape of islands as a function of their size, and also quantify the film height distribution and roughness as a function of coverage. We do also briefly compare the development of film

roughness with coverage at 365 K with behavior observed at lower temperatures. Second, in Sec.3, we shall develop and apply a theoretical framework which can elucidate the evolution of 3D island shapes prior to coalescence in this complex film growth system. We develop a *step dynamics model* [8-10] focusing on the growth of each individual island by incorporation of atoms deposited within its "capture zone" on the substrate. One retains a discrete description of the vertical layers within the island, but describes the step edge bounding each 2D layer by a continuous circular curve. Thus, the model must appropriately specify the rate of growth of the radius for each level, as well as providing a criterion for nucleation or creation of new top layer islands [8-10]. Within this formulation, we incorporate what we believe is the essential physics for this system: (i) strain reduced bonding at the edges of larger islands, and enhanced bonding at island edges in higher layers (due to relaxation towards a bulk Ag fcc structure), which together promote 3D island growth; (ii) stronger adsorption of Ag atoms on top of the second layer due to QSE which promotes the formation of mesa-like 3-high islands, and inhibits nucleation of the 4^{th} layer. We make a physically reasonable selection of energetic parameters and present the associated model predictions. Finally, we provide our conclusions in Sec.4.

2. EXPERIMENTAL PROCEDURES AND OBSERVATIONS

A surface of a single-grain icosahedral $Al_{72}Pd_{19.5}Mn_{8.5}$ was cut perpendicularly to a fivefold axis within ±0.25° and mechanically polished with diamond paste down to 0.25 μm. Clean surface was prepared in an ultra-high vacuum system with base pressure of $4x10^{-11}$ mbar by repeated cycles of ion sputtering (Ar^+, 0.5-2.5 keV, 30 min.) and annealing (up to 940 K). Such a preparation produces a surface with a bulk-terminated terrace-step

morphology [1]. The structural quality of the 5-fold surface was checked down to atomic scale with STM, comparing against bulk structural models [11, 12]. Ag was evaporated from an Omicron electron-beam-heated evaporator with internal flux monitor modified to resemble a Knudsen cell. The deposition flux was around 10^{-3} ML/sec keeping the pressure below 2 x 10^{-10} mbar during deposition. The flux calibration of the Ag source is obtained via directly measuring the coverage from the STM images. The imaging was acquired at the deposition temperatures for the growing Ag films with an Omicron VT-STM. The STM data were processed using an image processing freeware [13].

2A. ISLAND MORPHOLOGIES

Our previous investigations of the initial stages of deposition for coverages θ up to θ~0.1 ML in this system indicated that 2D Ag islands form by heterogeneous nucleation at trap sites corresponding to so-called dark-star (dS) sites on the substrate [14]. These dS sites are saturated by islands for deposition at 300 K and below [14, 15], but only partially populated at higher temperatures [14]. This behavior was described within a rate equation formulation [14] where nucleation was enhanced at traps sites due to stronger absorption relative to terrace sites. Data was fit choosing a critical size of i=5 (corresponding to the smallest stable cluster being a pentagonal starfish shaped island with five arm atoms surrounding a central atom) for temperatures from 365 K down to some value below 300 K [16]. More recent detailed and comprehensive analyses of the models for quasicrystal structure have indicated that *not* all dS sites are *identical*, so plausibly those populated by Ag islands at 365 K constitute somewhat stronger adsorption sites for Ag than the others [12].

Figure 1 shows a series of semi-three dimensional STM images that demonstrate the development of the film morphologies for coverages, θ = (a) 0.26 ML, (b) 0.7 ML, (c) and 1 ML Ag films deposited at 365 K on a fivefold surface of i-Al-Pd-Mn. Fig.1 (d) shows line profiles from *typical* individual Ag islands in (a)-(c), which fall into distinc regions of island height. As total coverage increases, 1-layer-high Ag islands become 2-layer-high and then they transform into 3-layer-high, flat-top islands. Once the 3-layer-high mesas form, the islands grow laterally while keeping their height constant although ultimately 4 and higher layer islands develop.

Figure 2 shows the corresponding film height distributions, i.e., the area of islands or mesas as a function of their height and also corresponding areal occupancies of the each layer. To determine the height of the individual Ag island, the STM images were divided into smaller sections so that each section contained only one Ag island, and then, an areal height histogram was obtained based on the local region of the island, from which the height of the each island was measured. In addition, at the same time, the area of the each island was determined via applying an appropriate height threshold to the STM image. Here, for each total coverage value, about 120 islands were analyzed from the STM images spanning a total area equal to $1x10^6$ nm^2. The islands that formed at the step edges were excluded in our analysis.

As it can be seen from Fig. 2 (a) and (b), islands with a specific number of layers actually have a distribution of heights. The average height of 1-, 2-, 3- and 4-layer-high islands is 0.26 nm, 0.53 nm, 0.82 nm and 1.06 nm. The spread of heights for islands with a specific number of layers is 0.08 nm. None of these values corresponds to any interplanar spacing of bulk fcc Ag. The variation of the height may be mainly due to the small structural

differences of the each island not due to the bias conditions. Since, we also did bias dependent experiments from -0.95 V to +0.95 V where we did not observe any significant bias dependent height change for the Ag islands in this system.

The data in Fig. 2 (c) reveals that even at a lower Ag coverage of 0.26 ML majority (ca. 60%) of the 2D islands which form initially (as described above for $\theta \sim 0.1$ ML films) have already transformed into 3D multilayer islands. As shown in Fig. 2 (d), by 0.7 ML, the strong propensity for the selection of 3-layer-high islands is evident. More specially, 1- and 2-layer-high islands were converted to 3-layer-high islands as coverage increased and hence about 90% of the total islands are 3-layer-high. This propensity persists for 1-1.5 ML Ag films which differ from those at 0.7 ML mainly by the lateral expansion of 3-layer-high islands. Nucleation of 4-layer-high islands is rare at 0.7 ML, but more prevalent for higher coverages.

More detailed examination of the STM data at the lower coverage of 0.26 ML reveals that the propensity for selection of 3-layer-high islands is even stronger than suggested by the corresponding height histogram in Fig. 2 (c). Note that at 0.26 ML, there is a significant spread in island sizes (measured by the number of atoms or the volume). If one size selects the larger islands, then the majority of these islands already have a height of 3 layers. In other words, it takes a certain minimum number of atoms before an island can achieve the selected height, but then this height is strongly favored in subsequent growth. As indicated above, once islands reach a height of 3 layers, they tend to spread laterally adopting a mesa-like structure bounded by relatively steep side walls. Thus, for this system it appears that the height (and more generally the shape) of islands is primarily determined by their size, at least for heights up to 3 layers. Thus, the height of an island of a certain size is largely independent

of features of the local environment of that island such as the area of its capture zone [17]. However, at 0.26 ML, there are some 1-layer-high islands whose sizes are larger than that of the 2-layer-high islands and there are also some 2-layer-high islands whose sizes are larger than that of the 3-layer-high islands. All of these observations suggest that nucleation process of a new layer has also a stochastic side.

Examination of the images at 0.7 ML or 1 ML also indicates that the rare 4-layer-high islands tend to correspond to those islands which have the largest size. This should be expected since inhibited nucleation of the 4^{th} layer (described below) will be facilitated the larger the size of the 3^{rd} supporting layer. However, 4^{th} layer nucleation is a highly stochastic process, so sometimes this occurs by chance on smaller three-layer-high islands.

Figure 3 shows the structure of one-layer-high Ag island. It is so clear the Ag adapts the fivefold symmetry of the quasicrystalline structure of the substrate. Since the structure is not fcc type for the first-layer, one expects that the Ag film is highly strained. Our previous studies at 300K for this system showed that as the height of the island increased the structure of the Ag islands transformed into fcc type[15, 18].

2B. KINETIC ROUGHENING

For film coverages approaching 2 ML, there is a significant coalescence of the height-selected 3-layer-high (and other) islands which reduces the rate of film roughening. On these larger coalesced platforms, nucleation of higher layers is facilitated, as indicated above for 4^{th} layer nucleation. The resulting morphologies of thicker films appear to be fairly smooth without any strong preference for any specific height above 3. Fig.4 shows the evolution of the film roughness, W (the root-mean-square variation of the film height distribution), with

coverage for deposition at 365 K, as well as for lower T. To elucidate behavior at 365 K, it is instructive to consider an idealized model for exclusive formation of perfect 3-layer-high islands which then grow laterally until forming a complete flat 3-layer-high film (before nucleation of higher layers). In this model, one has

$$W = d\ 3(\theta/3)^{1/2}(1-\theta/3)^{1/2} \text{ for } \theta \leq 3 \text{ ML}, \qquad (1)$$

This behavior is shown as a dashed curve in Fig.4 where d denotes the average interlayer spacing with a value of 0.26 nm for this system. For growth at 365 K up to 2 ML, the overall behavior of W is close to this form: below $\theta \sim 1$ML, W is somewhat lower since some islands are less than 3 layers high; above $\theta \sim 1$ ML, W is somewhat higher due to nucleation of higher layers before completion of the 3rd layer.

For growth at 300 K, upwards transport is operative leading to rapid formation of 3D islands. However, upward transport is not efficient enough for these islands to readily achieve selected height, and consequently one finds instead a range of smaller island heights. Correspondingly W initially increases quickly, but then decreases around $\theta \sim 1$ML as these islands undergo significant coalescence (this coalescence-induced smoothing regime occurring at a lower coverage than for taller islands). For even low T of 127 K or 200K, upward transport is evidently severely inhibited. Consequently, film growth is significantly smoother than at 300 K or higher. Generally, the observed behavior at low T lies between that for conventional layer-by-layer growth where $W = d\ \theta^{1/2}\ (1-\theta)^{1/2}$ for $\theta \leq 1$, and that for rough Poisson growth where $W = d\ \theta^{1/2}$ (both shown as dot-dashed curves in Fig.4) [19].

3. STEP DYNAMICS MODELING OF THE GROWTH OF INDIVIDUAL 3D ISLANDS

As indicated in Sec.1, our step dynamics formulation represents the atomic layers within a single multilayer 3D island by concentric circles with radii r_i for layers i=1, 2, 3…. The island is located at the center of a circular capture zone of radius R, and incorporates all atoms which are deposited within that capture zone. Below, r denotes the distance from the center of the island. Complete model specification involves prescribing the evolution of the radii, r_i, as well as the conditions for creation of new top layers. See Fig. 5 (a). In the following, we use dimensionless units for lateral areas and distances where the mean area per adsorption site is set to unity. Thus, the unit of distance reflects the average separation between adjacent adsorption sites of a few angstroms. Based on the data in Fig.1, the typical capture zone radii, R, (roughly half mean island separation) are in the range of R ~ 50-100. Also, the transition from 2D to 3D growth occurs when the radii r_1 of the 1^{st} layer islands reaches roughly $r_1 \sim 10$.

Step dynamics models have been applied previously to describe both steepening and slope selection of 3D islands or “mounds” formed during homoepitaxial growth in the presence of a step edge barrier inhibiting downward transport [20, 21]. Growth was considered mainly in the lower temperature regime of irreversible capture of diffusing atoms at steps. Step dynamics modeling has also been used to describe post-deposition relaxation necessarily in the regime of reversible attachment at step edges [22]. The current treatment incorporates aspects of both types of studies. However, the Ag/5-f-i-Al-Pd-Mn system is extremely complex, with many unknown energetic parameters controlling film growth. Thus,

our modeling should be viewed only as semi-quantitative, indicating physically plausible selections for these parameters.

3A. BASIC STEP DYNAMICS FORMULATION

The rate of change of the radii, r_i, for various layers within the 3D island are determined by the net attachment fluxes of diffusing adatoms to these step edges [8-10, 20-22]. These are obtained by solving the appropriate deposition-diffusion equations for the adatom density, n, on each terrace. See Fig.5 (b). Below, n_{eq}^{i+} (n_{eq}^{i-}) denotes the adatom density directly above (below) step i as determined by attachment-detachment equilibrium. We assume that there is no barrier for attachment to ascending steps, but an Ehrlich-Schwoebel step-edge barrier, δ, inhibiting attachment to descending steps. The latter can be characterized by an attachment length $L_{ES} = \exp(\beta\delta) - 1$ for inverse temperature $\beta=1/(k_BT)$. Finally, let F denotes the deposition flux in ML per unit time, and D denote the terrace diffusion coefficient. Then, on the annular terrace bounded by descending step i and ascending step i+1, one solves the boundary value problem:

$$d/dt\ n = F + D\nabla^2 n \approx 0 \text{ for } r_{i+1} < r < r_i, \text{ with}$$

$$n = n_{eq}^{(i+1)-} \text{ at } r=r_{i+1}, \text{ and } \partial/\partial r\ n = -(n - n_{eq}^{i+})/L_{ES} \text{ at } r=r_i. \qquad (2)$$

We will decompose the solution to (2) as a sum of "deposition" and "equilibration" parts, $n = n_{dep} + n_{eq}$. Here, n_{dep} is the solution of (2) after setting $n_{eq}^{i+} = n_{eq}^{(i+1)-} = 0$ corresponding to irreversible attachment at steps. Also, n_{eq} is the solution to (2) after setting

F to zero, but retaining the non-zero equilibrium densities at step edges. The total attachment fluxes, J, integrating along steps are correspondingly decomposed into "deposition" and "equilibration" components. One can identify a single equilibribration flux $J_{eq}^{i\to i+1}$ across the terrace, defined as the *net flux* of atoms detaching from step i and attaching to step i+1, which has the form

$$J_{eq}^{i\to i+1}/F = 2\pi\,(D/F)\,[(L_{ES}/r_i) + \ln(r_i/r_{i+1})]^{-1}\,[n_{eq}^{(i+1)-} - n_{eq}^{i+}]. \quad (3)$$

For the deposition flux, one must separately specify the fluxes of atoms, $J_{dep}^{i+} > 0$ and $J_{dep}^{(i+1)-} > 0$, deposited on the terrace $r_{i+1} < r < r_i$ attaching to step i from above, and to step i+1 from below, respectively. From mass conservation, it immediately follows that

$$[J_{dep}^{i+} + J_{dep}^{(i+1)-}]/F = \pi(r_i^2 - r_{i+1}^2). \quad (4)$$

Of course, the relative magnitude of these two fluxes depends on the magnitude of the step edge barrier, with $J_{dep}^{i+} \to 0$, as $\delta\to\infty$. See the Appendix for details.

The basic evolution equation for step i located between steps i-1 and i+1 has the form

$$d/dt\,(\pi\, r_i^2) = J_{eq}^{i-1\to i} - J_{eq}^{i\to i+1} + J_{dep}^{i-} + J_{dep}^{i+}. \quad (5)$$

Separate treatments for the bottom and top steps are required. These simply account for the feature that all atoms deposited on the substrate (within the island's capture zone) attach to the lower step, and all atoms depositing on top of the highest layer island attach to the top

step. One must also specify the condition for creation of new top layer islands. In this system, adatom densities are quite high, so one expects island nucleation occurs quickly once conditions are right for survival of new islands with radii r≈1. Thus, we create new islands as soon as there would be a net flux of attachment to such islands. This generally requires that the radius of the supporting layer be sufficiently large that adatom detachment from its edge is enhanced by strain effects.

3B. INCORPORATION OF QSE, STRAIN, AND LAYER-DEPENDENT STEP BINDING

Much of the essential physics underlying development of height-selected islands is incorporated into the specification of the equilibrium adatom densities at step edges. The equilibrium adatom densities, $n_{eq}^{i\pm}$, at step edges are determined from the corresponding adatom chemical potentials, $\mu_{ad}^{i\pm} = -E_{ads}^{i\pm} + kT \ln(n_{eq}^{i\pm})$ [23], where $E_{ads}^{i\pm} > 0$ denote the adsorption energy of the adatom on the underlying layer (i.e., layer i for n_{eq}^{i+}, and layer i-1 for n_{eq}^{i-}), These chemical potentials are determined by the requirement that they equal the chemical potential, μ_{step}^{i}, for step i which is written as $\mu_{step}^{i} = - E_{ads}^{i-} - E_{step}^{i} + \mu_{rep}^{i}$. Here, $E_{step}^{i} > 0$ denotes the contribution associated with lateral binding energy of adatoms at the step, and μ_{rep}^{i} denotes the contribution due to step-step repulsion which only becomes important for closely spaced steps. See the Appendix. Setting $\Delta E_{ads}^{i} = E_{ads}^{i+} - E_{ads}^{i-}$, one obtains the key results

$$n_{eq}^{i-} = \exp[\beta(-E_{step}^{i} + \mu_{rep}^{i})], \text{ and } n_{eq}^{i+} = n_{eq}^{i-} \exp[\beta \Delta E_{ads}^{i}]. \quad (6)$$

Thus, n_{eq}^{i-} is independent of the adsorption energies, in contrast to n_{eq}^{i+}.

In our modeling, all adsorption energies will be chosen equal except for binding on top of the 2nd layer which is enhanced due to QSE by $\Delta E^{QSE}>0$ (a few 10's of meV). This reflects the preference for 3-high islands. Thus, one has that $n_{eq}^{2+} = n_{eq}^{2-} \exp[\beta\Delta E^{QSE}] > n_{eq}^{2-}$, and $n_{eq}^{3+} = n_{eq}^{3-} \exp[-\beta\Delta E^{QSE}] < n_{eq}^{3-}$, but all other $n_{eq}^{i+} = n_{eq}^{i-}$. These inequalities underlie the enhancement of growth of the 3rd layer, and inhibition of nucleation of the 4th layer.

To complete the model specification, we decompose the lateral binding energy at the step as $E_{step}^{i} = E_{step}^{i}(r_i) = E_b^{i} - \alpha_i/r_i - \varepsilon\, f(r_i/r_c)$. The first term, E_b^{i}, denotes the lateral binding energy in the absence of curvature effects or strain. This can depend on layer index i. The second term accounts for reduced binding due to higher step edge curvature. The step energy, α_i, is chosen to satisfy $\alpha_i \approx E_i^{b}/3$ based on behavior for fcc(111) surfaces with nearest-neighbor interactions. The last term accounts for reduced binding to step edges in larger islands once the radius, r_i, becomes comparable to $r_c \approx 10$ due to a buildup of strain. The maximum strain-related reduction in bonding for very large islands corresponds to ε. Thus, f(x) must increase from 0 to 1 with increasing x, and for simplicity we choose $f(x) = 1\text{-}e^{-x}$.

3C. PARAMETER SELECTION AND NUMERICAL SIMULATIONS

In our modeling, we choose a fairly high terrace diffusion barrier $E_d \approx 0.57$ eV for Ag on top of "rough" Ag layers in multilayer islands. This exceeds $E_d \approx 0.45$ eV for smoother Ag(100) surfaces [10]. The step edge barrier is chosen as $\delta \approx 0.10-0.15$ eV, typical values for Ag homoepitaxial systems [10]. The attempt frequency for all hops is chosen as $\nu = 10^{12}$

s^{-1} and the deposition flux is $F = 10^{-3}$ ML/s matching experiment. Thus, since $D = \nu \exp(-\beta E_d)$, one has that $D/F \approx 10^{7.1}$ and $L_{ES} \approx 23$ at 365 K. For Ag adatoms on fivefold i-Al-Pd-Mn, nearest-neighbor binding is quite weak as adsorption sites are generally far-separated [14, 24]. However, adatom separations in higher layers should tend to relax back toward bulk fcc values, noting that the upper surfaces of thick Ag films grown at 300 K exhibit fcc(111) structure. Thus, the adatom binding should increase somewhat with increasing layer height. Consequently, below we choose $E_i^b = 0.27, 0.30, 0.32, 0.33,\ldots$ eV for $i = 1, 2, 3, 4,\ldots$ respectively, so $\Delta E_i^b = E_{i+1}^b - E_i^b > 0$ (cf. $E^b \approx 0.40$ eV for Ag(100), and $E^b \approx 0.60$ eV for Ag(111) surfaces) [10]. We now analyze some key features of island growth at 365 K for this choice of parameters.

First, consider "triggering" of the transformation from 2D to 3D islands when $r_1 \approx 10$. This requires that the total flux, $J_{eq}^{1\to2} + J_{dep}^{2-}$, of atoms attaching to a just formed 2nd layer island of radius $r_2 \approx 1$ should be *positive* (so that the island will grow rather than shrink). One has that $J_{dep}^{2-} / F \approx 0.6\, \pi\, r_1^2 \approx 10^{2.3}$ (see the Appendix) and from (3) for the equilibration flux that

$$J_{eq}^{1\to2}/F \approx 10^{3.5} \left(\exp[\beta(\varepsilon\, f(r_1/r_c) + 0.090/r_1)] - \exp[\beta(\varepsilon\, f(r_2/r_c) + 0.100/r_2 - \Delta E_1^b)]\right). \qquad (7)$$

The magnitude of $J_{eq}^{1\to2}$ will typically dominates that of J_{dep}^{2-}, so the condition for nucleation of the 2nd layer is that the exponent in the 1st term of (7) dominate that of the 2nd term. Physically, this means that the combined effect of increased strain for the larger 1st layer island and the enhanced binding in the 2nd layer dominate the effect of higher curvature of the

2^{nd} layer island to produce a positive flux. For $r_1 \approx r_c \approx 10$, $r_2 \approx 1$, and $\Delta E_1^b = 0.03$ eV, this implies that $\varepsilon \geq 0.1$ eV, so we choose $\varepsilon = 0.1$ eV below. For continued growth after 2^{nd} layer nucleation, $J_{eq}^{1\to2}$ is large and comparable to the flux of atoms attaching to the 1^{st} layer step due to deposition on the substrate, J_{dep}^{1-}. Thus, there is a significant uphill flow of atoms facilitated by stronger binding in the 2^{nd} layer and promoting 3D island growth. Similarly, nucleation and growth of the 3^{rd} layer is facilitated by enhanced binding in the 3^{rd} layer relative to the 2^{nd} layer ($\Delta E_2^b > 0$).

Second, consider the role of QSE with regard to formation of 3^{rd} and 4^{th} layer islands. We choose $\Delta E^{QSE} \approx 0.037$ eV based on DFT studies for various thin metal films [4-6]. Examination of the expression for $J_{eq}^{2\to3}/F$ analogous to (7) indicates that this flux is enhanced both by QSE, $\Delta E^{QSE} > 0$, and by enhanced binding in the 3^{rd} layer relative to the 2^{nd}, $\Delta E_2^b > 0$. This produces nucleation of the 3^{rd} layer for $r_2 < 10$ (see below). Both effects also promote rapid expansion of the 3^{rd} layer and the development of mesa-like, 3-layer-high islands with steep edges. This follows from the large value of

$$J_{eq}^{2\to3}/F \approx 10^{3.1}\, e^{\beta\varepsilon}\, [\exp(+\beta\Delta E^{QSE}) - \exp(-\beta\Delta E_2^b)] \approx 10^{4.7} \qquad (8)$$

for $r_3 >> r_2 >> 1$ (neglecting step-step interactions), noting that this flux is much smaller and determined by curvature differences for $\Delta E^{QSE} = \Delta E_2^b = 0$. Examination of the expression for $J_{eq}^{3\to4}/F$ analogous to (7) indicates that the effect of QSE dominates that of enhanced binding in the 4^{th} (relative to the 3^{rd}) layer ($\Delta E^{QSE} > \Delta E_3^b$) tending to keep this flux negative,

inhibiting nucleation of the 4th layer. Thus, nucleation can only occur if this negative flux is counterbalanced by sufficiently large deposition flux, $J_{dep}^{4-}/F \approx \pi r_3^2$ which requires large r_3.

Numerical analysis of our step dynamics model was performed with the above parameter choice. This analysis involved integration of the coupled non-linear equations (5) for the radii of different layers in the 3D island. Each time the radius of the top layer reaches a critical value for nucleation of the next layer, one introduces a new equation for the evolution of the radius of that island which starts with a value $r_{top} = 1$. The equation for the layer must then be updated to account for the presence of this new top layer. Results shown in Fig.6 illustrate that the model recovers the key features of island formation seen in experiment: a transition to 3D island growth when the first layer island radius reaches $r_1 \approx 10$; subsequent development and lateral spreading of a mesa-like 3-layer high island with steep edge (corresponding to closely spaced values for r_1, r_2 and r_3); and delayed nucleation of the 4th layer occurring only when $r_1 \approx 47$.

4. CONCLUSIONS

Growth of Ag films on a fivefold i-Al-Pd-Mn surface is shown to exhibit strong quantum size effects (QSE) in the form of 3D islands with a strong preference for the selection of a height of 3 layers. We develop and apply a step dynamics formulation to provide for the first time a characterization of the development of 3D islands and their height selection for a system exhibiting QSE. The key physical features driving the behavior in this system and which were incorporated into our step dynamics model (i.e., strain induced weaken of binding at step edges, enhanced binding in higher layers, and enhanced adsorption

in specific higher layers) should be present in a variety of other systems exhibiting 3D growth and QSE.

APPENDIX: FURTHER DETAILS OF THE STEP DYNAMICS FORMULATION

The solution to the boundary-value problem (2) for the adatom density, n, on a terrace bounded by a descending circular step of radius r_i and an ascending circular step of radius r_{i+1} ($<r_i$) has the form $n(r) = -r^2 / (4D/F) + c_1 \ln r + c_2$. The constants c_i are determined by the boundary conditions. The total fluxes for net attachment on the bounding step edges are given by $J = \pm 2\pi\, r\, D\, \partial n/\partial r\,|_{step}$, where + (-) applies for $r = r_{i+1}$ ($r = r_i$). In Sec.3A, we have described the decomposition on n and J into "deposition" and "equilibration" parts. The explicit form of the single equilibration flux across the terrace is given in (3). The explicit forms for the deposition fluxes for attachment to ascending step i+1, $J_{dep}^{(i+1)-}$, and descending step i, J_{dep}^{i+}, are

$$J_{dep}^{(i+1)-}/F = \pi\, r_{i+1}^2\, ([\tfrac{1}{2}\,(r_{i+1}^2/r_i^2) - \tfrac{1}{2} + (L_{ES}/r_i)(r_{i+1}/r_i)^2][\ln(r_{i+1}/r_i) + L_{ES}/r_{i+1}]^{-1} - 1)$$

$$J_{dep}^{i+}/F = \pi\, r_i^2\, (1 - [\,\tfrac{1}{2} - \tfrac{1}{2}\,(r_{i+1}^2/r_i^2) + (L_{ES}/r_i)][\ln(r_{i+1}/r_i) + L_{ES}/r_{i+1}]^{-1}) \qquad (9)$$

From (10), one immediately obtains the mass conservation condition (4). In Sec.3B, we specified the form of the chemical potential, μ_{step}^i, for step i, and extracted the associated equilibrium adatom densities. The contribution, μ_i^{rep}, associated with step-step repulsion has the form [22]

$$\mu_i^{rep} \approx 2\gamma/(r_{i-1} - r_i)^3 - 2\gamma/(r_i - r_{i+1})^3, \quad (10)$$

where step i between steps i+1 and i-1. Thus, μ_i^{rep} increases as step i catches up to step i-1 ahead of it, and decreases as the trailing step i+1 catches up to i. For the bottom (top) step in the island, only the negative (positive) term appears. These terms inhibit steps from getting too close and prohibit step crossing in our model. In our model, we choose γ = 0.05 to 0.1 eV. As γ increases, the separation between the steps increases. However, for this range of values, the change in step separations is a few unit cells and hence the results are virtually the same.

ACKNOWLEDGEMENTS

This work was supported primarily by NSF Grant CHE-0414378. BU was supported by the Division of Materials Sciences, Basic Energy Sciences, US Department of Energy (USDOE). The work was performed at the Ames Laboratory which is operated for the USDOE by Iowa State University under Contract No. DE-AC02-07CH11358.

REFERENCES

[1] T.-C. Chiang, Surf. Sci. Rep. **39**, 181 (2000).

[2] A. R. Smith, K.-J. Chao, Q. Niu, and C.-K. Shih, Science **273**, 226 (1996).

[3] L. Gavioli, K. R. Kimberlin, M. C. Tringides, J. F. Wendelken, and Z. Zhang, Phys. Rev. Lett. **82**, 129 (1999).

[4] V. Yeh, L. Berbil-Bautista, C. Z. Wang, K. M. Ho, and M. Tringides, Phys. Rev. Lett. **85**, 5158 (2000).

[5] K. L. Man, Z. Q. Qiu, and M. S. Altman, Phys. Rev. Lett **93**, 236104 (2004).

[6] B. Unal, F. Qin, Y. Han, D. J. Liu, D. Jing, A. R. Layson, C. Jenks, J. W. Evans, and P. A. Thiel, Phys. Rev B **76**, 195410 (2007).

[7] V. Fournée, H. R. Sharma, M. Shimoda, A. P. Tsai, B. Unal, A. R. Ross, T. A. Lograsso, and P. A. Thiel, Phys. Rev. Lett. **95**, 155504 (2005).

[8] P. Politi, G. Grenet, A. Murty, A. Ponchet, and J. Villain, Phys.Rep. **324**, 271 (2000).

[9] T. Michely, and J. Krug, *Islands, Mounds, and Atoms: Patterns and Processes in Crystal Growth Far from Equilibrium* (Springer Verlag, Berlin, 2004).

[10] J. W. Evans, P. A. Thiel, and M. C. Bartelt, Surf. Sci. Rep. **61**, 1 (2006).

[11] V. Fournée, and P. A. Thiel, J. Phys. D: Appl. Phys. **38**, R83 (2005).

[12] B. Unal, C. J. Jenks, and P. A. Thiel, unpublished results (2008).

[13] I. Horcas, R. Fernandez, J. M. Gomez-Rodriguez, J. Colchero, J. Gomez-Herrero, and A. M. Baro, Rev. Sci. Instr. **78**, 013705 (2007).

[14] B. Unal, V. Fournée, K. J. Schnitzenbaumer, C. Ghosh, C. J. Jenks, A. R. Ross, T. A. Lograsso, J. W. Evans, and P. A. Thiel, Phys. Rev B **75**, 064205 (2007).

[15] V. Fournée, T. C. Cai, A. R. Ross, T. A. Lograsso, J. W. Evans, and P. A. Thiel, Phys. Rev. B **67**, 033406 (2003).

[16] In [14], island density data fit with i=5 yields a sharp decrease above 300 K, as well as plateau below (trap saturation). However, for low enough T, one expects irreversible island formation (i=1). The onset of this regime occurs around 270 K when the rate of aggregation of diffusing adatoms with islands, Kagg = F/Ntrap, exceeds the dimer dissociation rate Kdiss = 1013 exp[-(Ed+Eb)/(kBT)] for diffusion barrier Ed=0.55eV and bond strength Eb=0.01eV. .

[17] For heterogeneous nucleation where essentially all islands are formed in the very early stages of deposition, the size of each island is clearly proportional to its capture zone area. However, for persistent nucleation as in this system [14], this simple relationship fails as size also depends on the time of nucleation. .

[18] V. Fournee, A. R. Ross, T. A. Lograsso, J. W. Evans, and P. A. Thiel, Surface Science **537**, 5 (2003).

[19] The measured W for low coverages at 127 K and 200 K appears to drop below the nominal minimum value for nominal layer-by-layer growth (with single layer high islands residing on a perfectly flat substrate). This reflects the feature that the quasicrystalline substrate is quite rough (peak to peak roughness ~ 0.1 nm) and thus island atoms are partly "buried" in the substrate. Here, the film height distribution does not show separate peaks for the islands and substrate.

[20] J. Krug, Physica A **313**, 47 (2002).

[21] M. Li, and J. W. Evans, Phy. Rev. Lett. **95**, 256101 (2005).

[22] D. Margetis, P.-W. Fok, M. J. Aziz, and H. A. Stone, Phys. Rev. Lett. **97**, 096102 (2006).

[23] T. L. Hill, *Statistical Thermodynamics* (Addison-Wesley, London, 1960).

[24] C. Ghosh, D.-J. Liu, K. J. Schnitzenbaumer, C. J. Jenks, P. A. Thiel, and J. W. Evans, Surf. Sci. **600**, 2220 (2006).

Figure Captions

Figure 1. (Color online) Semi-three dimensional STM images for Ag films for (a) 0.26 ML, (b) 0.70 ML, and (c)1.0 ML. (d) Line profiles from (typical) individual Ag islands showing the sequence of island shapes versus the size of the islands as a function of coverage. The sizes of the images are 243 nm x 243 nm. The tunneling conditions for the images are + 0.95-0.97 V, 0.44 nA.

Figure 2. Corresponding island height distributions showing the island area versus island height for (a) 0.26 ML and (b) 0.70 ML. Areal occupancy of the each layer for (c) 0.26 ML and (d) 0.7 ML.

Figure 3. (Color online) A 23.4 nm x 19.6 nm STM image showing the pseudomorphic structure of one-layer-high Ag island. The tunneling condition is + 0.99 V, 0.46 nA.

Figure 4. Film roughness, W, versus total coverage, θ, for 127 K, 200 K, 300 K and 365 K. W_1 for layer-by-layer growth, W_2 for Poisson growth and W_3 for ideal 3-layer-high growth.

Figure 5. (a) Schematic of the 3D island geometry for the step dynamics modeling. (Cross-sectional view of 3-layer-high island showing radii r_i with $r_3<r_2<r_1$ and well as capture zone radius R.) Schematic also superimposes the PES for the binding energy of single Ag atoms. (b) Schematic of the adatom density around the terrace bounded by steps 2 and 3 showing the influence of QSE.

Figure 6. Results of step dynamics simulations showing the island radius of each layer versus total coverage. The simulation values are QSE = 0.037 eV, R = 25.0 nm, E_d = 0.57 eV, ε = 0.1 eV, γ = 0.05 eV, δ = 0.15eV, r_c = 2.5 nm, α_1 = 0.0900 eV, α_2 = 0.1000 eV, α_3 = 0.1030 eV, α_4 = 0.1134 eV , E_1 = 0.27 eV, E_2 = 0.30 eV, E_3 = 0.32 eV, E_4 = 0.33 eV.

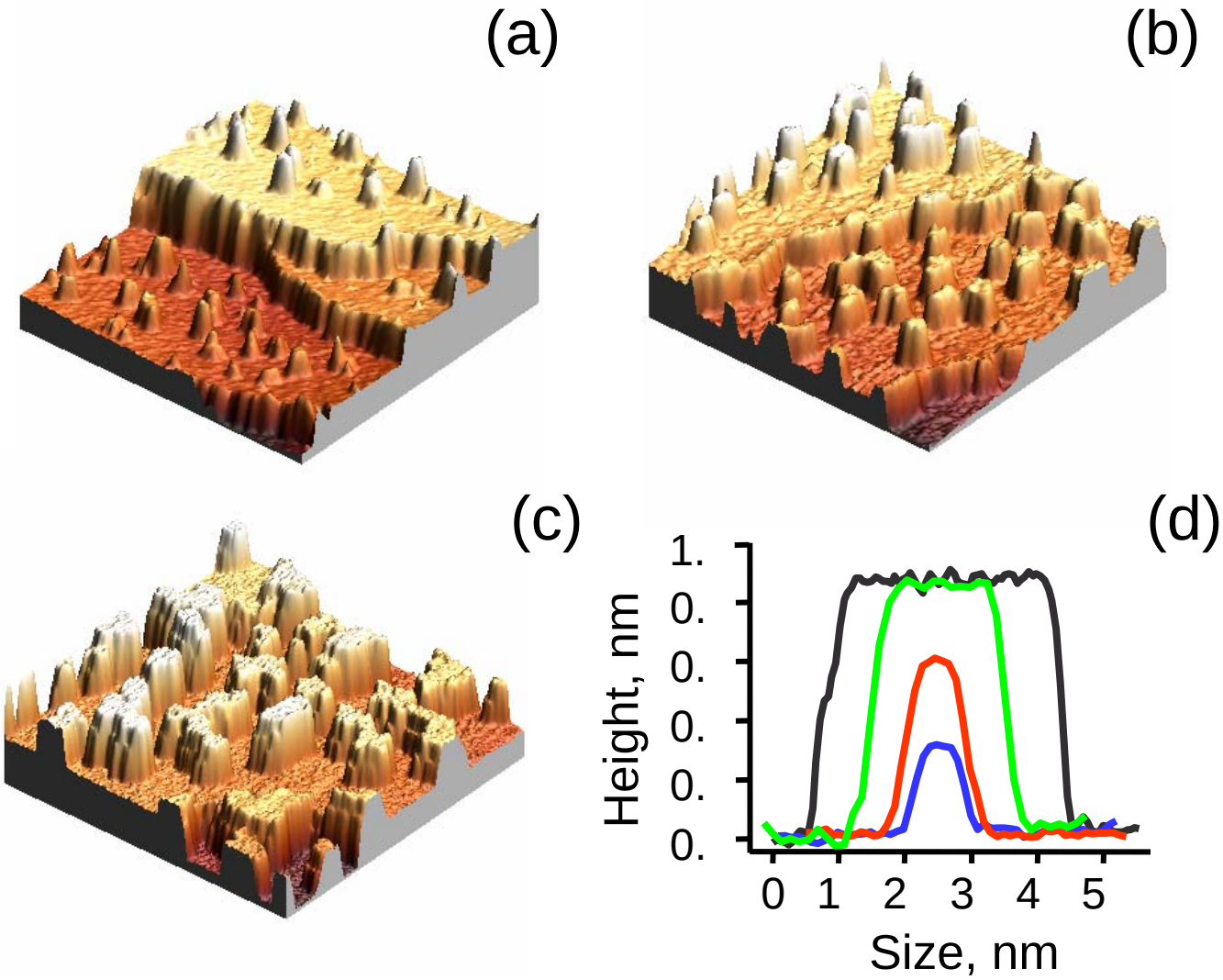

Figure 1

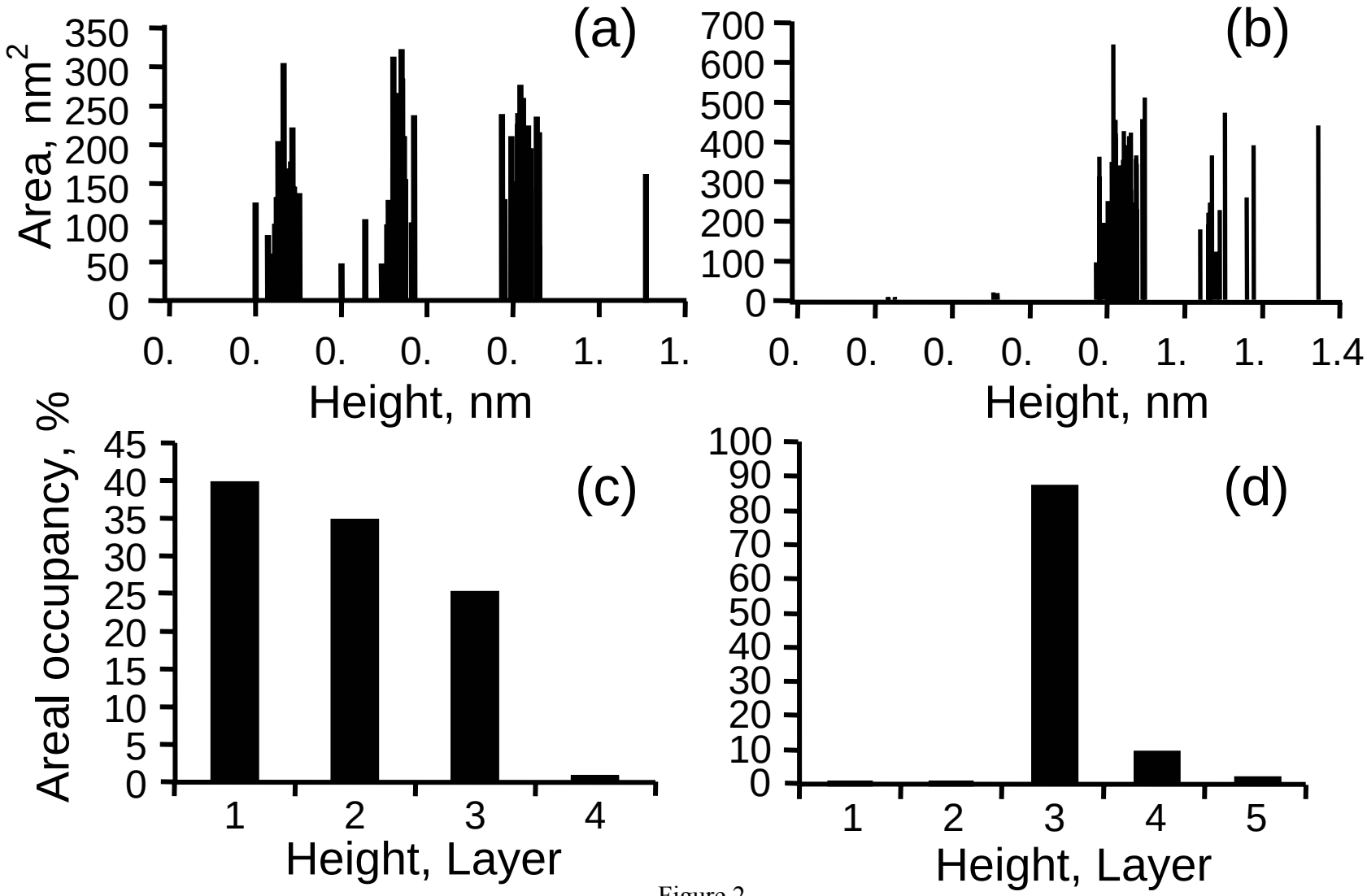
(a)
(b)
(c)
(d)
Area, nm2
Height, nm
Areal occupancy, %
Height, Layer
350
300
250
200
150
100
50
0
700
600
500
400
300
200
100
0
45
40
35
30
25
20
15
10
5
0
100
90
80
70
60
50
40
30
20
10
0
0.
0.
0.
0.
0.
1.
1.
1.4
1
2
3
4
5

Figure 2

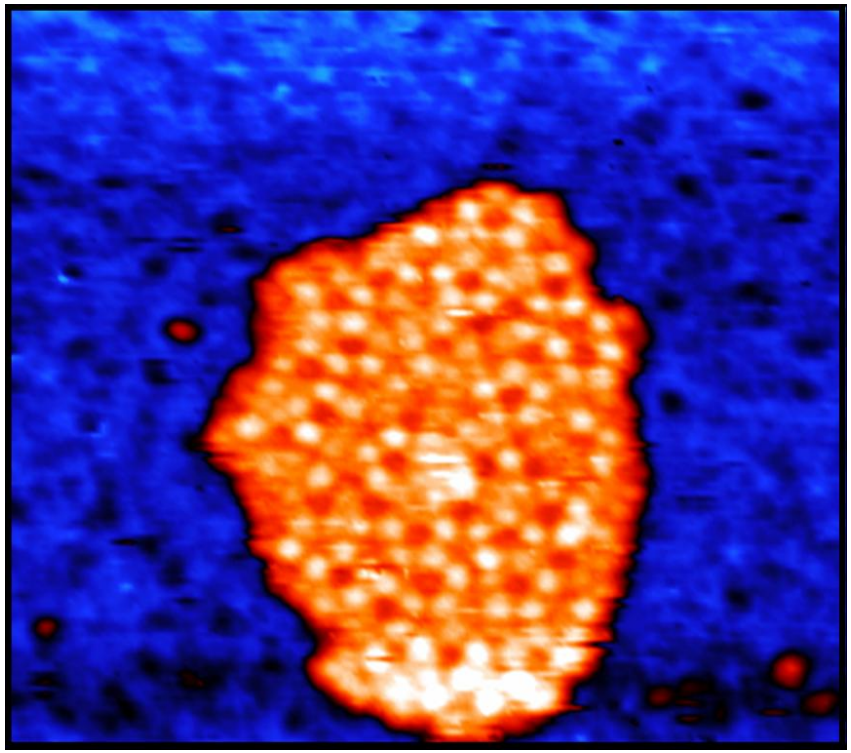

Figure 3

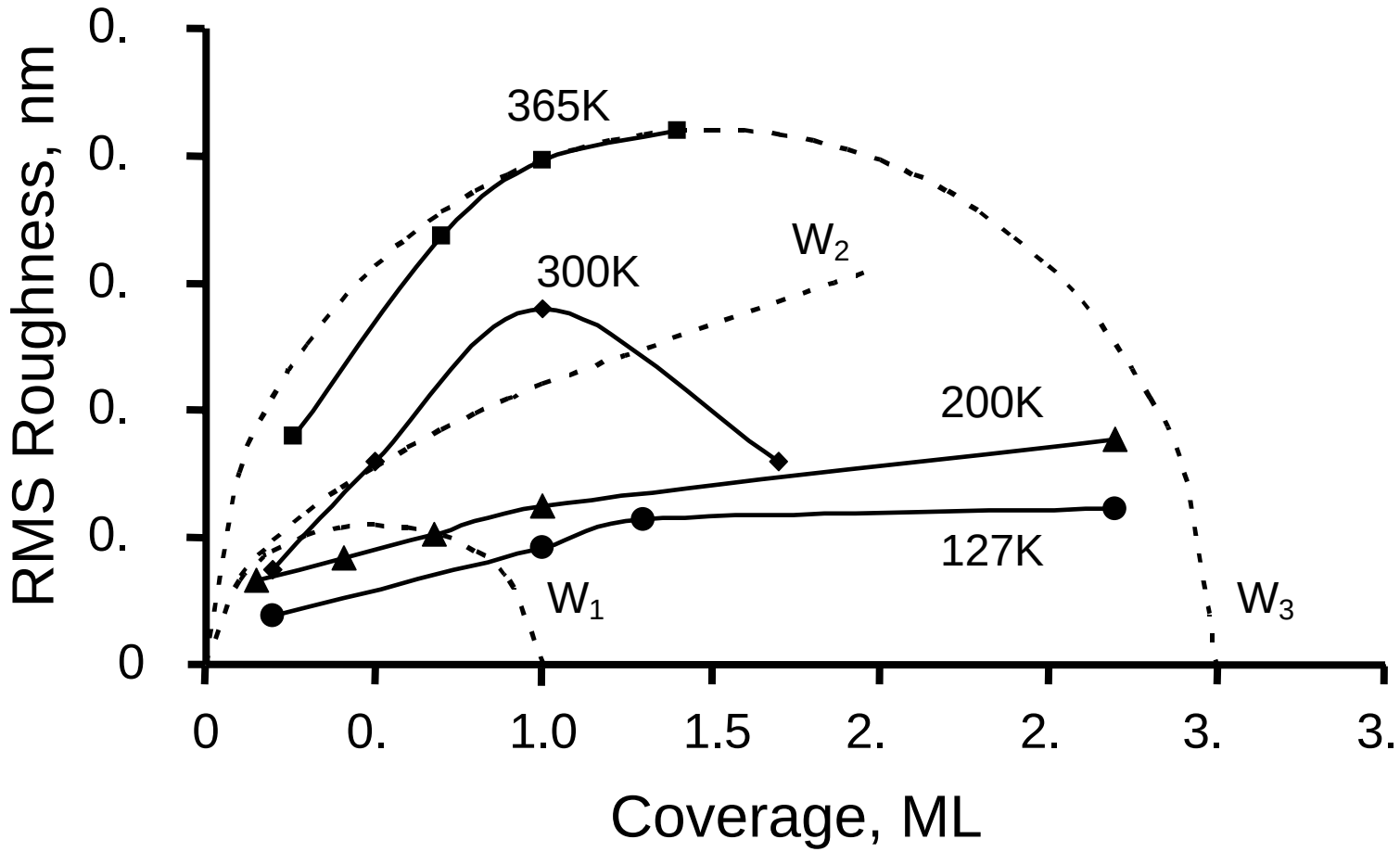
RMS Roughness, nm
0.
0.
0.
0.
0
365K
300K
200K
127K
W1
W2
W3
0
0.
1.0
1.5
2.
2.
3.
3.
Coverage, ML

Figure 4

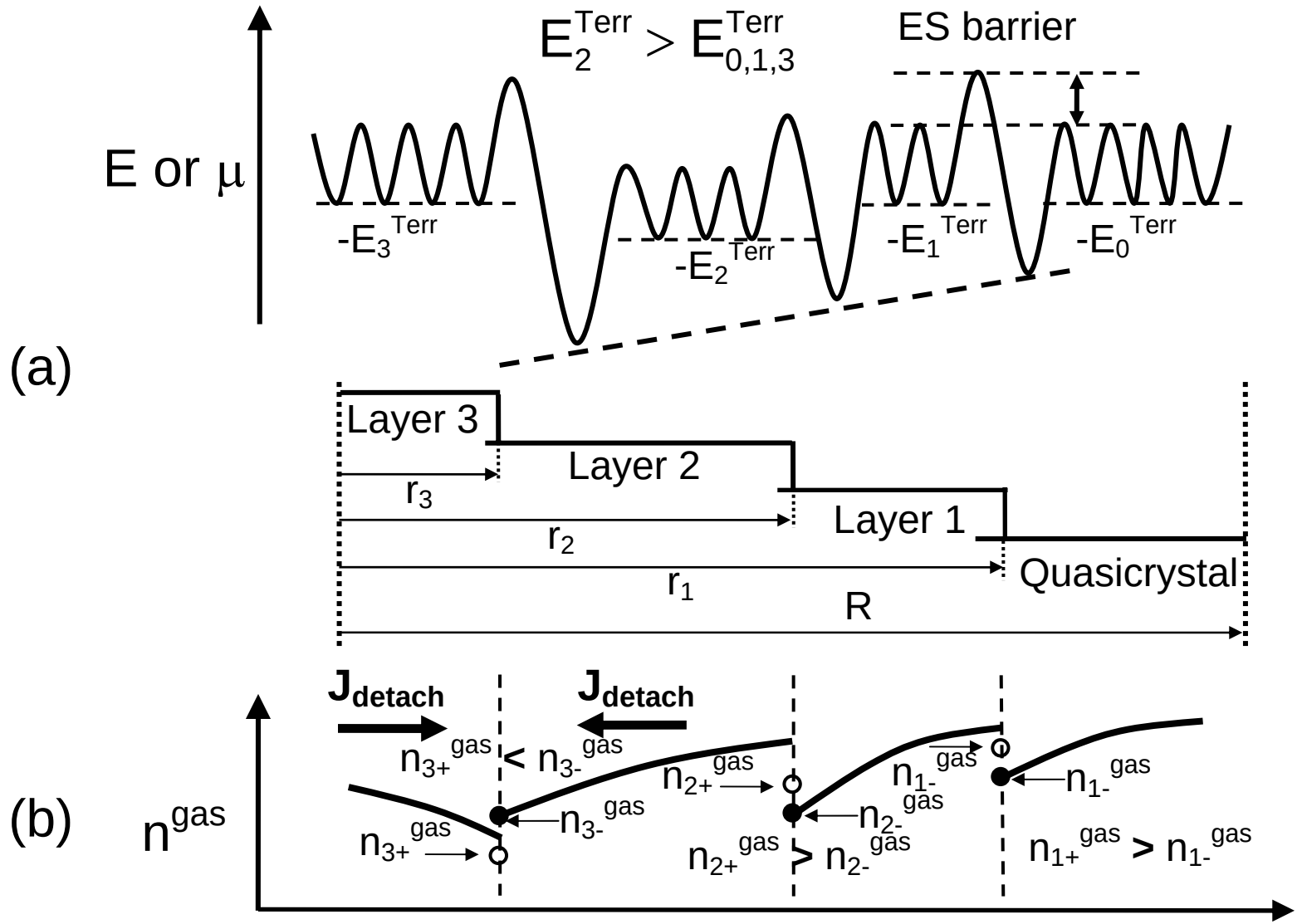
E or μ
$E_2^{Terr} > E_{0,1,3}^{Terr}$
ES barrier
$-E_3^{Terr}$
$-E_2^{Terr}$
$-E_1^{Terr}$
$-E_0^{Terr}$
(a)
Layer 3
Layer 2
Layer 1
Quasicrystal
r_3
r_2
r_1
R
(b)
n^{gas}
J_{detach}
J_{detach}
$n_{3+}^{gas} < n_{3-}^{gas}$
n_{2+}^{gas}
n_{1-}^{gas}
n_{1-}^{gas}
n_{3-}^{gas}
n_{2-}^{gas}
n_{3+}^{gas}
$n_{2+}^{gas} > n_{2-}^{gas}$
$n_{1+}^{gas} > n_{1-}^{gas}$

Figure 5

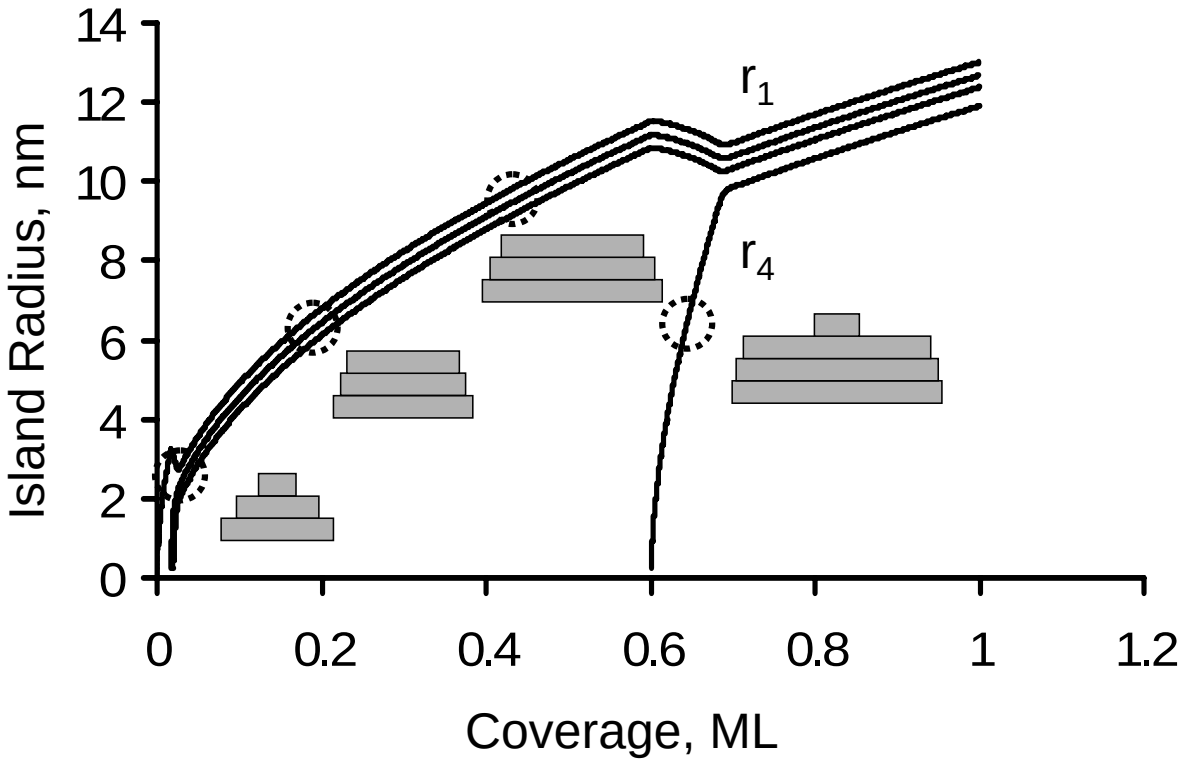
Island Radius, nm
Coverage, ML
r1
r4
0
2
4
6
8
10
12
14
0
0.2
0.4
0.6
0.8
1
1.2

Figure 6

SCANNING TUNNELING MICROSCOPY AND DENSITY FUNCTIONAL THEORY STUDY OF INITIAL BILAYER GROWTH OF AG FILMS ON NIAL(110)

A paper published in *Physical Review B*

Baris Unal, Feili Qin, Yong Han, Da-Jiang Liu, Dapeng Jing,

A.R. Layson, C. J. Jenks, J.W. Evans, and P. A. Thiel

Abstract

Scanning tunneling microscopy (STM) studies of the deposition of Ag on bcc NiAl(110) in the temperature range of 200 K to 300 K reveal an initial bilayer growth mode. In this regime, which encompasses at least the first two levels of bilayer islands, the film appears to have an fcc Ag(110)-like structure. Selection of this structure reflects an almost perfect lateral match between the Ag(110) and NiAl(110) lattice constants. Density functional theory (DFT) analysis of supported Ag films with an ideal fcc(110) structure on NiAl(110) indicates that the bilayer growth mode is promoted by a quantum size effect. However, the system does not exhibit perfect Ag(110) film growth. STM analysis reveals that the tops of Ag islands are decorated by a ripple structure even in the initial levels of growth, and also shows a deviation from Ag(110)-like bilayer growth to Ag(111)-like monolayer growth for thick films. DFT analysis is also applied to provide some insight into the observed deviations from perfect Ag(110) film structure.

I. Introduction

There has been extensive experimental and theoretical analysis for both homoepitaxial and heteroepitaxial growth of thin metal films.[1-3] The great majority of these studies have used single-element single-crystal substrates. However, using instead intermetallics as substrates or "templates" for thin film growth provides significant additional possibilities for guiding film structure and morphology. This strategy could potentially lead to novel nanostructures with tailored properties for surface enhanced Raman spectroscopy, catalysis, magnetism, or other applications.

To explore such possibilities, in this paper, we examine the structure of Ag films grown on one such substrate, the binary alloy NiAl(110). This combination of materials is structurally intriguing because the bulk structures of the substrate and film are fundamentally different, NiAl being CsCl (bcc-like, $a_{NiAl} = 0.289$ nm) and Ag being fcc ($a_{Ag} = 0.408$ nm). However, there is virtually perfect in-plane lattice matching between Ag(110) and NiAl(110). This feature is illustrated in **Fig. 1(a)-(b)**. Consequently, this system provides an ideal candidate in which to study morphological evolution during heteroepitaxy in the absence of a lateral mismatch strain. In particular, it is of interest to determine whether Ag adopts the fcc(110) structure atop this NiAl template.

The NiAl surface has attracted much attention in the past, for several main reasons. First, NiAl is of technological importance in high-temperature applications such as turbines.[4] Second, thin layers of alumina can be grown on this surface that are both well-ordered and conductive. These layers serve as tractable models for the alumina supports common in heterogeneous catalysts.[5] Third, the electronic structure of NiAl(110) includes a small depression in the density of states at the Fermi edge.[6] This feature has led to its selection as a

substrate for growth of one dimensional atomic wires both theoretically[7] and experimentally[8-10] (the latter being formed via atomic manipulation at low temperature), with focus on fundamental electronic and magnetic traits of the wires.

As a result of this widespread interest, the NiAl surface is reasonably well-characterized. As shown in **Fig. 1(a)**, the arrangement of atoms in the (110) plane is anisotropic, consisting of rows of Ni and Al atoms in a 1:1 stoichiometry. In a previous structure determination using multiple scattering analysis of intensity-voltage variation of low-energy electron diffraction (LEED) spots,[11] the (110) surface was found to be bulk-terminated, except for two features. The first was a rumpling of the top layer in which the Al atoms protrude above the Ni atoms by 0.02 nm. The second was a first interlayer expansion of a few percent (assuming that the Al atoms define the topmost plane). The structure was confirmed by medium energy ion scattering,[12] and by X-ray scattering.[13] This characterization was further supported by density functional (DFT) calculations,[7, 14] and reconfirmed in our own analysis.

Numerous studies of Ag thin film growth on a variety of other substrates have been reported. From these, a few pertinent generalizations can be drawn. First, Ag films do not alloy with other transition metal substrates at room temperature. Alloying occurs in some systems, but only at temperatures of ca. 500 K or above.[15-31] While Ag can insert into surface planes of pure Al substrates, [32] Ag is not known to react with surfaces of alloys containing Al and earlier transition metals such as Ni or Pd at room temperature. [33, 34] Presumably, this is because the Al-Ni bond is much stronger than the Al-Ag or Ni-Ag bond, as reflected in the heats of formation of the respective 1:1 alloys.[35-37] Thus, alloying is not anticipated in the present work, wherein Ag is deposited at 200 K and 300 K. Second, the low surface energy

of Ag usually leads the first few layers to ‘wet’ the substrate, although strain can trigger three-dimensional growth in higher layers (Stranski-Krastanov growth). An example of the latter is Ag on W(110).[17, 38] Finally, clean films of Ag (and also Au) that are sufficiently thick—on the order of 10-50 layers or more—tend to exhibit an fcc(111) orientation or be vicinal to the (111).[e.g. 33, 39-42] This tendency prevails on diverse substrates, although details of the film morphology such as twinning and defect structure may depend upon the interface, and some exceptions can be found.

In Sec. II, we provide some background on our experimental procedures and on our supporting DFT calculations. In Sec. III, we present the main results of our study. First, we describe scanning tunneling microscopy (STM) observations for multilayer growth of Ag films mediated by nucleation and growth of islands within each level. In this paper, “layer” denotes an essentially flat, low-index atomic plane, whereas “level” corresponds to islands of a specific height, labeled according to sequence of appearance with increasing Ag coverage. We will argue that two Ag(110)-like layers—i.e., a (110) bilayer—comprise each of the first two levels. We will propose that as the film thickens, a transition occurs and eventually single Ag(111)-like layers—i.e. (111) monolayers—comprise each level. DFT analyses of benchmark ideal fcc Ag(110) film structures supported on a NiAl(110) substrate are then presented together with evidence that a quantum size effect promotes the initial bilayer growth. We also describe more subtle deviations features of growth including rippling of the tops of Ag islands. Additional DFT analysis of other film structures is presented which elucidates the rippling and which also provides insight into the deviation from bilayer growth for thicker films. Some further discussion is provided in Sec. IV. An Appendix briefly

describes the adsorption site of isolated Ag adatoms on NiAl(110), adatom diffusion, and the Ag-Ag interactions that lead to the observed island shapes.

II. Details of Experiments and Calculations

A NiAl single crystal was grown using the Bridgman technique.[43] The samples were oriented and sectioned from the ingot by electrical discharge machining. The NiAl surface was oriented to within ± 0.25^{o} of the (110) orientation, then polished using standard metallographic techniques. The polished sample was mounted on an Omicron heater and introduced into an ultrahigh-vacuum chamber equipped with Auger electron spectroscopy (AES), LEED and STM. The base pressure of the chamber was 2×10^{-11} Torr. The sample was cleaned by repeated cycles of Ar^{+} sputtering (20 min., 1.5 KeV, T = 300 K) followed by annealing to 1200 K for 2 hours, until the surface was judged clean by AES, LEED and STM. The annealing temperature corresponds to about 2/3 of the melting point, 1915 K. STM images were processed using WSXM software.[44]

STM images reveal that these sample preparation procedures can produce a NiAl(110) surface with broad terraces (up to 1 μm wide). In the data presented in this work, specifically, the terraces were up to 110 nm wide for deposition of Ag at 300 K, and up to 260 nm at 200 K. The terraces were separated by monoatomic steps and step bunches. Line scans across these steps indicated a step height of 0.204 $\pm$ 0.006 nm, nearly equal to the value of 0.2014 nm expected from the bulk lattice constant of NiAl. We were thereby able to calibrate the z-piezo in the STM, a key requirement for our subsequent characterization of vertical surface structure.

In our thin film growth studies, Ag was evaporated from a commercial Omicron

source. However, this source had a rather open design, and so we modified it with a cap containing a 1.25 mm orifice. This made the arrangement more like a true Knudsen cell. The base pressure was below 10^{-10} Torr during deposition. Flux calibration of the source was achieved by measuring the coverage directly from the STM images at low coverage. The estimated flux value was 1.6×10^{-3} bilayers s^{-1} (where a bilayer is defined as two layers of a perfect Ag(110) film) for the studies conducted at a surface temperature of 300 K, and 3.3×10^{-3} bilayers s^{-1} for those done at 200 K.

Some STM data are also reported for comparative studies of Ag deposition on Ag(110). These experiments were performed in a different chamber, with base pressure below $1x10^{-10}$ Torr. The Ag(110) sample was cleaned by repeated cycles of Ar^+ sputtering (20 min, 0.5 KeV, T ≈ 300K) followed by annealing at 700 K. The Ag was deposited at 220 K, and the flux was 4.5×10^{-2} monolayers s^{-1}.

For our electronic structure calculations, we used DFT with the generalized gradient approximation (GGA) proposed by Perdew, Burke, and Ernzerhof.[45] The single-particle Kohn-Sham equations[46] were solved using the plane-wave-based Vienna *ab initio* simulation package (VASP).[47] The electron-ion interactions were described by the projector augmented-wave (PAW) approach.[48] The energy cutoff for the plane-wave basis was set to be the default value for freestanding or supported Ag(110) films. The converged magnitude of the forces on all relaxed atoms was always less than 0.1 eV/nm. To prevent spurious interactions between adjacent replicas of the thin film system, we used a vacuum layer that was 1.5 nm thick in the direction perpendicular to the surface. The optimized lattice constants were 0.2896 nm for NiAl, and 0.4168 nm for Ag, to be compared with experimental values of 0.289 and 0.408 nm, respectively. These theoretical lattice constants were used in all subsequent calculations.

As background for our analysis of supported Ag films on NiAl(110) presented below, some brief remarks on the DFT predictions for the structure of the clean NiAl(110) surface follow. Our DFT calculations reproduced the experimental results reasonably well. For instance, the vertical separation between surface Ni and Al atoms is 0.017 nm from our DFT [for a 21-layer NiAl(110) slab], whereas it is 0.016 nm from X-ray scattering,[13] and 0.022 nm from LEED.[11] The first interlayer spacing[49] is larger than the bulk value by 3.1% from our DFT, compared with 3.8±0.6% from X-ray scattering,[13] 4.6% from LEED,[11] and 5.0±2.0% from MEIS.[12] Our calculations further showed that the surface energy of clean NiAl(110) is 1.57 J/m^2 for the fully-relaxed surface. This is, as might be expected, comparable to but lower than the value obtained from a previous DFT analysis of a fixed (unrelaxed) substrate, 1.65 J/m^2.[50] Furthermore, it is higher than the surface energy of Ag(110), 1.24 – 1.42 J/m^2.[51, 52] Hence, surface energy differences should drive Ag(110) films to grow layer-by-layer on NiAl(110), although this prediction is rather crude because it ignores the interfacial energy.

Finally, one might anticipate quantum size effects associated with the finite thickness of the slab of NiAl(110) substrate used in calculations below for supported Ag films. Indeed, calculations for NiAl(110) slabs of various thickness did indicate some variation of the surface energy of thin Ag films. However, in this work comparisons are made while holding the NiAl slab thickness constant, so this effect should not impact our analysis of relative energetics associated with supported Ag films of various thicknesses.

III. Experimental and Theoretical Results for Ag Films on NiAl(110)

A. Ag island step heights from STM data

Figures 2 and **3** show STM images of Ag islands deposited on NiAl(110) at 200 K and 300 K, respectively, for various film thicknesses (the associated coverages being reported in units of Ag(110) bilayers), together with representative information about step heights. From the STM images shown in the top row of each figure, it is clear that Ag forms two-dimensional (2D) islands. These islands are large and display highly anisotropic, rectangular shapes. Diffusion across terraces is sufficiently rapid at 300 K that, for a terrace width of about 100 nm or less and for the deposition rate specified above, Ag islands grow outward from steps as long finger-like protrusions. This behavior corresponds to step flow growth. Diffusion is slower at 200 K, so that islands nucleate and grow in the middle of terraces, as well as at step edges. See the Appendix for a brief discussion of terrace diffusion of individual Ag adatoms on NiAl(110), together with the strong anisotropy in adatom interactions which produces elongated islands, and the adsorption site.

Histograms of the pixel heights in a smaller region of the surface (chosen within a single terrace of the substrate) are shown in the middle row of each figure. The separations between peaks (which are labeled by the level of islands above the substrate) correspond to the average island or step heights, d, within the sampled region. The bottom rows show representative line profiles, from which representative values of the step heights, d, can also be derived. (Profiles are taken from a variety of images at different locations on the surface, not just from the images shown.) We analyze both line profiles and histograms because profiles show individual characteristics, while histograms obscure individual peculiarities but provide objective average values.

As an aside, note that the average coverage quoted above the STM images does not correspond exactly to the average level of the film surface in the sampled region, where the latter can be extracted from the histograms. There are two reasons for this discrepancy. First, histograms are taken from small areas in which the local coverage can fluctuate significantly. Second, the density of Ag atoms depends on the level, as will be clear from the discussion below.

Figure 4 and **Table I** show average values of *d*, determined from histograms, for islands in different levels. The results are virtually identical when line profiles are used. It can be seen that there is no significant difference between step heights at 200 K or 300 K. The step height is 0.32 nm for the first-level islands, and 0.29 nm for the second-level islands, at both temperatures. These are about twice the value expected for an Ag(110) monolayer. As the island level increases (moving higher up in the film) the step height decreases and eventually levels off in the range of 0.21-0.24 nm.

Electronic effects could influence measurements of step height. This possibility is strongest for the first-level islands, i.e. those directly atop the NiAl(110) substrate. Electronic effects can be revealed by changing the tunneling bias. A measurement of step height, for islands within the first level at 200 K, vs. tunneling voltage is shown in the inset to **Fig. 4** by the triangular symbols, corresponding to the top abscissa. The step height of 0.32 nm does not change strongly with bias voltage, and hence we conclude that 0.32 nm is a topographic value (reflecting positions of ion cores). For higher-level islands, where growth resembles homoepitaxy, an electronic effect known as Smoluchowski smoothening could conceivably influence STM measurements if the islands were very small (containing a few tens of atoms)

and closely-spaced (within a few tenths of nm).[53] However, the islands in our data are much too large and well-separated for the Smoluchowski effect to be significant.

It is instructive to compare these Ag islands with ones grown on the (110) surface of bulk Ag. The latter are shown in **Fig. 5(a)** for deposition at 220 K. Like the Ag/NiAl(110) islands, the Ag/Ag(110) islands are flat and elongated. The histogram in **Fig. 5(c)** reveals that they have a step height of $d = 0.15$ nm. Furthermore, this is the step height of intrinsic surface terraces on Ag(110), which is also shown by **Fig. 5(b)**. This value of d equals the bulk interplanar spacing, 0.145 nm, as shown in **Fig. 1(b)**.

The step height for Ag/Ag(110) is about half of the value for the first- and second-level islands of Ag/NiAl(110). *Whereas Ag islands on bulk Ag(110) form single layers, we propose that Ag islands on NiAl(110) are essentially Ag(110) bilayers, at least in the first two levels.* The structure of an Ag bilayer of Ag(110) on NiAl(110) is illustrated in **Fig. 1(d),** and for completeness the structure of an Ag(110) monolayer is illustrated in **Fig. 1(c)**.

As noted above, the average island height decreases as island level increases. At the high-coverage limit, the heights of the Ag islands, 0.21-0.24 nm, are bracketed by those expected for Ag(111), 0.236 nm, or Ag(100), 0.204 nm, but are significantly larger than the step height of Ag(110), 0.145 nm. *This indicates that bilayer growth does not continue, and that the atomic structure is not that of perfect Ag(110), in the higher-level islands. Specifically, we propose that there is a transition from Ag(110)-like bilayer growth to Ag(111)-like monolayer growth.* See also Sec. III.D.

Finally, it should be noted that islands are sometimes observed within the second level which do not fit the above description. These are illustrated in **Fig. 6**. These anomalous islands are always 2 nm wide, and they range in length from about 5 nm to 30 nm. We find

them only within the second level. They are 0.09-0.11 nm higher than the surrounding Ag surface constituting the top of first-level islands. Very occasionally, they merge with normal (higher and wider) bilayer islands, as in **Fig. 6(d)**. In such a case, the width of the anomalous island is still 2 nm but its height is about 0.14 nm. These single-layer Ag islands may serve as precursors to the bilayer, within the second level.

B. Benchmark DFT studies of structure and energetics for an ideal fcc Ag(110)/NiAl(110) film: Rational for initial bilayer growth.

We have performed extensive DFT calculations to assess the energetics of ideal Ag(110) films of various thicknesses on the NiAl(110) substrate. In the surface free energy calculations, we used a (1x1) lateral unit cell, thus enforcing perfect lateral periodicity. We used 15x15x1 k-mesh. Ag atoms in the first layer are located at the site between Ni atoms of the substrate, the preferred binding site for isolated Ag adatoms on this surface. (See the Appendix.) The structure of the NiAl(110) surface changes very little when these Ag(110) films are added. This feature has been checked for films on a 5-layer NiAl(110) slab with the bottom layer fixed. At the interface, there is still the rumpled NiAl structure similar to that of the freestanding NiAl(110) surface mentioned in Sec. I. As the Ag(110) film grows thicker (from 1 to 22 layers), the distance between the top-layer Al atom center and its nearest Ag atom center decreases from 2.03 Å, converging to 1.99 Å. The interlayer spacing between two Ag(110) layers is close to the bulk value of 1.47 Å.

From an evaluation of the stability of ideal Ag(110) films as a function of thickness, DFT provides a rationale for bilayer growth. The quantity that best reflects the stability of the film as a function of its thickness in layers, L, is

$$\alpha_L \equiv \gamma_{\mathrm{t}} + \gamma_{\mathrm{b}} + \gamma_{\mathrm{i}} - \gamma_{\mathrm{t},0} - \gamma_{\mathrm{b},0} = \frac{E_L - E_0 - N_L E_{\mathrm{c}}}{A} .$$

(1)

Here, γ_t, γ_b, and γ_i are the free energies of the top surface, bottom surface, and interface, respectively. Generally speaking, all three energies are functions of film thickness. E_L is the total energy including the NiAl substrate, N_L is the total number of Ag atoms in the added L-layer Ag film, E_c is the cohesive energy per atom of bulk fcc Ag, and A is the surface area. The subscript "0" corresponds to no Ag layer on the substrate. In our analysis, total energies (free energies at zero temperature) are calculated starting with a 5-layer NiAl(110) slab as the substrate with the bottom layer fixed, and adding layers of Ag(110). **Figure 7(a)** shows the resulting α_L vs. L for the first three bilayers. Oscillations with bilayer period develop and persist to thicker films together with some beating (not shown). It is clear that the most stable configurations (corresponding to minima in α_L) occur when films are 2, 4, and 6 layers thick.

The quantity α_L describes the energetics of an *extended* surface of an Ag(110) film supported on NiAl(110). One should also ask whether the adsorption or binding energy, $E_a<0$, of an individual, *isolated* Ag atom on perfect Ag(110) films of various thicknesses L would oscillate similarly. This would be relevant to the initial stage of formation of each new bilayer. The relevant calculations are performed using a (2x3) lateral unit cell with a 6x4x1 k-mesh. In order to make the computation more efficient, the NiAl substrate is decreased to 4 layers in contrast to the above calculations, tests showing that this does not affect the basic results.

Figure 7(b) reveals that the adatom adsorption energy indeed oscillates with a 2-layer periodicity. These oscillations persist for thicker films (not shown). Comparing the values at the minima and maxima shows that it is significantly more favorable for an adatom to adsorb atop the first Ag layer (L=1) than atop the NiAl(110) substrate (L=0). It is significantly more favorable to adsorb atop layer L=3 than layer L=2, and to absorb atop layer L=5 than layer L=4, etc. This underlies the tendency for bilayer growth. Furthermore, adsorption on higher even-numbered layers (corresponding to L=2, 4, 6) is progressively less favorable than on the NiAl(110) substrate (the maxima in Fig. 7(b) connected by a dotted line move to higher values). This naturally leads each successive level of Ag to wet the surface, in accord with the crude surface energy arguments of Sec. II.

The oscillations in α and E_a are promoted by a quantum size effect (QSE). This effect originates from quantum confinement of electrons in the vertical direction within the Ag film when the structural dimensions of a film become comparable to the mean free path of electrons. More specifically, the stability pattern of a metal film depends on satisfying a matching condition involving the Fermi wavelength λ_F and the film interlayer spacing d.[54] If λ_F and d satisfy the condition $jd = i\,\lambda_F/2$, where j and i are integers, then the film will exhibit an oscillating stability with j-layer oscillation when $j \neq i$, and no oscillation when $j = i$. For a Ag(110) film, d = 0.145 nm and λ_F = 0.5228 nm. Then when i = 1, j =1.8, which is close to the integer 2. This indicates that the Ag(110) film has a primary stability oscillation with a period of 2 layers, in agreement with the DFT results for the first few layers.

The step heights calculated for the Ag(110) bilayers are shown in **Table I**. At the fourth bilayer, the step height has reached the asymptotic limit for thick films, 0.294 nm. For the first two levels, theory agrees well with experiment, supporting the interpretation that

they are epitaxial Ag(110) bilayers. At and especially beyond the third level, however, there develops a significant difference between calculation and experiment. This suggests that there is a transition from the QSE-stabilized structure to a different one at higher levels. See Sec.III.A.

C. Ripples on the upper surface of the Ag(110) film

Rather than displaying the "ideal" Ag(110) structure in the first two levels, the upper surface of the Ag islands exhibits a lateral structure consisting of linear ripples or stripes. Such features also occur in higher levels which do not have Ag(110) structure (as surmised above based on their step heights). This ripple or stripe feature is shown in **Fig. 8**. The stripes can be divided into two groups on the basis of their appearance and separation. The first types are imaged as depressions, i.e. dark lines, about 0.02 nm deep and either 0.8 or 1.2 nm apart. These depressions are illustrated in **Fig. 8(a)-(b)**. The second type appears as protrusions, i.e. bright lines, about 0.02-0.05 nm high and separated by 3.3 nm (**Fig. 8(d)**). Between these protrusions, depressions are usually visible. Ripples separated by other distances, such as 1.8, 2.3, and 2.6 nm, can also be found, but they are uncommon. The ripples develop as a function of increasing film height or level. The depressions appear in the first level, but the 3.3-nm protrusions appear only in upper levels. Ripples are aligned across island steps, as is obvious in **Fig. 8(d)-(e)**.

Our DFT analysis of ideal Ag(110) film structures in Sec. III.B used a (1x1) lateral unit cell, thus enforcing lateral periodicity and excluding rippling. However, we have also performed a less restrictive DFT analysis which indicates that depressions in the first level could be due to a slight spontaneous rippling in the fcc(110) bilayer structure, i.e., rippling is

not incompatible with and might reasonably be expected for perturbed Ag(110) bilayer structures. These additional DFT calculations were performed using (n x 1) supercells, placing 2n Ag atoms (to represent the first level islands) on top of a slab of 6 layers of NiAl(110) substrate. The first 5 layers of the substrate were allowed to relax.

For n = 2 (with a period 0.82 nm), a rippled structure with an amplitude of 0.009 nm is found. This structure is energetically more favorable than the unrippled one by 2 meV per unit cell. With n = 3 and therefore a period of 1.23 nm, a rippling consisting of 2 rows of high Ag separated by one row of lower Ag atoms is found. The amplitude is again about 0.009 nm. The structure is favored by about 0.9 meV per unit cell, over the flat structure. See **Fig. 9** for side views for n=2 and n=3. With n = 4, aside from a period 0.82 nm rippled structure (trivially obtained from two of the above-mentioned n=2 structures), another (metastable) structure with 1.64 nm periodicity and even larger ripples can be found. However, it is less favored than the flat structure. For the n=2 and n=3 structures, the periods of the ripples are in good agreement with those observed experimentally, and the amplitude of the rippling agrees to within a factor of 2. One cannot give a simple unambiguous identification of the dominant driving force for rippling, but one might note that while the lateral mismatch between the substrate and Ag(110) film is small, there is significant strain inherent in the different crystal structures of the two materials (bcc-like vs. fcc).

Of course, one should not expect DFT to reliably predict such small energy differences between the unrippled and rippled structures. However, the calculations do show that it is plausible for rippled structures to have slightly lower energies. Note that the effect on determining film structure of this small energy difference per unit cell is cumulative: for Ag films with long islands or rows of atoms, the energy difference between an unrippled and

rippled structure per row is the energy difference per atom, times the length of the row. Furthermore, since the topological difference between the flat and rippled structures is very small, one can argue that there is very little (if any) energy barrier for the transition between them, so the system will easily find the rippled structure if it is indeed more energetically favorable. The fact that both separations (0.8 and 1.2 nm) are observed in experiment indicates that there is a competition between the two, which may be affected by factors such as defects or growth history.

Since we do not have a detailed model for the structure of the Ag film above the first two bilayers, it is more difficult to characterize the 3.3-nm protrusions that appear on higher terraces. The amplitude of these ripples seems to increase gradually from the second level to the fourth; in the fourth and higher levels, their amplitude is constant at about 0.05 nm. The progression with level height is illustrated in **Fig. 10**, where one of the Ag islands crosses a step edge at the arrow. Different levels are labeled numerically. The 3.3-nm protrusions are clearly more pronounced on the 4-level Ag islands than on the 3-level island, and least of all on the 2-level island. Hence, the development of the 3.3-nm protrusions seems to correlate with the decrease in step height (and transition from bilayer to monolayer growth) shown in **Fig. 4** and **Table I**. That is to say, in levels 2 to 4, the step height decreases and the protrusions develop in parallel. At and above level 4, both features are constant.

D. Other structures of the Ag film

We should emphasize that for initial Ag film growth on NiAl(110), our DFT calculations indicate that there is <u>not</u> a strong energetic driving force preferring the Ag(110) structure over all other structures. Indeed, there are a variety of monolayer structures

composed of local hexagonal, i.e., Ag(111)-like, and square, i.e., Ag(100)-like, motifs for which we find that DFT actually predicts a lower energy per atom than the Ag(110) structure (although the energy difference is only ~0.02 eV/atom). However, these structures do not match the experimentally measured island or step heights. Assuming that these structures do actually have lower energy than Ag(110)-like films (which is unclear given the uncertainty in DFT predictions), one must conclude that their formation is kinetically hindered relative to that of Ag(110) films. In this regard, we have found that the lowest energy position for a single Ag atom adjacent to a complete row of Ag atoms on the substrate is at the bridge site between two Ni atoms in the Ag(110) position, rather than in a closer three-fold hollow position compatible with alternative denser structures. Thus, it is plausible that nucleation and growth the Ag(100) structure is favored, and conversion to another structure is inhibited.

We have also performed additional DFT analysis to explore specific aspects of the stability of Ag(110) bilayer islands. We describe two such analyses here:

(i) We have analyzed the single bilayer Ag(110) structure with even larger (nx1) lateral unit cells than described in Sec. 3.3. These calculations have revealed that for $n \geq 4$, it is energetically favorable for the bilayer structure to convert to a structure with a higher density of atoms in the first layer than the second layer. However, transition to such a structure from a perfect or slightly rippled (with lateral period 0.82 or 1.23 nm) bilayer (110) structure is generally activated, perhaps providing a rationale for why these structures are not realized, according to our proposed model, for the initial stages of film growth.

(ii) We have also performed a DFT analysis to explore the structure of Ag(110) bilayer islands of finite width. Here, we found a tendency for atoms in the first layer in a narrow island to contract laterally. This contraction provides the driving force for the above-

mentioned rippled structures, and potentially for Ag(111)-like domain walls between Ag(110) regions.

Next, we consider the structure of thick films. As indicated above, our STM studies for prolonged growth reveal that ultimately, thick Ag films on NiAl(110) appear to develop an Ag(111)-like structure. For a 40-layer film grown at 300 K, we find that islands are more isotropic compared with the highly elongated islands observed for thin films. The island edges are also faceted, with facets frequently displaying the 120^{o} angles expected for an Ag(111)-like hexagonal structure. These features are shown clearly in **Fig. 11**.

Perhaps the most complicated aspect of growth is the transition from initial Ag(110) bilayer growth to the ultimate Ag(111)-like monolayer growth. If the initial growth did have an ideal Ag(110) structure, then it would be more difficult to rationalize the transition away from this structure given the lack of lateral mismatch in this system. However, we have shown in Sec. III.C that the film never has an ideal Ag(110) structure, displaying rippling even in the lowest levels. This initial rippling feature and perhaps the effect of substrate defects (such as deviations from stoichiometric surface composition, buried dislocations, and steps) could all produce perturbations from the ideal Ag(110) structure that might grow with film thickness. This could naturally lead to a reduction with increasing film height of the barrier to development of non-Ag(110) structures, and thus ultimately lead to the formation of the Ag(111)-like structure.

IV. Summary and Discussion

The main outcome of the present investigation is the finding that Ag films grow in an Ag(110) bilayer mode on NiAl(110), at least in the first two levels. The tendency for bilayer

growth of these films is promoted by a QSE. The QSE, in turn, reflects a barrier to electron propagation at both the Ag-vacuum and Ag-NiAl interfaces.

Formation of bilayer islands on the nanometer scale has been observed in some other metal on metal film growth systems in the initial submonolayer stages of deposition. These systems include Ag/Fe(100),[55, 56], Co/Cu(111),[57, 58] Au/Ag(110),[59] and Fe/Cu_3Au(001).[60] Several mechanisms have been suggested to drive such bilayer growth including magnetostriction effects, a combination of strain and exchange processes, and QSE. A surfactant can also force bilayer growth.[61] Sometimes there is a barrier to formation of bilayer islands which restricts their nucleation to steps, or near to steps, on the surface.[56, 58] One could easily conclude that to be the case here as well if only data at 300 K were available, but the 200 K data prove that is not true, in the Ag/NiAl(110) system. Instead, preferential nucleation at steps at 300 K here is due to heteroepitaxial step flow, i.e. preferential Ag atom capture at existing steps due to rapid diffusion across terraces on the time scale of deposition.

Many other systems have been reported to exhibit QSEs.[62, 63] Usually, the film is a low-melting metal or semimetal, the most common ones being Ag, Cu, Pb, and Bi. Substrates are semiconductors (Si, GaAs) and higher-melting elemental metals (Ni, Fe, Co, V). Additionally, quasicrystals (a type of intermetallic) can support QSEs.[64] Usually these substrates have a gap or a pseudogap that serves to confine valence electrons within the film. In the present case, the existence of a barrier at the Ag-NiAl interface can be rationalized similarly in terms of the small reduction in the electron density of states at the Fermi edge in NiAl(110).[6] Note also that in the electronic growth model, the period of oscillation depends

on the Fermi surface; the 2-layer period observed here is a feature specific to the details of the Ag/NiAl(110) system.

Finally, we reiterate the particularly appealing feature of the Ag/NiAl(110) system which both motivated and facilitated this study: the almost perfect lateral match between the NiAl(110) substrate and Ag(110) film. As noted above, this allows analysis of heteroepitaxial growth in the absence of a strong lateral mismatch strain. However, it also leads to the formation of an interface between substrate and film with a simple and natural structure amenable to detailed high-level theoretical analysis of the supported films (which is not possible for some more complex metal-on-semiconductor or metal-on-quasicrystal systems).

Acknowledgments

This work was supported primarily by NSF Grant CHE-0414378. DJL was supported by the Division of Chemical Sciences, Basic Energy Sciences, US Department of Energy (USDOE). The work was performed at the Ames Laboratory which is operated for the USDOE by Iowa State University under Contract No. DE-AC02-07CH11358.

APPENDIX: BINDING SITES AND DIFFUSION BARRIERS FOR ISOLATED AG ADATOMS ON NIAL(110)

We have performed a fairly comprehensive DFT evaluation of the potential energy surface for the adsorption or binding energy (as a function of lateral position) of an isolated Ag adatom on NiAl(110). This analysis shows that the most favorable adsorption site is at the bridge site between two nearest-neighbor Ni atoms, as shown in **Fig. 1(c)**. In these calculations, the adsorption energy is defined as $E_a = E_{tot} - E_{slab}$, where E_{tot} is the total energy of the slab plus the adatom, and E_{slab} is the total energy of the slab without the adatom. In calculating E_a, we use a 2×3 supercell with 4×4×1 k mesh. The result is E_a = –2.72 eV for this Ni bridge site. The next-most-favorable site is the quasi-threefold site that lies slightly off-center from the Al-bridge site, defined by a triangle of Al-Al-Ni, where E_a = -2.52 eV. The determination of the Ni-bridge as the favored site for Ag adsorption agrees with the experimental result of Wallis et al., derived from atomically-resolved STM.[65] Our DFT analysis also indicates that the barrier for diffusion of Ag between the Ni bridge sites is about 0.27 eV (either in the direction parallel or perpendicular to the Ni rows shown in Fig.1(a)).

It is not immediately clear why the Ni-bridge site should be favored over the Al-bridge site. For fcc(100) surfaces of pure Al and Ni, our DFT calculations show that the adsorption energies of Ag adatoms at fourfold hollow sites are essentially identical, i.e. -2.80 eV on Al vs. -2.78 eV on Ni. For the (111) faces, Ag actually prefers Al, the binding energy at threefold hollow sites being -2.32 eV on Al vs. -2.12 eV on Ni. These calculations use the true physical lattice constants for the Ni and Al surfaces. However, if we use a single bulk lattice constant (the average of the two, 0.378 nm) to make a comparison that is more

relevant to the bimetallic alloy, then on the fcc(100) faces, the binding preference is reversed: the binding energy is 0.31 eV lower (more negative) on Ni than on Al. If this difference is prorated according to the number of metal atoms at the adsorption site, then on NiAl(110), one expects Ag to prefer the Ni-bridge site by about 0.15 eV, close to the value calculated of 0.20 eV. We therefore suggest that the site preference is very sensitive to the Ni-Ni (or Al-Al) separation at the alloy surface.

Finally, we briefly remark on the extension of these DFT analyses to Ag adatom pair interactions. Not surprisingly, one finds a much stronger attractive interaction between Ag on neighboring Ni bridge sites aligned with the Ni rows rather than orthogonal to these rows. This explains the tendency for islands to be strongly elongated in the direction of the Ni rows, analogous to the elongation of Ag islands on Ag(110) in the direction of the rows of Ag in the top surface layer.

References

[1] J. W. Evans, P. A. Thiel, and M. C. Bartelt, *Surf. Sci. Rep.* **61**, 1 (2006).

[2] H. Brune, *Surf. Sci. Rep.* **31**, 121 (1998).

[3] R. Q. Hwang and M. Bartelt, *Chem. Rev.* **97**, 1053 (1997).

[4] V. K. Sikka, S. C. Devvi, S. Viswanathan, R. W. Swindeman, and M. L. Santella, *Intermetallics* **8**, 1329 (2000).

[5] J. Libuda and H.-J. Freund, *Surf. Sci. Rep.* **57**, 157 (2005).

[6] S.-C. Lui, M. H. Kang, E. J. Mele, and E. W. Plummer, *Phys. Rev. B* **39**, 13149 (1989).

[7] J. Hong, *Phy. Rev. B* **73**, 092413 (2006).

[8] N. Nilius, T. M. Wallis, and W. Ho, *Science* **297**, 1853 (2002).

[9] N. Nilius, T. M. Wallis, M. Persson, and W. Ho, *Phys. Rev. Lett.* **90**, 196103 (2003).

[10] M. Persson, *Phys. Rev. B* **70**, 205420 (2004).

[11] H. L. Davis and J. R. Noonan, *Phys. Rev. Lett.* **54**, 566 (1985).

[12] S. M. Yalisove and W. R. Graham, *Surf. Sci.* **183**, 556 (1987).

[13] X. Torrelles, F. Wendler, O. Bikondoa, H. Isern, W. Moritz, and G. R. Castro, *Surf. Sci.* **487**, 97 (2001).

[14] M. H. Kang and E. J. Mele, *Phys. Rev. B* **36**, 7371 (1987).

[15] T.-H. Kim, B.-Y. Choi, Y. J. Song, W. G. Park, S.-J. Kahng, and Y. Kuk, *Phys. Rev. B* **67** (2003).

[16] H. Roder, R. Schuster, H. Brune, and K. Kern, *Phys. Rev. Lett.* **71**, 2086 (1993).

[17] C. Deisl, E. Bertel, M. Burgener, G. Meister, and A. Goldmann, *Phys. Rev. B* **72** (2005).

[18] D. B. Danko, M. Kuchowicz, R. Szukiewicz, and J. Kolaczkiewicz, *Surf. Sci.* **600** (2006).

[19] T. Valia and M. Milun, *Surf. Sci* **315**, 81 (1994).

[20] M. Pivetta, F. Patthey, and W.-D. Schneider, *Surf. Sci.* **532-535** (2003).

[21] H. Noro, R. Persaud, and J. A. Venables, *Surf. Sci.* **357-358** (1996).

[22] M. Parschau, D. Schlatterbeck, and K. Christmann, *Surf. Sci.* **376** (1997).

[23] D. Schlatterbeck, M. Parschau, and K. Christmann, *Surf. Sci.* **418** (1998).

[24] T. Ito, K. Umezawa, and S. Nakanishi, *Applied Surface Science* **130-132** (1998).

[25] S. Nakanishi, K. Umezawa, M. Yoshimura, and K. Ueda, *Phys. Rev. B* **62** (2000).

[26] R. Schuster, H. Roder, K. Bromann, H. Brune, and K. Kern, *Phys. Rev. B* **54** (1996).

[27] M. Batzill and B. E. Koel, *Europhys. Lett.* **64** (2003).

[28] G. A. Attard and D. A. King, *Surf. Sci* **222** (1989).

[29] K. L. Man, Y. J. Feng, and M. S. Altman, *Phys. Rev. B* **74**, 085420 (2006).

[30] P. Pervan and M. Milun, *Surf. Sci.* **264** (1992).

[31] R. Fisher, T. Fauster, and W. Steinmann, *Phys. Rev. B* **48** (1993).

[32] V. Fournée, J. Ledieu, T. Cai, and P. A. Thiel, *Phys. Rev. B* **67**, 155401 (2003).

[33] V. Fournée, T. C. Cai, A. R. Ross, T. A. Lograsso, J. W. Evans, and P. A. Thiel, *Phys. Rev. B* **67**, 033406 (2003).

[34] V. Fournee, A. R. Ross, T. A. Lograsso, J. W. Evans, and P. A. Thiel, *Surf. Sci.* **537**, 5 (2003).

[35] S. S. Lim, P. L. Rossiter, and J. E. Tibballs, *Calphad* **19**, 131 (1995).

[36] L. Hammer, H. Graupner, V. Blum, K. Heinz, G. W. Ownby, and D. M. Zehner, *Surf. Sci* **412/413**, 69 (1998).

[37] Landolt-Börnstein, *Phase Equilibria, Crystallographic and Thermodynamic Data of Binary Alloys* (Springer, Berliin, 1991).

[38] E. Bauer, H. Poppa, G. Todd, and P. R. Davis, *J. Appl. Phys.* **48**, 3773 (1977).

[39] K. Reichelt and H. O. Lutz, *J. Cryst. Growth* **10**, 103 (1971).

[40] V. Y. Aristov, M. Bertolo, K. Jacobi, F. Maca, and M. Scheffler, *Phys. Rev. B* **48**, 5555 (1993).

[41] G. Neuhold, L. Bartels, J. J. Paggel, and K. Horn, *Surf. Sci.* **376**, 1 (1997).

[42] K.-J. Chao, Z. Zhang, P. Ebert, and C. K. Shih, *Phys. Rev. B* **60**, 4988 (1999).

[43] Single crystals synthesisized at the Materials Preparation Center. See: www.mpc.ameslab.gov.

[44] I. Horcas, R. Fernandez, J. M. Gomez-Rodriguez, J. Colchero, J. Gomez-Herrero, and A. M. Baro, *Rev. Sci. Instr.* **78**, 013705 (2007).

[45] J. P. Perdew, K. Burke, and M. Ernzerhof, *Phys. Rev. Lett.* **77**, 3865 (1996).

[46] W. Kohn and L. J. Sham, *Phys. Rev. A* **140**, 1133 (1965).

[47] G. Kresse and J. Hafner, *Phys. Rev. B* **47**, 558 (1993).

[48] G. Kresse and J. Joubert, *Phys. Rev. B* **59**, 1758 (1999).

[49] *Note: The location of any layer is potentially complicated by rumpling. The experimental studies (Refs. 11-13) do not detect rumpling in the second NiAl layer, only the first. The interlayer spacing is usually taken from experiment as the distance between the second layer and the plane containing the topmost Al atoms. In DFT, we find a rumpling in the second layer of 0.003 nm, which would probably be undetectable by experiment, and which has a very small effect on the interplanar*

spacing. In DFT, we take the first interplanar spacing as the separation between adjacent planes of Al atoms (2007).

[50] V. M. Kuznetsov, R. I. Kadyrov, and G. E. Rudenskii, *J. Mater. Sci. Technol.* **14**, 320 (1998).

[51] L. Vitos, A. V. Ruban, H. L. Skriver, and J. Kollár, *Surf. Sci.* **411**, 186 (1998).

[52] M. J. Mehl and D. A. Papaconstantopoulos, *Phys. Rev. B* **54**, 4519 (1996).

[53] P. Bedrossian, B. Poelsema, G. Rosenfeld, L. C. Jorritsma, N. N. Lipkin, and G. Comsa, *Surf. Sci.* **334**, 1 (1995).

[54] F. K. Schulte, *Surf. Sci.* **55**, 427 (1976).

[55] D.-A. Luh, T. Miller, J. J. Paggel, M. Y. Chou, and T.-C. Chiang, *Science* **292**, 1131 (2001).

[56] K. L. Man, Z. Q. Qiu, and M. S. Altman, *Phys. Rev. Lett.* **93**, 236104 (2004).

[57] J. Ferrón, L. Gómez, J. J. de Miguel, and R. Miranda, *Phys. Rev. Lett.* **93**, 166107 (2004).

[58] H. W. Chang, F. T. Yuan, Y. D. Yao, W. Y. Cheng, W. B. Su, C. S. Cheng, C. W. Lee, and W. C. Cheng, *J. Appl. Phys.* **100**, 084304 (2006).

[59] P. Fenter and T. Gustafsson, *Phys. Rev. B* **43**, 12195 (1991).

[60] A. Verdini, L. Floreano, F. Bruno, D. Cvetko, A. Morgante, F. Bisio, S. Terreni, and M. Canepa, *Phys. Rev. B* **65**, 233403 (2002).

[61] C. Deisl, K. Swamy, E. Bertel, G. Meister, and A. Goldmann, *Surf. Sci* **600**, 2900 (2006).

[62] M. Milun, P. Pervan, and D. P. Woodruff, *Rep. Prog. Phys.* **65**, 99 (2002).

[63] M. C. Tringides, M. Jalochowski, and E. Bauer, *Phys. Today* **April 2007**, 50 (2007).

[64] V. Fournée, H. R. Sharma, M. Shimoda, A. P. Tsai, B. Unal, A. R. Ross, T. A. Lograsso, and P. A. Thiel, *Phys. Rev. Lett.* **95**, 155504 (2005).

[65] T. M. Wallis, N. Nilius, and W. Ho, *J. Chem. Phys.* **119**, 2296 (2003).

Table and Figure Captions.

Table I. Heights of majority islands, in nm, in different levels. (Examples of minority, or "anomalous" islands are given in Fig. 6 and described in the text.) When two numbers are given for a single island level from STM data, the top entry is for deposition at 200 K and the bottom for 300 K. Data are provided for both height histogram and line profile analysis. For the line profiles, each entry is based upon at least six profiles. In the DFT calculations, the first-level step heights are derived from the difference between the height of the ion cores of the top Ag atoms, and the average height of the ion cores of the Ni and Al atoms in the top substrate layer.

Figure 1. (Color online) Depictions of idealized surface structures, using coordinates output from DFT calculations. (a) Clean NiAl(110). (b) Clean Ag(110). (c) NiAl(110) with a monolayer of Ag. Ag adopts the Ni-bridge sites, as discussed in the Appendix. (d) NiAl(110) with two layers of Ag(110).

Figure 2. STM data for Ag deposited on NiAl(110) at 200 K, as a function of coverage (measured in units of Ag(110) bilayers) shown above the STM images. The top row (a-d) shows STM images of size 100 nm x 100 nm. The middle row (e-h) shows pixel height histograms from a small areas of the surface corresponding to a single terrace of the substrate (and not necessarily from within the image in the top row). Peaks in the histograms are labeled with the island level. The average level is not exactly equal to the total coverage given the transition from bilayer to monolayer growth. The average level height from the histogram also depends strongly on the small area sampled, but not the step heights. The bottom row (i-l) shows representative step profiles for the levels indicated.

Figure 3. STM data for Ag deposited on NiAl(110) at 300 K, with increasing coverage (measured in units of Ag(110) bilayers) shown above the STM images. Top row (a-d) shows STM images of size 100 nm x 100 nm, middle row (e-h) shows pixel height histograms (not necessarily from the image in the top row), and bottom row (i-l) shows representative step profiles for the levels indicated. Peaks in the histograms are labeled with the island level.

Figure 4. Experimental step heights, from pixel height histograms in STM images. Circles and diamonds show step heights at 200 K and 300 K, respectively, as a function of Ag island level (lower abscissa). Each pair of data points is slightly offset from the exact value of the island level (i.e. offset horizontally), to avoid overlap. Actual values are given in Table I. The horizontal dashed lines show ideal step heights based on interplanar spacings in bulk Ag, for a (110) bilayer (BL) and for various types of monolayers (ML). Triangles show step heights measured as a function of bias voltage (top abscissa) for islands in level 1.

Figure 5. (a) STM image of Ag deposition on Ag(110) at 220 K. The Ag coverage is 0.3 monolayers, image size is 270 nm × 270 nm, scanning current is 0.3 nA, and scanning voltage is +1 V. (b). Histogram of pixel heights from area ***b*** in part (a), encompassing two terrace step edges. (c). Histogram of pixel heights from area ***c*** in part (a), encompassing several islands on a single terrace.

Figure 6.Examples of anomalous islands, indicated by arrows, following deposition of Ag at 200 K. These are atop first level islands. In Fig. 6(a), one of these islands bridges two regions with ‘normal’ step heights, illustrating its likely origin as a Ag(110)

monolayer. In each vertical pair, the top frame is the normal constant current image, and the bottom frame is the differentiated version. Each image is 50 nm x 50 nm.

Figure 7. (a) DFT calculation of α_L as a function of Ag(110) film thickness L. The Ag films are supported by a 5 layer NiAl(110) slab. (b) DFT calculation of adsorption energy E_a as a function of Ag(110) film thickness L. The Ag films are supported by a 4 layer NiAl(110) slab. The dashed line connecting the maxima indicates that the adsorption energy becomes progressively less favorable on higher bilayers.

Figure 8. Examples of ripples in the Ag islands at various levels. The top row shows images in the constant current mode, which makes depressions distinguishable from protrusions. The bottom row shows images that have been differentiated, which makes the ripples more identifiable. Each image is 23 nm x 23 nm. (a) First level, 300 K, depressions with period 1.2 nm. (b) First level, 300 K, depressions with period 0.8 nm. (c) First level, 200 K, depressions with both 0.8 and 1.2 nm periods. (d) Third and fourth levels, 300 K, 3.3 nm protrusions, plus depressions. (e) Fifth and sixth levels, 300 K, mixed periods with dislocations. The dislocations form a vertical column in the image. The white arrows point to two examples.

Figure 9. (Color online) DFT predictions for the rippled structure of an Ag(110) bilayer of periodicity (a) n=2 and (b) n=3. To make the rippling visible, all deviations (of all species, in all directions) from the unrippled bilayer Ag(110) atom positions are magnified by a factor of 10. Open circles are Ag, darkest circles are Ni, and light gray circles are Al.

Figure 10. (Color online) Development of protrusion-ripples in levels 2, 3, and 4 of Ag films. At the arrow, the Ag film crosses a NiAl step and consequently the Ag island level increases from 3 to 4. The image size is 51 nm x 51 nm. (a) constant current image (0.5nA, +1 V). (b) differentiated image.

Figure 11. [(a)-(b)] STM images of a Ag film, about 40 layers thick, on NiAl(110) at 200 K. Several sets of 120^{o} angles are illustrated with the white lines. The images have been differentiated to accentuate the step edges. Each image size is 100 nm x 100 nm.

Table 1

Island Level	STM histograms	STM line profiles	DFT of Ag(110) bilayer films on NiAl(110)
1	0.324 ±0.010	0.334 ± 0.027	0.340
	0.317 ± 0.027	0.324 ± 0.027	
2	0.294 ± 0.008	0.292 ± 0.012	0.290
	0.283 ± 0.005	0.282 ± 0.013	
3	0.265 ± 0.006	0.263 ± 0.017	0.295
	0.267 ± 0.002	0.254 ± 0.017	
4	0.248 ± 0.008	0.248 ± 0.020	0.294
	0.236 ± 0.007	0.242 ± 0.018	
5	0.241 ± 0.015	0.237 ± 0.019	0.293
	0.234 ± 0.009	0.237 ± 0.020	
6	0.239 ± 0.014	0.234 ± 0.018	0.294
	0.213 ± 0.012	0.233 ± 0.024	
7	0.220 ± 0.010	0.225 ± 0.010	0.293
	0.212 ± 0.011	0.225 ± 0.013	
8	0.233 ±0.014	0.224 ± 0.017	0.294
	—	—	
9	0.221 ± 0.009	0.215 ± 0.020	0.292
	—	—	

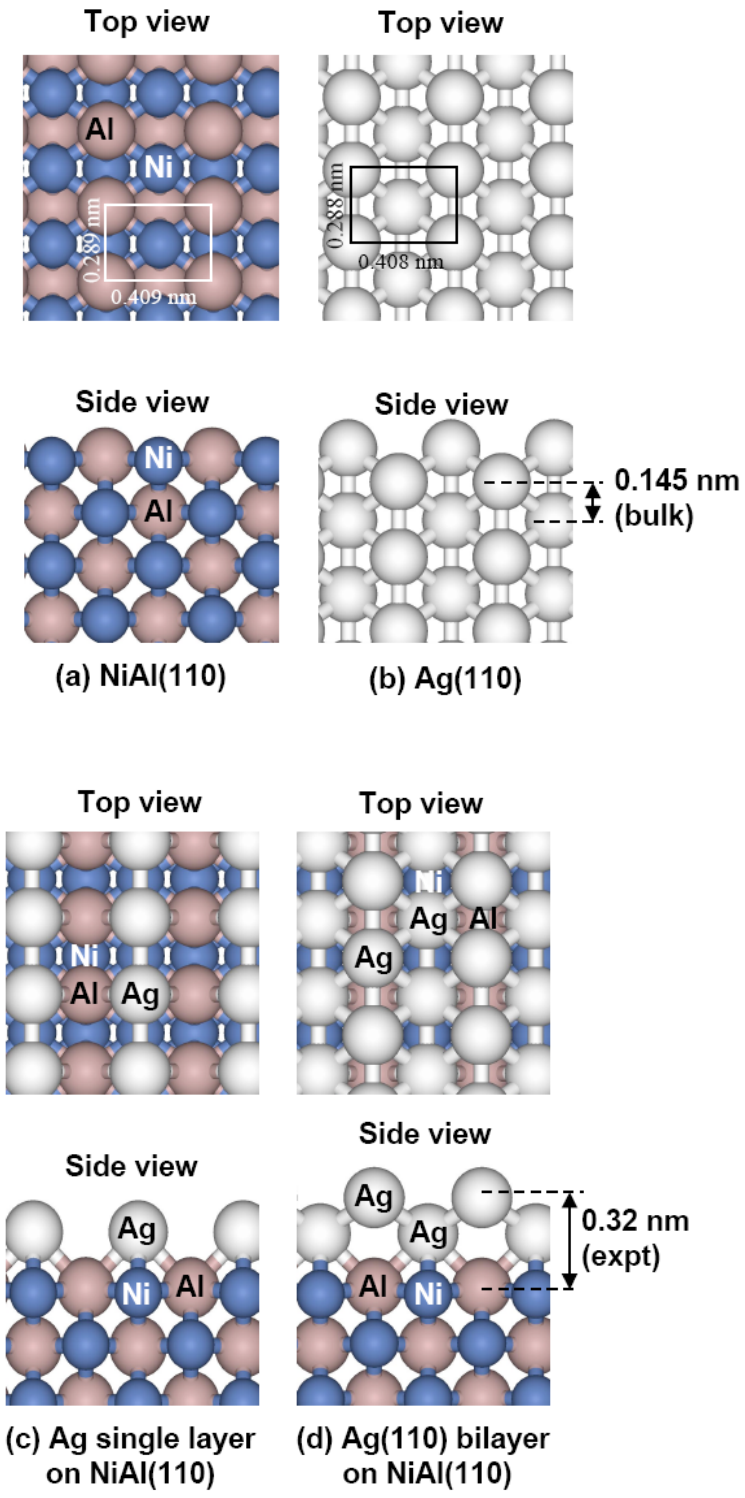
Top view
Top view
Al
Ni
0.289 nm
0.409 nm
0.288 nm
0.408 nm
Side view
Side view
Ni
Al
0.145 nm
(bulk)
(a) NiAl(110)
(b) Ag(110)
Top view
Top view
Ni
Al
Ag
Ni
Ag
Al
Ag
Side view
Side view
Ag
Ni
Al
Ag
Ag
Al
Ni
0.32 nm
(expt)
(c) Ag single layer on NiAl(110)
(d) Ag(110) bilayer on NiAl(110)

Figure 1

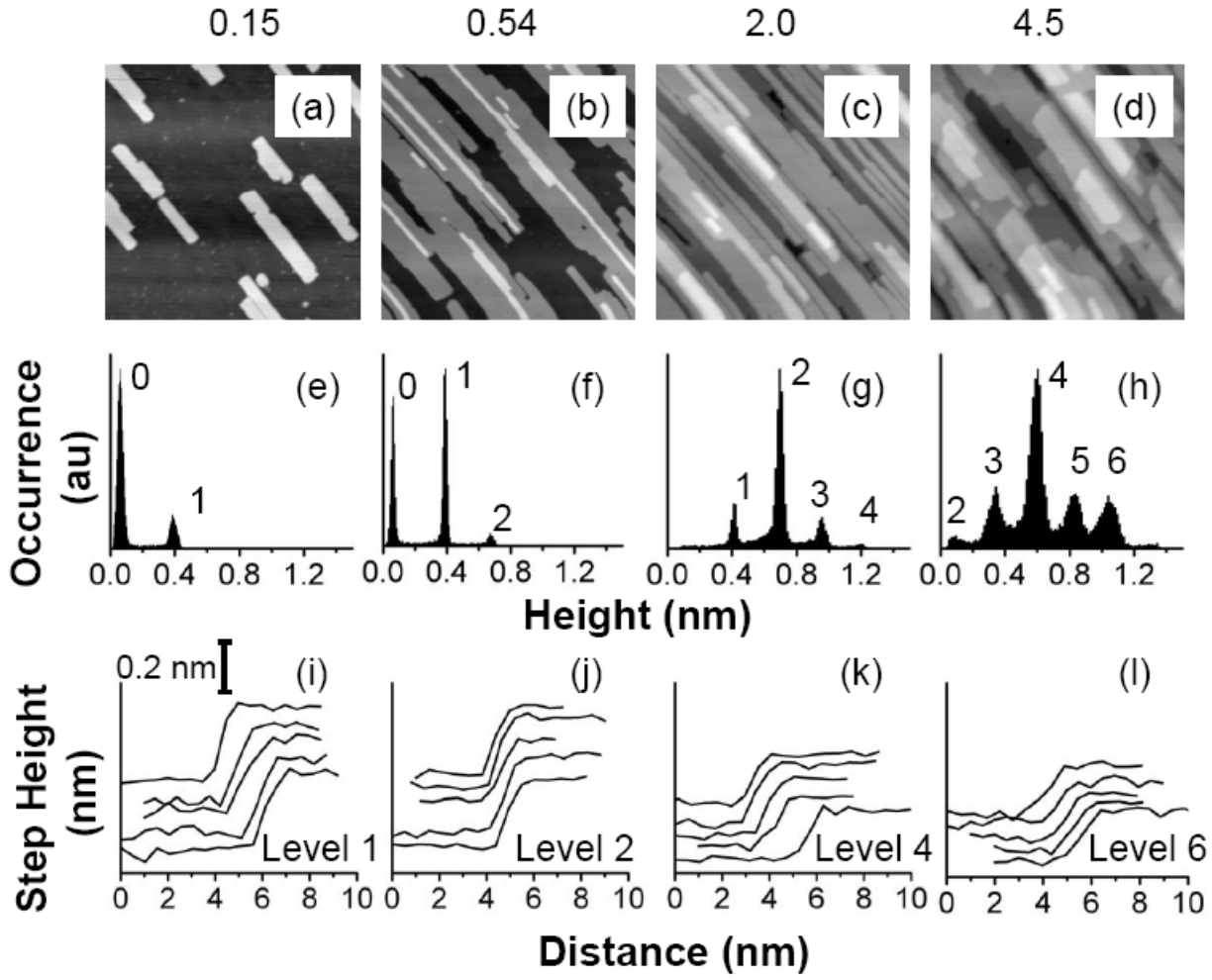
0.15
0.54
2.0
4.5
(a)
(b)
(c)
(d)
Occurrence (au)
(e)
(f)
(g)
(h)
Height (nm)
0.2 nm
(i)
(j)
(k)
(l)
Step Height (nm)
Level 1
Level 2
Level 4
Level 6
Distance (nm)

Figure 2

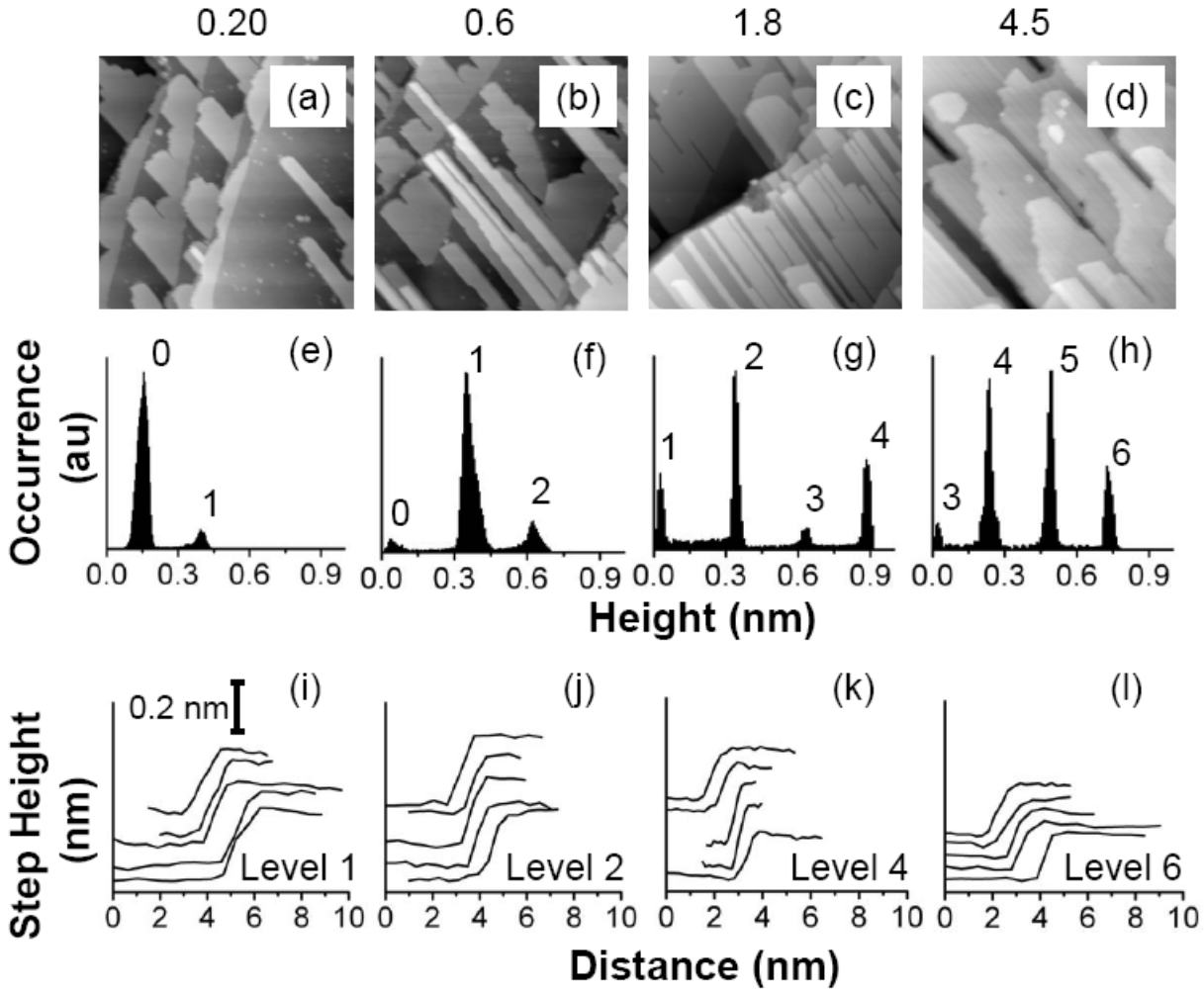
0.20
0.6
1.8
4.5
(a)
(b)
(c)
(d)
Occurrence (au)
(e)
(f)
(g)
(h)
Height (nm)
0.2 nm
(i)
(j)
(k)
(l)
Step Height (nm)
Level 1
Level 2
Level 4
Level 6
Distance (nm)

Figure 3

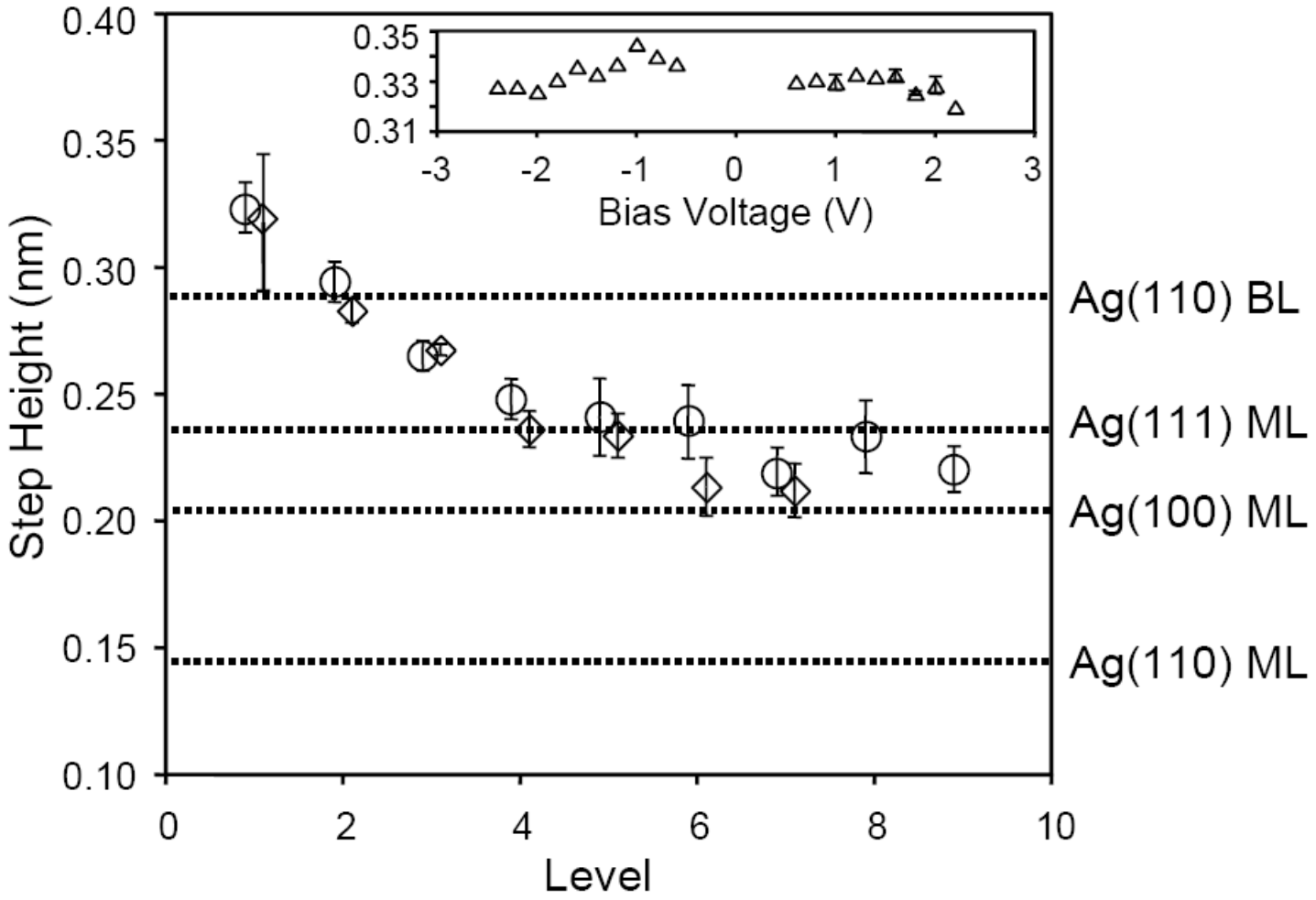
0.40
0.35
0.30
0.25
0.20
0.15
0.10
Step Height (nm)
0
2
4
6
8
10
Level
0.35
0.33
0.31
-3
-2
-1
0
1
2
3
Bias Voltage (V)
Ag(110) BL
Ag(111) ML
Ag(100) ML
Ag(110) ML

Figure 4

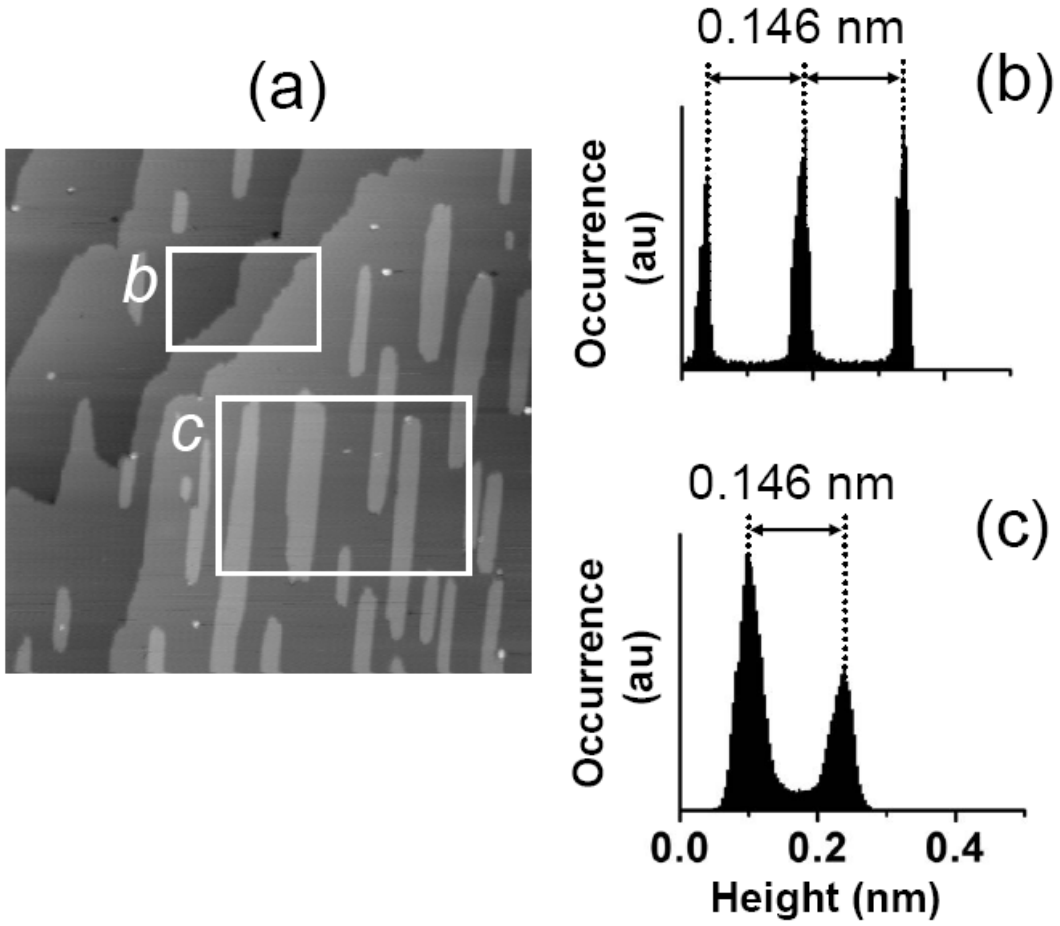
(a)
b
c
0.146 nm
(b)
Occurrence
(au)
0.146 nm
(c)
Occurrence
(au)
0.0
0.2
0.4
Height (nm)

Figure 5

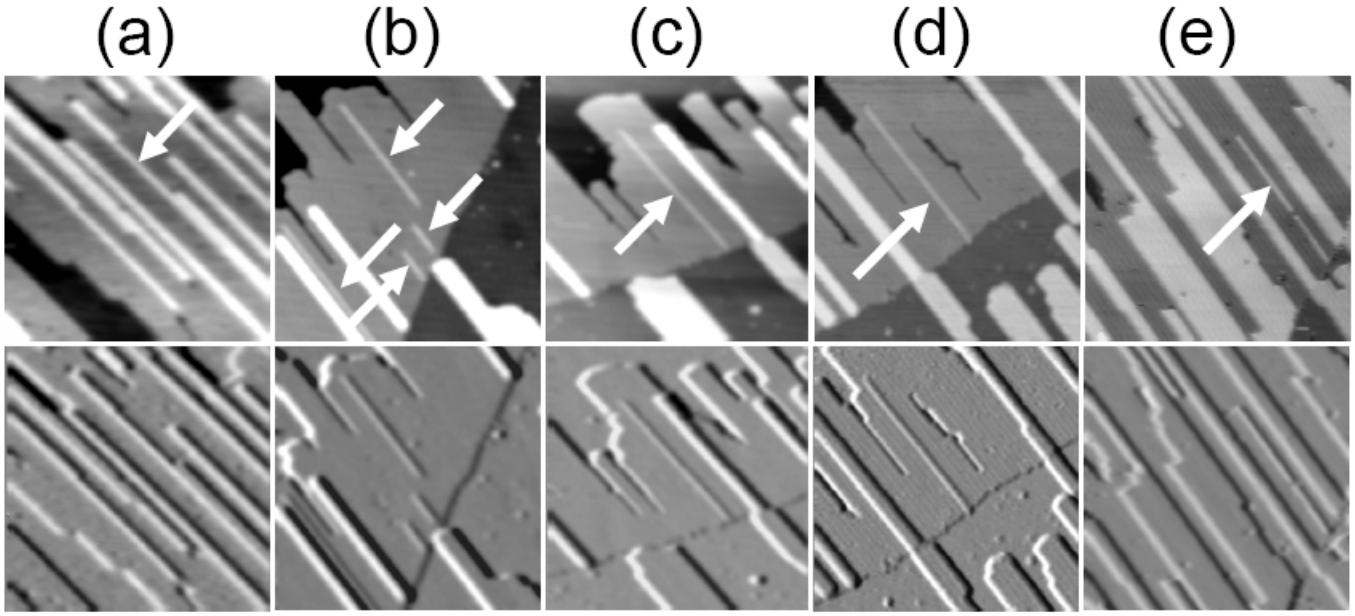

Figure 6

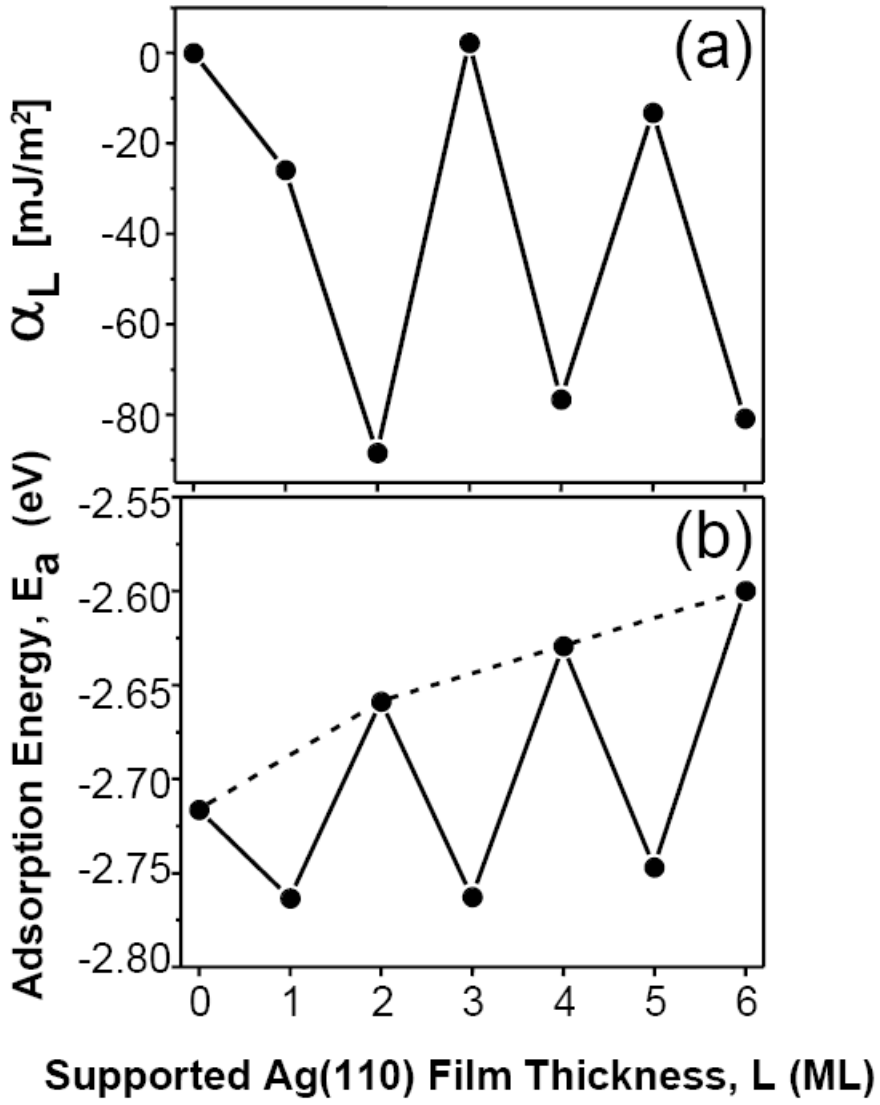
(a)
(b)
α_L [mJ/m^2]
Adsorption Energy, E_a (eV)
0
-20
-40
-60
-80
-2.55
-2.60
-2.65
-2.70
-2.75
-2.80
0
1
2
3
4
5
6
Supported Ag(110) Film Thickness, L (ML)

Figure 7

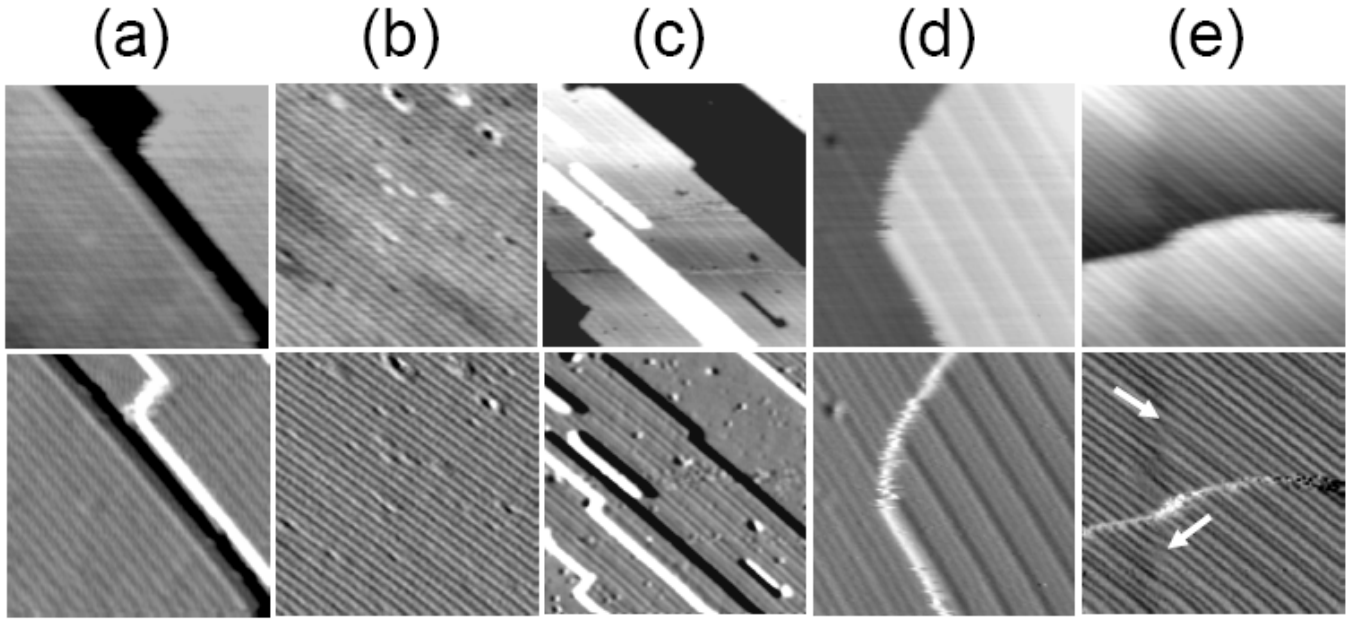

Figure 8

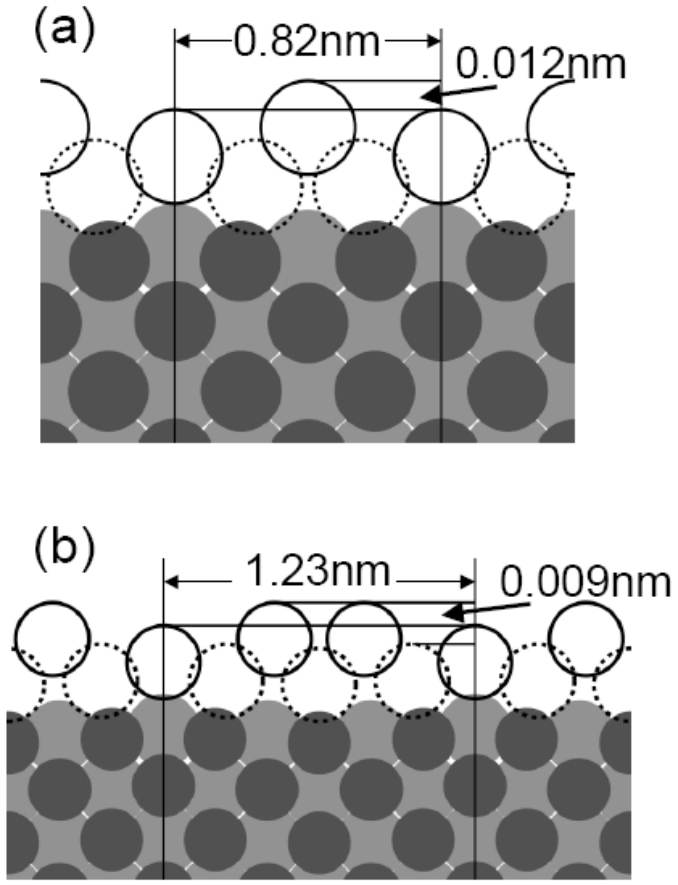

Figure 9

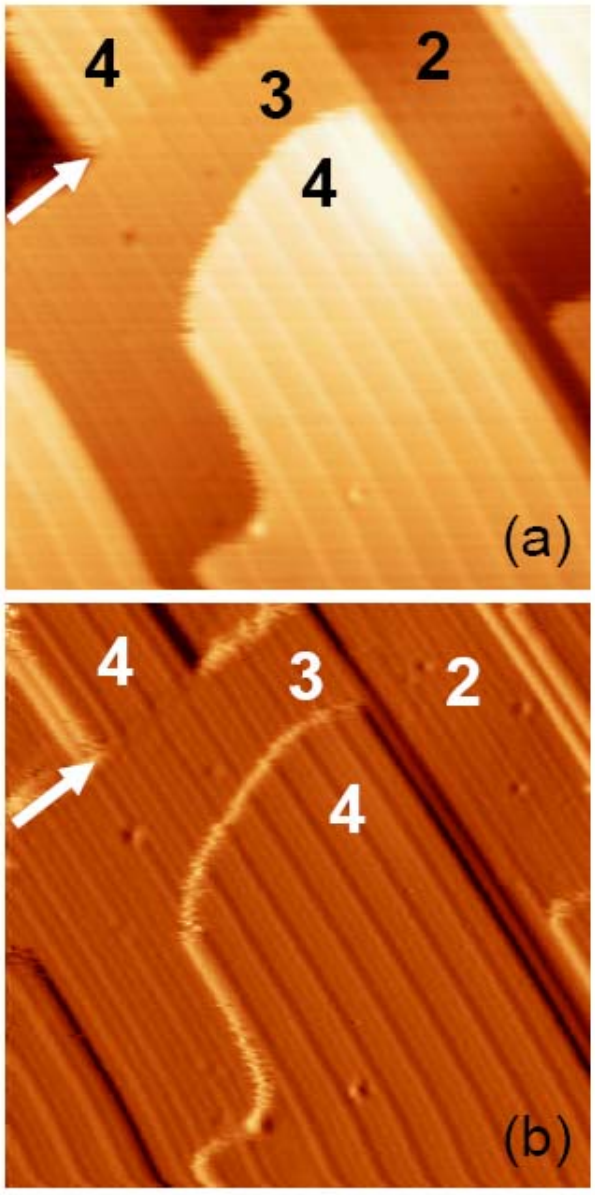

Figure 10

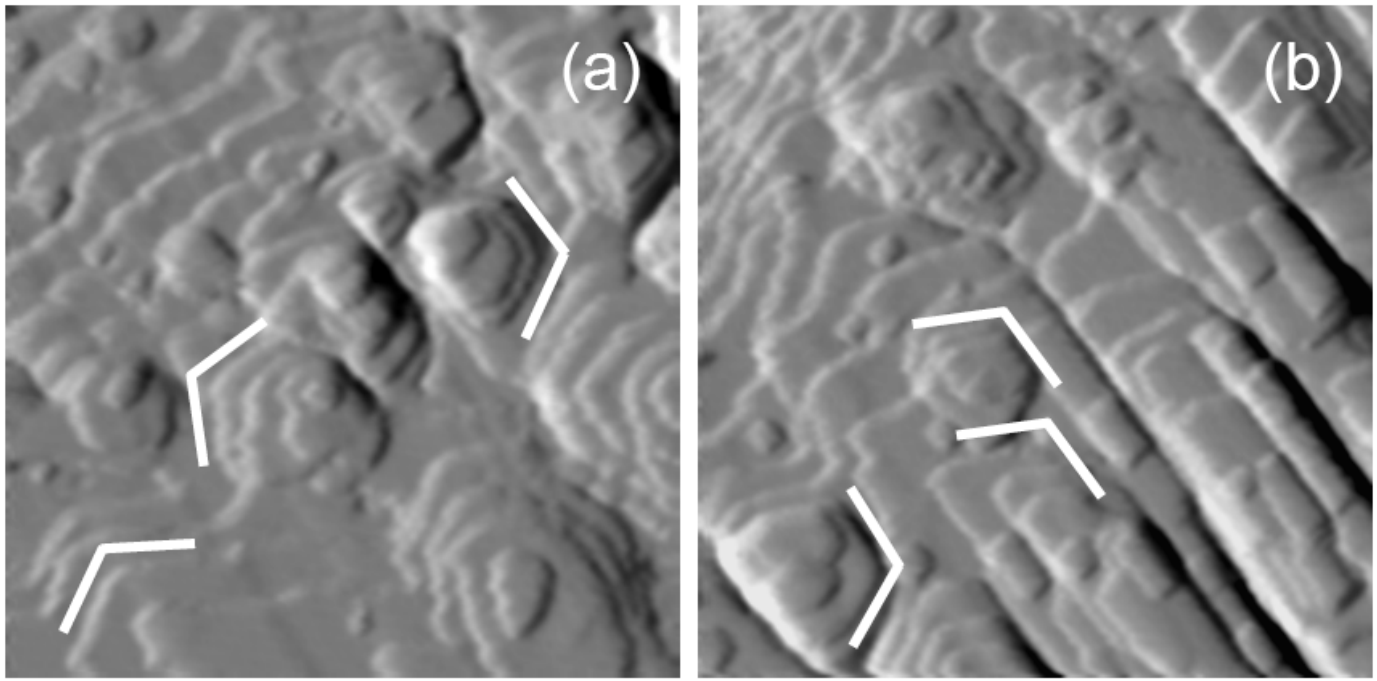

Figure 11

GENERAL CONCLUSIONS

The present work in this dissertation mainly focuses on the clean fivefold surfaces of i-Al-Pd-Mn quasicrystals as well as the nucleation and growth of Ag films on these surfaces. In addition, Ag film growth on NiAl(110) has been explored in the frame of this dissertation. First, we have investigated the equilibration of a fivefold surface of icosahedral Al-Pd-Mn quasicrystal at 900-915 K and 925-950 K, using Omicron variable temperature scanning tunneling microscope (STM). Annealing at low temperatures resulted in many voids on some terraces while the others were almost void-free. After annealing at 925-950K, void-rich terraces became much rarer. Our STM images suggest that through growth and coalescence of the voids, a different termination becomes exposed on host terraces. All of these observations in our study indicate that even after the quasicrystalline terrace-step structure appears, it evolves with time and temperature. More specifically, based on the STM observations, we conclude that during the annealing a wide range of energetically similar layers nucleate as surface terminations, however, with increasing temperature (and time) this distribution gets narrower via elimination of the metastable void-rich terraces.

Next, we have examined the bulk structural models of icosahedral Al-Pd-Mn quasicrystal in terms of the densities, compositions and interplanar spacings for the fivefold planes that might represent physical surface terminations. In our analyses, we mainly have focused on four deterministic models which have no partial or mixed occupancy but we have made some comparisons with an undeterministic model. We have compared the models with each other and also with the available experimental data including STM, LEED-IV, XPD and LEIS. In all deterministic models, there are two different families of layers (a pair of planes),

and the nondeterministic model contains similar group of planes. These two families differ in terms of the chemical decoration of their top planes. Hence, we name them as Pd+(with Pd) and Pd-(without Pd). Based on their planer structure and the step height, it can be said that these two families can be viable surface terminations. However, besides the Pd content, these two sets differ in terms of relative densities of their top planes as well as the gap separating the layer from the nearest atomic plane. The experimental data and other arguments lead to the conclusion that the Pd- family is favored over the Pd+. This has an important implication on the interpretation of local motifs seen in the high resolution STM images. In other words, the dark stars are not formed by cut-Bergmans rather they are formed by cut-Mackays.

Our detailed analysis shows that the dense planes are very similar in all the models with respect to their atomic densities, average chemical composition and positions along the five fold axis. Our analysis also shows that previously identified local motifs such as dark stars, white flowers, rings etc in the Pd+ layers do exist in the Pd- layers of all the available models for i-Al-Pd-Mn quasicrystals. However, the chemical decoration of the local motifs namely, dark stars and white flowers, are model dependent. Therefore, these features may be used to identify which bulk structural model describes real quasicrystal structure best.

Third, we have investigated the nucleation and growth of Ag islands on fivefold surface of i-Al-Pd-Mn quasicrystal. We observed that the island density is constant from 127 K to 300 K but it decreases as temperature increases beyond 300K. To model this behavior, we have developed a mean field rate equation model which takes into account the enhanced nucleation at traps relative to nucleation at regular terrace sites. The best fit to the model suggest that the critical sizes for the nucleation at both sites are large, especially, at traps where 6 Ag atoms from stable clusters, and that binding between Ag atoms at traps is

stronger than at regular terrace sites. In addition, the potential energy surface for single Ag adatom suggests that the dark star sites are the strongest binding sites and hence they are the traps for the Ag adatoms.

We have also studied the growth of Ag films on fivefold i-Al-Pd-Mn surface at 365K. We have observed that at this deposition temperature, most of the Ag segregates into steeped-edge, flat- top, three-layer-high islands. This growth mode (i.e. height selection) signals the quantum size effect (QSE). We have developed and applied a step dynamics formulation to provide, for the first time, a characterization of the development of 3D islands and their height selection for a system exhibiting QSE. From the model, we have concluded that transition from 2D to 3D islands is facilitated by strain build-up as the islands grow, and enhanced step binding in higher layers due to the relaxation of the film to fcc type (the natural structure of Ag). The height selection is driven by QSE which facilitate nucleation of 3^{rd} layer and inhibits the nucleation of 4^{th} layer.

Finally, we have reported our investigation of Ag growth on NiAl(110) surface at 200K and 300K. In this system, we have observed that Ag films grow in a Ag(110) bilayer mode on NiAl(110), at least in the first two layers. Our density functional theory analysis of supported Ag films with ideal fcc(110) structure on NiAl(110) suggests that the bilayer growth Ag films are promoted by QSE effects. On the other hand, even if there is an almost perfect lateral match between the NiAl(110) and Ag(110) lattice constants, the growth of Ag films are not perfect. Indeed, our STM studies have showed that ripple structure exists even on top of the first bilayer islands and also as coverage increases there is a deviation from Ag(110)-like bilayer growth to Ag(111)-like monolayer growth.

APPENDIX A. SUPPLEMENTAL MATERIALS FOR CHAPTER 4.

Baris Unal, C.J. Jenks, and P.A. Thiel

Figure 5. Schematic depiction of atomic planes in the PK model. The z-axis is the 5-fold axis. The spatial coordinate is labeled "(z)" because this is the notation used by the authors of the model.The height of each line is proportional to the planar atomic density. Within each vertical bar, black is Al, green is Pd, and red is Mn. The light rectangle encloses a triplet.

Figure 6. Schematic depiction of atomic planes in the QG model. The x-axis is the 5-fold axis. The spatial coordinate is labeled "(x)" because this is the notation used by the authors of the model. The height of each line is proportional to the planar atomic density. Within each vertical bar, black is Al, green is Pd, and red is Mn. The light rectangle encloses a triplet.

Figure 7. Schematic depiction of atomic planes in the Boudard model. The z-axis is the 5-fold axis. The spatial coordinate is labeled "(z)" because this is the notation used by the authors of the model.The height of each line is proportional to the planar atomic density. Within each vertical bar, black is Al, green is Pd, and red is Mn. The light rectangle encloses a triplet.

Table V. Compositions and densities of individual planes and layers in the Pd- and Pd+ types of terminations in the KG model. In the KG model, a layer is a pair of planes.

Set A in KG Model (Pd– viewed from positive X to negative X or Pd+ viewed from negative X to positive X)				
Location (nm)	Composition (at.%)	Density (Atoms/ nm^2)	Combined Composition (at.%)	Total density of the terminations (Atoms /nm^2)
10.71	Al(100.00)	9.12	Al(81.33), Pd(17.77), Mn(0.90)	14.16
10.66	Al(49.02), Pd(48.53), Mn(2.45)	5.04		
10.30	Al(100.00)	6.74	Al(71.02), Pd(9.91), Mn(19.07)	14.11
10.26	Al(44.86), Pd(18.86), Mn(36.28)	7.37		
9.64	Al(100.00)	8.80	Al(71.32), Pd(26.13), Mn(2.55)	14.10
9.60	Al(23.62), Pd(69.58) , Mn(6.80)	5.29		
9.24	Al(100.00)	4.76	Al(57.29), Pd(24.18), Mn(18.53)	13.63
9.19	Al(35.05), Pd(36.77), Mn(28.18)	8.86		
8.58	Al(100.00)	7.74	Al(68.02), Pd(17.77), Mn(14.21)	14.18
8.53	Al(29.21), Pd(39.33) , Mn(31.46)	6.44		
7.92	Al(100.00)	9.01	Al(76.15), Pd(22.84), Mn(2.01)	14.08
7.87	Al(32.70), Pd(61.62) , Mn(5.68)	5.07		
7.51	Al(100.00)	6.11	Al(64.01), Pd(16.68), Mn(19.31)	14.03
7.46	Al(37.05), Pd(29.18) , Mn(33.77)	7.92		
6.85	Al(100.00)	8.38	Al(75.26), Pd(21.59), Mn(3.15)	13.91
6.80	Al(36.67), Pd(55.26) , Mn(8.07)	5.53		
6.19	Al(100.00)	8.99	Al(83.40), Pd(16.40), Mn(0.20)	13.78
6.14	Al(50.60), Pd(48.80) , Mn(0.60)	4.79		
5.78	Al(100.00)	6.86	Al(70.89), Pd(11.64), Mn(17.47)	14.01
5.73	Al(41.54), Pd(23.38) , Mn(35.08)	7.15		
5.12	Al(100.00)	8.88	Al(72.69), Pd(24.91), Mn(2.40)	14.20
5.07	Al(25.55), Pd(67.91) , Mn(6.54)	5.32		
4.71	Al(100.00)	5.12	Al(58.04), Pd(22.22), Mn(19.74)	13.68
4.66	Al(32.56), Pd(35.71) , Mn(31.73)	8.56		
4.05	Al(100.00)	7.87	Al(73.41), Pd(17.20), Mn(9.39)	14.30
4.00	Al(39.49), Pd(39.13) Mn(21.38)	6.42		

Table VI. Compositions and densities of individual planes and layers in the Pd- and Pd+ types of terminations in the KG model. In the KG model, a layer is a pair of planes.

Set B in KG Model (Pd– viewed from positive X to negative X or Pd+ viewed from negative X to positive X)				
Location (nm)	Composition (at.%)	Density (Atoms/ nm^2)	Combined Composition (at.%)	Total density of the terminations (Atoms /nm^2)
3.80	Al(100.00)	9.12	Al(80.97), Pd(17.77), Mn(1.26)	14.05
3.85	Al(48.04), Pd(48.53), Mn(3.43)	4.93		
4.21	Al(100.00)	6.70	Al(69.67), Pd(10.81), Mn(19.52)	14.11
4.26	Al(42.61), Pd(20.45) Mn(36.94)	7.41		
4.87	Al(100.00)	8.77	Al(71.93), Pd(25.15), Mn(2.92)	14.21
4.92	Al(25.72), Pd(66.56) , Mn(7.72)	5.44		
5.27	Al(100.00)	4.60	Al(56.49), Pd(25.74), Mn(17.77)	13.51
5.32	Al(34.70), Pd(38.63), Mn(26.67)	8.91		
5.93	Al(100.00)	7.60	Al(67.91), Pd(17.51), Mn(14.58)	14.06
5.98	Al(30.79), Pd(37.77) , Mn(31.44)	6.46		
6.60	Al(100.00)	8.82	Al(75.22), Pd(22.68), Mn(2.11)	14.09
6.65	Al(30.56), Pd(63.54) , Mn(5.90)	5.26		
7.00	Al(100.00)	5.94	Al(62.68), Pd(17.72), Mn(19.60)	13.95
7.05	Al(35.82), Pd(30.47) , Mn(33.71)	8.02		
7.66	Al(100.00)	8.26	Al(75.38), Pd(21.46), Mn(3.16)	14.12
7.71	Al(38.07), Pd(53.98) , Mn(7.95)	5.86		
8.32	Al(100.00)	8.99	Al(83.18), Pd(16.62), Mn(0.20)	13.85
8.37	Al(50.44), Pd(48.97) , Mn(0.59)	4.86		
8.73	Al(100.00)	6.72	Al(70.82), Pd(10.90), Mn(18.28)	14.03
8.78	Al(42.65), Pd(21.43) , Mn(35.92)	7.31		
9.39	Al(100.00)	8.82	Al(71.82), Pd(25.43), Mn(2.75)	14.00
9.44	Al(23.84), Pd(68.73),Mn(7.43)	5.18		
9.80	Al(100.00)	5.12	Al(57.92), Pd(23.07), Mn(19.00)	14.08
9.85	Al(33.12), Pd(36.67), Mn(30.21)	8.89		
10.46	Al(100.00)	7.87	Al(71.34), Pd(17.20), Mn(11.47)	14.05
10.51	Al(34.78), Pd(39.13), Mn(26.09)	6.17		

Table VII. Compositions and densities of layers in the Pd- and Pd+ types of terminations in Yamamoto model. In the Yamamoto model, a layer is a group of planes as defined in Sec. VI and Fig. 4.

Set A in Yamamoto Model (Pd– viewed from positive Z to negative Z or Pd+ viewed from negative Z to positive Z)		
Location (nm)	Composition (at.%)	Total density of the terminations (Atoms /nm^2)
4.89–4.81(Al) 4.86–4.80(Pd) 4.86–4.81(Mn)	Al(83.42), Pd(8.89), Mn(7.69)	11.57
4.47–4.38(Al) 4.43–4.39(Pd) 4.45–4.39(Mn)	Al(73.88), Pd(23.37), Mn(2.75)	12.35
3.81–3.69(Al) 3.75–3.73(Pd) 3.79–3.73(Mn)	Al(77.75), Pd(14.48), Mn(7.77)	12.89
3.16–3.08(Al) 3.13–3.08(Pd) 3.13–3.07(Mn)	Al(89.75), Pd(2.69), Mn(7.56)	11.60
2.74–2.65(Al) 2.67–2.66(Pd) 2.72–2.66(Mn)	Al(76.57), Pd(17.68), Mn(5.75)	11.44
2.09–1.97(Al) 2.02–2.00(Pd) 2.06–2.01(Mn)	Al(77.77), Pd(13.81), Mn(8.42)	12.56
1.67–1.58(Al) 1.63–1.60(Pd) 1.66–1.55(Mn)	Al(75.22), Pd(20.91), Mn(3.87)	12.77
1.02–0.93(Al) 0.95–0.93(Pd) 0.99–0.93(Mn)	Al(75.55), Pd(16.76), Mn(7.69)	12.08
0.36–0.28 (Al) 0.33–0.27(Pd) 0.36–0.28 (Mn)	Al(86.34), Pd(5.86), Mn(7.81)	11.98

Table VIII. Compositions and densities of layers in the Pd- and Pd+ types of terminations in Yamamoto model. In the Yamamoto model, a layer is a group of planes as defined in Sec. VI and Fig. 4.

Set B in Yamamoto Model (Pd– viewed from positive Z to negative Z or Pd+ viewed from negative Z to positive Z)		
Location (nm)	Composition (at.%)	Total density of the terminations (Atoms /nm^2)
0.06–0.15(Al) 0.10–0.14(Pd) 0.07–0.14(Mn)	Al(77.40), Pd(20.14), Mn(2.46)	13.54
0.71–0.80(Al) 0.78–0.80(Pd) 0.74–0.80(Mn)	Al(77.61), Pd(13.53), Mn(8.86)	12.71
1.37–1.44(Al) 1.40–1.44(Pd) 1.39–1.45(Mn)	Al(89.51), Pd(3.34), Mn(7.15)	11.99
1.79–1.88(Al) 1.86–1.87(Pd) 1.80–1.87(Mn)	Al(72.56), Pd(21.95), Mn(5.49)	13.02
2.43–2.53(Al) 2.51–2.52(Pd) 2.46–2.51(Mn)	Al(78.07), Pd(13.28), Mn(8.65)	12.52
2.86–2.94(Al) 2.90–2.93(Pd) 2.87–2.93(Mn)	Al(75.80), Pd(20.48), Mn(3.72)	13.08
3.51–3.60(Al) 3.57–3.60(Pd) 3.53–3.59(Mn)	Al(75.96), Pd(16.56), Mn(7.48)	12.62
4.16–4.24(Al) 4.20–4.25(Pd) 4.19–4.25(Mn)	Al(85.63), Pd(6.49), Mn(7.88)	11.94
4.58–4.67 (Al) 4.65–4.66(Pd) 4.60–4.66(Mn)	Al(75.79), Pd(21.09), Mn(3.12)	13.48

Table IX. Compositions and densities of individual planes and layers in the Pd- and Pd+ types of terminations in the PK model. In the PK model, a layer is a pair of planes.

Set A in PK Model (Pd– viewed from positive X to negative X or Pd+ viewed from negative X to positive X)				
Location (nm)	Composition (at.%)	Density (Atoms/ nm^2)	Combined Composition (at.%)	Total density of the terminations (Atoms /nm^2)
4.80	Al(97.35), Mn(2.65)	8.17	Al(70.64), Pd(25.55), Mn(1.81)	13.94
4.75	Al(31.09), Pd(68.35),Mn(0.56)	5.78		
4.14	Al(87.95), Mn(12.05)	8.90	Al(81.51), Pd(10.64), M(7.85)	13.61
4.09	Al(69.48), Pd(30.52)	2.52		
3.73	Al(100)	6.98	Al(69.80), Pd(25.06), Mn(5.15)	14.15
3.68	Al(41.81), Pd(48.28), Mn(9.91)	7.18		
3.07	Al(91.70),Mn(8.30)	8.60	Al(79.84), Pd(15.01), Mn(5.15)	13.92
3.02	Al(60.47), Pd(39.53)	5.32		
2.66	Al(100.00)	4.78	Al(64.72), Pd(25.95), Mn(9.33)	13.58
2.61	Al(46.12), Pd(39.63), Mn(14.25)	8.80		
2.00	Al(99.33), Mn(0.67)	7.71	Al(68.07), Pd(30.08), Mn(1.85)	13.92
1.95	Al(29.24), Pd(67.44),Mn(3.32)	6.21		
1.34	Al(90.95), Mn(0.05)	8.82	Al(81.02), Pd(13.28), Mn(5.70)	13.90
1.29	Al(64.10), Pd(35.90)	5.09		
0.93	Al(100.00)	5.79	Al(70.82), Pd(21.47), Mn(7.71)	13.79
0.88	Al(49.34), Pd(37.27),Mn(13.39)	8.00		
0.27	Al(94.20), Mn(5.80)	8.18	Al(74.13), Pd(22.46), Mn(3.41)	13.85
0.22	Al(45.50), Pd(54.50)	5.67		
-0.39	Al(87.91), Mn(12.09)	8.86	Al(83.06), Pd(9.11), Mn(7.83)	13.69
-0.44	Al(74.15), Pd(25.85)	4.83		
-0.80	Al(100.00)	6.87	Al(70.85), Pd(25.31), Mn(3.84)	13.90
-0.85	Al(42.08), Pd(50.29),Mn(7.63)	7.03		

Table IX. Continued…Compositions and densities of individual planes and layers in the Pd- and Pd+ types of terminations in the PK model. In the PK model, a layer is a pair of planes.

Set A in PK Model (Pd– viewed from positive X to negative X or Pd+ viewed from negative X to positive X)				
Location (nm)	Composition (at.%)	Density (Atoms/ nm^2)	Combined Composition (at.%)	Total density of the terminations (Atoms /nm^2)
-1.46	Al(90.69), Mn(9.31)	8.64	Al(88.85), Pd(13.31), Mn(5.83)	14.04
-1.50	Al(64.33), Pd(35.67)	5.40		
-1.86	Al(100.00)	4.98	Al(66.21), Pd(24.53), Mn(9.26)	13.58
-1.91	Al(46.64), Pd(38.73), Mn(14.63)	8.60		
-2.52	Al(97.83), Mn(2.17)	7.76	Al(68.98), Pd(29.43), Mn(1.59)	13.80
-2.57	Al(32.59), Pd(66.55),Mn(0.86)	6.04		
-3.18	Al(90.43), Mn(9.57)	8.85	Al(81.45), Pd(12.39), Mn(6.16)	13.81
-3.23	Al(65.28), Pd(34.72)	4.96		
-3.59	Al(100.00)	6.50	Al(72.30), Pd(21.71), Mn(5.98)	13.88
-3.64	Al(48.84), Pd(40.11), Mn(11.05)	7.48		
-4.25	Al(91.71), Mn(8.29)	8.46	Al(78.59), Pd(16.37), Mn(5.04)	13.92
-4.30	Al(58.30), Pd(41.70)	5.47		

Table X. Compositions and densities of individual planes and layers in the Pd- and Pd+ types of terminations in the PK model. In the PK model, a layer is a pair of planes.

Set B in PK Model (Pd– viewed from positive X to negative X or Pd+ viewed from negative X to positive X)				
Location (nm)	Composition (at.%)	Density (Atoms/ nm^2)	Combined Composition (at.%)	Total density of the terminations (Atoms /nm^2)
-4.50	Al(90.59), Mn(9.41)	8.77	Al(81.72), Pd(12.31), Mn(5.97)	14.07
-4.46	Al(66.33), Pd(33.67)	5.30		
-4.10	Al(100.00)	4.83	Al(67.62), Pd(23.40), Mn(8.98)	13.61
-4.05	Al(49.65), Pd(36.38), Mn(13.97)	8.79		
-3.44	Al(98.67), Mn(1.33)	8.01	Al(67.65), Pd(31.13), Mn(1.21)	13.81
-3.39	Al(26.11), Pd(72.82), Mn(1.07)	5.81		
-2.78	Al(89.64),Mn(10.36)	8.96	Al(81.23), Pd(12.04), Mn(6.73)	13.73
-2.73	Al(65.60), Pd(34.40)	4.77		
-2.37	Al(100.00)	6.43	Al(70.35), Pd(23.91), Mn(5.74)	14.02
-2.32	Al(45.24), Pd(44.16), Mn(10.60)	7.59		
-1.71	Al(92.91), Mn(7.09)	8.49	Al(77.79), Pd(17.86), Mn(4.35)	13.88
-1.66	Al(53.73), Pd(46.27)	5.39		
-1.05	Al(82.88), Mn(17.12)	8.83	Al(84.55), Pd(4.16), Mn(11.29)	13.31
-1.00	Al(87.79), Pd(12.21)	4.48		
-0.64	Al(99.87), Mn(0.13)	7.67	Al(68.60), Pd(28.99), Mn(2.41)	13.87
-0.59	Al(28.77), Pd(65.92),Mn(5.31)	6.20		
0.02	Al(90.78), Mn(9.22)	8.95	Al(81.05), Pd(13.03), Mn(5.92)	13.93
0.07	Al(63.56), Pd(36.44)	4.98		
0.43	Al(100.00)	5.62	Al(68.80), Pd(23.66), Mn(7.54)	13.95
0.48	Al(48.70), Pd(38.91), Mn(12.39)	8.32		
1.09	Al(96.00),Mn(4.00)	8.24	Al(72.54), Pd(25.07), Mn(2.39)	13.80
1.14	Al(38.17), Pd(61.83)	5.56		

Table X. Continued…Compositions and densities of individual planes and layers in the Pd- and Pd+ types of terminations in the PK model. In the PK model, a layer is a pair of planes.

Set B in PK Model (Pd– viewed from positive X to negative X or Pd+ viewed from negative X to positive X)				
Location (nm)	Composition (at.%)	Density (Atoms/ nm^2)	Combined Composition (at.%)	Total density of the terminations (Atoms /nm^2)
1.75	Al(88.54),Mn(11.46)	8.91	Al(82.94), Pd(9.52), Mn(7.54)	13.77
1.80	Al(72.16), Pd(27.84)	4.86		
2.16	Al(100.00)	6.74	Al(70.52), Pd(24.69), Mn(4.79)	13.92
2.20	Al(42.53), Pd(48.13), Mn(9.34)	7.18		
2.82	Al(91.53), Mn(8.47)	8.43	Al(79.62), Pd(15.25), Mn(5.13)	13.82
2.86	Al(61.30), Pd(38.70)	5.38		
3.22	Al(100.00)	4.67	Al(64.56), Pd(26.17), Mn(9.27)	13.40
3.27	Al(45.25), Pd(40.43), Mn(14.32)	8.73		
3.88	Al(99.19), Mn(0.81)	7.62	Al(68.66), Pd(30.23), Mn(1.11)	13.93
3.93	Al(31.92), Pd(66.61), Mn(1.47)	6.31		
4.54	Al(90.88), Mn(9.12)	8.83	Al(81.24), Pd(12.92), Mn(5.83)	13.87
4.59	Al(64.14), Pd(35.86)	5.03		

Table XI. Compositions and densities of individual planes and layers in the Pd- and Pd+ types of terminations in the QG model. In the QG model, a layer is a pair of planes.

Set A in QG Model (Pd– viewed from positive X to negative X or Pd+ viewed from negative X to positive X)				
Location (nm)	Composition (at.%)	Density (Atoms/ nm^2)	Combined Composition (at.%)	Total density of the terminations (Atoms /nm^2)
25.57	Al(100.00)	4.73	Al(72.19), Pd(27.81)	13.45
25.93	Al(57.33), Pd(42.67)	8.72		
24.91	Al(95.61), Mn(7.39)	7.69	Al(71.88), Pd(24.03), Mn(4.09)	13.78
24.87	Al(46.23), Pd(53.77)	6.09		
24.25	Al(71.22), Mn(28.78)	8.95	Al(67.79), Pd(13.67), Mn(18.54)	13.89
24.20	Al(61.58), Pd(38.42)	4.94		
23.85	Al(96.41), Mn(3.59)	5.94	Al(63.38), Pd(35.08), Mn(1.54)	13.63
23.80	Al(38.56), Pd(61.44)	7.68		
23.19	Al(81.75), Mn(18.25)	8.31	Al(74.98), Pd(13.90), Mn(11.11)	13.65
23.14	Al(64.47), Pd(35.53)	5.34		
22.52	Al(73.20), Mn(26.80)	8.81	Al(76.27), Pd(6.04), Mn(17.69)	13.37
22.48	Al(82.23), Pd(17.77)	4.56		
22.12	Al(93.93), Mn(6.07)	6.99	Al(68.68), Pd(28.20), Mn(3.12)	13.70
22.07	Al(41.98), Pd(58.02)	6.71		
21.46	Al(71.00), Mn(29.00)	8.67	Al(72.74), Pd(8.93), Mn(18.33)	13.86
21.41	Al(75.73), Pd(24.27)	5.20		
21.05	Al(99.34), Mn(0.66)	5.16	Al(69.75), Pd(29.99), Mn(0.26)	13.40
21.00	Al(51.23), Pd(48.77)	8.24		
20.39	Al(91.79), Mn(8.21)	7.76	Al(71.60), Pd(23.72), Mn(4.68)	13.60
20.34	Al(44.81), Pd(55.19)	5.85		
19.73	Al(71.88), Mn(28.12)	8.82	Al(1.61), Pd(10.10), Mn(18.29)	13.58
19.68	Al(71.09), Pd(28.91)	4.76		
19.32	Al (95.11), Pd(4.89)	6.20	Al(62.33), Pd(35.45), Mn(2.22)	13.67
19.72	Al(34.95), Pd(65.05)	7.47		
18.66	Al(75.69), Mn(24.31)	8.50	Al(75.90), Pd(8.98), Mn(15.12)	13.73
18.61	Al(76.24), Pd(23.76)	5.23		
18.00	Al(74.87), Mn(25.13)	8.81	Al(77.43), Pd(5.69), Mn(16.88)	13.16
17.95	Al(82.67), Pd(17.33)	4.34		

Table XI. Continued… Compositions and densities of individual planes and layers in the Pd- and Pd+ types of terminations in the QG model. In the QG model, a layer is a pair of planes.

Set A in QG Model (Pd– viewed from positive X to negative X or Pd+ viewed from negative X to positive X)				
Location (nm)	Composition (at.%)	Density (Atoms/ nm^2)	Combined Composition (at.%)	Total density of the terminations (Atoms /nm^2)
17.59	Al(93.56), Mn(6.44)	7.22	Al(69.83), Pd(26.75), Mn(2.42)	13.62
17.54	Al(43.03), Pd(56.97)	6.40		
16.93	Al(70.82), Mn(29.18)	8.76	Al(69.92), Pd(11.36), Mn(18.72)	13.68
16.88	Al(68.31), Pd(31.69)	4.92		
16.52	Al(97.93), Mn(2.07)	5.61	Al(66.24), Pd(32.91), Mn(0.85)	13.59
16.48	Al(43.96), Pd(56.04)	7.98		
15.86	Al(86.44), Mn(13.56)	8.07	Al(73.74), Pd(18.18), Mn(8.08)	13.67
15.82	Al(55.01), Pd(44.99)	5.59		
15.20	Al(72.94), Mn(27.06)	8.86	Al(74.25), Pd(7.96), Mn(17.79)	13.48
15.16	Al(76.75), Pd(23.25)	4.61		
14.80	Al(94.28), Mn(5.72)	6.62	Al(65.64), Pd(31.58), Mn(2.78)	13.61
14.75	Al(38.63), Pd(61.37)	6.99		
14.14	Al(72.38), Mn(27.62)	8.55	Al(74.72), Pd(7.90), Mn(17.38)	13.59
14.09	Al(78.69), Pd(21.31)	5.04		
13.73	Al (100.00)	4.80	Al(72.10), Pd(27.90)	13.32
13.68	Al(56.53), Pd(43.47)	8.52		
13.07	Al(93.41), Mn(6.59)	7.57	Al(71.84), Pd(24.46), Mn(3.70)	13.48
13.02	Al(44.21), Pd(55.79)	5.91		
12.41	Al(72.24), Mn(27.76)	8.69	Al(68.32), Pd(13.70), Mn(17.98)	13.52
12.36	Al(61.09), Pd(38.91)	4.83		
12.00	Al(95.79), Mn(4.21)	5.98	Al(64.57), Pd(33.55), Mn(1.88)	13.66
11.95	Al(39.34), Pd(60.66)	7.68		
11.34	Al (79.16), Mn(20.84)	8.29	Al(75.30), Pd(11.92), Mn(12.78)	13.62
11.29	Al(69.18), Pd(30.82)	5.32		
10.68	Al(75.39), Mn(24.61)	8.79	Al(77.63), Pd(5.96), Mn(16.40)	13.31
10.63	Al(82.13), Pd(17.87)	4.51		
10.27	Al(93.17), Mn(6.83)	7.35	Al(70.85), Pd(25.49), Mn(3.66)	13.77
10.22	Al(45.07), Pd(54.93)	6.42		

Table XI. Continued… Compositions and densities of individual planes and layers in the Pd- and Pd+ types of terminations in the QG model. In the QG model, a layer is a pair of planes.

Set A in Q–G Model (Pd– viewed from positive X to negative X or Pd+ viewed from negative X to positive X)				
Location (nm)	Composition (at.%)	Density (Atoms/ nm^2)	Combined Composition (at.%)	Total density of the terminations (Atoms /nm^2)
9.61	Al(96.12), Mn(30.88)	8.79	Al(71.62), Pd(8.67), Mn(19.71)	13.77
9.56	Al(7.60), Pd(23.96)	4.98		
9.20	Al(99.21), Mn(0.79)	5.49	Al(72.98), Pd(26.63), Mn(0.39)	13.71
9.15	Al(46.74), Pd(53.26)	8.22		
8.54	Al(91.54), Mn(8.46)	7.98	Al(74.57), Pd(20.35), Mn(5.08)	13.48
8.49	Al(49.10), Pd(50.90)	5.51		
7.88	Al(70.30), Mn(29.70)	8.91	Al(71.85), Pd(8.59), Mn(19.55)	13.59
7.83	Al(74.84), Pd(25.16)	4.68		
7.47	Al(93.56), Mn(6.44)	6.74	Al(65.93), Pd(30.94), Mn(3.13)	13.85
7.43	Al(39.72), Pd(60.28)	7.11		

Table XII. Compositions and densities of individual planes and layers in the Pd- and Pd+ types of terminations in the QG model. In the QG model, a layer is a pair of planes.

Set B in QG Model (Pd– viewed from positive X to negative X or Pd+ viewed from negative X to positive X)				
Location (nm)	Composition (at.%)	Density (Atoms/ nm^2)	Combined Composition (at.%)	Total density of the terminations (Atoms /nm^2)
6.97	Al(100.00)	4.89	Al(66.90), Pd(33.10)	13.45
7.02	Al(46.93), Pd(53.07)	8.56		
7.63	Al(91.96), Mn(8.04)	7.69	Al(71.83), Pd(23.72), Mn(4.45)	13.86
7.68	Al(46.93), Pd(53.07)	6.17		
8.29	Al(71.80), Mn(28.20)	8.95	Al(68.76), Pd(13.07), Mn(18.16)	13.89
8.34	Al(63.26), Pd(36.74)	4.94		
8.70	Al(95.69), Mn(4.31)	6.04	Al(62.12), Pd(36.00), Mn(1.88)	13.63
8.75	Al(36.18), Pd(63.82)	7.59		
9.36	Al(78.29), Mn(21.71)	8.31	Al(74.98), Pd(11.80), Mn(13.21)	13.65
9.41	Al(69.84), Pd(30.16)	5.34		
10.02	Al(73.20), Mn(26.80)	8.81	Al(76.27), Pd(6.04), Mn(17.69)	13.37
10.07	Al(82.23), Pd(17.77)	4.56		
10.43	Al(93.43), Mn(6.57)	6.99	Al(69.07), Pd(27.54), Mn(3.39)	13.64
10.47	Al(43.11), Pd(56.89)	6.65		
10.09	Al(70.28), Mn(29.72)	8.73	Al(71.39), Pd(9.65), Mn(18.95)	13.70
11.13	Al(73.36), Pd(26.64)	4.96		
11.49	Al(98.29), Mn(1.71)	5.47	Al(68.72), Pd(30.59), Mn(0.69)	13.53
11.54	Al(48.63), Pd(51.37)	8.05		
12.15	Al(88.69), Mn(11.31)	8.01	Al(73.35), Pd(20.00), Mn(6.65)	13.62
12.20	Al(51.45), Pd(48.55)	5.61		
12.82	Al(71.88), Mn(28.12)	8.82	Al(73.39), Pd(8.14), Mn(18.46)	13.45
12.86	Al(76.28), Pd(23.72)	4.63		
13.22	Al(93.91), Mn(6.09)	6.56	Al(65.33), Pd(31.75), Mn(2.93)	13.69
13.27	Al(38.91), Pd(61.09)	7.13		
13.88	Al(71.42), Mn(28.58)	8.67	Al(74.37), Pd(7.58), Mn(18.05)	13.80
13.93	Al(79.41), Pd(20.59)	5.12		
14.29	Al(100.00)	4.59	Al(69.66), Pd(30.34)	13.29
14.34	Al(53.90), Pd(46.10)	8.70		

Table XII. Continued…Compositions and densities of individual planes and layers in the Pd- and Pd+ types of terminations in the QG model. In the QG model, a layer is a pair of planes.

Set B in QG Model (Pd– viewed from positive X to negative X or Pd+ viewed from negative X to positive X)				
Location (nm)	Composition (at.%)	Density (Atoms/ nm^2)	Combined Composition (at.%)	Total density of the terminations (Atoms /nm^2)
14.95	Al(93.83), Mn(6.17)	7.62	Al(71.42), Pd(25.12), Mn(3.46)	13.58
15.00	Al(42.73), Pd(57.27)	5.96		
15.61	Al(71.59), Mn(28.41)	8.82	Al(68.91), Pd(12.64), Mn(18.45)	13.61
15.66	Al(63.95), Pd(36.05)	4.79		
15.61	Al(71.59), Mn(28.41)	8.82	Al(68.91), Pd(12.64), Mn(18.45)	13.61
15.66	Al(63.95), Pd(36.05)	4.79		
16.02	Al(96.97), Mn(3.03)	5.97	Al(65.35), Pd(33.33), Mn(1.32)	13.72
16.07	Al(41.00), Pd(59.00)	7.75		
16.68	Al(83.10), Mn(16.90)	8.35	Al(75.51), Pd(14.10), Mn(10.40)	13.68
16.73	Al(63.36), Pd(36.64)	5.33		
17.34	Al(73.62), Mn(26.38)	8.86	Al(75.85), Pd(6.60), Mn(17.55)	13.32
17.39	Al(80.29), Pd(19.71)	4.46		
17.75	Al(93.51), Mn(6.49)	7.04	Al(68.94), Pd(27.71), Mn(3.35)	13.60
17.80	Al(42.72), Pd(57.28)	6.56		
18.41	Al(69.35), Mn(30.65)	8.70	Al(72.63), Pd(7.83), Mn(19.54)	13.71
18.46	Al(78.40), Pd(21.60)	5.01		
18.82	Al(99.73), Mn(0.27)	5.12	Al(68.04), Pd(31.85), Mn(0.10)	13.48
18.86	Al(48.78), Pd(51.22)	8.36		
19.48	Al(92.80), Mn(7.20)	7.889	Al(72.98), Pd(22.80), Mn(4.22)	13.46
19.52	Al(44.96), Pd(55.04)	5.58		
20.14	Al(72.29), Mn(27.71)	8.70	Al(70.48), Pd(11.42), Mn(18.10)	13.43
20.18	Al(67.08), Pd(32.92)	4.72		
20.54	Al(94.84), Mn(5.16)	6.31	Al(64.71), Pd(32.87), Mn(2.42)	13.74
20.59	Al(38.21), Pd(61.79)	7.43		
21.20	Al(75.67), Mn(24.33)	8.47	Al(75.16), Pd(9.66), Mn(15.18)	13.66
21.25	Al(74.30), Pd(25.70)	5.20		
21.86	Al(76.93), Mn(23.07)	8.79	Al(78.17), Pd(6.38), Mn(15.45)	13.24
21.91	Al(80.67), Pd(19.33)	4.44		

Table XII. Continued…Compositions and densities of individual planes and layers in the Pd- and Pd+ types of terminations in the QG model. In the QG model, a layer is a pair of planes.

Set B in QG Model (Pd– viewed from positive X to negative X or Pd+ viewed from negative X to positive X)				
Location (nm)	Composition (at.%)	Density (Atoms/ nm^2)	Combined Composition (at.%)	Total density of the terminations (Atoms /nm^2)
22.27	Al(93.17), Mn(6.83)	7.35	Al(70.59), Pd(25.75), Mn(3.66)	13.77
22.32	Al(44.51), Pd(55.49)	6.42		
22.93	Al(69.75), Mn(30.25)	8.79	Al(70.01), Pd(10.69), Mn(19.30)	13.77
22.98	Al(70.46), Pd(29.54)	4.98		
23.34	Al(98.46), Mn(1.54)	5.62	Al(66.37), Pd(33.00), Mn(0.63	13.58
23.39	Al(44.06), Pd(55.94)	7.96		
24.00	Al(88.54), Mn(11.46)	7.98	Al(74.57), Pd(18.55), Mn(6.88)	13.48
24.49	Al(53.60), Pd(46.40)	5.51		
24.66	Al(70.63), Mn(29.37)	8.91	Al(73.53), Pd(7.13), Mn(19.34)	13.59
24.71	Al(79.12), Pd(20.88)	4.68		
25.07	Al(92.84), Mn(7.16)	6.81	Al(66.99), Pd(29.49), Mn(3.52)	13.85
25.12	Al(41.99), Pd(58.01)	7.04		

Table XIII. Compositions and densities of individual planes and layers in the Pd- and Pd+ types of terminations in the Boudard model. In the Boudard model, a layer is a pair of planes.

Set A in Boudard Model (Pd– viewed from positive X to negative X or Pd+ viewed from negative X to positive X)				
Location (nm)	Composition (at.%)	Density (Atoms/ nm^2)	Combined Composition (at.%)	Total density of the terminations (Atoms /nm^2)
4.98	Al(100.00)	8.02	Al(69.87), Pd(24.38), Mn(5.75)	13.59
4.93	Al(26.45), Pd(59.53), Mn(14.03)	5.57		
4.32	Al(88.92), Mn(11.08)	8.85	Al(79.28), Pd(13.45), Mn(7.27)	13.48
4.27	Al(60.91), Pd(39.09)	4.64		
3.91	Al(100.00)	6.58	Al(63.51), Pd(23.84), Mn(12.65)	13.64
3.86	Al(29.70), Pd(45.93), Mn(24.37)	7.06		
3.25	Al(96.13), Mn(3.87)	8.57	Al(72.69), Pd(24.62), Mn(2.69)	13.65
3.20	Al(33.16), Pd(66.15), Mn(0.69)	5.08		
2.85	Al (100.00)	4.63	Al(57.77), Pd(25.20), Mn(17.04)	13.21
2.80	Al(35.23), Pd(38.64), Mn(26.13)	8.568		
2.18	Al (100.00)	7.54	Al(67.84), Pd(23.37), Mn(8.79)	13.65
2.14	Al(27.86), Pd(52.43), Mn(19.71)	6.11		
1.52	Al(91.13), Mn(8.87)	8.81	Al(76.01), Pd(18.26), Mn(5.73)	13.63
1.48	Al(48.36), Pd(51.64)	4.82		
1.12	Al (100.00)	5.85	Al(60.91), Pd(24.73), Mn(14.36)	13.52
1.07	Al(31.22), Pd(43.51), Mn(25.26)	7.67		
0.46	Al (100.00)	8.27	Al(71.62), Pd(24.52), Mn(3.86)	13.59
0.41	Al(27.44), Pd(62.69), Mn(9.88)	5.32		
-0.20	Al(87.88), Mn(12.12)	8.79	Al(81.40), Pd(10.56), Mn(8.04)	13.27
-0.25	Al(68.64), Pd(31.36)	4.48		
-0.61	Al (100.00)	6.95	Al(65.26), Pd(23.48), Mn(11.26)	13.71
-0.66	Al(29.20), Pd(47.85), Mn(22.94)	6.75		
-1.27	Al(94.01), Mn(5.99)	8.69	Al(73.77), Pd(22.42), Mn(3.81)	13.68
-1.32	Al(38.53), Pd(61.47)	4.99		
-1.68	Al (100.00)	5.15	Al(58.78), Pd(25.07), Mn(16.15)	13.34
-1.73	Al(33.00), Pd(40.74), Mn(26.25)	8.19		

Table XIII. Continued…Compositions and densities of individual planes and layers in the Pd- and Pd+ types of terminations in the Boudard model. In the Boudard model, a layer is a pair of planes.

Set A in Boudard Model (Pd– viewed from positive X to negative X or Pd+ viewed from negative X to positive X)				
Location (nm)	Composition (at.%)	Density (Atoms/ nm^2)	Combined Composition (at.%)	Total density of the terminations (Atoms /nm^2)
-2.34	Al (100.00)	7.88	Al(69.11), Pd(23.82), Mn(7.07)	13.63
-2.39	Al(26.40), Pd(56.76), Mn(16.84)	5.74		
-3.00	Al(89.67), Mn(10.33)	8.83	Al(77.84), Pd(15.41), Mn(6.75)	13.50
-3.05	Al(55.46), Pd(44.54)	4.67		
-3.41	Al(100.00)	6.38	Al(62.17), Pd(24.61), Mn(13.22)	13.67
-3.46	Al(29.07), Pd(46.14), Mn(24.79)	7.29		
-4.07	Al(97.74), Mn(2.26)	8.49	Al(72.27), Pd(24.69), Mn(3.04)	13.62
-4.12	Al(30.09), Pd(65.56), Mn(4.35)	5.13		
-4.73	Al(87.10), Mn(12.90)	8.80	Al(84.22), Pd(7.05), Mn(8.73)	13.07
-4.78	Al(78.20), Pd(21.80)	4.27		

Table XIII. Compositions and densities of individual planes and layers in the Pd- and Pd+ types of terminations in the Boudard model. In the Boudard model, a layer is a pair of planes.

Set B in Boudard Model (Pd– viewed from positive X to negative X or Pd+ viewed from negative X to positive X)				
Location (nm)	Composition (at.%)	Density (Atoms/ nm^2)	Combined Composition (at.%)	Total density of the terminations (Atoms /nm^2)
-4.98	Al(100.00)	6.89	Al(64.79), Pd(23.68), Mn(11.54)	13.70
-4.93	Al(29.09), Pd(47.67), Mn(23.24)	6.80		
-4.32	Al(94.70), Mn(5.30)	8.68	Al(73.34), Pd(23.29), Mn(3.37)	13.68
-4.27	Al(36.29), Pd(63.71)	5.00		
-3.91	Al(100.00)	5.02	Al(58.60), Pd(25.06), Mn(16.35)	13.38
-3.86	Al(33.92), Pd(39.99), Mn(26.09)	8.36		
-3.25	Al(100.00)	7.79	Al(68.94), Pd(23.48), Mn(7.78)	13.59
-3.20	Al(27.21), Pd(55.02), Mn(17.77)	5.80		
-2.59	Al(89.87), Mn(10.13)	8.79	Al(77.39), Pd(16.00), Mn(6.60)	13.49
-2.54	Al(54.01), Pd(45.99)	4.71		
-2.18	Al (100.00)	6.24	Al(61.66), Pd(24.79), Mn(13.55)	13.64
-2.14	Al(29.36), Pd(45.68), Mn(24.96)	7.40		
-1.52	Al (98.33), Mn(1.67)	8.43	Al(71.94), Pd(24.81), Mn(3.25)	13.59
-1.48	Al(28.80), Pd(65.36), Mn(5.84)	5.16		
-0.86	Al(87.19), Mn(12.81)	8.79	Al(83.35), Pd(8.05), Mn(8.60)	13.14
-0.82	Al(75.50), Pd(24.50)	4.35		
-0.46	Al (100.00)	7.33	Al(66.54), Pd(23.18), Mn(10.28)	13.63
-0.41	Al(27.61), Pd(50.16), Mn(22.24)	6.30		
0.20	Al(92.76), Mn(7.24)	8.73	Al(74.75), Pd(20.60), Mn(4.65)	13.62
0.25	Al(42.38), Pd(57.62)	4.88		
0.61	Al (100.00)	5.51	Al(59.61), Pd(25.01), Mn(15.38)	13.47
0.66	Al(31.67), Pd(42.31), Mn(26.02)	7.96		

Table XIII. Continued…Compositions and densities of individual planes and layers in the Pd- and Pd+ types of terminations in the Boudard model. In the Boudard model, a layer is a pair of planes.

Set B in Boudard Model (Pd– viewed from positive X to negative X or Pd+ viewed from negative X to positive X)				
Location (nm)	Composition (at.%)	Density (Atoms/ nm^2)	Combined Composition (at.%)	Total density of the terminations (Atoms /nm^2)
1.27	Al (100.00)	8.14	Al(71.33), Pd(24.58), Mn(4.09)	13.58
1.32	Al(26.66), Pd(62.87), Mn(10.47)	5.44		
1.93	Al(88.68), Mn(11.32)	8.79	Al(79.59), Pd(12.95), Mn(7.46)	13.36
1.98	Al(62.02), Pd(37.98)	4.57		
2.34	Al (100.00)	6.70	Al(63.75), Pd(23.88), Mn(12.37)	13.68
2.39	Al(28.91), Pd(46.83), Mn(24.25)	6.97		
3.00	Al(96.04), Mn(3.96)	8.57	Al(72.83), Pd(24.68), Mn(2.50)	13.61
3.05	Al(33.17), Mn(66.83)	5.04		
3.41	Al(100.00)	4.37	Al(57.58), Pd(25.55), Mn(16.87)	13.29
3.46	Al(34.06), Pd(39.72), Mn(26.22)	8.55		
4.07	Al(100.00)	7.65	Al(67.96), Pd(23.41), Mn(8.64)	13.60
4.12	Al(26.78), Pd(53.48), Mn(19.73)	5.95		
4.73	Al(90.70), Mn(9.30)	8.79	Al(76.55), Pd(17.41), Mn(6.04)	13.56
4.78	Al(50.32), Pd(49.68)	4.77		

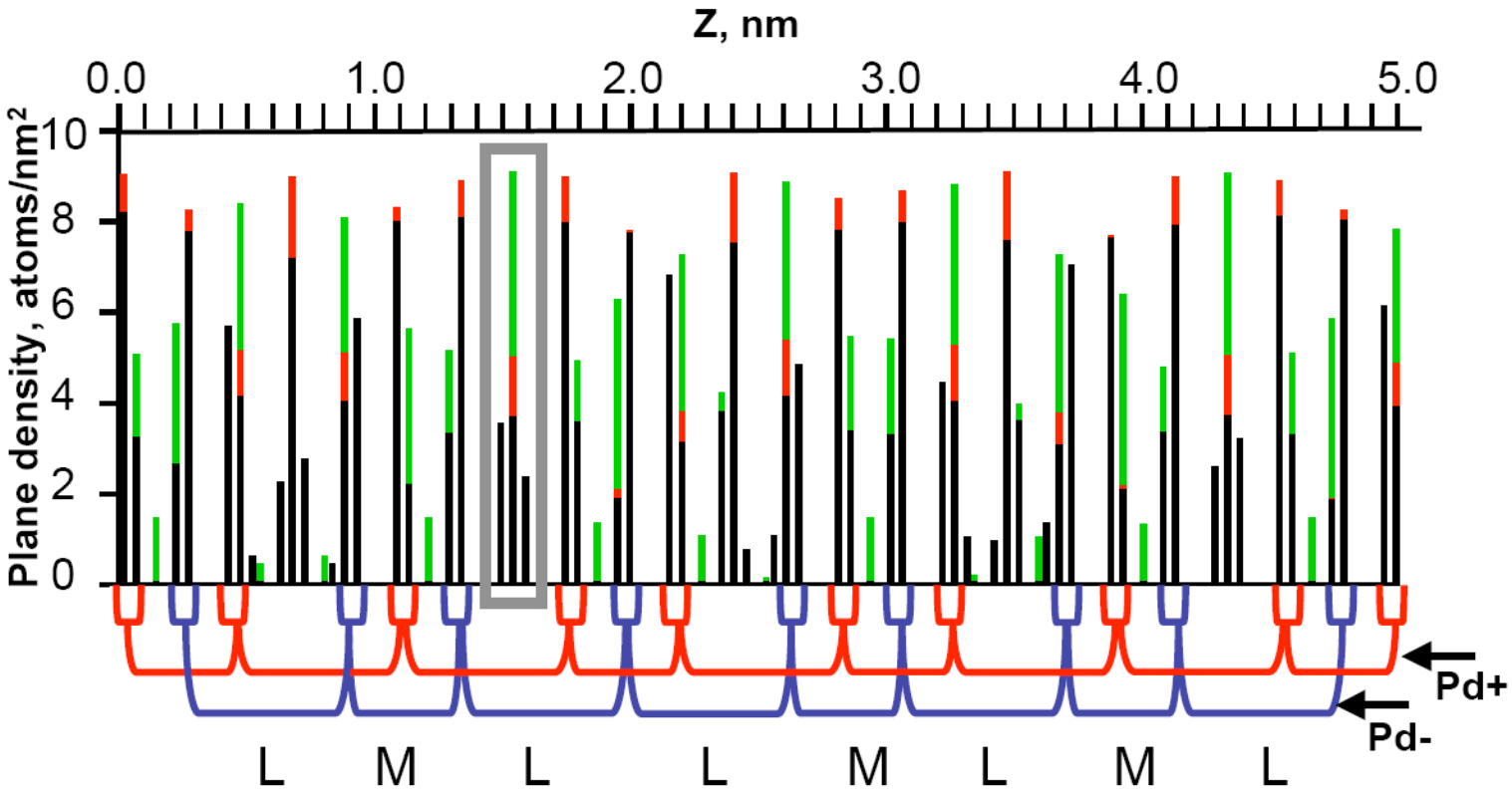
Z, nm
0.0
1.0
2.0
3.0
4.0
5.0
Plane density, atoms/nm²
10
8
6
4
2
0
Pd+
Pd-
L
M
L
L
M
L
M
L

Figure 5

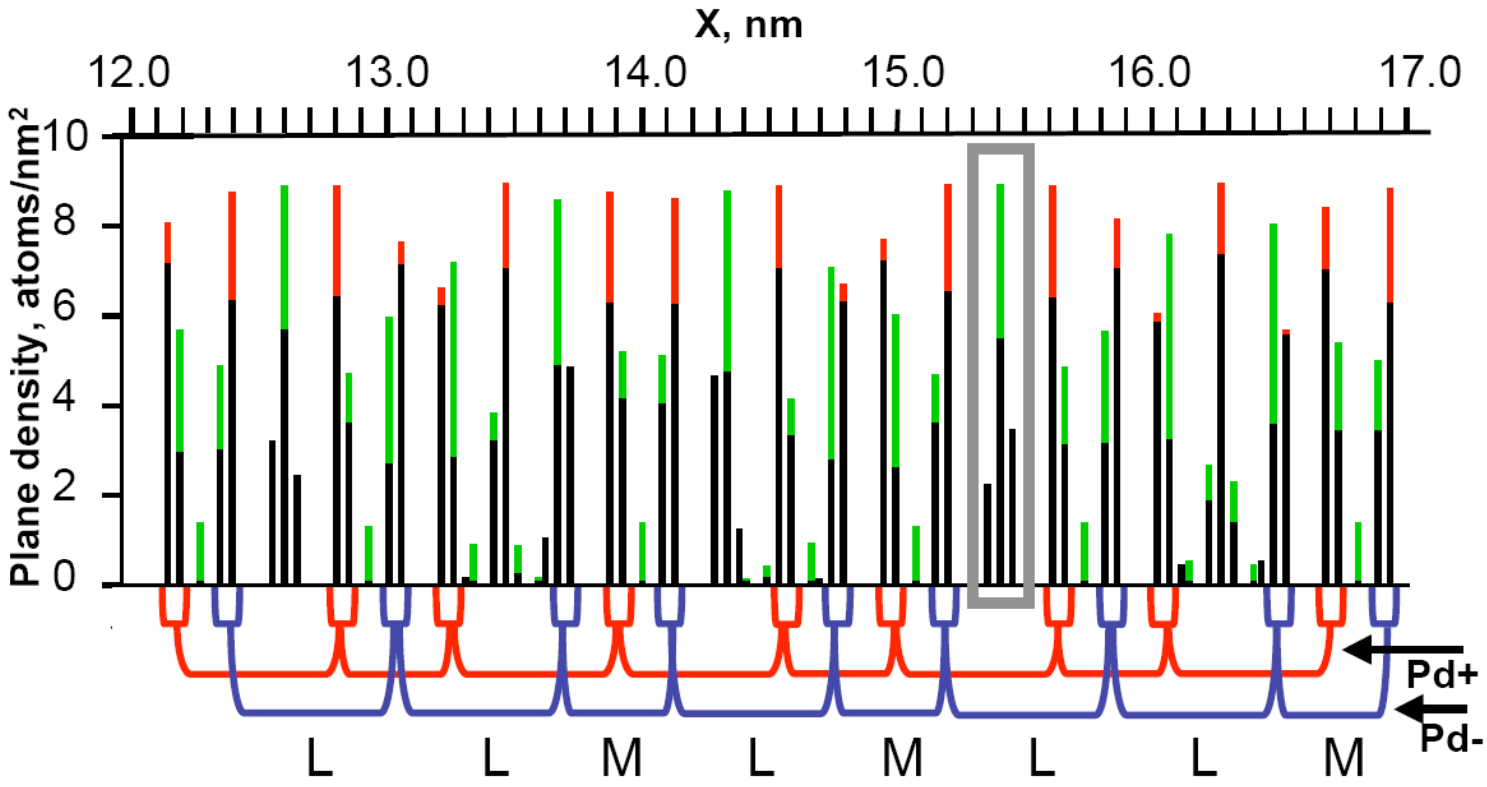
X, nm
12.0
13.0
14.0
15.0
16.0
17.0
Plane density, atoms/nm²
10
8
6
4
2
0
Pd+
Pd-
L
L
M
L
M
L
L
M

Figure 6

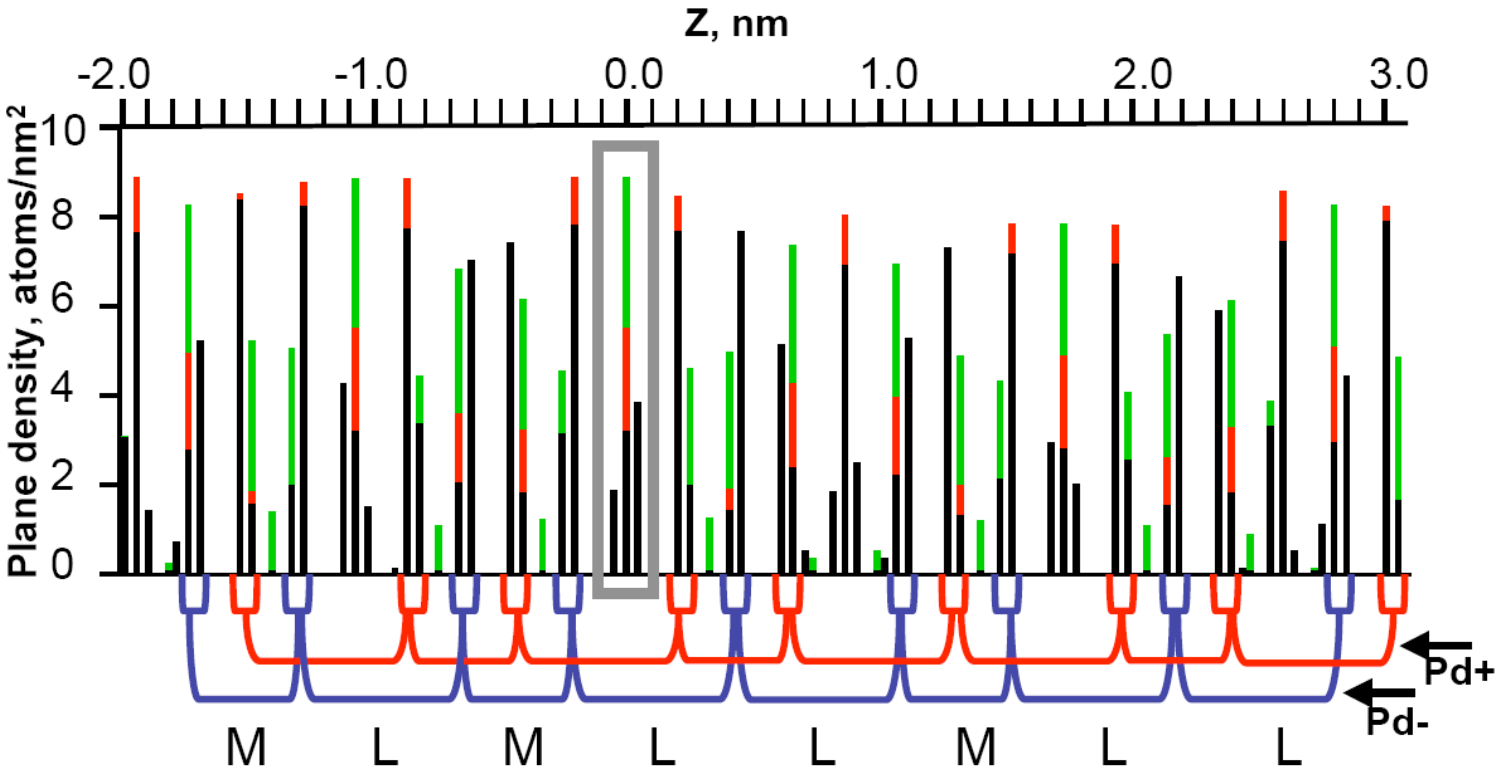
Z, nm
-2.0
-1.0
0.0
1.0
2.0
3.0
Plane density, atoms/nm²
0
2
4
6
8
10
Pd+
Pd-
M
L
M
L
L
M
L
L

Figure 7

APPENDIX B. STM DATA COLLECTION RECORD

Table 1. STM database of experiments on fivefold surface of i-Al-Pd-Mn

Folder name	File name[#]	Sample Treatment[*] (Annealing Temp., Annealing time, Ag coverage, deposition flux)	Image description	Images used in the paper[+]
5f-AlPdMn	031604	953K, 3 hours	A few images with voids on some terraces, images quality is not great	
	031704	923K, 1 hour 40min Cooling rate:28K/min	Periodic structures, definitely not quasicrystalline	
	031904	923K, 2 hours 30min Cooling rate:16K/min	Large terraces, high resolution images from some terraces where dark stars and white flowers can be clearly seen, voids on some terraces	m15-Fig. 5. a[9]
	032004	923K, 2 hours 30min Cooling rate:1.9K/min	Very similar to 031904	
	041104	905-923K, 2 hours 30min Cooling rate:8.9K/min	Very similar to 031904 but temperature varies on the sample	
	041804	905-925K, 3 hours Cooling rate:100K/min	Large terraces, voids on some terraces	
	050704	905-925K, 3 hours 25min Cooling rate:117K/min	Very similar to 031904.But, Temperature varies on the sample.	m54-Fig. 4.a[1] m99-Fig.1.c[1] m117-Fig.5.a[1] m104-Fig. 5.b[9]
	050904	905-923K, 3 hours 25min Cooling rate:16K/min	Very similar to 031904	
	051304	913K, 3 hours	Very similar to 031904	

Table 1. Continued… STM database of experiments on fivefold surface of i-Al-Pd-Mn

Folder name	File name[#]	Sample Treatment[*] (Annealing Temp., Annealing time, Ag coverage, deposition flux)	Image description	Images used in the paper[+]
5f-AlPdMn	051404	900-913K, 3 hours 25min Cooling rate:8.5K/min	Very similar to 031904	m20-Fig 1.a[1]
	051804	900-923K, 3 hours Cooling rate:8.5K/min	Very similar to 031904	
	060404	923K, 3 hours 50min Cooling rate:9.4K/min	Periodic structures, definitely not quasicrystalline	
	061004	903K, ~4 hours Cooling rate:10K/min	Voids on some terraces, bumps ~10nm	
	061804	910K, 3 hours Cooling rate:9.7K/min	Lots of screw dislocations, voids on some terraces, not a great surface	
	061904	910K, 3 hours Cooling rate:9.7K/min	Voids, darks stars are visible but images are not so great	
	062004	910K, 3 hours 25min Cooling rate:10.5K/min	Voids on some terraces, bumps ~5nm	
	062104	903K, ~4 hours Cooling rate:10.3K/min	Terraces with straight step edges, voids, bumbs~5nm	
	062204	910K, 3 hours 10min Cooling rate:9.7K/min	Voids on some terraces, some of the voids are pentagonal, terraces with straight step edges, voids, bumbs~5nm	
	062304	913K, 3 hours 20min Cooling rate:13.3K/min	Voids on some terraces, bumps ~6nm	

Table 1. Continued… STM database of experiments on fivefold surface of i-Al-Pd-Mn

Folder name	File name[#]	Sample Treatment[*] (Annealing Temp., Annealing time, Ag coverage, deposition flux)	Image description	Images used in the paper[+]
5f-AlPdMn	062504	910K, 3 hours 50min Cooling rate:10.6K/min	Very similar to 031904	
	062704	899K, 2 hour 30min Cooling rate:9.9K/min	Voids on some terraces, bumps ~6nm, a screw dislocation in the middle of a terrace, images are not so great	
	062904	900K, ~4 hours Cooling rate:10.2K/min	Voids on some terraces, excellent high resolution images from several terraces adjacent to each other. Bumps ~10nm	m22-Fig.3.a[1] m26-Fig.3.b[1] m90-Fig. 3.c[1] m102-Fig. 2[1]
	070704	915K, 3 hours 35min Cooling rate:11K/min	Surface was not clean enough, huge bumps, voids on some terraces.	
	070904	905K, 3 hours 40min Cooling rate:10K/min	Voids on some terraces, some of the voids are pentagonal, star shaped void?, relatively good images, some part of the surface has huge bumps	
	071304	915K, 3 hours 45min Cooling rate:11K/min	Voids on some terraces, organized void pattern on some terraces	m21-Fig. 1.b[1]
	071904	920K, 3 hours 40min Cooling rate:11K/min	A few low quality images	
	080304	910K, 3 hours 40min Cooling rate:10K/min	Similar to 071904	

Table 1. Continued… STM database of experiments on fivefold surface of i-Al-Pd-Mn

Folder name	File name[#]	Sample Treatment[*] (Annealing Temp., Annealing time, Ag coverage, deposition flux)	Image description	Images used in the paper[+]
5f-AlPdMn	080904	921K, 4 hours 10min Cooling rate:11.6K/min	Pits on some terraces, at the bottom of pits, lots of voids are visible. One ~0.1nm deep pentagonal void with ~40 nm edge length. A ~3nm deep pit on one terrace.	
	081004	913K, 4 hours 10min Cooling rate:11.3K/min	Voids, bumps~6nm	
	081304	913K, ~4 hours Cooling rate:11.5K/min	Voids, terraces with straight step edges	
	081704	910K, ~4 hours Cooling rate:9.2K/min	Voids on some teraces	
	082404	906K, ~4 hours Cooling rate:9.3K/min	Voids on some teraces	
	082504	913K, ~4 hours Cooling rate:9.3K/min	Lots of screw dislocations, incomplete terraces.	
	082704	916K, 3 hours 20min Slow cooling.	Periodic structure domain co-exist with quasicrystalline one. Pentagonal void and pentagonal islands. Screw dislocations	m10-Fig. 6[9] m15-inset in Fig. 6[9]
	083004	913K, ~4 hours Cooling rate:11.5K/min	Terraces with straight and kinked step edges	
	083104	911K, ~4 hours Cooling rate:11.5K/min	Voids on some terraces	

Table 1. Continued… STM database of experiments on fivefold surface of i-Al-Pd-Mn

Folder name	File name[#]	Sample Treatment[*] (Annealing Temp., Annealing time, Ag coverage, deposition flux)	Image description	Images used in the paper[+]
5f-AlPdMn	090404	920K, ~3 hours Cooling rate:11.5K/min	Large terraces, voids on some.	
	090704	933K, ~2 hours Slow cooling.	Large terraces, voids on some, screw dislocations, lots of bumps~5nm, part of the surface is not clean enough	
	091004	933K, ~4 hours Cooling rate:11.5K/min	Similar to 083004	
	091304	933K, ~4 hours Cooling rate:11.5K/min	Similar to 090404 but with bumps on some terraces, several pits with voids at their bottoms	
	091404	915K, ~3 hours Cooling rate:11.5K/min	Similar to 090404	
	091504	913K, ~ 1 hour	Pits and voids	m1-Fig. 2[2]
	091804	918K, 2 hours	Similar to 090404 with bumps~3nm	
	091904	913K, 2 hours	Similar to 090404	
	092104	918K, 3 hours Cooling rate: 12.5K/min	Similar to 090404	
	092204	918K, 3 hours Cooling rate: 12.5K/min	Void and pits. Some pits are pentagonal.	
	120104	918K, 2 hours 30min	A few low quality images	
	120604	913K, 3 hours	Similar to 120104	
	122204	918K, 2 hours 30min	Terraces with kinked step edges. Medium resolution images from some terraces. Fivefold symmetry is visible.	

Table 1. Continued… STM database of experiments on fivefold surface of i-Al-Pd-Mn

Folder name	File name[#]	Sample Treatment[*] (Annealing Temp., Annealing time, Ag coverage, deposition flux)	Image description	Images used in the paper[+]
5f-AlPdMn	122404	903K, 3 hours Cooling rate: 11.4K/min	Voids on some terraces. High resolution images from some terraces. Darkstars and white flowers are visible on adjacent terraces.	
	122604	913K, 2 hours 30min 953K, 20 min Cooling rate: 11.1K/min	Large terraces, a few high resolution images, darkstars and white flowers	
	122704	908K, 2 hours 30min 918K, 30min Cooling rate: 10.3K/min	Voids and pits	
	122904	903K, 1 hour 953K, 2 hours Cooling rate: 11K/min	Similar to 120104	
	010205	950K, 3 hours Cooling rate: 11K/min	Excellent high resolution images, the best ever.	m15-Fig. 1[3] m57-Fig. 4.b[12] m60-Fig. 6.b[5] m66-to Pat[13]
	010405	943K, 2 hours 30 min Cooling rate: 10.5 K/min Ag deposition at 127 K Coverage: 0.2ML to 9.8ML Flux:~$1x10^{-3}$ ML/s	Large terraces. Pits and voids on some. Clean surface: m1-m5	m6-Fig 1. a[5]
	010805	939K, 3 hours Cooling rate: 11 K/min	Periodic structures, definitely not quasicrystalline.	
	011605	953 K, 3 hours Cooling rate: 11K/min	Large terraces	
	011705	950 K, 3 hours Cooling rate: 11K/min	Periodic structures. High resolution images but not quasiperiodic.	

Table 1. Continued… STM database of experiments on fivefold surface of i-Al-Pd-Mn

Folder name	File name[#]	Sample Treatment[*] (Annealing Temp., Annealing time, Ag coverage, deposition flux)	Image description	Images used in the paper[+]
5f-AlPdMn	012305	943 K, 3 hours Cooling rate: 12K/min	A few low quality images. The surface has cluster like features.	
	012405	943 K, 3 hours Cooling rate: 12K/min	Similar to 012305	
	012605	943 K, 3 hours Cooling rate: 9.5K/min	Very rough surface with cluster like features at different length scales. No terraces at all.	
	020505	893K, 1 hour 30 min; 908K, 1 hour	Voids on some terraces. Some part of surface has cluster like features.	
	020805	953K, 3 hours	Terraces but mainly very narrow.	
	021305	893K, 1 hour ; 908K, 30 min; 913K, 30 min	A few images with high resolution. Dark stars and white flowers are visible. Bumps~3nm	
	021405	933K, 2 hours; Ag deposition at 200 K. Coverage 0.15ML to 5.5 ML Flux ~2.5×10^{-3}ML/s	Large terraces. Screw dislocations. Clean surface: m1-m5 Image quality is not great.	m6-Fig. 1. b[5]
	022105	893K, 2 hour ; 903K, 30 min; 938K, 45 min	Terraces with kinked step edges.	
	022305	938K, 3 hours Ag deposition at 365 K. Coverage: 0.26ML to 1.4ML Flux~1×10^{-3} ML/s	Clean surface: m1-m6 Flat-top, steep-edge, ~0.8 nm high Ag islands formed. QSE effect.	m33-Fig. 1. e[5] m42-Fig. 1. a[7] m64-Fig. 1. b[7] m79-Fig. 1. c[7] m80-Fig. 3[10]
	030205	933K, 2 hours 30 min	Large terraces. Voids on some.	

Table 1. Continued… STM database of experiments on fivefold surface of i-Al-Pd-Mn

Folder name	File name[#]	Sample Treatment[*] (Annealing Temp., Annealing time, Ag coverage, deposition flux)	Image description	Images used in the paper[+]
5f-AlPdMn	030305	933K, 3 hours	A few images.	
	031205	908K, 3 hours 20 min	Voids on some terraces. Several high resolution images.	m1-Fig. 1[2]
	061005	948 K, 2 hours. The sample for Berkeley LEEM experiments	Large terraces, chicken-wire type appearance of steps.	
	061105	948 K, 2 hours 45min The sample for Berkeley LEEM experiments	Large terraces	
	061305	948 K, 2 hours 30 min The sample for Berkeley LEEM experiments	Clusters on terraces. Up to m21, after annealed surface; from m21 to m27 after annealed, steps form a chicken-wire network.	
	073105	903K, 4 hours The sample for Berkeley LEEM experiments	Large terraces, voids are elongated along a certain direction.	
	091005	2.2Ax8.5V, 2 hours; 2.3Ax9.0V, 10min	Large terraces, pits and .voids. Darks stars.	
	091105	2.2Ax8.5V, 2 hours; 2.3Ax9.0V, 15min	A few images with large terraces	
	091205	2.2Ax8.5V, 2 hours; 2.3Ax9.0V, 10min Ag deposition at 365 K. Coverage: 0.13ML to 2.5ML. Flux: 2.2×10^{-3} ML/s	Large terraces. Clean surface: m1-m7. *Pseudomorphic* Ag film growth. Bias dependent experiment. Total coverage is not uniform all over the surface	m15-Fig. 1. a[7] m30-Fig. 1. a[6]

Table 1. Continued… STM database of experiments on fivefold surface of i-Al-Pd-Mn

Folder name	File name[#]	Sample Treatment[*] (Annealing Temp., Annealing time, Ag coverage, deposition flux)	Image description	Images used in the paper[+]
5f-AlPdMn	092205	2.3Ax9.0V, 2 hours; 2.4Ax9.4V, 20min. Ag deposition at 365 K. Coverage: 0.15ML to 11ML. Flux~$2x10^{-3}$ML/s	Large terraces, dark stars, white flowers. Clean surface : m1-m4. Two different types of film growth ;1) from m5 to m61 2) from m62 to m340. Grain boundaries between the Ag islands are visible.	
	100605	940K, 2 hours 30min Ag deposition at 365 K. Coverage: 0.15ML to 10ML. Flux~$1x10^{-3}$ ML/s	Large terraces, fine features Clean surface : m1-m10. Grain boundaries between the Ag islands are visible.	
	101005	940K, 2 hours 30min Ag deposition at 345 K. Coverage: 0.15ML to 10ML. Flux~$1x10^{-3}$ ML/s	Large terraces, dark stars, white flowers. Clean surface : m1-m14. Grain boundaries between the Ag islands are visible.	m20-Fig. 1. d[6]
	101505	940K, 2 hours 30min Ag deposition at 365 K. Coverage: 0.1ML to 1ML. Flux~$1x10^{-3}$ ML/s	Large terraces. Clean surface: m1-m3	m16-Fig. 1. b[6]
	101605	940K, 2 hours 40min Ag deposition at 365 K. Coverage: 0.15ML Flux~$1x10^{-3}$ ML/s	Large terraces. Tip induced bumps.	
	110605	940K, 2 hours 30min	A few images with large terraces.	

Table 1. Continued… STM database of experiments on fivefold surface of i-Al-Pd-Mn

Folder name	File name[#]	Sample Treatment[*] (Annealing Temp., Annealing time, Ag coverage, deposition flux)	Image description	Images used in the paper[+]
5f-AlPdMn	110705	943K, 2 hours 30min Ag deposition at 365 K. Coverage: 0.1ML to 1ML. Flux~$1x10^{-3}$ ML/s	Large terraces, dark stars, white flowers. Clean surface : m1-m29.	
	110805	943K, 2 hours 30min Ag deposition at 365 K. Coverage: 0.24ML to 17ML. Flux~$1.3x10^{-3}$ ML/s	Large terraces. Clean surface : m1-m3. Grain boundaries between the Ag islands are visible.	
	112005	948K, 2 hours 30min	A few images with large terraces	
	112605	933K, 2 hours	Similar to 112305	
	120305	933K, 2 hours Ag deposition at 330K. Coverage: 0.5ML to 5.2ML. Flux~$1.6x10^{-3}$ ML/s	Large terraces. Clean surface : m1-m6. Second surface phase exists. Grain boundaries between the Ag islands are visible.	
	120905	911K, 3 hours	Large terraces with kinked step edges.	
	121005	913K, 3 hours Ag deposition at 365K. Coverage: 0.15ML to 1ML. Flux~$1x10^{-3}$ ML/s	Large terraces with screw dislocations. Clean surface: m1-m4	
	121105	923K, 3 hours	Terraces with screw dislocations. Uniform size protrusions on terraces.	
	121405	913K, 3 hours 30min	One image with dislocations.	
	121505	923K, 2 hours 45min	One image with step bunching.	

Table 1. Continued… STM database of experiments on fivefold surface of i-Al-Pd-Mn

Folder name	File name[#]	Sample Treatment[*] (Annealing Temp., Annealing time, Ag coverage, deposition flux)	Image description	Images used in the paper[+]
5f-AlPdMn	121905	923K, 3 hours Ag deposition at 365K. Coverage: 0.15ML to 1ML. Flux~$1x10^{-3}$ ML/s	Terraces with screw dislocations. Clean surface: m1-m4. Tried every point STS but without success due to tip and also noise.	
	122305	918K, 3 hours 10min	Large terraces. Fine features. *No darks stars* but some white flowers.	
	122805	918K, 2 hours 45min Ag deposition at 365K. Coverage: 0.7ML to 1.4ML. Flux~$3.9x10^{-3}$ ML/s	Periodic surface phase with atomic resolution. Clean surface: m1-m58	
	010606	920K, 2 hours; 908K, 1 hour; 933K, 3 min. Slow cooling.	Still periodic surface phase	
	010906	963K, 3 hours 10min;	Still periodic surface phase. Atomic resolution images. Dislocations.	
	011106	933K, 2 hours 45min.	Similar to 010906	
	011206	913K, 2 hours 45min; 953K, 1 hours.	One image. Very rough surface.	
	011806	903K, 2 hours 30min; 943K, 1 hour.	Terraces with kinked step edges. Lots of screw dislocations.	
	011906	973K, 45min; 1003K, 30min; Cooling rate: 8K/min	Finally terraces with dark stars and white flowers.	
	012306	963K, 3 hours; Ag deposition at 365K. Coverage: 0.2ML to ~1ML. Flux~$1x10^{-3}$ ML/s	Relatively large terraces. Clean surface: m1-m16. *Pseudomorphic* Ag films. See m40-m42.	

Table 2. STM database of experiments on 110 surface of NiAl

Folder name	File name[#]	Sample Treatment[*] (Annealing Temp., Annealing time, Ag coverage, deposition flux)	Image description	Images used in the paper[+]
NiAl	062906	1200K, 1 hour	Relatively narrow terraces with lots of pinning sites. Part of alumina layer that pins a terrace is visible. Holes with ~0.8nm diameter on the alumina layer	
	070206	1200K, 1 hour	Terraces with lots of pinning sites.	
	070306	1200K, 1 hour	Similar to 070206	
	070606	1200K, 1 hour	Similar to 070206	
	070806	1200K, 1 hour 25min	Similar to 070206	
	071006	1200K, 1 hour	Similar to 070206	
	071306	1123K, 1 hour	Similar to 070206	
	071806	1123K, 1 hour	Similar to 070206	
	071906	1123K, 1 hour	Similar to 070206	
	072006	1123K, 1 hour	Similar to 070206	
	072106	1113K, 1 hour	Similar to 070206	
	072406	1128K, 1 hour Ag deposition at 300K. Coverage (time): 0.4ML(2min) to 2.6ML(13min) Flux~3.2×10^{-3}ML/s	Relatively narrow terraces. Clean surface: m1-m2. Noisy images. Ag nucleates at step edges and forms finger like islands.	
	072506	1128K, 1 hour 30min	Narrow terraces with lots of pinning sites.	
	072706	1128K, 1 hour 30min	Similar to 072506 but the surface is getting better. A screw dislocation.	
	072806	1128K, 1 hour 30min	Similar to 072706	
	080306	1128K, 1 hour 50min	Similar to 072706	
	081006	1128K, 1 hour 50min	Surface is not clean enough. Tip is not so great, too.	

Table 2. Continued… STM database of experiments on 110 surface of NiAl

Folder name	File name[#]	Sample Treatment[*] (Annealing Temp., Annealing time, Ag coverage, deposition flux)	Image description	Images used in the paper[+]
NiAl	081306	1223K, 3 hours 30min Ag deposition at 300K. Coverage (time): 0.4ML(2min) to 20ML(105min) Flux=$3.2x10^{-3}$ ML/s	Narrow terraces ~100nm. Clean Surface: m1-12. Ag nucleates at step edges and forms finger like islands. Ripples on Ag islands.	m21-Fig. 3. a[8] m42-Fig. 3. b[8] m88-Fig. 3. c[8] m113-Fig. 3. d[8] m38-Fig. 8. a[8] m72-Fig. 8. b[8] m98-Fig. 8. d[8] m116-Fig. 8. e[8] m97-Fig. 10[8]
	081506	1223K, 2 hour 30min	Terraces with pinning sites	
	081806	1223K, 3 hours. Ag deposition at 127K. Coverage(time): 0.6ML(1min)to 31.5ML(75min) Flux ~$7x10^{-3}$ML/s	Narrow terraces ~70nm. Clean Surface: m1-10. Ag nucleates in terraces. Noisy data. Tip effects. A different Ag growth mode on some terraces, perhaps on alumina parts see m83-m87.	m27-Fig. 1. a[11]
	082306	1223K, 3 hours.	Two bad images.	
	090706	1223K, 2 hours 50min	Two images showing step bunching.	
	091106	1223K, 3 hours.	Step bunching. White protrusions on terraces.	
	091206	1223K, 2 hours 45min Ag deposition at 450K Coverage (time): 0.2ML(1min) to 15ML(75min) Flux = $3.2x10^{-3}$ ML/s	Step bunching. Clean surface: m14-m18 (image number stars from m14)	

Table 2. Continued… STM database of experiments on 110 surface of NiAl

Folder name	File name[#]	Sample Treatment[*] (Annealing Temp., Annealing time, Ag coverage, deposition flux)	Image description	Images used in the paper[+]
NiAl	091506	1223K, 2 hours 30min Ag deposition at 200K. Coverage: 0.3ML(1min) to 42ML(105min) Flux=6.6x10^{-3} ML/s	Relatively larger terraces, with step bunching. Clean surface :m1-m10. Bias dependent experiments (-2.4V to 2.4 V)	m36-Fig. 2. a[8] m133-Fig. 2. b[8] m163-Fig. 2. c[8] m201-Fig. 2. d[8] m147-Fig. 6. a[8] m116-Fig. 6. b[8] m104-Fig. 6. c[8] m142-Fig. 6. d[8] m152-Fig. 6. e[8] m137-Fig. 8. c[8] m225-Fig. 11.a[8] m230-Fig. 11.b[8]
	091906	1223K, 2 hours	A few low quality images.	
	092006	1223K, 1 hour	Not a clean surface.	
	092206	1223K, 2 hours 15min	Lots of step bunching.	
	092506	1223K, 2 hours	Similar to 092206. Tip effects.	
	092806	1223K, 2 hours. Ag deposition at 175K Coverage(time): 0.4ML (1min) Flux=6.6x10^{-3} ML/s	Clean surface: m1 Extreme tip effects.	m6-Fig. 1. c[11]
	100206	1223K, 2 hours Ag deposition at 150K Coverage(time): 0.4ML(1min) to 17ML(42min) Flux=6.6x10^{-3} ML/s	Clean surface: m1-m5 After m152, the sample is heated to 200K.	m8-Fig. 1. b[11]
	100306	300K	The same surface as 100206 but waited over night	
	100706	1223K, 2 hours 40min Ag deposition at 140K Coverage(time): 0.4ML(1min) Flux=6.6x10^{-3} ML/s	Large terraces. Clean surface: m1-m3 Tip effects.	

Table 2. Continued… STM database of experiments on 110 surface of NiAl

Folder name	File name[#]	Sample Treatment[*] (Annealing Temp., Annealing time, Ag coverage, deposition flux)	Image description	Images used in the paper[+]
NiAl	101106	1223K, 2 hours 40min Ag deposition at 185K Coverage(time): 0.4ML(1min) Flux=$6.6x10^{-3}$ ML/s	Terraces with pinning sites Clean surface: m1-m7 Tip effects.	
	102606	1223K, 2 hours	A few bad images	
	103106	1223K, 2 hours	Very large terraces ~300nm but not clean enough.	
	110306	1223K, 2 hours	Large terraces but a dirty tip.	
	110706	1223K, 2 hours 30min Ag deposition at 185K Coverage(time):0.4ML(1min) Flux=$6.6x10^{-3}$ ML/s	Very large terraces ~400nm. Clean surface: m1-m4 Noisy data.	
	111406	1223K, 2 hours	Very large terraces but dirty tip.	
	111806	1223K, 2 hours Ag deposition at 300K ***for flux calibration*** Coverage(time): 0.2 ML (20sec) Flux=$1.0x10^{-2}$ ML/s	Very large terraces ~500nm. Clean surface: m1-m6	
	111906	1223K, 2 hours Ag deposition at 300K ***for flux calibration*** Coverage(time): 0.9 ML (20sec) Flux=$4.5x10^{-2}$ ML/s	Very large terraces ~300nm. Clean surface: m1-m4. Noisy data.	
	112006	1223K, 2 hours Ag deposition at 300K ***for flux calibration*** Coverage(time): 1.1 ML (8sec) Flux=$1.4x10^{-1}$ ML/s	Very large terraces ~300nm. Clean surface: m1-m5. Noisy data.	

Table 2. Continued… STM database of experiments on 110 surface of NiAl

Folder name	File name[#]	Sample Treatment[*] (Annealing Temp., Annealing time, Ag coverage, deposition flux)	Image description	Images used in the paper[+]
NiAl	112206	1230K, 2 hours	Large terraces, cluster like huge features. Surface seems not clean enough.	
	121806	1273K, 2 hours	Large terraces, tip drops dirt and noisy data	
	010207	1303K, 1 hour 10min, 1353K, 10 min	Large terraces ~250nm, Tip effects.	
	010407	1303K, 1 hour 10min, 1353K, 20 min. Ag deposition at 140K, 0.4 ML, Flux=$6.7x10^{-3}$ ML/s	Large terraces ~250nm. Clean surface: m1-m3. Double tip effects.	m51-Fig. 3. a[11]
	010907	1303K, 2 hour 30min, 1353K, 20 min. Ag deposition at ? Coverage: 0.4 ML Flux= $6.7x10^{-3}$ ML/s	Large terraces ~250nm Clean surface: m1-m5. Tip effects.	
	011507	1303K, 2 hour 30min, 1353K, 15 min. Ag deposition at 250K Coverage: 0.4 ML to 10 ML Flux= $6.7x10^{-3}$ ML/s	Very large terraces ~600nm. Clean surface: m1-m6. Protrusions surrounded by depressions on clean surface.	
	011907	1303K, 1 hour 50min, 1353K, 20 min. Ag deposition at 100K Coverage: 0.4 ML (1 min) Flux= $6.7x10^{-3}$ ML/s	Relatively large terraces ~400nm. Clean surface: m1-m34. Very noisy data. Dirty tip.	
	012307	1303K, 1 hour 50min, 1353K, 20 min. Ag deposition at 300K Coverage: 0.4ML Flux= $6.7x10^{-3}$ ML/s	Very large terraces ~700nm. Clean surface: m1-14. Very dirty tip. Changed the tip after m20.	

Table 2. Continued… STM database of experiments on 110 surface of NiAl

Folder name	File name[#]	Sample Treatment[*] (Annealing Temp., Annealing time, Ag coverage, deposition flux)	Image description	Images used in the paper[+]
NiAl	012707	1303K, 2 hour 42min, 1353K, 15 min. Ag deposition at 50K Coverage: 0.4ML Flux= $6.7x10^{-3}$ ML/s	Very large terraces ~700nm. Clean surface: m1-m5. Extremely bad tip. Very noisy data.	
	013107	1303K, 1 hour 30min, 1353K, 15 min.	Large terraces. Very dirty tip.	
	020407	1303K, 3 hours, 1353K, 15 min. Ag deposition at 225K Coverage: 0.4ML Flux= $6.7x10^{-3}$ ML/s	Large terraces ~350nm. Clean surface: m1-m7. Very noisy data.	
	020707	1303K, 2 hours, 1353K, 15 min. Ag deposition at 275K Coverage: 0.4ML Flux= $6.7x10^{-3}$ ML/s	Very large terraces ~650nm. Clean surface: m1-m6. Dirty tip.	
	021107	1303K, 1 hour 40min, 1353K, 20 min.	Very low quality images. Bad surface.	
	021407	1303K, 1 hour 40min, 1337K, 15 min.	Similar to 021107	
	021707	1303K, 1 hour 35min, 1353K, 15 min. Ag deposition at 190K Coverage (time): 0.4ML (1 min) Flux= $6.7x10^{-3}$ ML/s	Very large terraces ~500nm. Clean surface: m1-m5. Double tip effects.	m46-Fig. 1. d[11]
	022207	1243K, 2 hour 15min, 1293K, 15 min.	Large terraces.	
	030207	1273K, 1 hour 40min, Ag deposition at 150K Coverage (time): 0.7 ML (10 sec) Flux= $7x10^{-2}$ ML/s	Large terraces ~300nm. Clean surface: m1. Tip effects.	
	031607	1203K, 1 hour 40min.	Terraces with pinning sites.	
	031807	1208K, 2 hours 30min	Similar to 031607	
	032107	1208K, 2 hours	One ugly image.	
	032707	1203K, 1 hour 30min.	Bad surface and dirty tip.	

Table 2. Continued… STM database of experiments on 110 surface of NiAl

Folder name	File name[#]	Sample Treatment[*] (Annealing Temp., Annealing time, Ag coverage, deposition flux)	Image description	Images used in the paper[+]
NiAl	033007	1203K, 2 hours 30min.	Similar to 032707	
	040307	1203K, 1 hour 30min.	Surface is getting better. Terraces with several pinning sites.	
	040507	1203K, 2 hours. Ag deposition at 150K Coverage(time): 0.4ML (10 min) Flux= $6.7x10^{-4}$ ML/s	Terraces with pinning sites Clean surface: m1-m5. Tip effects.	
	040907	1203K, 1 hour 50min Ag deposition at 150K Coverage(time): 1ML (7min) Flux= $2.3x10^{-3}$ ML/s	Terraces with pinning sites Clean surface: m1-m8. Very noisy data.	
	041807	1203K, 1 hour 50min Ag deposition at 150K Coverage(time): 0.3ML (2.5min) Flux= $2.0x10^{-3}$ ML/s	Terraces with pinning sites Clean surface: m1-m9. Very noisy data.	
	042507	1203K, 1 hour 30min Ag deposition at 150K Coverage(time): 0.4ML (1min) Flux= $6.7x10^{-3}$ ML/s	Terraces with pinning sites Clean surface: m1-m5. Very noisy data.	
	042907	1248K, 1hour 30min	Very large terraces ~500nm.	
	050407	1248K, 2 hours. Ag deposition at 150K Coverage(time): 0.4ML (1min) Flux= $6.7x10^{-3}$ ML/s	Terraces with pinning sites Clean surface: m1-m42. Very noisy data. Very bad tip.	
	051307	1248K, 1 hour 30min Ag deposition at 150K Coverage(time): 0.4ML (1min) Flux= $6.7x10^{-3}$ ML/s	Terraces with pinning sites Clean surface: m1-m7. Very noisy data. Very bad tip.	

Table 2. Continued… STM database of experiments on 110 surface of NiAl

Folder name	File name[#]	Sample Treatment[*] (Annealing Temp., Annealing time, Ag coverage, deposition flux)	Image description	Images used in the paper[+]
NiAl	060607	1248K, 1 hour 40 min.	Large terraces ~500nm	
	110807	1293K, 2 hours	Similar to 060607. New tip cleaning.	
	111107	1293K, 2 hours	Step bunching.	
	111307	1293K, 1 hour 20min Ag deposition at 140K Coverage(time): 0.4ML (1min) Flux= $6.7x10^{-3}$ ML/s	Terraces with pinning sites Clean surface: m1-m26. Noisy data. Very bad tip. Double tip effects.	
	120207	1333K, 1 hour 25min	Very rough surface	
	120307	1333K, 2 hours Ag deposition at 130K Coverage(time): 0.28ML (5 sec) Flux= $5.6x10^{-2}$ ML/s	Large terraces ~300nm Clean surface: m1-m5. ***Coarsening experiment (130K to 275K)***	m8-Fig. 3. b[11]
	120907	1300K, 2 hours Ag deposition at 140K Coverage(time): 0.3ML (5 sec) Flux= $5.6x10^{-2}$ ML/s	Large terraces ~300nm Clean surface: m1-m6. *An unsuccessful coarsening experiment attempt.*	
	121407	1273K, 2 hours Ag deposition at 140K Coverage(time): 0.3ML (5 sec) Flux= $5.6x10^{-2}$ ML/s	Large terraces ~300nm Clean surface: m1-m3. *An unsuccessful coarsening experiment attempt.*	
	122307	1200K, 2 hours	Terraces with pinning sites and bumps.	

Table 3. STM database of experiments on pseudo tenfold surface of ξ'-Al-Pd-Mn

Folder name	File name[#]	Sample Treatment[*] (Annealing Temp., Annealing time, Ag coverage, deposition flux)	Image description	Images used in the papers
Xsi-Prime AlPdMn	031705	803K, 1 hour 20min	Terraces with lots of pinning sites. Fine features are also visible.	
	040205	813K, 2 hours	A few images, lots of pinning sites.	
	040305	823K, 2 hours 20 min	Similar to 031705	
	041005	823K, 2 hours 20 min	Similar to 040205	
	041705	823K, 2 hours 20 min	Similar to 031705	
	042105	823K, 3 hours 20 min	Only two images with lots of pinning sites	
	042805	823K, 3 hours	Only two images with fine features	
	051005	823K, 3 hours 40 min	Large terraces with pinning sites, fine features	
	051305	823K, 2 hours 12 min	Only two images, large terraces with pinning sites and an image with fine features	
	051805	823K, 2 hours	Similar to 051005	
	052805	823K, 3 hours	A few images with fine features	
	053005	813K, 1 hours 40 min	Only one image, terraces with bumps	
	060105	803K, 3 hours	Similar to 051005	
	061605	883K, 2 hours 20 min; Ag deposition at 365 K. Coverage: 0.4ML to 5.0ML Flux: 2.2×10^{-3} ML/s	Very large terraces. Fine features. Clean surface: m1-m40	
	070105	893K, 2 hours 30min	Very rough surface. A few images with fine structure.	
	070205	833K, 1 hour 30min; 883K, 30 min; 893K, 5 min.	One image with bumps	

Table 3. Continued… STM database of experiments on pseudo tenfold surface of ξ′-Al-Pd-Mn

Folder name	File name[#]	Sample Treatment[*] (Annealing Temp., Annealing time, Ag coverage, deposition flux)	Image description	Images used in the papers
Xsi-Prime AlPdMn	070305	833K, 45min; 883K, 35 min; 893K, 5 min; 883K, 1 hour 5min	Terraces with fine features	
	070605	883K, 3 hours.	One image with fine features, void and an island(?)	
	071005	883K, ~3 hours.	A few images with fine features	
	082205	863-888K, 30 mins.	A few images with large terraces.	
	082305	883K, ~2 hours.	Large terraces with pinning sites. Voids. Fine features.	
	082405	883K, ~3 hours.	Only two images with large terraces	
	082505	863K, 3 hours; 903K, 10 min. Ag deposition at 420 K. Coverage: 0.1ML to 10.0ML	Large terraces, fine features, pentagonal pits, screw dislocations. Clean surface: m1-30	
	083105	863K, 3 hours; 903K, 10 min. Ag deposition at 127 K. Coverage: 0.27ML to 11.4ML Flux: 2.2×10^{-3} ML/s	Large terraces, fine features. Clean surface: m1-m15 Double tip effects.	
	090405	863K, 2 hours 30min; 903K, 10 min.	Large terraces, fine features.	
	090505	863K, 2 hours; 903K, 10 min. Ag deposition at 200 K. Coverage: 0.27ML to 11.4ML Flux: 2.2×10^{-3} ML/s	Large terraces, fine features. A secondary phase with fine features. Clean surface:m1-m18	

Table 4. STM database of experiments on twofold surface of d-Al-Cu-Co

Folder name	File name[#]	Sample Treatment[*] (Annealing Temp., Annealing time, Ag coverage, deposition flux)	Image description	Images used in the papers
2f-d-AlCuCo	111205	953K, 2 hours 30min	Large terraces. Two different types of terraces. One is rougher than the other. Atomic resolution. Atoms have ~0.88nm and 0.44nm periodicities along the ten fold axis. Phason defects.	
	112305	923K, 2 hours 50min	Similar to 111205 but no atomic resolution this time.	
	112705	953K, 2 hours	Similar to 111205	
	112805	953K, 2 hours 47min	Similar to 112305	
	120405	933K, 2 hours 30min	Similar to 111205 but no atomic resolution this time.	

 # Files were created on VT-STM PC computer (with Scala v4.1) in 224/225 Spedding Hall. The STM file names were coded as mmddyy when they were created and saved.

*** The samples used in the experiments:**

For 5f-i-Al-Pd-Mn;

1) ARR-4-12-2.1 ($Al_{70.2}Pd_{20.7}Mn_{9.1}$) from 03/16/2004 to 11/29/2004
2) ARR-1-92-1A ($Al_{70.22}Pd_{20.73}Mn_{9.05}$) from 11/29/2004 to 12/03/2005
3) WDM-1-84-6 ($Al_{69.8}Pd_{20.7}Mn_{9.5}$) from 12/09/2005 to 01/23/2006

For NiAl(110);

1) BPK-1-65 ($Ni_{50}Al_{50}$)

For ξ'-Al-Pd-Mn;

1) p-10f-$Al_{77.5}Pd_{19}Mn_{3.5}$

For 2f-d-Al-Cu-Co;

1) RM093 ($Al_{62.12}Co_{17.14}Cu_{19.74}$)

Note: The purity of the Ag beads used in the deposition experiments was 99.99 at %.

+ Images used in the following papers:

1) B. Unal, A.R. Ross, T.A.Lograsso, C. J. Jenks and P.A.Thiel, “Terrace selection during equilibration at an icosahedral quasicrystal surface”, Phys. Rev. B 71, 165411, 2005.
2) B. Unal, A.R. Ross, T.A.Lograsso, C. J. Jenks and P.A.Thiel, “Voids and pits on sputter-annealed fivefold terraces of icosahedral Al-Pd-Mn quasicrystals, Phil. Mag. 86, 816, 2006.
3) B. Unal, C. J. Jenks and P.A.Thiel, “Comparison between experimental surface data and bulk structure models for quasicrystalline AlPdMn: Average atomic densities and chemical compositions”, Phys. Rev. B 77, 195419, 2008.
4) B. Unal, C. J. Jenks and P.A.Thiel, “Adsorption sites on quasicrystal surfaces: Dark stars and white flowers”, will be submitted to Journal of Physics: Condense Matter.
5) “Nucleation and growth of Ag islands on fivefold Al-Pd-Mn quasicrystal surfaces: Dependence of island density on temperature and flux”, Phys. Rev. B 75, 064205, 2007.
6) B. Unal, J. W. Evans, T. A. Lograsso, A. R. Ross, C. J. Jenks and P. A. Thiel, “Terrace-dependent nucleation of small Ag clusters on a five-fold icosahedral quasicrystal surface”, Phil. Mag. 87, 2995, 2007.
7) B. Unal, V. Fournee, P. A.Thiel and J. W. Evans, “Growth of height-selected Ag islands on fivefold icosahedral AlPdMn quasicrystalline surfaces: STM analysis and step dynamics modeling”, will be submitted to Physical Review Letters.

8) B. Unal, F. Qin, Y. Han, D,-J. Liu, D. Jin, A. R. Layson, C. J. Jenks, J. W. Evans, P. A. Thiel, “Scanning tunneling microscopy and density functional theory study of initial bilayer growth of Ag films on NiAl(110)”, Phys. Rev. B 76, 195410, 2007.

9) J. Ledieu, R. McGrath, N.V. Richardson, Q. Chen, V. Fournee, T. Lograsso, A. Ross, K.J. Caspersen, B.Unal, J.W. Evans, and P.A. Thiel, “Step Structure on the Five-Fold Al-Pd-Mn Quasicrystalline Surface and on Related Surfaces”, Surf. Sci. 583, 4, 2005.

10) V. Fournee, H.R. Sharma, M. Shimoda, A.P.Tsai, B. Unal, A.R. Ross, T.A.Lograsso, and P.A.Thiel, ”Quantum Size Effects in Metal Thin Films Grown on Quasicrystalline Substrates”, Phys. Rev. Lett. 95, 155504, 2005.

11) Y. Han, B. Unal, F. Qin, D. Jin, C. J. Jenks, D.-J. Liu, P. A. Thiel, J. W. Evans,” Kinetics of Facile Bilayer Island Formation at Low Temperature: Ag/NiAl(110)”, Phys. Rev. Lett. 100, 116105, 2008.

12) P.A. Thiel, “Quasicrystal Surfaces”, Annu.Rev.Phys.Chem. 59, 129, 2008.

13) P.A.Thiel, “Review Paper”, 2009.

APPENDIX C. LOW ENERGY ELECTRON MICROSCOPY (LEEM)

This part of the dissertation demonstrates some of the highlights of the LEEM experiments done both in NCEM in Lawrence Berkeley National Laboratory and in Sandia National Laboratories. This work involves collaborations with Dr. Andreas Schmid, Dr. Yu Sato and Dr. Thomas Duden from NCEM as well as collaborations with Dr. Kevin McCarty and Dr. Norm Bartelt from Sandia National Laboratories.

LEEM has been used to investigate the fivefold surface of a i-Al-Pd-Mn quasicrystal from room temperature to high temperature. The temperature of the sample was measured with a two color pyrometer (in Sandia Lab). Figure 1 is a bright-field LEEM image from the fivefold surface of i-Al-Pd-Mn quasicrystal showing the surface morphology of "chicken wire" array of surface steps. In the LEEM image, both rhomohedral mesh-shapes (area near lower left) and hexagonal mesh-shapes (most areas other than lower left) coexist. It should be note that every terrace has the same LEEM contrast.

Figure 1. Bright-field LEEM image of high temperature quasicrystal surface at 905K. The electron energy is 4.4eV. The file is 1040800028. Image size, field of view (FOV) is 7μm.

In figure 2, a LEED pattern from the surface in figure 1 is given. The fivefold symmetry of the surface is obvious at this temperature.

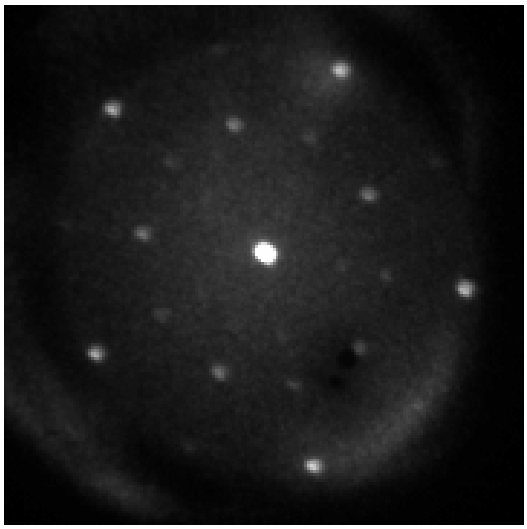

Figure 2. A LEED pattern from the high temperature surface at 837K. The electron energy is 5 eV. Image number is 122107m000.

In figure 3, there are two bright-field images from the same area showing “chicken wire” step structure on the majority of the surface at 300K. In figure 3(a) the difference in the LEEM contrast is emphasized at electron energy of 6.9 eV and in figure 3(b) the step contrast is emphasized at electron energy of 4.7 eV. Therefore, by varying the electron energy, it is possible to probe different features of the quasicrystal surface. In figure 4, two close-up bright-field images are given. Figure 5(a) shows the selected area BF-LEEM image with three contrasts at 300K. Figure 5(b) shows the selected area diffraction (SAD) of figure 5(a).Figure 6(a) demonstrates the bright-field image where three shades of contrast are also visible. Figure 6(b) shows the BF-LEEM-IV curves from the regions labeled in figure 6(a). It should be noted that the peaks are at the same locations and only relative intensities are different.

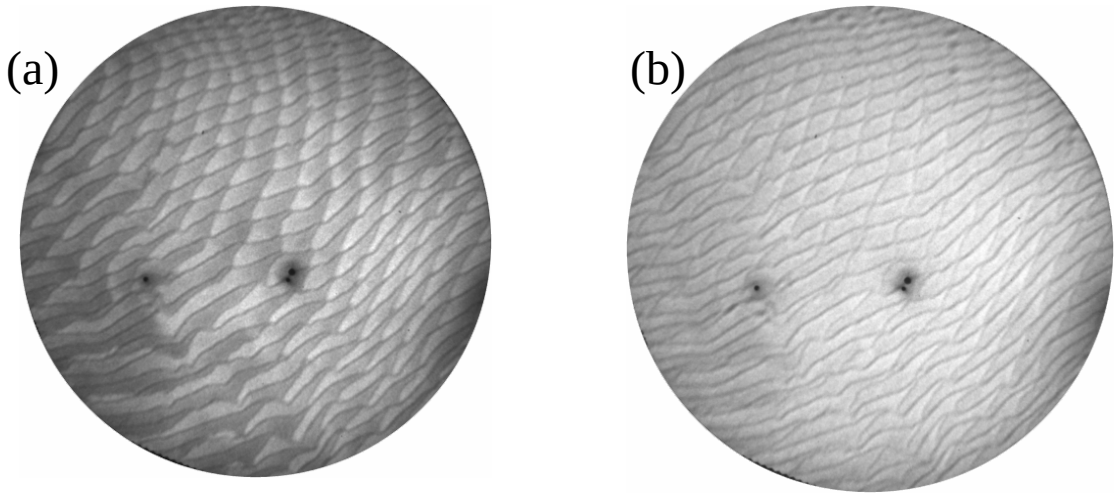

Figure 3. Two bright-field LEEM images show the same area at 300K. The electron energy is (a) 6.9 eV and (b) 4.7 eV. The image (FOV) size is 7 micrometer. The image numbers are for (a) 10308000014 and for (b) 10308000015.

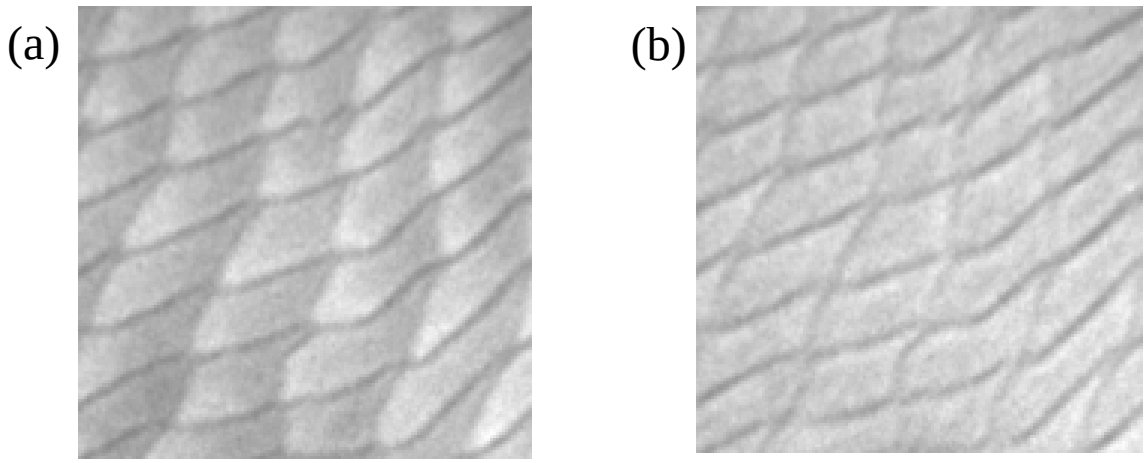

Figure 4. A close up of an area from the image figure 3(a), showing the LEEM contrast gradient across individual terraces. A close up of an area from the image figure 3(b), showing the steps bordering individual terraces.

(a)

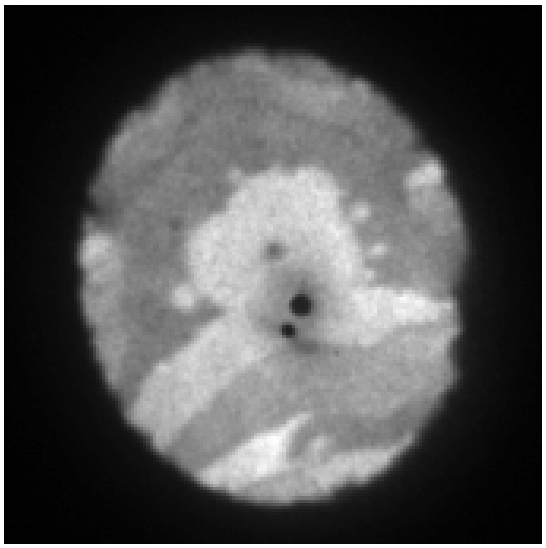

(b)

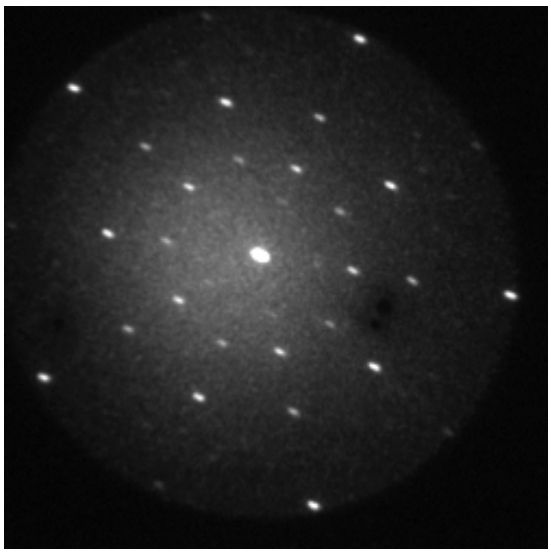

Figure 5. (a) SAD BF-LEEM image at 6.5eV at 300K. The image size is 1.75μm. (b) a LEED pattern from (a) at 11.9eV. Image numbers for (a) is 122007000007 and for (b) is 122007000009.

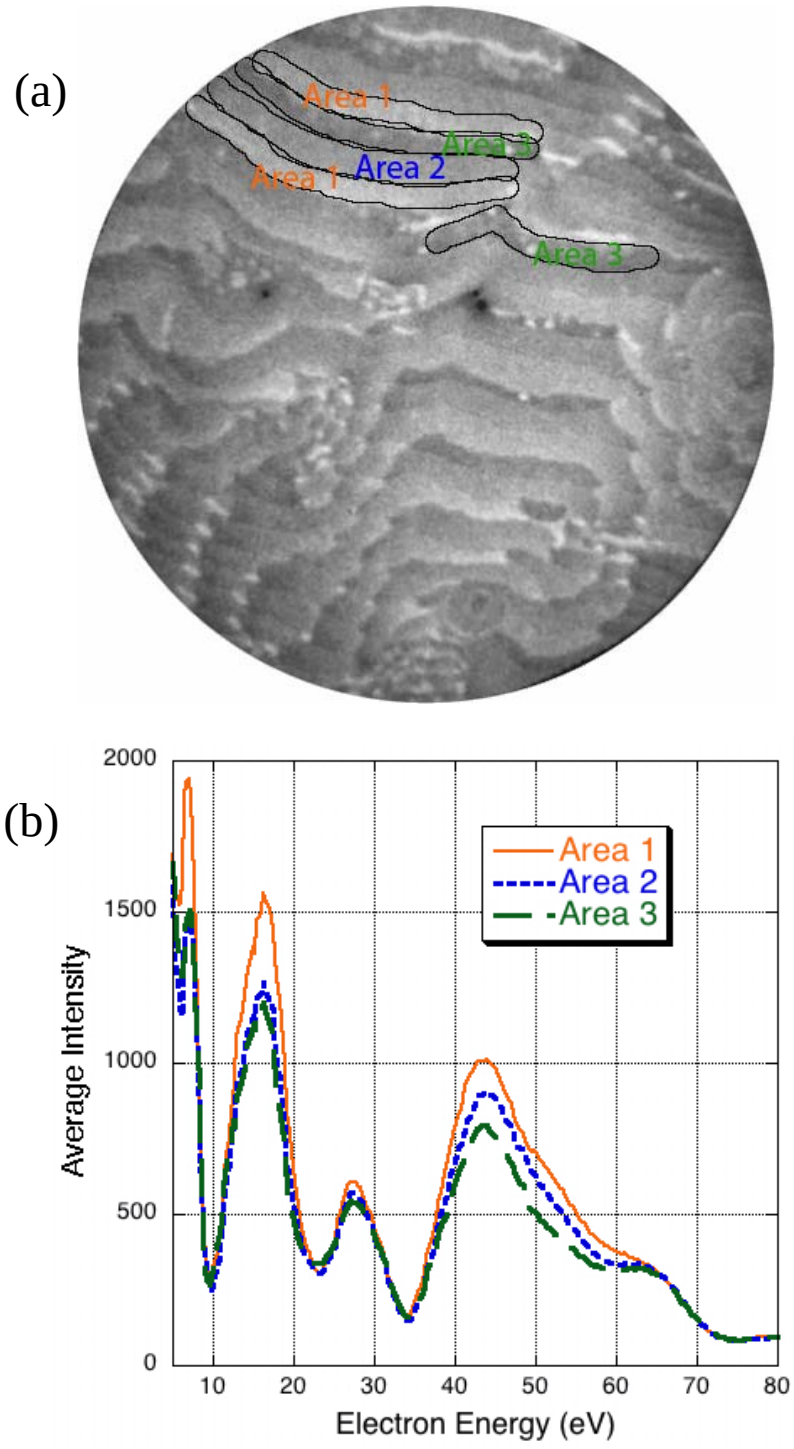

Figure 6. (a) A BF-LEEM image with three types of contrast at 300K. (b) LEEM-IV curves from the regions in (a). The file number is 122007e.

Figure 7 shows two bright-field LEEM-IV curves of the specular beam (00000) at 300K and 873K. The difference in the curves suggests that the high and the low temperature surfaces of the quasicrystal are different at least for this particular i-Al-Pd-Mn qc under the specific surface preparation.

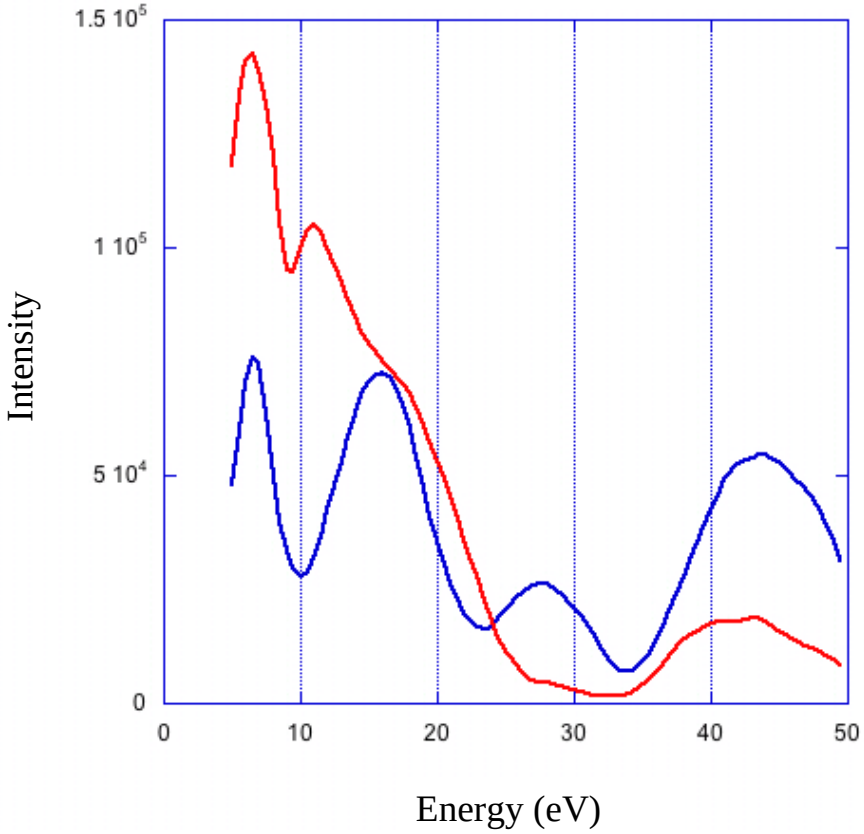

Figure 7. Bright-field LEEM-IV curves of the specular beam (00000). Blue is at 300K and red is at 873K. The file numbers for blue curve and red curves are 122107p and 122107m, respectively.

ACKNOWLEDMENTS

I would like to express my sincere appreciation to Professor Patricia A. Thiel for her support, guidance, and encouragement throughout my graduate study and my life in Ames, Iowa. I deeply appreciate the flexibility and independence that she provided during my PhD study. I am also grateful for her introducing me to the wonderful world of the quasicrystals, which still fascinates me. I must also thank her for giving me the opportunity to do research both in Lawrence Berkeley National Laboratory and in Sandia National Laboratories.

Starting from the first day, it has been absolutely enjoyable for me doing research with Pat and her group members. I am and I will always be proud of being a member of the Thiel's group.

I would like to express my sincere gratitude to Professor James W. Evans for the support and guidance that he has given me along the way. I have greatly appreciated the knowledge that he passed along to me about the modeling of thin film nucleation and growth. He was always there whenever I had a question.

I also wish to thank to all members, former and present in the Thiel and Evans research groups, who provided me the cooperative, friendly and supportive working atmosphere. Those are, including but not limited to, Dr. Cynthia Jenks, Dr. Erik Cox, Dr. Da-Jiang Liu, Dr. Feili Qin and Dr. Jack Barrow who was the first introducing the basics of the UHV to me in the beginning of my PhD journey. I do still remember the first STM image from a quasicrystal surface, which Jack and I took together and his impression was "Here you go man!… You have a nice surface and everything is working… Do your PhD!…"

My further gratitude goes to Dr. Andreas Schmid at Lawrence Berkeley National Laboratory. I really enjoyed doing research with him. I will never forget the time we spent together. Thanks to Dr. Kevin McCarty at Sandia Laboratories. The dinners we had around 1:30 to 2:00 am after the long LEEM experiments were unforgettable. I have not tasted better waffles than the one he made for me. They were just great! Thanks to Dr. Yu Sato. I enjoyed the time we spent together with the LEEM.

Many thanks to Professor Dan Shechtman. He always opened his doors with a big, sincere smile on his face whenever I had questions about quasicrystals. Many thanks to Professor Michael Tringides for the fruitful and enlightening QSE discussions. Thanks to Dr. Myron Hupalo. I always enjoyed talking with him about the STM/STS.

I would like to send a special thank to Professor Mufit Akinc who was the person suggested me to apply to the MSE PhD program in ISU, and he helped me during the first critical months of my life in Ames.

My thanks also go out to my friend, Emrah Simsek. Whenever I wanted to have coffee, he was always there to be my company. Without him, probably I have never learnt the details of ISU campus. I always enjoyed his company…

Finally, I wish to thank my family for the care, faith and the moral support. To my beautiful wife, Gülden: You had no idea when I said I would like to go to Ames, IA, USA for PhD study. You came with me without any hesitation, and left your family and your friends to start a new life with me in USA. You never complained about my work schedule even the times when I did not come to home because of long STM experiments. I am sincerely grateful to you for being so supportive of me and letting me do what I like to do the most,

research! Thank you for the care and the faith. Without your moral support, my life in USA would have been much tougher…